eman ta zabal zazu

Universidad del País Vasco
Euskal Herriko Unibertsitatea

Iridium(III)-based photoluminescent sensors for Ba^{2+} tagging: toward background-free Ba^{2+} sensing.

Ane Izaskun Aranburu Leiva

Doctoral Thesis

Supervisors: Dr. Zoraida Freixa and Dr. Fernando Cossio

Donostia, 2023

TABLE OF CONTENTS

GLOSSARY OF TERMS AND ABBREVIATIONS

$\beta\beta0\nu$	Neutrinoless Double Beta Decay
$\beta\beta2\nu$	Double Beta Decay
τ	Lifetime
Φ	Quantum yield
K_a	Association constant
AcOEt	Ethyl acetate
THF	Tetrahydrofuran
MeCN	Acetonitrile
DMSO	Dimethyl sulfoxide
EtOH	Ethanol
Et_3N	Triethylamine
MeOH	Methanol
DMF	Dimethylformamide
DME	Dimethoxyethane
DavePhos	2-Dicyclohexylphosphino-2′-(N,N-dimethylamino)biphenyl
XPhos	2-Dicyclohexylphosphino-2′,4′,6′-triisopropylbiphenyl
dba	Dibenzylideneacetone
dppf	1,1′-Ferrocenediyl-bis(diphenylphosphine)
NMR	Nuclear Magnetic Resonance
COSY	Correlated spectroscopy
DOSY	Diffusion-ordered spectroscopy
APT	Attached proton test
HMBC	Heteronuclear Multiple Bond Correlation
J	Coupling constant
m	multiplet

s	singlet
t	triplet
d	doublet
DFT	Density functional theory
ppy	Phenylpyridine
Bpy	Bipyridine
MLCT	Metal to ligand charge transfer
ILCT	Intraligand charge transfer
LLCT	Ligand to ligand charge transfer
MC	Metal centered charge transfer
HB	High energy band
LB	Low energy band
LUMO	Lowest Unoccupied Molecular Orbital
HOMO	Highest Occupied Molecular Orbital
ISC	Intersystem crossing
IC	Internal
IUPAC	International Union of Pure and Applied Chemistry
MW	Microwave

Chapter 1

Introduction

1.1 LEITMOTIV OF THIS THESIS

Scientists think that **matter and antimatter** were produced in equal amounts when the universe formed. Yet, the universe we inhabit appears to be made entirely of matter. So, where did antimatter end up?

In 1928, Paul Dirac predicted the existence of antimatter when he successfully merged Einstein's theory of special relativity with quantum mechanics. His equations had two solutions. One explained the ordinary electron while the other solution was the negative of the first, electron antiparticle, the positron. In 1932, the existence of antimatter was confirmed by the discovery of the positron by Carl Anderson. Antimatter particles present the same mass as their matter counterparts, but qualities such as the electric charge are opposite. Thus, the positively charged positron is the antiparticle to the negatively charged electron.

These particles, electron and positron, were defined as Dirac fermions, particles with spin ½ that are different from their antiparticle. Fermions and bosons are the two fundamental classes of subatomic particles (**Figure 1.1**). Fermions include all quarks and leptons and all composite particles made of an odd number of these. For instance, the proton is also a fermion, a composed fermion, it consists of two up quarks and a down quark and its antiparticle is the antiproton, is made of two up antiquarks and one down antiquark.

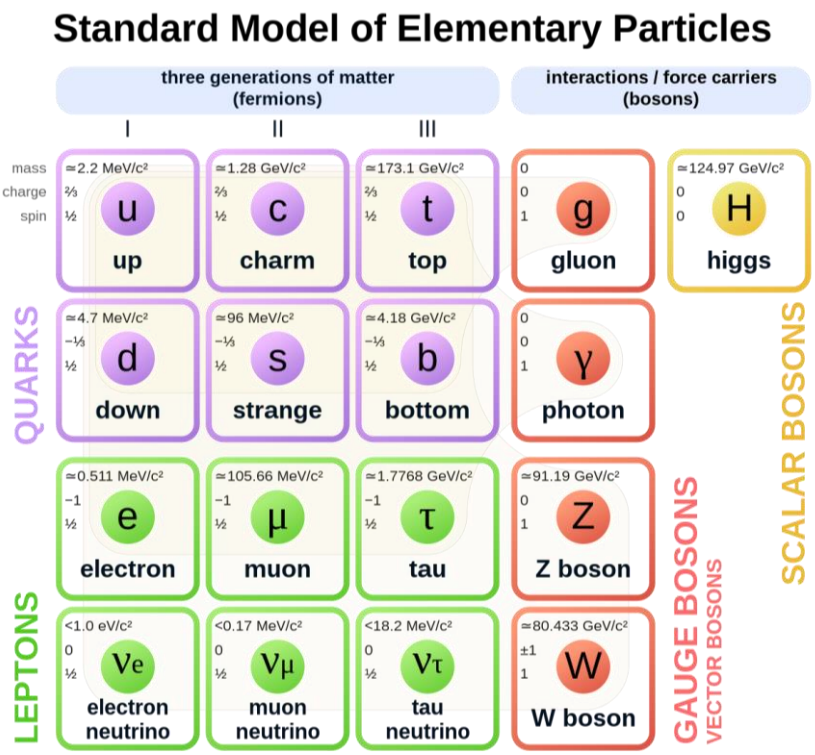

***Figure 1.1**. The Standard Model of particle physics was developed in stages throughout the latter half of the 20th century. It classifies all known elementary particles.*

Within the fermions, **Dirac fermions** refer to the particles that are different from their antiparticles (**Figure 1.2**). With the exception of neutrinos, all of the Standard Model fermions are known to behave as Dirac fermions. Whenever a Dirac fermion (e.g. electron) encounters its antiparticle (e.g. positron), they will annihilate each other, leaving behind pure energy. If, matter and antimatter, particle and antiparticle, are created in equal amounts and destroyed together in pairs, it seems the universe should contain nothing but leftover energy.

However, in 1937 an Italian physicist, Ettore Majorana, predicted the existence of another type of fermion: those in which a particle is its own antiparticle (**Figure 1.2**). Physicists have hypothesized that neutrinos—one of the most abundant fundamental particles in the universe—could be **Majorana fermion**. The neutrino being a Majorana fermion could be the answer to the origin of the matter observed in the universe today.

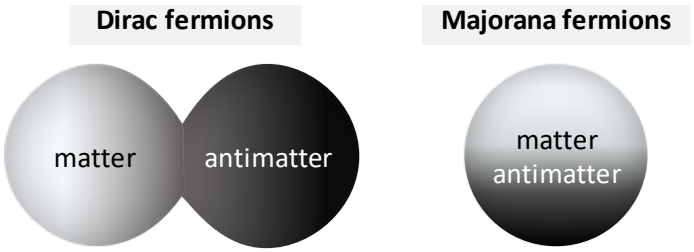

Figure 1.2. *An abstract illustration of Dirac and Majorana fermions behavior of matter and antimatter.*

The **neutrino**, ν, is a neutral elementary particle with spin of ½, classified as fermion (**Figure 1.1**). It is so named because it is electrically neutral (*neutr-*) and because its rest mass is so small (*-ino*) that particle physicists originally believed that neutrinos were massless. Thus, neutrinos typically pass through normal matter unimpeded and undetected. To the extent that despite their abundance, neutrinos are some of the most elusive particles to detect.

Pauli formulated the original idea of neutrinos existence in response to a problem in a beta decay, β, a process in which a neutron converts into an electron and a proton (**Figure 1.3**). The problem was that energy seemed to disappear in the reaction. Wolfgang Pauli proposed the solution in 1930, in what he called a "desperate remedy": a non-interacting particle was emitted in the decay process, a neutrino, with the missing energy.[1] Several decades later, in 1998, a team of Japanese scientists, working with the Super-Kamiokande detector, discovered that neutrinos actually have a mass.[2] Nevertheless, the nature of the neutrinos is not settled yet—they may turn out to be either Dirac or Majorana fermions.

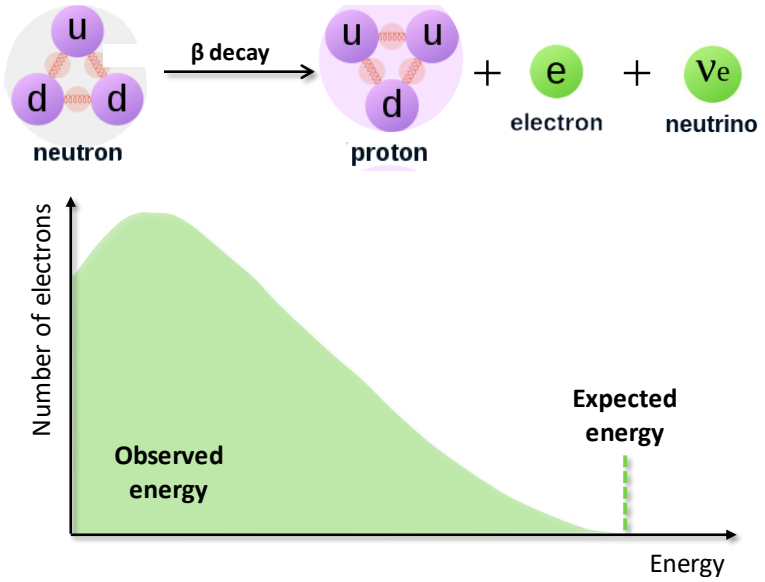

Figure 1.3. *β decay of a neutron and the expected vs observed energy of the created particles.*

To test the neutrinos' intrinsic nature, whether the neutrino is its own antiparticle, the physicists are looking for a **neutrinoless double beta decay**, 0νββ process. This is the only process known so far that could be able to experimentally demonstrate that neutrinos are Majorana particles. Thus, in the last two decades, the search for *neutrinoless double beta decay* phenomenon has evolved into one of the highest priorities for understanding neutrinos and the origin of matter.[3–6] In the next paragraphs, the neutrinoless double beta decay will be explained starting from the simple single beta decay process.

In nuclear physics, a beta decay is a type of radioactive decay in which a beta particle – fast energetic electron or positron– is emitted from an atomic nucleus. In beta plus decay, β^+, the proton is decayed to a neutron, forming a positron and a neutrino. On the contrary, in a beta minus decay, β^-, as illustrated in A in **Figure 1.4**, a neutron is converted to a proton, and in the process, an electron and an antineutrino are created.

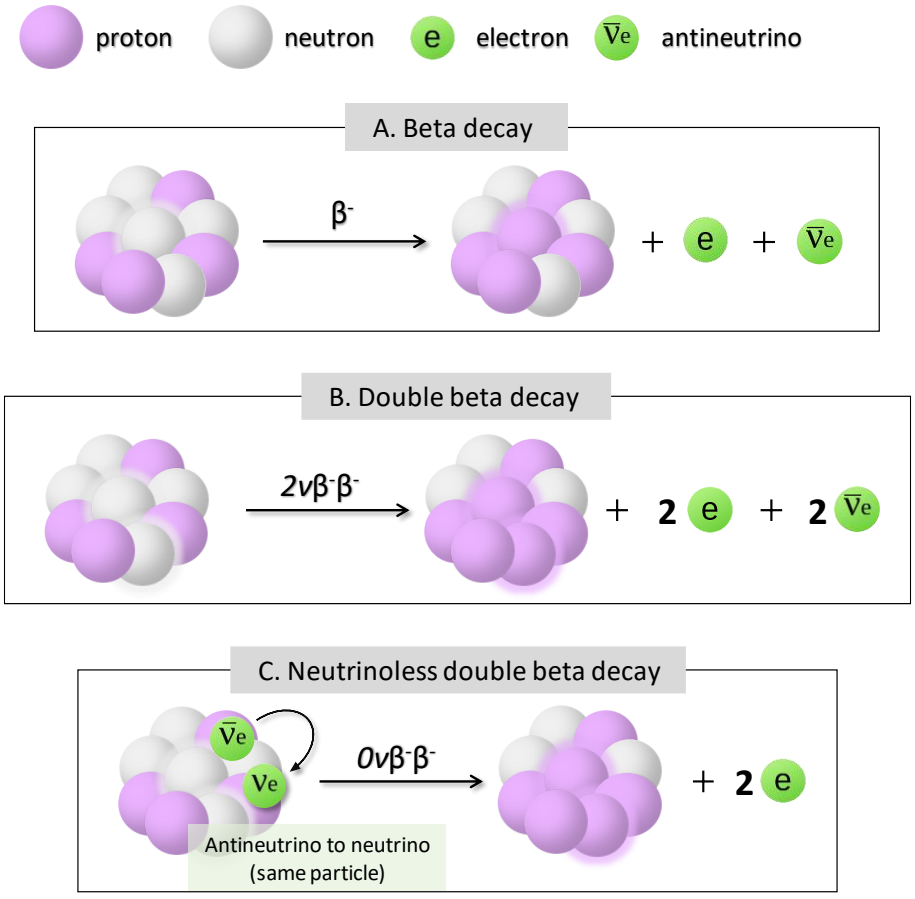

Figure 1.4. *The β decay processes explained in this section; all of them β⁻, a decay from a neutron to a proton.*

Double beta decay ($\beta^-\beta^-$), B in **Figure 1.4**, is a type of radioactive decay in which two neutrons are transformed simultaneously into two protons, inside an atomic nucleus, emitting two electrons and two antineutrinos. Thus, as represented in equation 1, an initial nucleus (A, Z), with total nucleon number A and proton number Z decays to $(A, Z+2)$:

$$(A, Z) \rightarrow (A, Z+2) + 2e^- + 2\bar{\nu}_e \qquad (1)$$

Double-beta decay was first considered in a 1935 paper by Maria Goeppert-Mayer.[7] She calculated and applied the probability of the simultaneous emission of two electrons and two neutrinos from two neutrons present in the same nuclei. Unstable nuclei may undergo 2νββ if single β-decay is energetically forbidden. Which means that, whereas in beta decay the Z+1 nucleus is more strongly bound than Z+2 and, for this reason, only occurs a single decay, the reverse situation occurs in a double beta decay process. Few nuclei are

capable of decaying via double beta decay, for example isotopes such as ^{48}Ca, ^{76}Ge, ^{96}Zr and ^{136}Xe, and they have typical lifetimes in the order of 10^{19}–10^{21} years.

As mentioned before, another type of double beta decay has been hypothesized, the neutrinoless double beta decay 0νββ, where only electrons would be emitted (C in **Figure 1.4**). This hypothesis has never been observed, which could only occur if the neutrino is a Majorana particle. It features the emission of one antineutrino turning into a neutrino to be absorbed by another nucleon, being an antineutrino and a neutrino the same particle i.e. a Majorana particle. In the final state, the only remaining entities are the nucleus with its changed proton and two electrons, as shown in equation 2:

$$(A, Z) \rightarrow (A, Z + 2) + 2e^{-} \qquad (2)$$

In such a manner, the sum of the energy of the electrons would be equal to the nuclei's energy loss. The experimental search for 0νββ is based on the detection and exact measurement of the sum of the kinetic energies of the two emitted electrons, and a sharp peak in the energy spectrum is the prime signature for all 0νββ experiments, illustrated as the orange peak in **Figure 1.5**. Therefore, if this peak happened, the Majorana character of the neutrino could be confirmed.

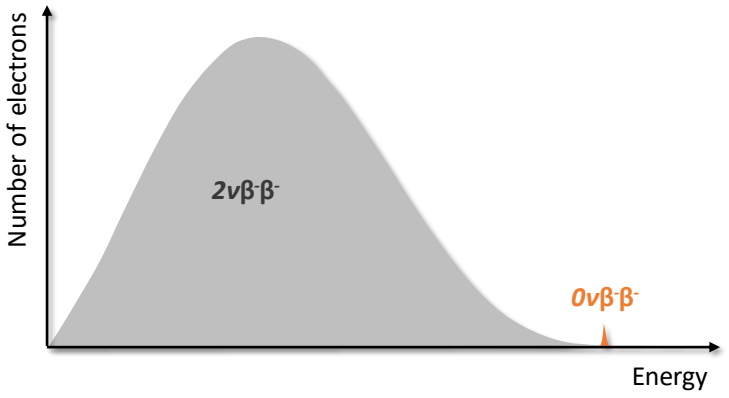

Figure 1.5. *Energy difference of the electron produced in a 2νββ or 0νββ decay.*

Double β decay, ββ, experiments have been searching for 0νββ phenomenon in several isotopes for more than half a century without finding clear evidence of a signal so far. In principle, 35 nuclei can undergo 0νββ, although realistically only nine emerge as interesting candidates and are under investigation in competitive experiments (**Figure 1.6**): ^{48}Ca, ^{76}Ge, ^{82}Se, ^{96}Zr, ^{100}Mo, ^{116}Cd, ^{130}Te, ^{136}Xe and ^{150}Nd.[8] None of them has shown

yet to be the ideal isotope for the experiment since factors such as the natural abundance, reasonably priced enrichment, and a well-understood and controlled experimental technique have to be conciliated.

Various experiments have been developed to pursue the 0νββ phenomenon; some of them are already acquiring data and many under progress for future improved experiments. To mention some examples, NEMO, the Neutrino Ettore Majorana Observatory, is a collaboration that started in the early 90s to search for 0νββ in elements such as ^{100}Mo and ^{82}Se. GERDA, the Germanium Detector Array, for instance is searching the double beta decay in ^{76}Ge at the underground Laboratori Nazionali del Gran Sasso. The ^{136}Xe is used in EXO experiment, Enriched Xenon Observatory, in the United States. In this case, the prototype has a 200 kg xenon liquid chamber with which the ^{136}Xe double beta decay was detected and limits were set for 0νββ. All these experiments are set in underground laboratories, due to the expected low rate of 0νββ events, to minimize the background radiation problem.

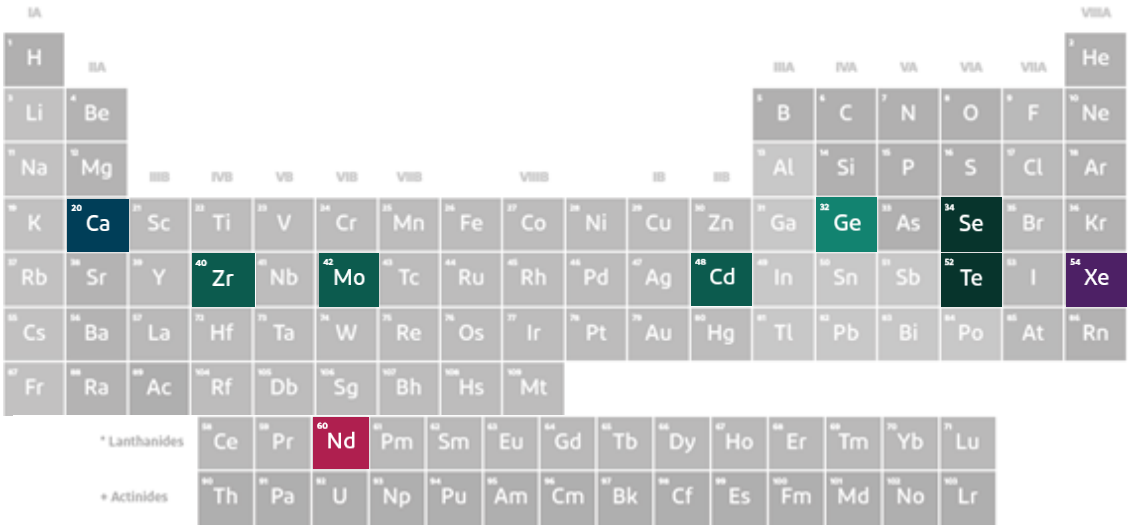

Figure 1.6. *Periodic table with highlighted elements employed to search the 0νββ decay.*

In this context, the **NEXT** experiment is an international collaboration that searches for the neutrinoless double-beta decay at the Canfranc Underground Laboratory in Canfranc, Huesca. NEXT stands for Neutrino Experiment with a Xenon TPC, therefore the detection concept consists of a Time Projection Chamber filled with high-pressure gaseous Xenon (HPXe-TPC), illustrated in **Figure 1.8**. In this case, the pursued event is

the neutrinoless double beta decay of ^{136}Xe, which would result in the formation of a doubly charged barium cation and two electrons (**Figure 1.7**).

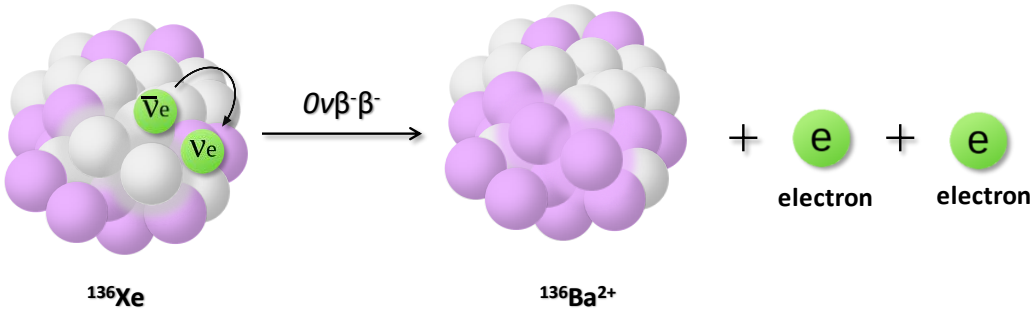

Figure 1.7. *The 0νββ decay of Xenon-136 to the dicationic Barium-136.*

As mentioned before, for this type of experiment, due to the large lifetime of a 0νββ decay of ^{136}Xe (which its lower limit set at 10^{26} years), a detector with very good energy resolution, very low background contamination and large target mass is needed. In general, in this type of search, the energy of the two electrons emitted in the double beta decay constitutes the most common observation exploited. This measurement differentiates between 0νββ and 2νββ events, the most common background process, as the summed energy of the electrons differs (**Figure 1.5**). Thus, the use of a detector with excellent energy resolution is necessary.

Nevertheless, the differentiation between 2νββ and 0νββ decays is not enough. External background processes, produced by cosmic rays and other radioactive isotopes present on the detectors materials can hinder the resolution of the experiment. In order to get rid of the background or spurious signals produced by these external sources, the experiments are built with ultrapure materials, operated in underground laboratories (to mitigate the impact of cosmic rays) and are protected by massive ultrapure shields. Nonetheless, to reach a background-free state, the synchronous detection of the formed barium cation seems reasonable, as in pure xenon gas, no known radioactive process will produce this ion in coincidence with two ejected electrons. As explained before, the double beta decay process transforms the parent nucleus (^{136}Xe, in our case) to a daughter nucleus (^{136}Ba), emitting two electrons and two antineutrinos (if the standard 2νββ mode). Then, if one was able to detect the barium nuclei, in coincidence

with the two emitted electrons, it will be immediate to separate background events from those electrons coming from double beta decays.

The possibility of barium-tagging in a xenon Time Projection Chamber was proposed in 1991 by Moe for the first time:[9]

> A distinctive feature of the double-beta-decay signature that has been neglected in direct counting experiments is the appearance of the daughter atom. The newly created nucleus, usually being stable, is not easily detected. The atomic physics of the daughter, however, may be considerably more accommodating, especially in the case of ionized ^{136}Ba arising from the double-beta decay of ^{136}Xe. The barium ion isolated in the xenon matrix may be detectable by its laser fluorescence. Coincident detection of the ion and the beta particles could well render background non-existent.

Since its proposal, over the last 20 years, the research in this field has incremented. Recently, in 2019, the nEXO collaboration used the counting of individual barium atoms in a solid xenon matrix.[10] The authors studied a tagging scheme using a cryogenic probe to trap the barium atom in a solid xenon matrix, where the barium atom is tagged through fluorescence imaging. They demonstrate the imaging and counting of individual barium atoms in solid xenon by scanning a focused laser across a solid xenon matrix deposited on a sapphire window.

In 2015, Nygren proposed the employment of a fluorescent molecular indicator as Ba^{2+} detector.[11] A fluorescent molecular indicator or sensor is a molecule with a response to optical stimulation that changes when it forms a supramolecular complex with a specific ion. Nygren hypothesized that the molecular indicator could be incorporated within a high-pressure gas xenon TPC and, by single-molecule fluorescence imaging techniques (SMFI), the detection limit of a single Ba^{2+}-bound sensor could be reached. **Figure 1.8** illustrates a simplified design of an HPXe-TPC. By applying an electromagnetic field to the detector, the electrons will travel towards the positively charged area (anode) of the detector. Once the electrons are mapped and their energy and drift properly checked, the trajectory of the heavier and slower Ba^{2+} cation could be anticipated to the point of

arrival on the cathodic side, where a monolayer of fluorescent sensors able to capture the daughter cation would be settled.

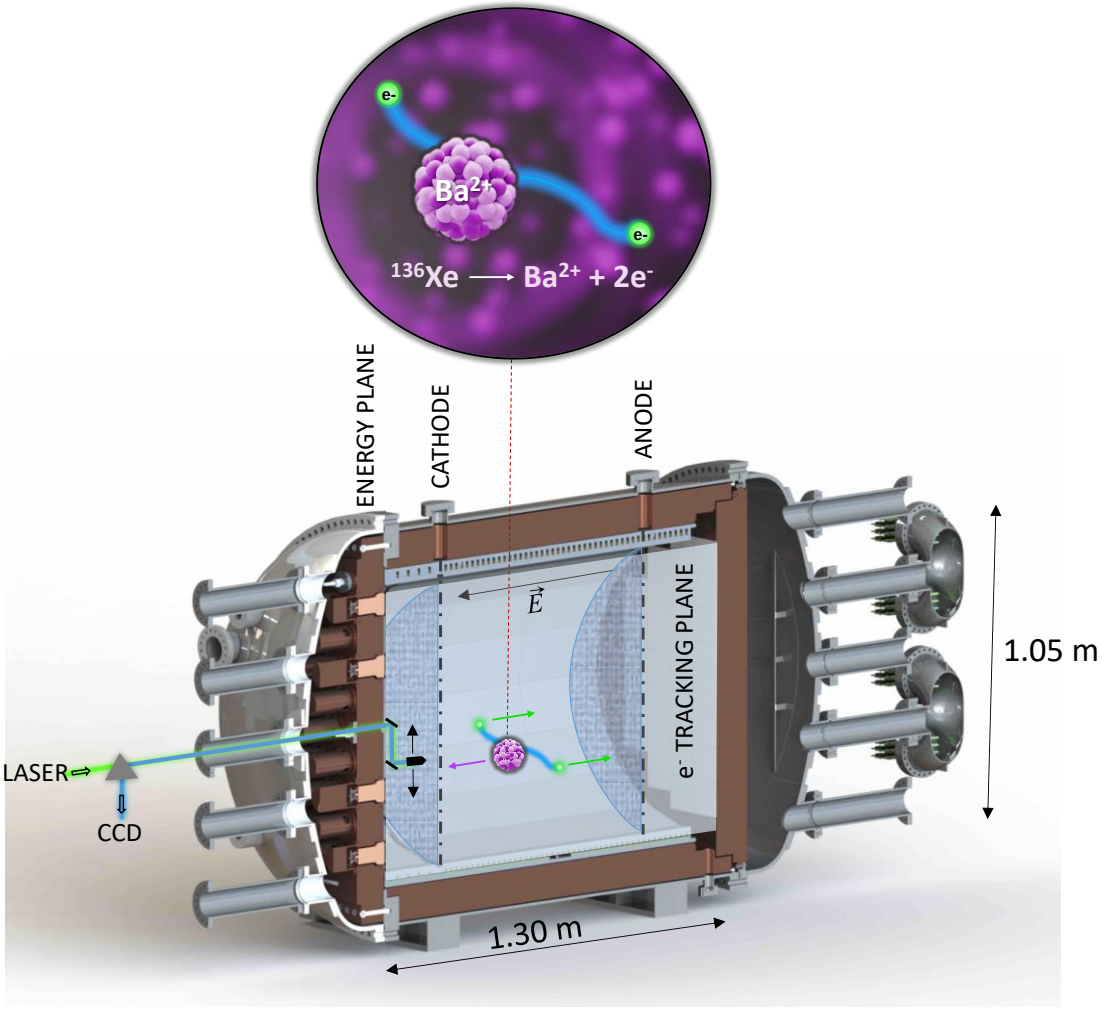

Figure 1.8. *A simplified scheme of an HPXe-TPC design, with the illustration of the paths of Ba^{2+} cation and the electrons.*

The concept of the fluorescence molecular indicator for Ba^{2+} was further developed by the same group and was followed by an initial proof-of-concept study.[12,13] In the study, individual Ba^{2+} ions were resolved on a thin quartz plate employing a commercial indicator Ca^{2+}, suspended in polyvinyl alcohol (PVA) to immobilize the molecular complex and facilitate optical imaging. However, this proof-of-concept is far from the ideal system. As listed by Woodruff et al., a barium sensor suitable for ion tagging in 0νββ needs to fulfill some requirements:[14] long excitation and emission wavelengths (> 350 nm), strong fluorescence of the barium-bound state together with a suppressed emission of the free state in the dry phase, a sufficient Stokes shift to allow dichroic

separation of excitation and emission light, etc. Besides, the surface density of indicators in the sensor needs to be high to ensure maximum ion capture efficiency.

In the last few years, inside the NEXT collaboration, many efforts have been put in the optimization of the design of these photoluminescent molecular indicators and their implementation for barium tagging. These approaches will be described in the following sections.

This thesis is part of the chemical R&D effort to implement Ba^{2+} tagging in the NEXT experiment using photoluminescent sensors.

1.2 PHOTOLUMINESCENT CHEMOSENSORS

The IUPAC defines a chemical sensor as:[15]

> A device that transforms chemical information, ranging from the concentration of a specific sample component to total composition analysis, into an analytically useful signal. The chemical information, mentioned above, may originate from a chemical reaction of the analyte or from a physical property of the system investigated.

A chemosensor, on the contrary, refers to the chemical origin of the sensor itself. It is associated with the creation of receptors from non-biological chemical entities. The idea of creating receptors from non-biological chemical entities most often means that chemical synthesis is used to create unnatural receptors, which are, likewise called "synthetic receptors."

In the context of designing and synthesizing a specific molecule to interact with a barium cation and formulate a recognizable signal, the desired indicator could be defined as a chemical chemosensor. Molecular sensors, or chemosensors, may be classified according to the operating principle, such as optical, electrochemical, magnetic or mass-sensitive sensors. Optical sensors are further subdivided based on the optical property they operate in (chemiluminescence, absorbance, reflectance, fluorescence…). Among these, photoluminescent molecular sensors are sensitive analytical tools for rapid chemical and biochemical measurement, widely utilized for the detection of

biomolecules or metal ions, due to their high sensitivity, high specificity, immune to light scattering, and ease of operation.[16–18] The first fluorescent chemosensor was described by F. Goppelsröder in 1867 for the determination of Al^{3+}.[19] Since then, photoluminescent chemosensors have become a very attractive research area with important applications in environmental science, analytical or biomedical chemistry, showing great promise in real-world situations and applications, including but not limited to: the detection of environmental waste pollutants, detection of chemical warfare agents, fluorescence guided surgery, whole body diagnostic imaging, etc.

In the following sections, a description of the photoluminescence phenomenon and a general picture of the structure, luminescent response and operating mechanisms of chemosensors are presented. The diverse mechanisms will be introduced with reported examples of luminescent sensors capable of sensing cations.

1.2.1 Photoluminescence

The emission of light from a material following the absorption of light or photon is defined as photoluminescence. The emitted photons energy will usually be lower than the absorbed one, because some of the energy will be lost during relaxation. Rates of emission can vary over a very wide range, depending on whether the transition is spin- and symmetry allowed or forbidden. When luminescence is due to a spin-allowed transition then it is called fluorescence, otherwise, phosphorescence.

When an atom absorbs an incoming photon, the energy of that photon can excite one of that atom's electrons to a higher energy level. Once the electron is in the excited state, many relaxation phenomena can occur in a molecule. Yet just the fluorescence and phosphorescence and a number of concepts related to these processes will be explained in more detail, as they are of our interest. The Jablonski diagram is a powerful tool for visualizing the possible transitions that can occur after a molecule has been photoexcited. A typical Jablonski diagram is shown in **Figure 1.9**.

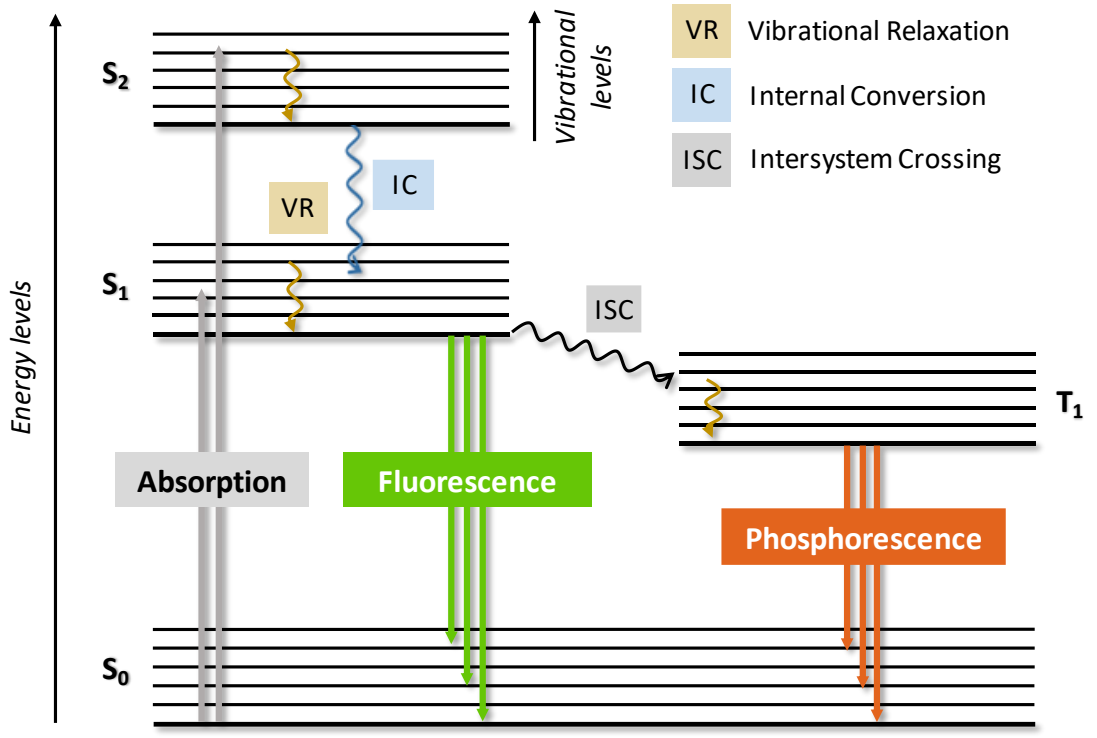

Figure 1.9. *Jablonski diagram of fluorescence and phosphorescence processes and other non-radiative processes.*

When a photon is absorbed by the molecule, one electron is promoted to a higher energy level and the molecule is now in an excited state. The ground state of a molecule is (almost) always a singlet state (S_0) and, at room temperature, the majority of molecules in a population will be in the lowest vibrational level of the ground state (Boltzmann distribution) and absorption is therefore shown to start from this level. Due to conservation of spin –Spin Selection Rule– absorption of a photon promotes the molecule from the S_0 to one of the vibrational levels of the singlet excited states (S_n). It is the fastest transition in the Jablonski diagram, occurring on a timescale of order 10^{-15} s.

The promoted molecule will first lose the gained energy by vibrational relaxation pathways. This can occur in an intramolecular way or to surrounding molecules intermolecularly (e.g. solvent), until the lowest vibrational level of the electronic state is reached. From S_2 to the lower lying single state can also occur by internal conversion (IC). The decay of the S_1 state back to the S_0 is an allowed transition (since both states have the same spin multiplicity) resulting in photoluminescence called fluorescence that occurs in the picoseconds to nanoseconds time scale. However, sometimes, intersystem

crossing (ISC) can happen from S_1 to T_1, depending on the nature of the excited molecule. As stated before, this intersystem crossing to the triplet state T_1 is a forbidden transition in idealized conditions, as it would violate the spin selection rule by undergoing a spin conversion. However, when a heavy atom is present in the molecule spin-orbit coupling between the spin angular momentum and the orbital angular momentum makes it weakly allowed, giving rise to spin-forbidden bands. That is, allowing singlet-triplet transition to happen. In these cases, the result is the relaxation from T_1, defined as phosphorescence. This phosphorescence is lower in energetic radiation, and the decay rate to the ground state S_0 is slower compared to fluorescence (from microseconds to seconds time scale).

Several photoluminescent parameters are used to describe the performance of a luminescent molecule. The molar absorption coefficient ε, also known as the extinction coefficient, is a measurement of how strongly a chemical species absorbs light at a given wavelength. In other words, it refers to how well the species absorbs the particular wavelength of radiation that is being shined on it. It is an intrinsic property of the species. The Beer Lambert law, in equation 3, relates the absorbance to the molar absorption coefficient, c being the molar concentration of the dissolution measured and *l* the optical length path.

$$A = \varepsilon \cdot c \cdot l \tag{3}$$

The lifetime, τ, is a feature related to the emission, which is a measure of the time spent by a molecule in the excited state. These values, for organic molecules would be around 10^{-9}-10^{-7} s. On the contrary, for metal complexes they become longer by orders of magnitude. For example in the case of $[Ru(bpy)_3]^{2+}$, because of the presence of a Ru(III) ion, the lifetime of the lowest spin forbidden excited state is about 1 μs in MeCN.[20] This parameter allows us to sub-classify the process into fluorescence and phosphorescence.

The quantum yield, Φ, expresses the ratio between the number of molecules undergoing a photo-initiated process and the number of absorbed photons (equation 4), which for emitting fluorophores would mean the ratio between the number of photons emitted divided by the number of photons absorbed. It describes how efficiently a fluorophore converts the excitation light into luminescence.

$$\Phi_f = \frac{Number\ of\ emitted\ photons}{Number\ of\ absorbed\ photons} \quad (4)$$

Notably, quantum yield is independent of instrument settings, however the environment can affect quantum yield, usually resulting from changes in the rates of non-radiative decay. Fluorescence quantum yield is measured on a scale from 0 to 1.0, but is often represented as a percentage. If a process has several steps, the final quantum yield will be the multiplication of the quantum yield of the several processes. Fluorescence quantum yields are measured by comparison to a standard of known quantum yield or in the absolute quantum yield method, an integrating sphere is used to capture all light emitted by the sample, avoiding the need for a reference standard.

The Stokes shift is referred to the difference, in energy, wavenumber or frequency units, between positions of the band maxima of the absorption and emission spectra of the same electronic transition (**Figure 1.10**). When a molecule (in its ground state) absorbs a photon, it gains energy and converts into its excited state. Before the emission of the photon, the molecule will relax and consequently, the emitted photon has less energy than the absorbed photon, this energy difference being reflected in the Stokes shift. It is primarily the result of two phenomena: vibrational relaxation and solvent reorganization.

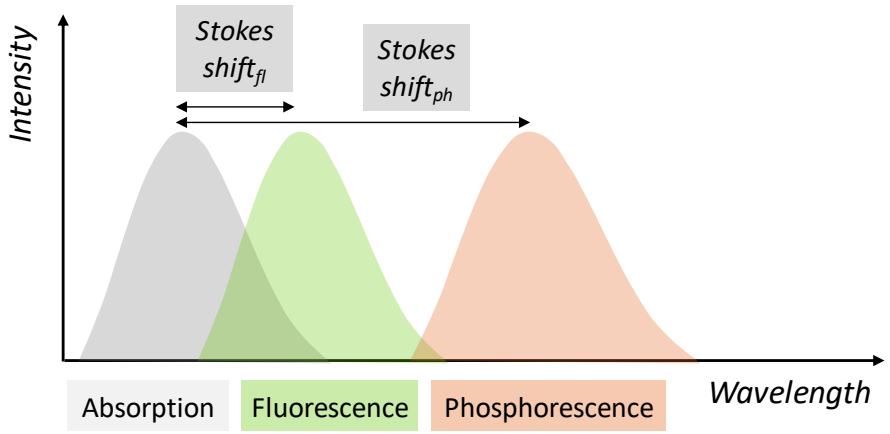

Figure 1.10. *Representation of the Stokes shift of a fluorescence and a phosphorescence emission.*

The photophysics of organic compounds is usually characterized by typically small Stokes shifts, meaning that their absorption and emission profiles are overlapping to some extent. On the other hand, the emission from phosphorescent metal complex is

characterized by a relatively large Stokes shift. This shift originates from the fact that the intersystem crossing between the singlet and triplet state of the same excited electronic configuration is accompanied by a stabilization, which means that the energy gap between the excited state and ground state is reduced, and hence the emission profile is red-shifted.

The terms bathochromic or red-shifted, refer to the shift of an absorption or emission band to higher wavelengths (i.e. lower energy, see **Figure 1.11**). On the contrary, hypsochromic or blue-shifted is employed when the absorption or emission band shifts to lower wavelengths (i.e. higher energy). The Intensity of a spectral band can increase or decrease, defined as hyperchromic and hypochromic events, respectively.

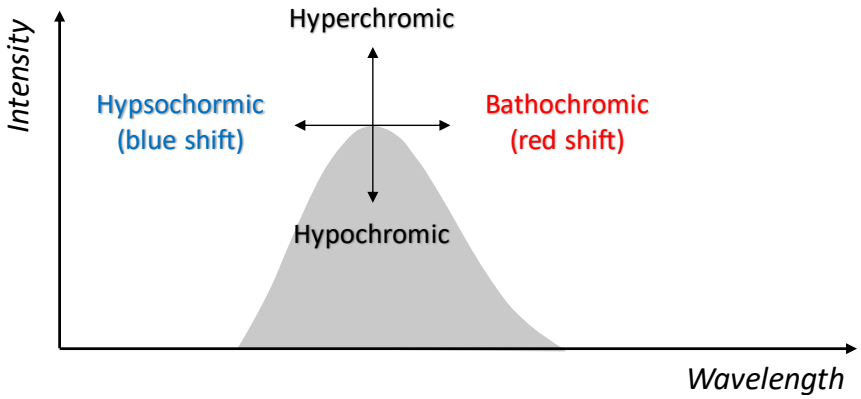

Figure 1.11. *Representation of the possible shifts a band can suffer.*

In terms of photoluminescent chemical sensing, all the photoluminescence parameters described in this section will affect the performance of the sensor.

1.2.2 Chemosensors

In general, the structure of the molecular sensors consists of two main parts: namely, a receptor or binding site and a signaling unit or fluorophore (**Figure 1.12**). The binding site provides fast and reversible binding to the analyte and is responsible for its selective capture. The fluorophore is the domain responsible of signaling the recognition event. Optionally, a linker or/and spacer are added to the design. Adding a linker can permit the sensor to anchor on a suitable surface or biomolecule.

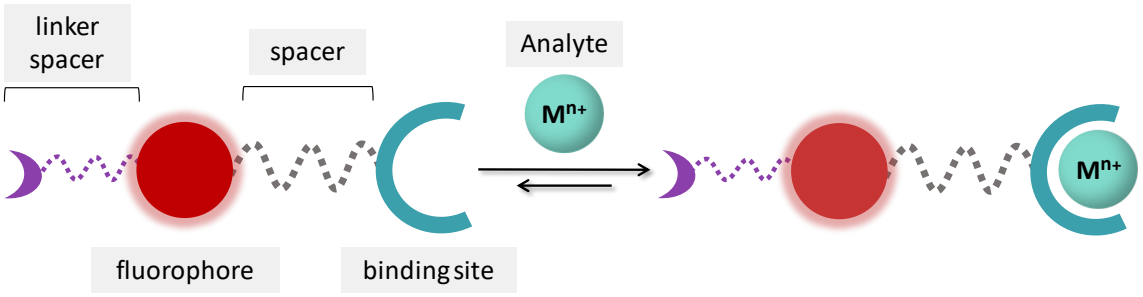

Figure 1.12. *Structure of a chemosensor, used for sensing of an analyte to produce a detectable signal.*

In supramolecular chemistry, the sensor (present in larger quantities) is commonly defined as guest, while the target analyte is referred as host, deriving in the widely known concept "host-guest" chemistry. Thus, most known supramolecular sensors are built on a foundation of host-guest chemistry, based on a binding-based sensing approach. This differs from reactivity-based sensing mode, which primarily relies in irreversible chemical reactions.

Often to determine attributes related to host-guest or supramolecular chemistry (selectivity and binding constant) the luminescent response of a chemosensor is used. The quantitative analysis of the intermolecular interactions is imperative to describe the sensing performance.

The sensors operation or efficiency is most commonly addressed by supramolecular titration methods. Here, the guest is gradually added to the host system while monitoring a specific spectroscopic response (NMR signal shift, UV-vis absorption on emission) that is sensitive to the supramolecular interaction of interest at meaningful concentrations. The resulting information is then compared and fitted to binding models to obtain information such as the association constant K_a and stoichiometry of the assembly. The equations 4 and 5, for instance, would belong to the equilibrium of a host-guest reaction based on a 1:1 stoichiometry.

$$H + G \rightleftarrows HG \tag{5}$$

$$K_a = \frac{[HG]}{[H] \cdot [G]} \tag{6}$$

The binding constant K_a, or association constant, is a particular case of general equilibrium constants, which measures the binding affinity between two or more molecules at equilibrium. In the host-guest or sensor-analyte context, the binding affinity describes how strongly an analyte binds its receptor. It is influenced by non-covalent intermolecular interactions such as hydrogen bonding, electrostatic interactions, hydrophobic and Van der Waals forces between the two molecules.

The presence of isosbestic points obtained in UV-vis titration experiments can indirectly state the stoichiometry of a host-guest system, which can be further studied by the method of continuous variations (Job Plot). To do this, the mole fraction of the guest is varied while keeping the total concentration of the host and guest constant. The concentration of the host–guest complex is then plotted against the mole fraction yielding a curve with a maximum. The position of the maxima determines the stoichiometry of the system, which in the case of 1:1 appears at 0.5 of the mole fraction of the guest.

Generally, achieving selective interactions between a synthetic receptor and analyte, the host and the guest, requires a knowledge of the relevant binding affinities and specificities. Designing a good sensor needs to combine it with an educated selection of a fluorescent scaffolds based on their corresponding photophysical properties. Over the past 30 years, luminescent chemosensors have evolved to incorporate many optical-based modalities and strategies. In this context, these sensors could be classified based on their luminescent response or their operating mechanism.

1.2.2.1 Luminescent response

The luminescent sensors could be classified by their luminescent response. Based on their signaling response “off-on”, “on-off” and ratiometric sensors can be distinguished. Ideally, fluorescent sensors should respond to the analyte in a reliable manner under the conditions associated with the target. In the first two types of sensors, the cation binding causes a change in the emission intensity (**Figure 1.13**). If the intensity increases (i.e. by cancelling a non-radiative relaxation process), it will derive in an “off-on” or “switch on” system. On the contrary, if the intensity decreases upon binding the analyte (i.e. by favoring a non-radiative relaxation process), it will yield the so-called “on-off” or

"switch off" system. An off-on sensor typically provides a higher signal-to-noise ratio than an on-off switch.

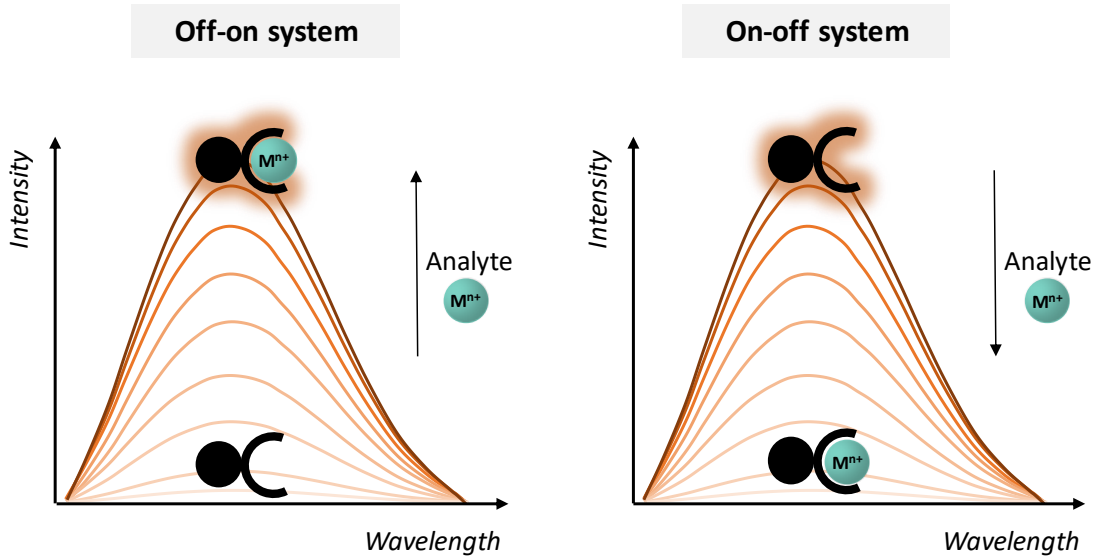

Figure 1.13. *Representation of the emission of an "off-on" and an "on-off" molecular sensor.*

However, quantification of the aimed analyte using only the emission intensity at a single wavelength can sometimes be problematic, because interferences can arise from a variety of analyte-independent factors, such as the light scattered by the sample matrix, fluctuations of the excitation source, the microenvironment around the probe, and variations of the local concentration of the probe. Thus, to obtain a reliable measurement for this type of sensors the intensity alteration, the ratio I_{on}/I_{off} in the measuring region, needs to be high enough to compensate for these residual effects.

Such drawbacks could be overcome by the simultaneous measurement of more than one spectral band, as in the so-called ratiometric response systems. By definition, ratiometric fluorescent sensors measure analyte-induced fluorescence intensity changes at two or more emission bands at different wavelengths.[21] Similar to the internal reference approach used in many other analytical methods, ratiometric fluorescence sensing features increased signal-to-noise ratio and, thus, offers a more reliable quantification.

Hence, for a ratiometric response, the free and cation-bound sensor system needs to contain two well-differentiated emission bands under the same excitation wavelength. These systems can be the result of two possible situations, illustrated in **Figure 1.14**: the

free sensor and the bound-sensor present single but clearly distinguished emission bands (a); alternatively, the free sensor is a dual emitter (with a high-energy band, HB, and a low-energy band, LB) and the ratio between this two emissions changes upon analyte binding (b). A third situation is a special case of the latter in which one of the emissions remains unaffected by cation binding (c). For ratiometric sensors, the intensity ratio difference of the two spectral bands will determine the discrimination capacity of the measurement. In other words, the variation of the intensity ratio between the low-energy band, I_{LB}, and the high-energy band, I_{HB}, is used to quantify the analyte concentration.

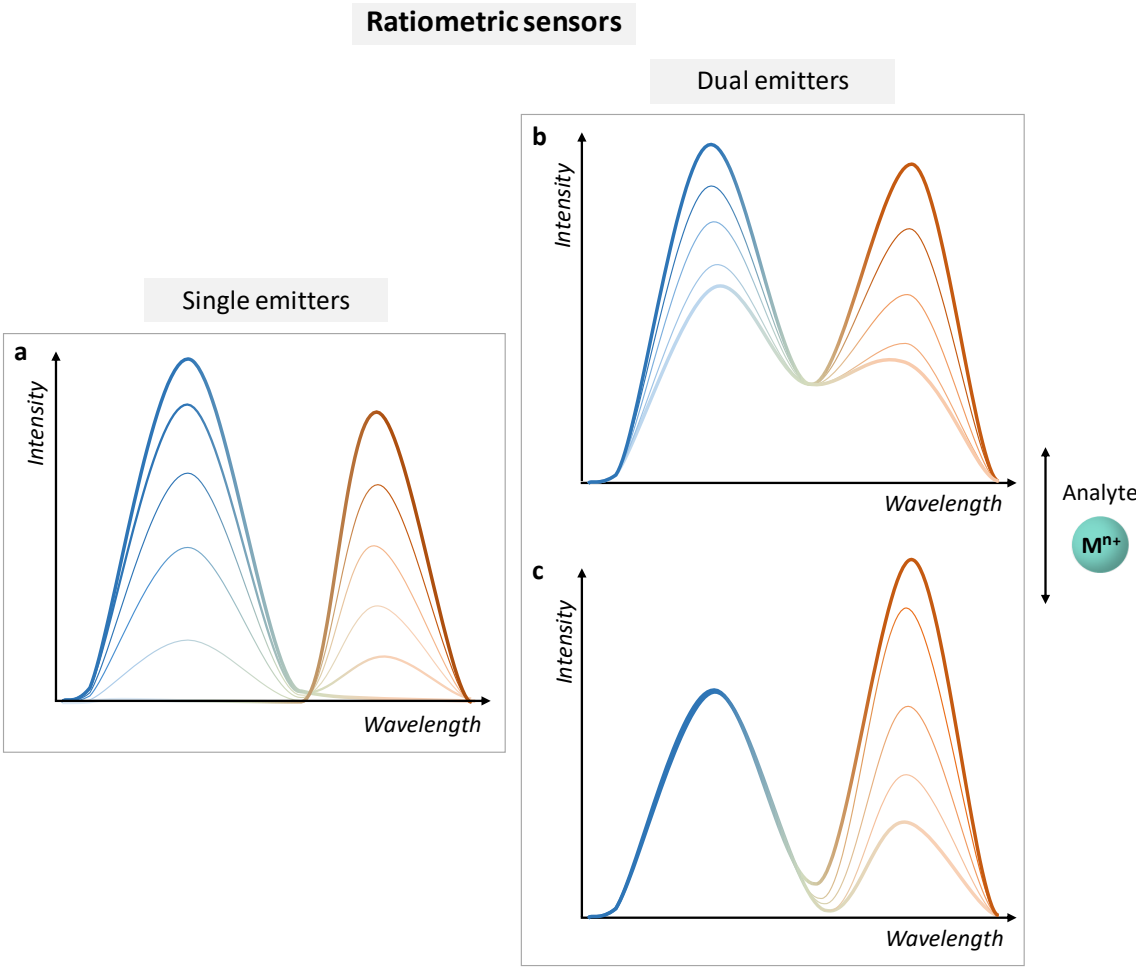

Figure 1.14. *Representative emission spectra of ratiometric sensors, discerning between a) singlet emitters and b) and c) dual emitters.*

The dual emission of a single molecular system can be the result of diverse molecular mechanisms. If there is a single emitter, the various emissions can be the result of different singlet excited states, simultaneous fluorescence and phosphorescence

emissions, Thermally Activated Delayed Fluorescence (TADF) phenomena, Twisted Intramolecular Charge Transfer (TICT), etc. On the other hand, the presence of two electronically disconnected fluorophores in the same molecule.[22] Additionally, ratiometric systems can also be constructed by adding an analyte-independent fluorophore used as reference signal.

1.2.2.2 Operating mechanism

Chemosensors can additionally be sub-divided based on the photochemical mechanism associated to their luminescent response. For instance, Photoinduced Electron Transfer (PET), Photoinduced Charge Transfer (PCT) or Föster Resonance Energy Transfer (FRET) are some of the common mechanisms utilized in the design of traditional cation sensors to modify the signal response of luminophores upon cation-binding. These, and the more recently uncovered mechanisms of excimer emission or Aggregation-Induced Emission (AIE), will be described in this section. For cation sensing, and based on the literature reported to date, each mechanism will generally derive in either an off/on or a ratiometric system, summarized in **Table 1.1**. To illustrate the possible responses related to each mechanism, some examples found in the literature will be introduced in the next sections.

Table 1.1. *Summary of the presented mechanisms for cation sensing with the common response upon cation binding.*

Mechanism	Response
PET	off/on
ICT	Ratiometric
FRET	Ratiometric
Excimer	Ratiometric
AIE	off/on

1.2.2.2.1 Photo induced electron transfer PET

Photoinduced electron transfer (PET) from a donor (D) to an acceptor (A) leads to the formation of a charge-separated state consisting of the donor radical cation and the acceptor radical anion.[23] As in other photochemical contexts, intermolecular and/or intramolecular PET is in direct competition with many other radiative and non-radiative

deactivation processes occurring in the excited states of molecular systems. Overall, PET leads to a decrease of both lifetimes and emission quantum yields.

Based on their emission response the most common situation encountered is the “turn on” sensor, where the emission of the free sensor is PET-quenched and after cation binding PET is not operative and the emission is “enhanced” (**Figure 1.15**). In these cases, the binding unit acts like the electron donor and the fluorophore as the acceptor. To act as a PET-based sensor, the receptor site should possess a relatively high-energy unbounded electron pair. Secondary and tertiary amines intramolecularly linked to the fluorophore systems are the most widespread sensor design used for this purpose. The electron transfer takes place from the electron lone-pair on the nitrogen atom of the amino moiety to fluorophore skeleton, leading to a quenching of the fluorescence. When the nitrogen atom interacts strongly with a cation (through its electron lone-pair), PET is inhibited and a drastic enhancement of fluorescence is observed.

In other words, in the absence of the analyte, after photoexcitation an electron is promoted from the HOMO to the LUMO, both located at the fluorophore (**Figure 1.15**). Because the HOMO of the receptor site is at a higher energetic level than the HOMO of the fluorophore, a rapid intramolecular electron transfer occurs between the HOMO of the receptor and the lowest lying SOMO (singly-occupied molecular orbital) of excited fluorophore, quenching the fluorescence. When the analyte binds the receptor, the HOMO energy of the binding unit is stabilized and the electron transfer will no longer be possible, “turning on” the fluorescence relaxation pathway.

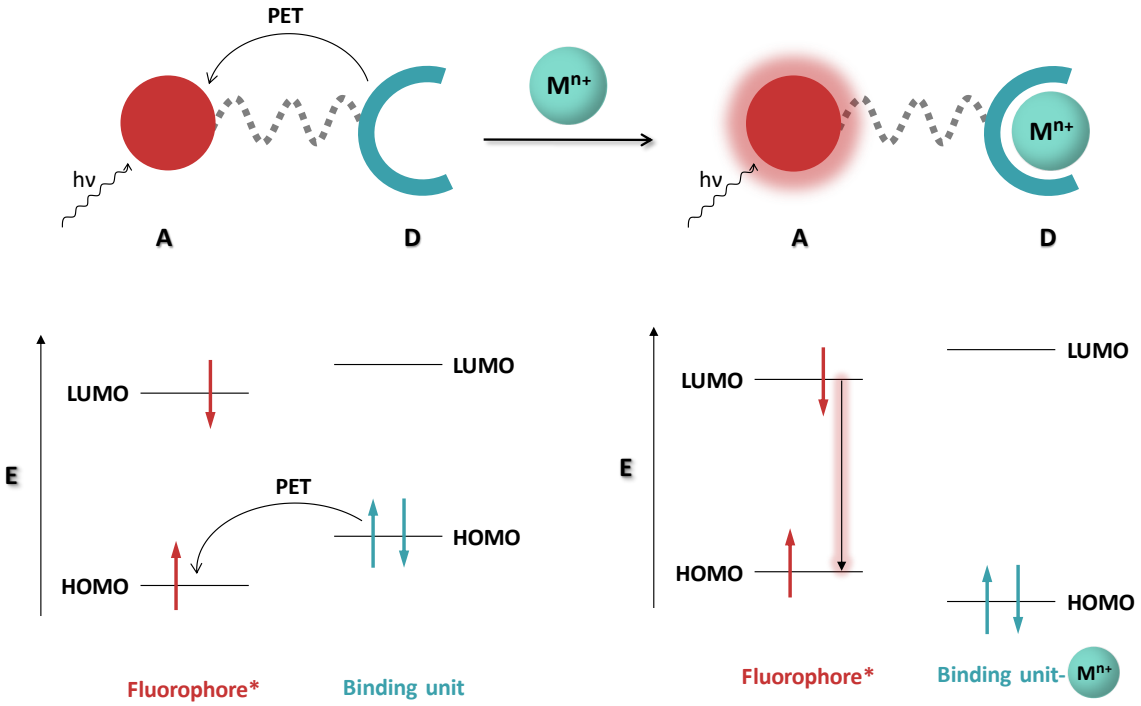

Figure 1.15. *Schematic representation of Photoinduced Electron Transfer process that turns on the fluorescence emission upon cation (M^{n+}) binding.*

Often, other mechanisms that could be responsible of the fluorescence quenching are neglected. The detection of radical ions with time-resolved spectroscopies is required to certify the existence of PET.[24] Unfortunately, not many papers report the mechanistic studies required to unambiguously prove the PET participation in the process. Fahrni et al. reported a family of pyrazoline derivatives to sense Cu(I), that indeed proved to function by PET mechanism (**Figure 1.16**).[25] The structure consists of an aryl ring at the 5-position of the pyrazoline, electronically decoupled from the π-system of the fluorophore, with an appended 16-membered trithiazacyclohexadecane macrocycle, acting as the metal-receptor moiety for PET switching. Upon saturation with Cu(I) in methanol, the sensor achieved a 29-fold fluorescence enhancement (I_{on}/I_{off}). Upon protonation of the aniline nitrogen, the PET process was also inhibited, which confirms the involvement of the electron lone-pair of the nitrogen in the macrocycle in the sensing process. Detailed time-resolved fluorescence and transient absorption experiments elucidated the role of the proposed excited-state relaxation pathways.

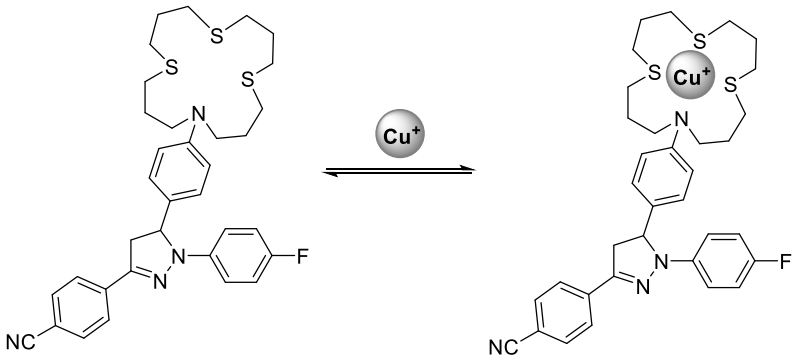

Fahrni 2010

Figure 1.16. *PET based Cu^{+} sensor, reported by Fahrni et al.*[25]

1.2.2.2.2 Intramolecular Charge Transfer (ICT)/Photoinduced Charge Transfer (PCT)

Another phenomena frequently used to construct luminescent sensors is intramolecular charge transfer (ICT). Usually ICT-based sensors behave as ratiometric probes. ICT-based sensor contain an electron-donating and an electron-accepting groups within a conjugated π system connecting both fluorophore and receptor.[26] Upon excitation, a redistribution of electrons from the electron-donating to the electron-accepting group happens, creating a dipole moment with in the molecule. One can distinguish two possible designs, as depicted in **Figure 1.17**. When the electron donor (D) is located at the cation-receptor site, the binding of the analyte reduces its electron-donating character and a blue-shifted spectrum is expected. Conversely, if the cation interacts with the acceptor group (A), it enhances the electron-withdrawing character of this group; the absorption spectrum is thus red-shifted.

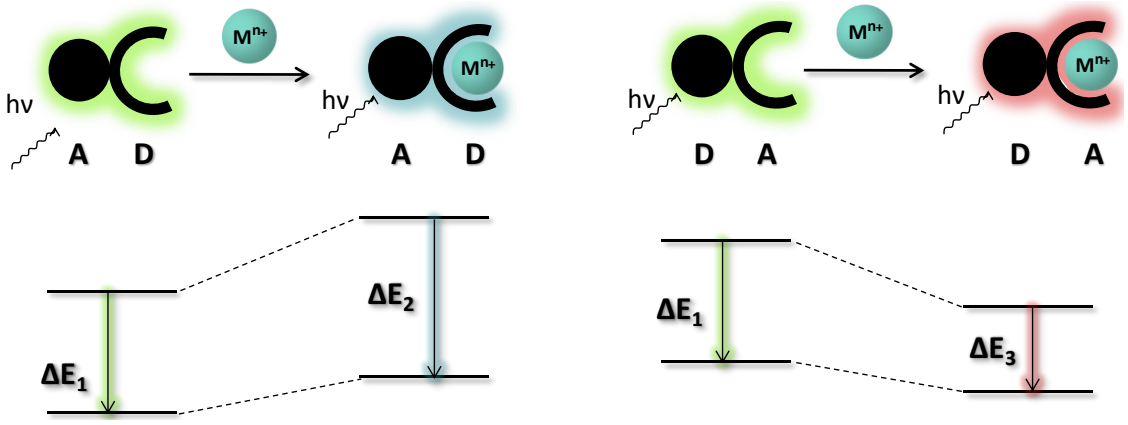

Figure 1.17. *Schematic representation of Intramolecular Charge Transfer processes (ICT) that modify the fluorescence emission of a ratiometric sensor in the presence of cations M^{n+}.*

Therefore, as mentioned before ratiometric (bicolor) cation probes will be obtained based on ICT mechanism. For instance, a ratiometric chemosensor for Hg^{2+} was reported by Cui et al., where the donor is located at the receptor site and the acceptor resides on the fluorophore, which causes a blue shifted emission upon dication binding (**Figure 1.18**).[27] The ability of the aniline nitrogen atoms to participate in π-electron conjugation is reduced upon binding to Hg^{2+}. This effect was confirmed by ^1H NMR spectroscopy. When 20 equivalents of Hg^{2+} ions were added to a solution of the sensor, the ^1H NMR signals assigned to the seven aromatic protons experience slight downfield shifts and are broadened. This was attributed to a deshielding effect arising from the decrease of the electron density on the coumarin fluorophore. A shift of the emission band of ~100 nm (from 567 to 475 nm) was achieved in the presence of Hg^{2+} ions. Additionally, the fluorescence intensity ratio I_{567}/I_{475} changed significantly from 11.9 to 0.4, corresponding to a variation factor of 30.

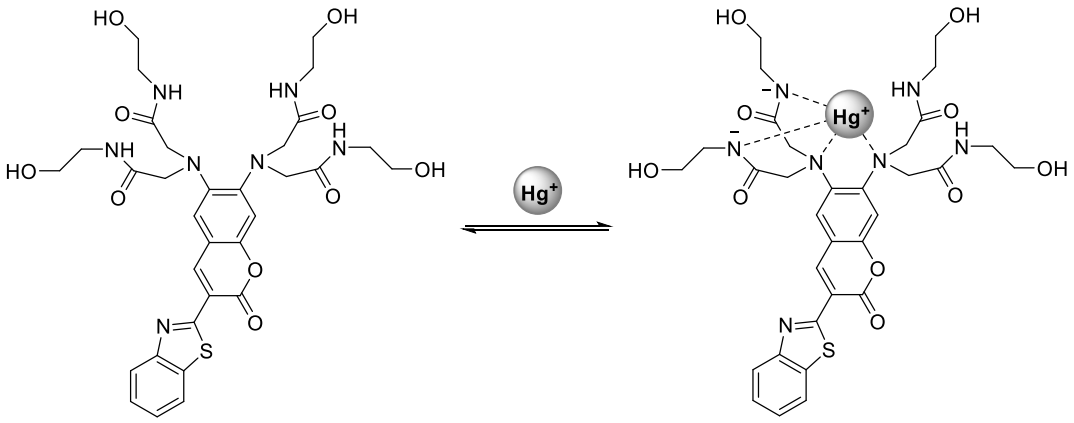

Cui 2005

Figure 1.18. *ICT based Hg^+, reported by Cui et al.*[27]

Most ratiometric ICT sensors result in a hypsochromic shift upon cation binding. Nevertheless, some ICT sensors for cations do show a bathochromic shift when the acceptor is on the cation-receptor site of the sensor (**Figure 1.17**). For instance, the sensor described by Fahrni et al. revealed a red-shifted emission caused by Zn^{2+} chelation, from 483 to 520 nm (**Figure 1.19**).[28] The ratio of the integrated fluorescence intensities between 510 and 570 nm and 440 and 495 nm increased from 0.7 to 2.6 upon saturation with Zn(II), corresponding to a variation factor of 3.7. Several ratiometric proves for Zn^{2+} based on this type of structure have been reported in the last years.[29–31]

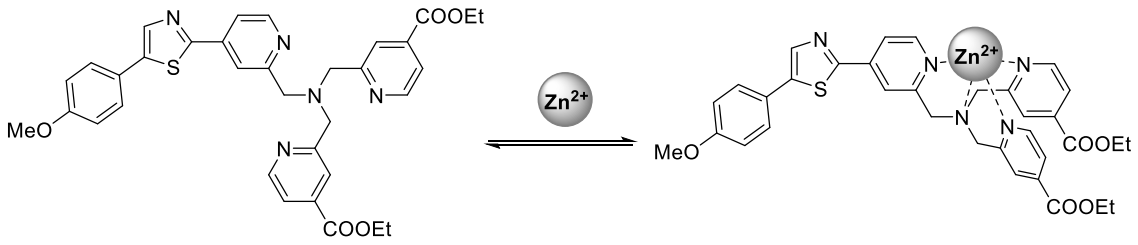

Figure 1.19. *ICT based Zn^{2+} sensor, reported by Fahrni et al.*[28]

1.2.2.2.3 Fluorescence Resonance Energy Transfer (FRET)

Fluorescence Resonance Energy Transfer (FRET) is a non-radiative energy transfer process through long-range dipole–dipole interactions between the donor–acceptor pairs.[32] In other words, it could be represented as a molecule (or system) composed of two chromophores, which is excited in the absorption or excitation band of the donor, and the acceptor gets excited with the energy of the donors' relaxation, "as if" the donor emitted a photon to excite the acceptor, despite being a non-emissive charge transfer. Thus, upon photoexcitation, the electronic excitation energy of the donor in its excited state can be transferred to the acceptor in its ground state. For molecules to undergo FRET, some requirements must be fulfilled: (1) the donor–acceptor pair should be positioned in proximity of each other (typically 10–100 Å), a requirement that helps rationalize the distance dependency of FRET and its efficiency, (2) the emission spectra of the donor should overlap with the absorption spectra of the acceptor (**Figure 1.21**), (3) the donor emission moment, the acceptor absorption moment, and their separation vector must be in a favorable mutual orientation.

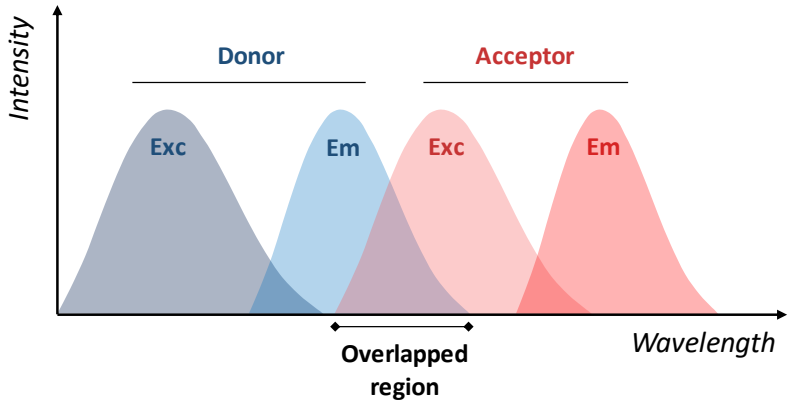

Figure 1.20. *Representation of the normalized excitation and emission spectra of the donor and acceptor in a FRET system.*

FRET-based sensors display a ratiometric response to cation detection. If FRET mechanism is activated upon cation binding, the emission suffers a bathochromic shift. On the contrary, if FRET is deactivated upon cation interaction, the emission will shift hypsochromicaly, as illustrated in **Figure 1.21**. In the context of cation sensing, to exploit this mechanism, the strategy involves the modification of the absorbance properties of the acceptor fluorophore or the emissive properties of the donor, to either inhibit or procure the overlapping of the emission of the donor with the excitation energy of the acceptor.

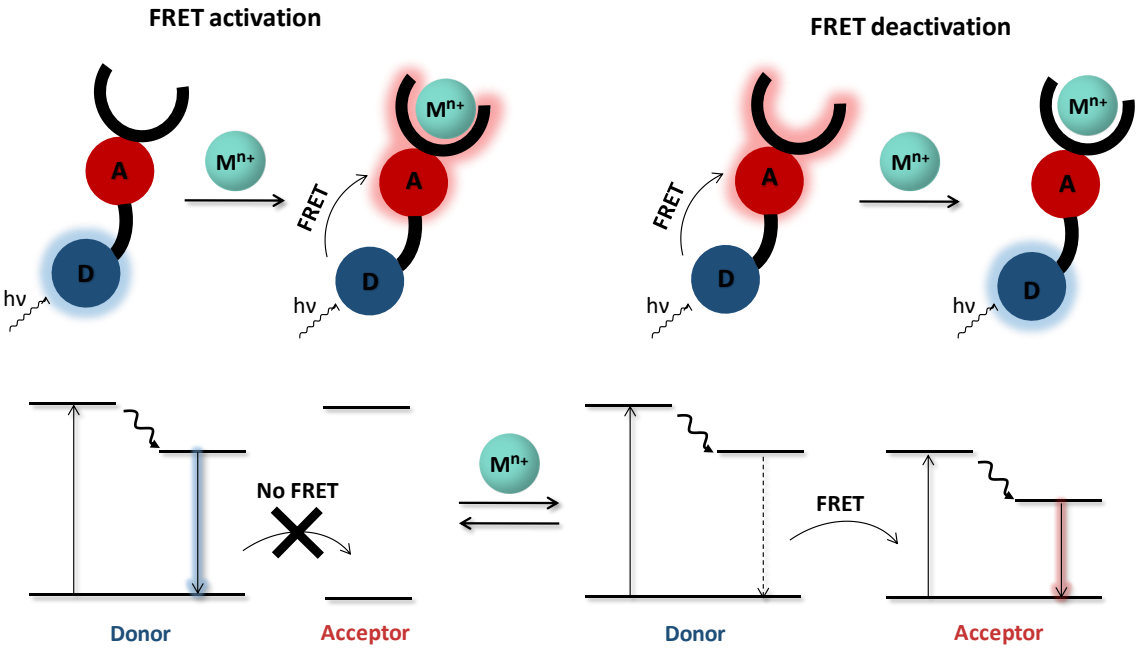

Figure 1.21. *Representative scheme of FRET based ratiometric sensors, where the ICT change occurs in the acceptor moiety upon M^{n+} binding.*

An examples of FRET deactivation upon cation binding was reported by Guo et al., as shown in **Figure 1.22**.[33] It is a coumarin based ratiometric sensor for labile Zn^{2+} based on the Zn^{2+}-induced deactivation of the FRET process, producing a blue-shifted emission. It showed an 80 nm separation upon Zn^{2+} chelation, from 480 to 560 nm, with high specificity and affinity. The intensity ratio of I_{480}/I_{560} increased with the decrease of FRET efficiency. The system was constructed with the union of a coumarin derivative (CPBT), an oxadiazole and tripyridyl moiety (ASBD-TPEA) as receptor unit. FRET mechanism is active when the sensor is unbound. When the receptor of the ASBD binds Zn^{2+}, decreasing the electron-donating ability of the 4-amino group, the ICT is weakened. Thus, the ASBD-TPEA emission suffers a large blue shift that diminishes the spectral-

overlap between the emission of the donor, the coumarin, and the absorption of the acceptor, the oxazoline, leading to a significant decrease in the FRET efficiency of CPBT.

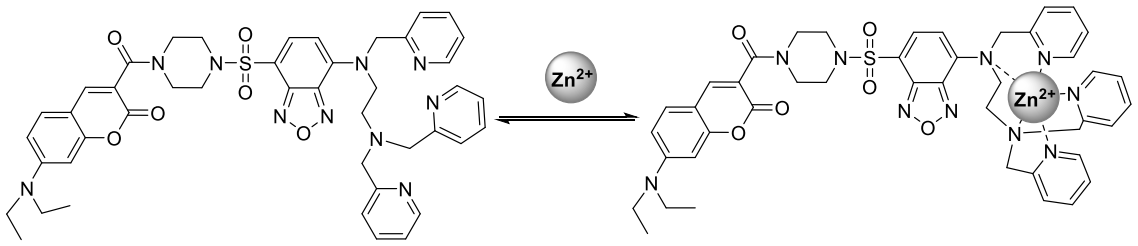

Guo 2020

Figure 1.22. *FRET based Zn^{2+} sensor, reported by Guo et al.*[33]

Chen et al. developed a quinoline and anthracene bearing sensor for Zn^{2+} (**Figure 1.23**).[34] The free sensor showed a strong and structured fluorescence centered at 420 nm, corresponding to the emission band of the anthracene. Upon Zn^{2+} addition, this emission was gradually quenched while a new emission band appeared at 500 nm. This ratiometric response was attributed to the internal charge transfer within the quinolone, resulting in FRET activation, as the emission band of anthracene, the donor, overlaps the excitation band of the Zn^{2+}-bound quinolone, the acceptor. The fluorescence intensity ratio (I_{497}/I_{420}) increased from 0.6 to 7.5.

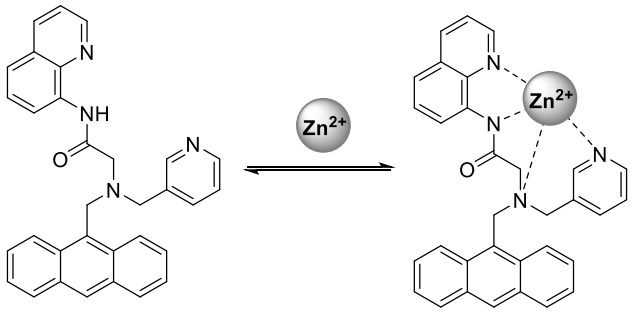

Chen 2014

Figure 1.23. *FRET based Zn^{2+} sensor, reported by Chen et al.*[34]

1.2.2.2.4 Excimer/Exciplex Formation

An excimer, originally short for excited dimer, is a short-lived dimeric or heterodimeric molecule formed from two species. The term excimer, was defined in the 1960's in terms of a molecular complex formed by interaction of an excited molecule and its ground state counterpart.[35] Such "excited dimer" exhibited dual fluorescence (**Figure 1.24**),

which are associated with the monomeric fluorophore and a broad distinguished red-shifted emission, ascribed to the complexed excited molecular pair.

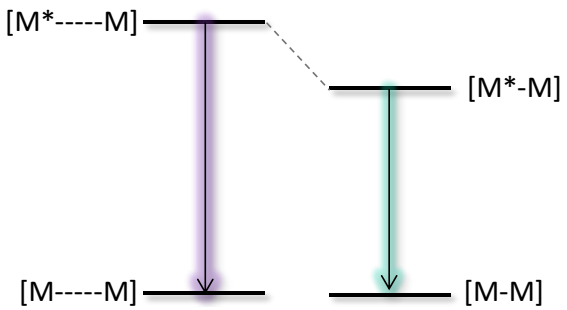

Figure 1.24. *Energy diagram for the relation between the loosely bound monomer pair [M-----M] and an excimer [M*-M].*

This double emission permits the construction of excimer-based ratiometric sensors. This type of molecular sensor is designed in such a manner that the interaction of the analyte with the recognition unit of the probe alters the fluorophore–fluorophore distance. According to the structure of the complexing moiety, in the review of Leray et al. these sensor systems were classified into five classes: chelators, podands, crown ethers, cryptands, and calixarenes.[36] The excimer formation can be formed intramolecularly, by fluorophores residing in the same molecule (a in **Figure 1.25**), or intermolecularly (b in **Figure 1.25**). In the former, the cation binding to the sensor may favor or hinder the excimer formation.

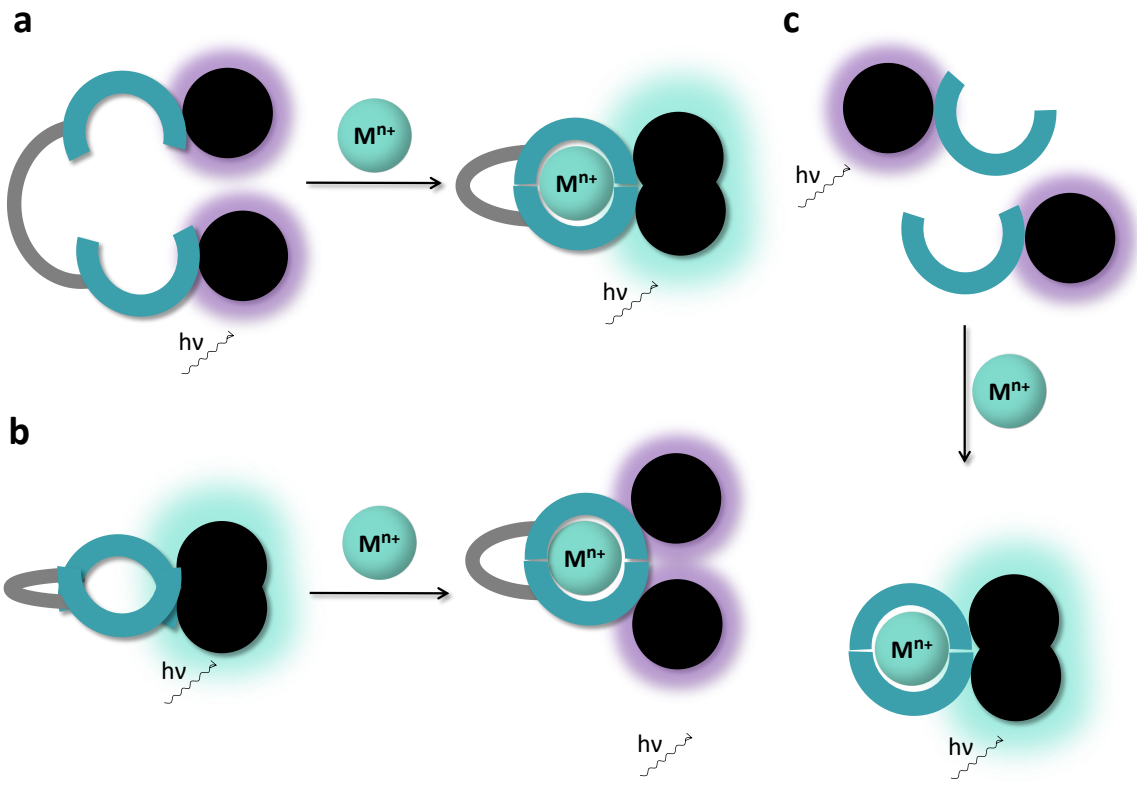

Figure 1.25. *Schematic representation showing the formation and disorganization of excimers in the presence of M^{n+}. a) intramolecular or b) intermolecular.*

For instance, Saitz et al. reported a calix[4]arene derivative with thiourea spacers and methylene–pyrenes, as intramolecular sensor, which presents opposite responses depending on the cation (**Figure 1.26**).[37] It showed a ratiometric response towards Hg^{2+} and Ag^{+}, by enhancing and decreasing the intramolecular excimer emission, respectively. DFT and TD-DFT computational studies were carried out and used to identify possible binding modes that explain the observed response during fluorescence titrations. Calculations revealed the presence of different binding sites depending on the conformation of the sensor, suggesting a reasonable explanation for non-linear changes in fluorescence depending on the physical nature of the interaction between metal center and the conformer. The Ag^{+} is cooperatively stabilized by Ag–S through-bond; while Hg^{2+} is mainly stabilized by N and O atoms through-space interactions enclosing the Hg^{2+} cation inside the cavity. In the latter case, the stacking is considerably more accentuated and plausibly more rigid due to the through-space interactions.

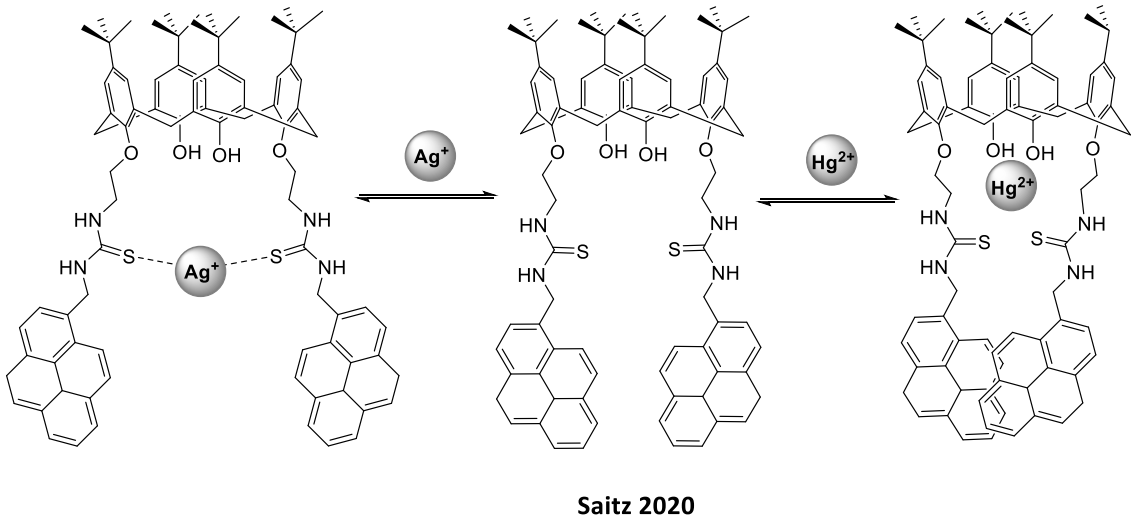

Figure 1.26. *Excimer based Hg^{2+} and Ag^{+} sensor, reported by Saitz et al.*[37]

A pyrene-containing Schiff base fluorescent ratiometric probe for the detection of Cu^{2+} as an intermolecular exciplex formation was reported by Sun et al. (**Figure 1.27**).[38] In MeCN-HEPES buffer solutions with one equivalent of cation addition, the emission intensity ratio I_{470}/I_{409} increased from 0.14 to 4.12, yielding a variation factor of 28.

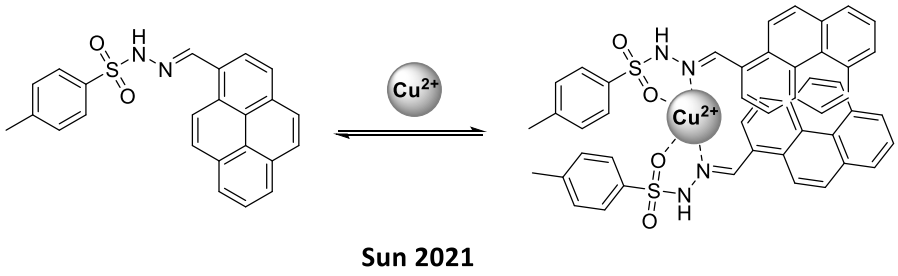

Figure 1.27. *Exciplex-based Hg^{2+} sensor, reported by Sun et al.*[38]

1.2.2.2.5 Aggregation-Induced Emission (AIE)

Aggregation-induced emission (AIE) refers to the photophysical effect where the luminescence of aggregates is stronger than that of the dispersed state. This phenomenon was recently formulated by Tang and co-workers (in 2001), and since then AIE has evolved from a simple luminescent phenomenon to a multidisciplinary research field, including its exploitation as a sensing mechanism.[39]

The majority of AIE-based cation sensors utilize metal–ligand coordination interaction. The AIE-based chemosensors contain ligands or binding functional species that are able to coordinate with cationic analytes, causing structural and chemical variations such as

self-assembly or dis-assembly that eventually render either turning-on or quenching of emission of chemosensing systems. Chemosensor–cation interactions may form, from soluble non-emissive monomers, insoluble coordination complexes or coordination polymers that aggregate and trigger an emission turn-on (**Figure 1.28**). This enhancement is attributed to the restriction of intra-molecular motion, comprising both RIR, restriction of intramolecular rotation, and RIV, restriction of intra-molecular vibration, recognized as a general mechanism for AIE.[40]

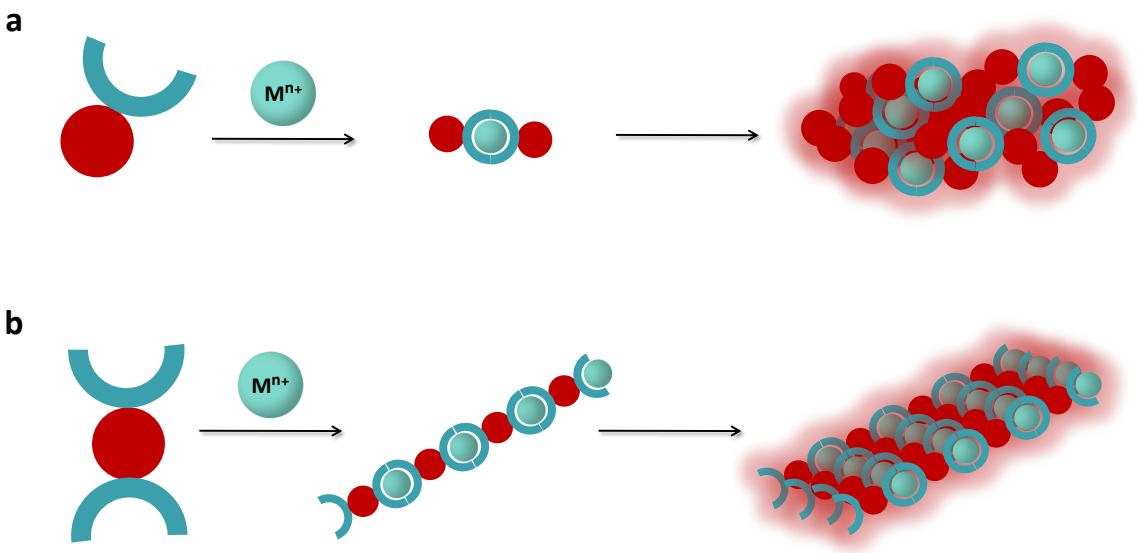

Figure 1.28. *Aggregation Induced Emission representative structures.*

Su et al. reported a ratiometric sensor based on a 9,14-diphenyl-9,14-dihydrodibenzo[a,c]phenazine (DPAC) skeleton with an appended tetraphenylethylene (TPE) unit (**Figure 1.29**).[41] The free sensor displays two emission bands, being the less energetic one at 600 nm more intense than the one at 475 nm. Upon the addition of Hg^{2+}, the fluorescence peak at 600 nm decreased slightly, whereas the luminescence at 475 nm intensified dramatically. The emissive response of this sensor is attributed to the fact that, in the free form thephenyl rings of free TPE unit have free rotations. Therefore, after excitation, the TPE fragment of the unbound sensor decays through radiationless channels, and therefore the fluorescence signal of TPE is "silent" being the DPAC orange-red luminescence the dominant emission. In sharp contrast, when Hg^{2+} and Ag^{+} were added, the coordination between the recognition moieties and the cations affords complexes with lower solubility leading to aggregation. The formation of

aggregates restricts the intramolecular vibrations of DPAC, and the intramolecular rotations of TPE, rigidifying their conformations due to RIM. In this situation, the DPAC is forced to adopt a bent configuration, leading to the TPE blue emission the dominating band of the spectrum.

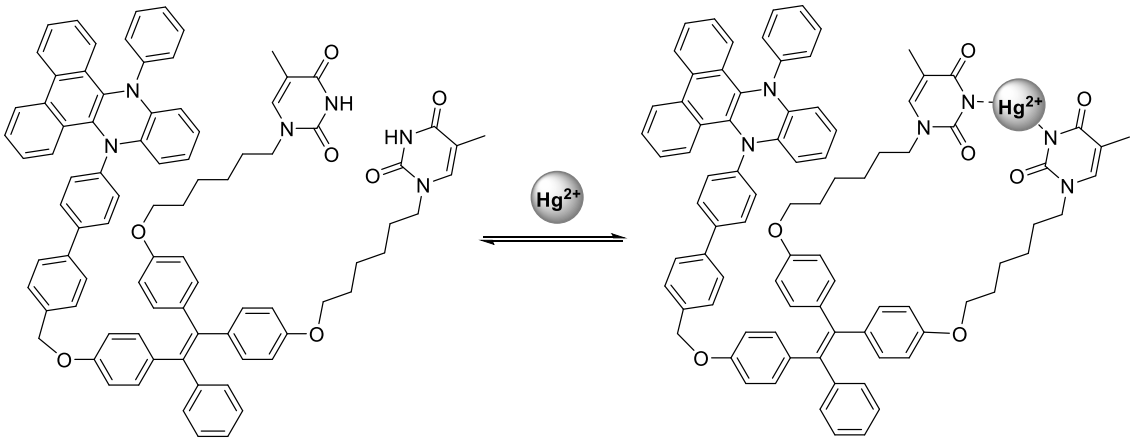

Su 2017

Figure 1.29. *AIE based Hg^{2+} sensor, reported by Su et al.*[41]

Tang et al. reported a salicyladazine-based probe, for the selective detection of Ca^{2+} by incorporating the negatively charged iminodiacetate groups as chelating ligands (**Figure 1.30**).[42] In the absence of Ca^{2+} ion, the probe is well dispersed in aqueous solutions and the emission is almost off, whereas in the presence of Ca^{2+} ion, the probe forms highly emissive fibrillar aggregates through electrostatic and chelating interactions between the iminodiacetate groups and Ca^{2+}. The aggregation yielded an 11.5-fold emission enhancement with a maximum emission wavelength at 560 nm.

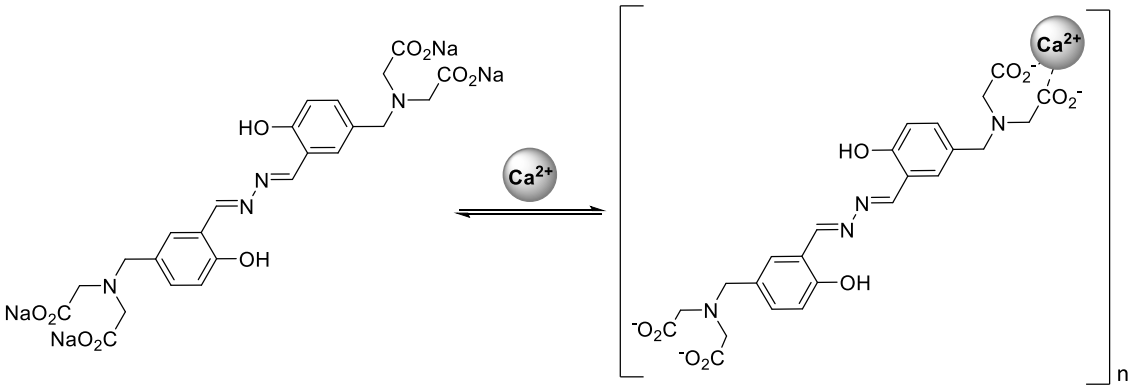

Tang 2018

Figure 1.30. *AIE based Ca^{2+} sensor, reported by Tang et al.*[42]

1.3 Ba^{2+} CHEMOSENSORS

As described in the first section, single molecule fluorescence detection of barium is investigated for enhancing the sensitivity and robustness of a neutrinoless double beta decay search in ^{136}Xe, the discovery of which would alter our understanding of the nature of neutrinos and the early history of the Universe. A key developmental step is the synthesis of barium-selective chemosensors to be implemented into ongoing experiments in high-pressure ^{136}Xe gas. In this section, a comprehensive overview of Ba^{2+} molecular chemosensors reported to date will be chronologically introduced, followed by the structures proposed and developed by the NEXT collaboration. As last example, the FBI sensor, a ratiometric sensor developed at Prof. Cossío's group for Ba^{2+}-tagging, which is the predecessor structure for the three 3rd generation FBIs discussed in this thesis, will be specifically discussed.

The first chemosensor reported for Ba^{2+} was described in 2004 by Akashi et al (**Figure 1.31**).[43,44] A selective and sensitive fluorescence detection of Ba^{2+} among alkali metal and alkaline earth metal cations was achieved in aqueous media by the combination of a pyrene-functionalized monoazacryptand-type fluorophore and the micelles formed by a non-ionic surfactant Triton X-100. The addition of surfactant helped in the solubilization of the indicator by creating a less polar environment. In the free state the fluorescence of the pyrene ring is quenched due to PET from the amino group. Upon complexation with a metal cation, the nitrogen lone-pair no longer participates in PET, causing the recovery of the fluorescence, displaying a structured band around 400 nm. Thus, this mechanism results in an intensity-based sensor governed by cation binding.

In 2005, Yano et al. reported another PET-based Ba^{2+} sensor with an off/on response (**Figure 1.31**).[45] The quantum yield of the free sensors was measured to be 0.0033, as PET quenched the emission. Upon cation interaction, an emission band appeared at around 370 nm. The association constant was measured by UV-vis and fluorescence titrations, giving $1.6 \cdot 10^5$ and $7.7 \cdot 10^4$ M^{-1} values, respectively. Even though the structure presents two receptor sites, the host-guest stoichiometry for Ba^{2+} was reported to be 1:1. In the case of the complexation with Ca^{2+} and Sr^{2+}, 1:2 host–guest complexation was suggested.

A year later, an excimer-based fluorescent sensor was reported by Poggi et al (**Figure 1.31**).[46] The bis-15-crown-5-naphthalenediimide structure displayed a strong fluorescence enhancement upon interaction with Ba^{2+}, a broad band centered at 440 nm. This selective enhancement was ascribed to a specific self-assembling fluorescence enhancement process, due to the formation of [2+2] species in which an intramolecular excimer was allowed to form. An enhancement factor of 35-fold was obtained after the addition of Ba^{2+}.

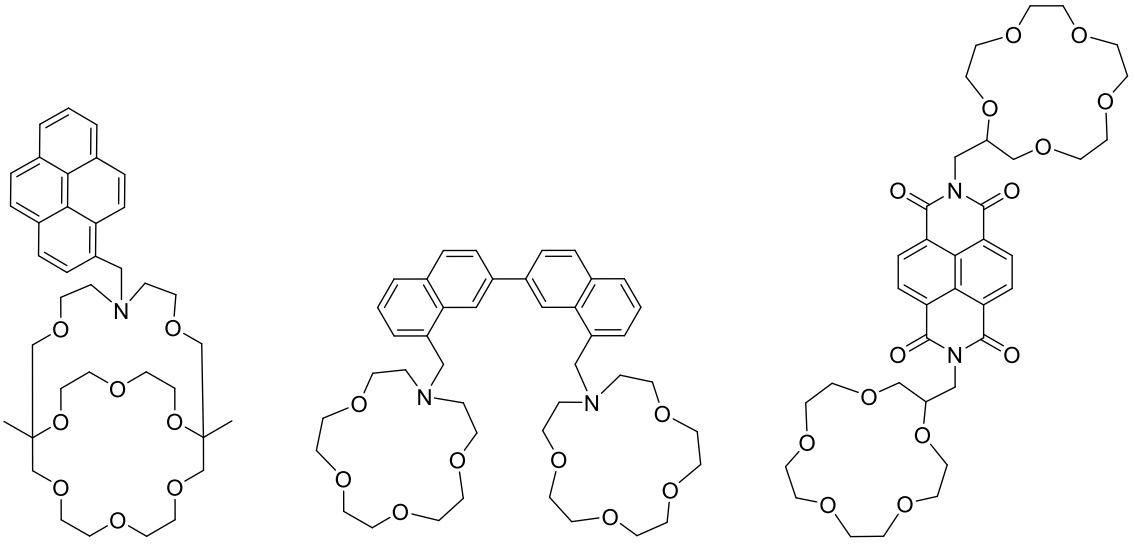

Akashi 2004 **Yano 2005** **Poggi 2006**

Figure 1.31. *Ba^{2+} sensors, reported by Akashi et al.[43], Yano et al.[45] and Poggi et al.[46]*

In 2008, a complex system with a rhodamine and BODIPY bearing calix[4]arene structure was published as a Ba^{2+} and Hg^{2+} sensor (**Figure 1.32**).[47] Upon Ba^{2+} addition, the fluorescent intensity of the sensor increased by over 15. The fluorescence intensity enhancement could be attributed to the capture of Ba^{2+} by the crown ether then resulting in the reduction of the electron-donating ability of oxygens to the BODIPY moiety. Thus, the PET process is partially suppressed, which causes an enhancement in emission.

In 2011, Unno et al. described a very similar structure as the one described before by Yano et al. in **Figure 1.31**.[48] However, in this case, instead of bearing two naphthalene moieties, the sensor was constructed with two anthracene fluorophores (**Figure 1.32**). The same operating mechanism led to a fluorescence enhancement at 472 nm. The

binding constant was $6.63 \cdot 10^5$ M^{-1}, apparently, a higher value compared to the one obtained before for the analogous structure.

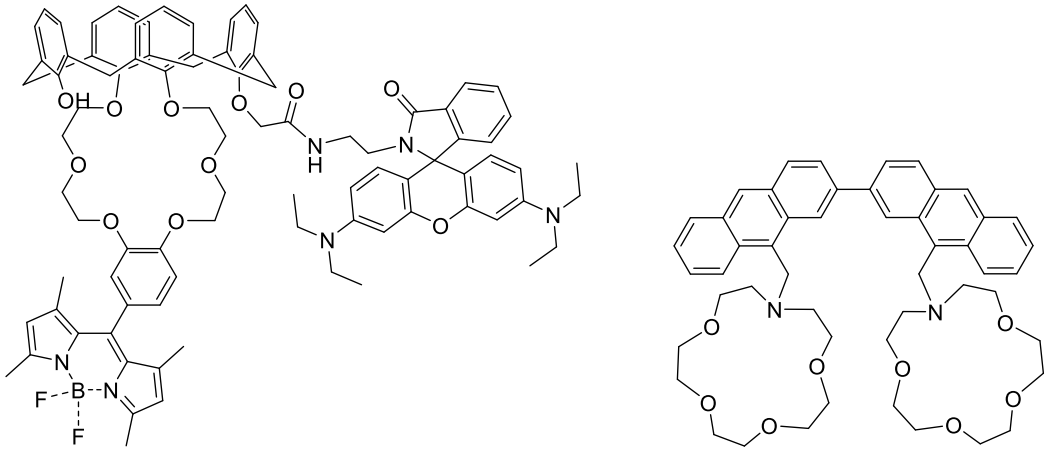

Zhu 2008 **Unno 2011**

Figure 1.32. *Ba^{2+} sensors, reported by Zhu et al.[47] and Unno et al.[48]*

In 2011, Jang et al described a benzothiazole-based chemosensor with mixed S,N donor sites (**Figure 1.33**).[49] The binding units were incorporated in a highly flexible tripodal framework, which facilitated the complexation of larger-sized metals, such as Ba^{2+}. The chemosensor resulted in a sensitive and selective Ba^{2+} recognition through the enhancement of the fluorescence intensity in a THF/H_2O solvent mixture, although a discrimination factor of only one was obtained. This inferior intensity enhancement was attributed to molecular rigidification.

In the same year, the structure 1,2-diimino host was designed by Sykes et al. as a luminescence sensor, exhibiting enhanced selectivity for Ba^{2+} ion (**Figure 1.33**).[50] E/Z isomerization, typical of imines, was responsible of a non-radiative deactivation of the excited state. However, the diimine dimer, reported by Sykes et al., based on 1,2-phenylenediamine showed luminescence specificity toward Ba^{2+} in MeCN solution, binding in a H:G = 1:2 manner. The luminescence was attributed to the restriction of the E/Z Isomerization of the imine groups by noncovalent/coordinate-covalent interactions between adjacent crown ether rings and/or steric influences.

A second sensor based on aza-crown ethers was reported the same year, based on 3,4-dimethylthieno[2,3-b]thiophene bearing two monoaza-15-crown-5 ethers at 3- and 4-

positions presented by Feng et al. (**Figure 1.33**).[51] The fluorescence intensity of the band in the region of 320–410 nm was enhanced upon Ba^{2+} addition, generating a 23-fold increment, because the PET process was blocked by coordination of the nitrogen atoms to the metal ions. A Job plot analysis of the fluorescence response indicated the formation of 1:1 complex with Ba^{2+}. The ionic diameter for Ba^{2+} (2.70 Å) is larger than the effective cavity diameter for aza-15-crown-5 (1.7–2.2 Å), thus forming an intramolecular sandwich complex.

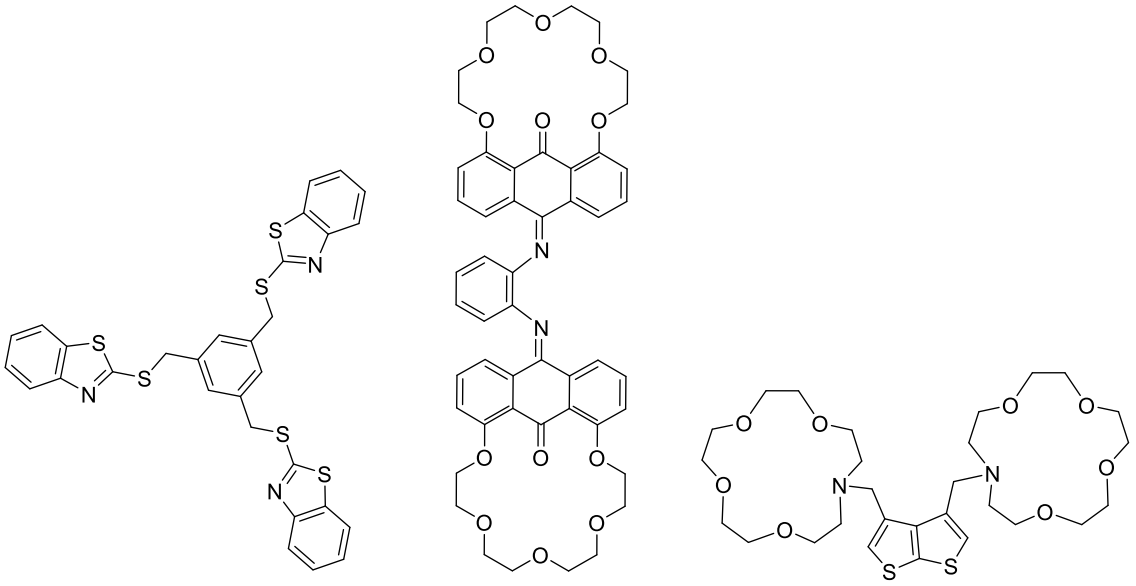

Jang 2011 **Sykes 2011** **Feng 2011**

Figure 1.33. *Ba^{2+} sensors, reported by Jang et al.[4943], Sykes et al.[50] and Feng et al.[51]*

In 2013, Ushakov et al. synthesized different *N*-methylbenzoaza-crown-containing benzothiazole, pyridine, and quinoline styryl dyes which demonstrated high performance as optical molecular sensors for alkali and alkaline-earth metal cations (**Figure 1.34**).[52] They functioned as cation-triggered emitters. The enhanced characteristics of these fluorophores were assigned to the higher electron-donating ability of the nitrogen atom in benzoaza-crown-ether moiety upon cation binding, and to the preorganization of the macrocyclic moiety toward complex formation with cations. Up to 61-fold enhancement of the emission intensity was reported.

In 2015, Wang et al. described a simpler structure as Ba^{2+} sensor, based on N-salicylidene-3-aminopyridine (**Figure 1.34**).[53] In this class of sensor, fluorescence

quenching is dominant because of the isomerization of C=N moiety, and therefore, the coordination of a metal ion with this type of structures gives a remarkable fluorescence enhancement by blocking the C=N isomerization. The H:G binding stoichiometry was determined to be 2:1 by continuous variation methods, where the cation was bound to the sensors from the pyridine and the nitrogen of the C=N moiety. The OH of the phenol remained unaltered.

In 2018 Duan et al. described a new aza-15-crown-5 derivative bearing coumarin and hydrazone moieties, which showed a fluorescent sensing behavior and selectivity toward Ba^{2+} by 2-fold fluorescence enhancement (**Figure 1.34**).[54] A H:G 1:1 binding stoichiometry was determined with a binding constant of $4 \cdot 10^4\ M^{-1}$.

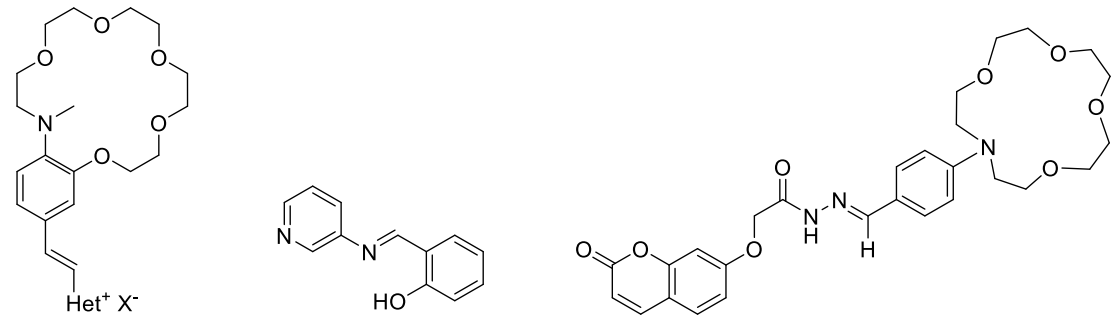

Ushakov 2013 **Wang 2015** **Duan 2018**

Figure 1.34. *Ba^{2+} sensors, reported by Ushakov et al.[5243], Wang et al.[53] and Feng et al.[54]*

In 2019, three novel Ba^{2+} sensors were reported, not based on aza-crown ethers receptors. Chaudhary et al. reported a sulfur-incorporated naphthoquinone-based structure was tested for the efficient and selective sensing Ba^{2+} ions in semi-aqueous medium (**Figure 1.35**).[55] The Ba^{2+} ions induced an enhancement in the fluorescence of the title ligand at 670 nm, attributed to encapsulation of the cations via coordination with the oxygen and sulfur donor sites of the molecule, rigidifying the structure. This sensor presented a H:G stoichiometry of 1:2.

The second sensor, Kongsriprapan et al. reported a very simple structure based on a naphthalene as a high selectivity water-soluble fluorescence probe for the detection of Ba^{2+} with a fluorescence turn-on signal at 350 nm (**Figure 1.35**).[56] The cation interacts with the carboxylic acids forming a 1:1 H:G complex.

Lastly, a new phenoxazine-based chemosensor was developed by Yoo et al. and proven to be a selective and sensitive chemosensor for Ba^{2+} ion detection (**Figure 1.35**).[57] This chemosensor displayed turn-on fluorescence response toward Ba^{2+} and emitted a strong fluorescence emission spectrum with a 125-fold increase in fluorescence intensity. The chemosensor functioned through the intramolecular charge transfer mechanism, which was confirmed by DFT studies.

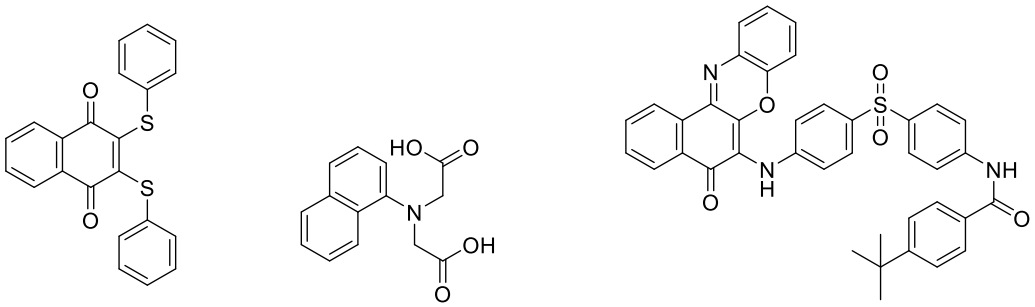

Chaudhary 2019 **Kongsriprapan 2019** **Yoo 2019**

Figure 1.35. *Ba^{2+} sensors, reported by Chaudhary et al.[55], Kongsriprapan et al.[56] and Feng et al.[57]*

The most relevant characteristics of the sensors introduced in this section are summarized in **Table 1.2**. As it can be recognized, the total of the Ba^{2+} dication sensors reported until 2020 were described as off/on sensors. Moreover, the most common mechanism of detection for Ba^{2+} relies on the quenching of the photoinduced electron transfer of the free fluorophore.

Certainly, in view of the described examples, crown ethers have been widely employed as Ba^{2+} receptor, the 18-crown-6, the 15-crown-5 or their nitrogen-containing aza-crown analogous. Crown ethers present a category of well-known cyclic host molecules comprising ether groups that result in a remarkable selectivity to different cations, based on the highly electronegative cavity. The main advantage of these coordinating groups is that the system is pre-organized, thus allowing to minimize the entropic penalty associated with coordination. The main issue of these cyclic systems is that the restriction of conformational freedom makes these moieties less tolerant to structural changes, although this can reflect in a higher selectivity.

Table 1.2. *Summary of the Ba^{2+} organic sensors reported to date.*

Author	Response	Fluorescence enhancement		Mechanism	K_a
		f_λ $[(I-I_0)/I_0]$	Fold $[I/I_0]$		
Akashi 2004	off/on	-	-	PET	-
Yano 2005	off/on	-	-	PET	$1.5 \cdot 10^5$
Poggi 2006	off/on	-	35	Excimer	-
Zhu 2008	off/on	-	15	PET	$1.68 \cdot 10^5$
Unno 2011	off/on	-	-	PET	$6.63 \cdot 10^5$
Jang 2011	off/on	1	-	Rigidif.	$4.28 \cdot 10^3$
Sykes 2011	off/on	-	7	ICT/Rigidif.	$1.1 \cdot 10^7$
Feng 2011	off/on	-	23	PET	$1.80 \cdot 10^5$
Ushakov 2013	off/on		61	Twisted ICT	$10^5 – 10^8$
Wang 2015	off/on	0.94	-	PET	$2 \cdot 10^6$
Duan 2018	off/on	-	2	PET	$4 \cdot 10^4$
Chaudhary 2019	off/on	-	14	PET	$3.29 \cdot 10^3$
Kongsriprapan 2019	off/on	-	-	PET	-
Yoo 2019	off/on	-	125	ICT/exciples	$1 \cdot 10^6$

In 1967, Pedersen accidentally discovered that crown ethers could selectively accommodate alkali cations.[58] The driving force for the complexation is the coordination interactions between metal cations and oxygen atoms in crown ethers. As revealed in the previous examples, it is also possible to introduce other heteroatoms as nitrogen or sulfur. The repeating units of crown ethers are water- and organo-soluble amphiphilic ethylene oxide moieties; therefore, they can be used in both aqueous and organic media. The selectivity is dependent on the size of the macrocycle (**Figure 1.36**). For instance, the previously introduced sensors demonstrate the capacity of 15-crown-5 and 18-crown-6 to bound Ba^{2+} dication.

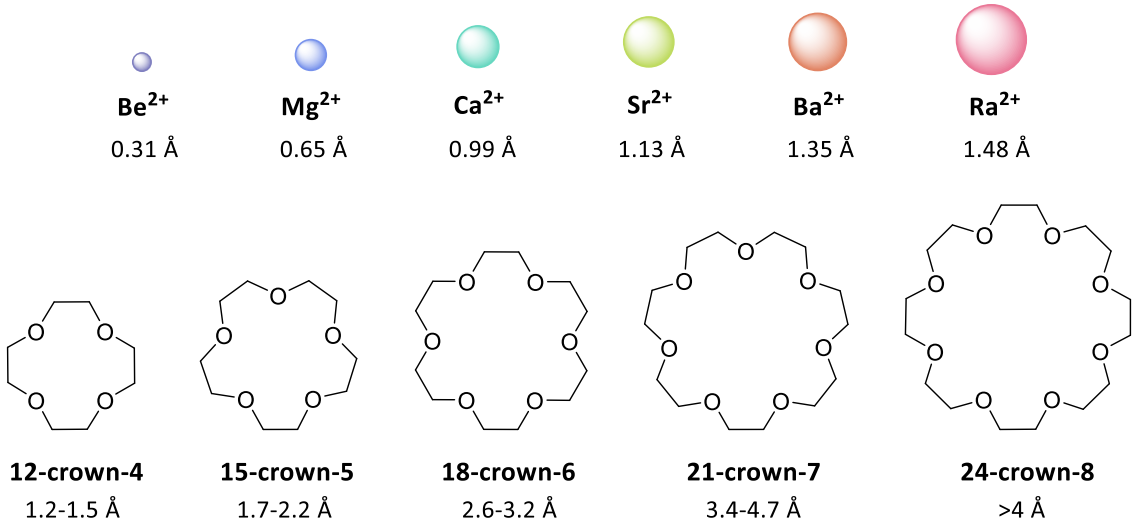

Figure 1.36. *Comparison of the dication radii of the alkaline earth metals and several crown ethers with their average inner diameters.*

1.3.1 NEXT

As described in the introduction, ahead of the NEXT project, in 2016, Nygren proposed the use of single molecule fluorescence imaging for Ba^{2+} single molecule atom detection in the NEXT experiment. In that early communication, the employment of a couple of sensors with aza-crowns as off/on fluorescent sensors was suggested.[11] Following this idea, by using an indicator optimized to sense Ca^{2+} (**Figure 1.37**), a sensor to detect the presence of bulk Ba^{2+} cations in aqueous solution using a fiber-coupled optical system was developed by the same group.[12] An intensity enhancement ratio of 85 was achieved for barium detection. They concluded that this sensitivity was promising enough to invest in further explorations of sensors able to capture barium ions and exhibit Ba^{2+}-induced fluorescence enhancement in dry noble environments.

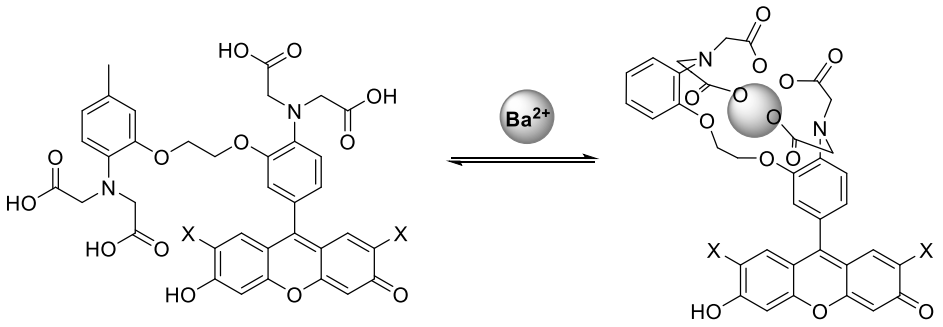

X = Cl, **Fluo-3**
X = F, **Fluo-4**

Figure 1.37. *Structure of sensors* ***Fluo-3*** *and* ***Fluo-4****, proposed by Nygren for* Ba^{2+} *sensing.*

In 2019, two families of dry-phase barium chemosensor molecules were developed within the NEXT collaboration, by Woodruff et al. (**Figure 1.38**).[14] The off/on sensor family was initially composed of two different fluorophores, the pyrene and the anthracene, linked with a methylene group to three differently sized aza-crown ethers as the receptor moieties. The diethanolamine linear moiety was not expected to bind the cation but was included as control system. These PET-based sensors were studied in MeCN solutions and, as already observed in previous Ba^{2+} sensor reports, the **18c6** species showed the strongest fluorescence response. A stoichiometry of 1:1 for all of them and a K_a of $6.25 \cdot 10^4$ M^{-1} for the **18c6-an** sensor was reported.

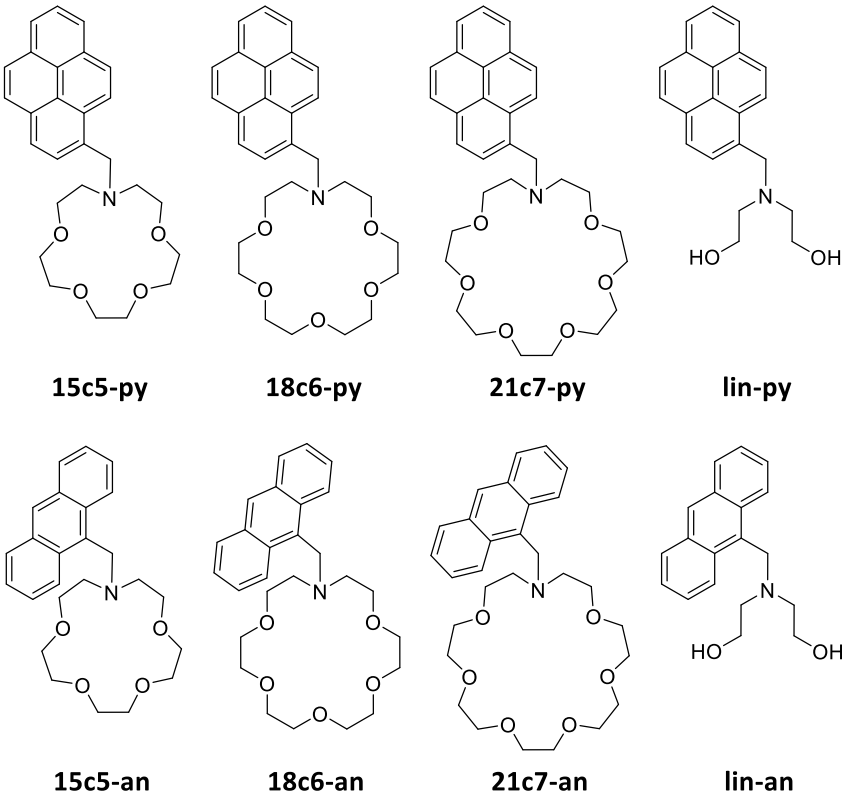

Figure 1.38. *The sensor family developed by Woodruff et al. for Ba^{2+} sensing, inside the NEXT collaboration.*

Furthermore, dry fluorescence studies of pre-chelated solutions were performed. The samples were prepared by drying some drops of each wet sample on a glass plate and drying the glass on a hot plate. They conclude that in the dry phase **18c6-an** responded with almost no intrinsic background from the free (off) state, and was susceptible to sense Ba^{2+} through fluorescence microscopy.

In 2020 and 2021, another family of mono- and di-aza-crown naphthalimide fluorescent sensors were reported by the same group (**Figure 1.39**).[59,60] Again, the 18-crown sized cycles showed better results compared to 15-crown-5 and 21-crown-7. The emission of these PET-based sensors is quenched in the free state and upon Ba^{2+} addition, an emission band at 530 nm appears, behaving as off/on sensors. K_a values between $1.3 \cdot 10^6$ - $1.7 \cdot 10^6$ M^{-1} were reported for **1B**, **1D** and **1E** in MeCN solutions. **1E** showed solution phase emission enhancements of 22-fold in the presence of Ba^{2+}. In this case, the sensors were supported in cyanoacrylate film over a glass slide and SMFI microscopy was employed for sensing single Ba^{2+} ions with these fluorophores.

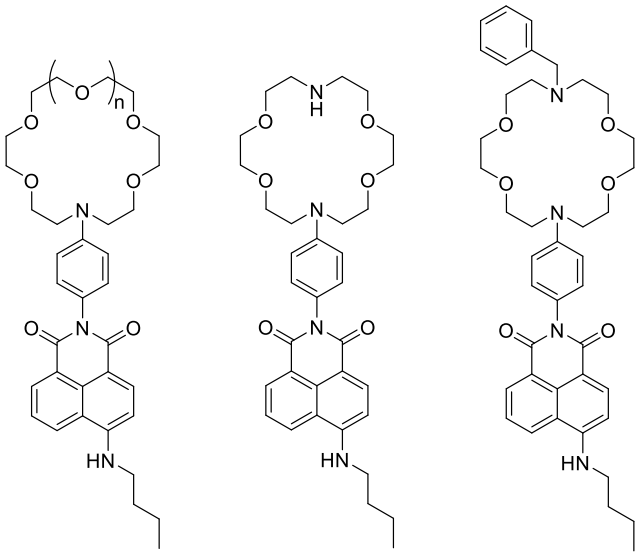

Figure 1.39. *Naphthalimide-based Ba^{2+} sensor family reported by Woodruff et al.*

1.3.2 FBI

In 2020, the group of Prof. Cossio published the development of a new family of ratiometric Ba^{2+} sensor, named Fluorescent Bicolour Indicator, shortened as **FBI** (**Figure 1.40**).[61] The **FBI** concept was considered the basis of a new strategy for barium-tagging sensor in a future HPXe experiment searching for ββ0ν decays.

The **FBI** design was based in a structural transformation of the fluorophore core upon interaction with Ba^{2+}. Thus, the **FBI** was capable of changing its color emission upon chelation with a barium cation, behaving as a ratiometric sensor for Ba^{2+}. Furthermore, due to the large emission shift exhibited of 61 nm, the authors described the indicator as a *bicolor* sensor. The binding constant was measured to be of $5.26 \cdot 10^4$ M^{-1} in MeCN solution, with a discrimination factor, in area of the bound sensor, in the order of 180. They also demonstrated that this chelation and shift was only produced with barium and that the indicator response did not form supramolecular complexes with light elements in the alkaline earth elements (such as Be^{2+}, Ca^{2+} and Mg^{2+}) as well as with other close alkali ions that are frequently found in the environment, such as Na^+ and K^+.

In dry medium, using silica as a physical support, they demonstrated that the **FBI** had discrimination factor of $2.5 \cdot 10^4$. This was proved by sublimating barium perchlorate

($Ba(ClO_4)_2$) on **FBI** molecules deposited on a silica pellet and using a two photon absorption microscopy setup. In their words, "it was the first time that the formation of a Ba^{2+} supramolecular complex in a dry medium was achieved".

FBI is composed of three parts, as shown in **Figure 1.40**. In blue, the fluorophore core, a benzo[a]imidazo[5,1,2-cd]indolizine fragment; in green, a rotating aryl ring acting as a spacer; and finally, in red, a 1-aza-18-crown-6 macrocycle, as the receptor unit.

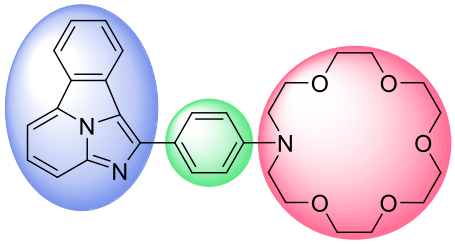

FBI

Figure 1.40. *Structure of* ***FBI****, with the three components shaded in color.*

As described by the authors, two of the key components of the structure were designed in a conscious manner. The first one, the fluorophore core, a nitrogen-containing aromatic polyheterocycle, where there is a nitrogen atom able to interact with the Ba^{2+} cation. The second one refers to the aromatic ring, connected to the indolizine by a free-rotating σ bond able to rotate and decouple it from the fluorophore, and able to form a cation-π interaction with Ba^{2+}. **Figure 1.41** summarizes the strategy applied in the **FBI** structure for Ba^{2+} binding and the expected blue shift of the emission.

In the free form of the sensor, i.e. not bound to barium, the indolizine core and the phenylene spacer are coplanar, forming a largely conjugated fluorophore. In a MeCN solution, the emission band of the free sensor is centered at 490 nm. Upon barium chelation, the cation interacts with the nitrogen of the core, the azacrown receptor and with the rotated phenylene spacer. This structural rearrangement causes a loss of conjugation between the aromatic ring from the indolizine core and the aromatic spacer, restricting the fluorescent emitter to the indolizine core. All these structural changes produce a blue-shift of the emission spectrum of the compound. The Ba^{2+}-bound FBI presents a structured band emission between 420-460 nm.

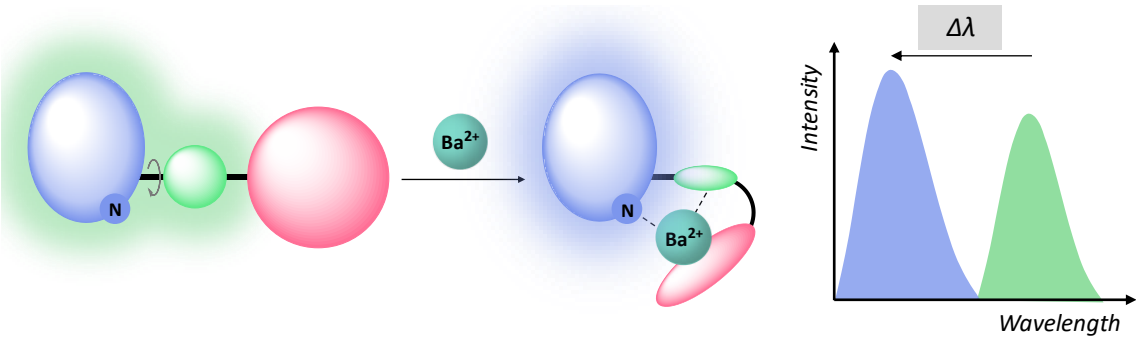

Figure 1.41. *The schematic structures for two component fluorophores in presence and in absence of Ba^{2+} and the expected emission spectra for both species.*

The cyclazine present in the structure is an interesting 12 π-electronic system, which resembles the spinning toy with the structure of delocalized 10 π-electron aromatic system and the handle corresponding to the nitrogen lone pair, which is not rotated (**Figure 1.42**). Hence, the structure has a symmetry plane.

Figure 1.42. *Illustration of a simple cyclazine with the lone electron pair of the nitrogen compared to a spinning toy, to represent the symmetry plane.*

60 years ago, Boekelheide was the first one to synthesize the cyclazine and he proposed a [8+2] mechanism for the reaction.[62] In this reaction, defined as [8+2] cycloaddition, an indolizine fragment reacts with a dienophile, an alkene or an acetylene (**Scheme 1.1**). From a practical point of view, cyclazines and their benzo derivatives are interesting entities. On the one hand, as they are fluorescent compounds they are promising candidates for luminescent applications.[63] On the other hand, biological activity was also found in cyclazines, their use as estrogens and anti-inflammatory compounds has been demonstrated in the last years.[64,65] The indolizine fragment is a π-excessive heterocycle where the highest electron population is on the C-3 carbon atom, causing that the major part of the chemistry of indolizines is based on the simple electrophilic addition and substitution at this position.[66] At the same time, it is well known the aforementioned

[8+2] cycloaddition, where the tetraene carbon framework of the indolizine bicycle plays the role of an 8 π-electron fragment.[67]

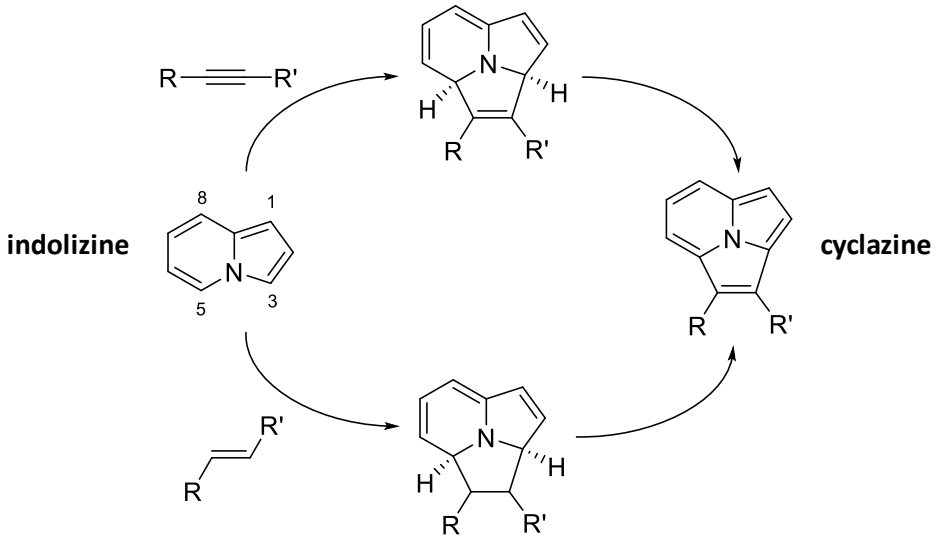

Scheme 1.1. *Formation of the cyclazine structure from an indolizine fragment by reacting with an alkene or acetylene.*

1.4 IRIDIUM COMPLEXES

Although to date, as detailed in the previous section, most organic based compounds have been reported for Ba^{2+} sensing, transition-metal based complexes for cations detection have been widely reported. Indeed, complexes including those of platinum(II), ruthenium(II), rhenium(I) and iridium(III) have been extensively utilized as probes for anions, metal ions, and biomolecules.[68] In this venue, phosphorescent Ir(III) complexes have attracted great interest due to their structural and luminescent advantages, including properties such as the ease of structure modification by ligand tuning or the long-time phosphorescent emission. For this reason, in the last decade, several iridium-based photoluminescent structures have been applied for cation sensing.

Iridium is a third-row transition metal, a member of the group of “precious metals”, discovered in 1803 by the English chemist Tennant, as an impurity in platinum. The name derives from the Latin Iris, the Greek goddess of rainbows, because of the striking and varied colors of the different iridium salts in solution. Despite the chemical diversity offered by the iridium element, with a wide range of oxidation states (-3, -1, 0, +1, +2, +3, +4, +5, +6, +7, +8, +9), +1 and +3 are its most common oxidation states. The cation

Ir(I) is a $5d^8$ electron system and forms tetra- and penta-coordinate complexes whose molecular geometry is square planar or trigonal bipyramidal, respectively. In the Ir(III) oxidation state, iridium is a $5d^6$ center, deriving in hexa-coordinated and octahedral iridium complexes. This last family of Ir(III) octahedral complexes are the central structure of one of the most widely known phosphorescent complexes. The octahedral Ir(III) complex family bearing C^N cyclometalated ligands possess outstanding photophysical properties that make these compounds highly desirable in various luminescent applications. Compared to the fluorescent emission of organic fluorophores, these cyclometalated Ir(III) complexes generally display long-lived phosphorescence, exhibit large Stoke shifts, and present high quantum yields.

The most commonly employed luminescent octahedral iridium $5d^6$ complexes are bis- and tris- cyclometalated, which broadens the range of potentially available structures, generating ionic or neutral complexes. Archetypal phenylpyridine and bipyridine based Ir(III) bis- and tris-cyclometalated complexes, $[Ir(ppy)_3]$ and $[Ir(ppy)_2(bpy)]^+$, are shown in **Figure 1.43**. Cyclometalated Ir(III) complexes can be categorized as heteroleptic when different ligands are integrated to the iridium center (e. g. bis-cyclometalated complexes) or homoleptic when three identical bidentate ligands are involved in the complex.

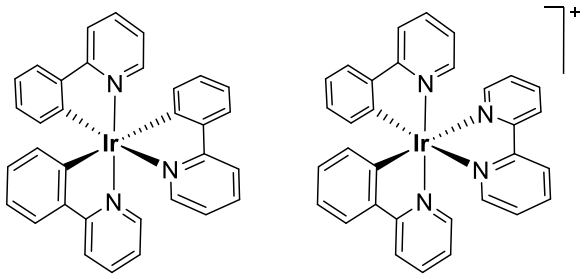

$[Ir(ppy)_3]$ $[Ir(ppy)_2(bpy)]$

Figure 1.43. *Sterochemical diagrams of representative archetypal neutral and cationic Ir(III) cyclometalates.*

In addition, Ir(III) complexes have an octahedral structure, generating different optical isomers depending on how the ligands are coordinated. In the case of homoleptic tris-cyclometalated complexes, facial and meridional geometrical isomers are presented (**Figure 1.44**). The facial isomer is the thermodynamic product, since it is formed mainly

because of the strong trans effect exerted by the donor carbon. The meridional isomer is the kinetic product. Both isomers have different photophysical properties, with the facial isomer being the one with a luminescence quantum yield one order of magnitude higher than that of the meridional isomer. Moreover, these octahedral complexes are chiral, but in the vast majority of the cases, they are obtained and used as racemates (Λ and Δ).

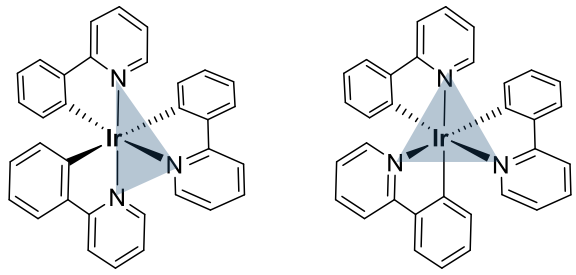

Figure 1.44. *Stereochemical diagrams of meridional and facial Ir(ppy)$_3$.*

As schemed in **Scheme 1.2**, both types of cyclometalated Ir(III) complexes, the cationic and neutral, are commonly synthesized through two steps: first with the formation of the dichloride-bridged dinuclear Ir(III) complex $[Ir(C\hat{}N)_2(\mu\text{-}Cl)]_2$ from the reaction between the cyclometalating ligand (HC^N) and hydrated $IrCl_3$. The bis- and tris-cyclometalated derivatives are usually obtained by cleavage of the chloride-bridge dimer in presence of a halide abstractor and subsequent reaction with the third ligand (in the presence of a base if required). As mentioned before, through this route, Ir(III) compounds are obtained as racemic mixtures of the Δ and Λ enantiomers, although, this two enantiomers can be separated through different methods.[69–71] As mentioned before, for tris-cyclometalated complexes, two isomers are possible, facial and meridional, being the latest synthesized under moderate conditions and isomerized to the facial isomer by heat or light. Often in the literature, the prefix is omitted, and it is assumed that the facial isomer is being discussed because these are generally much more emissive than the meridional is.

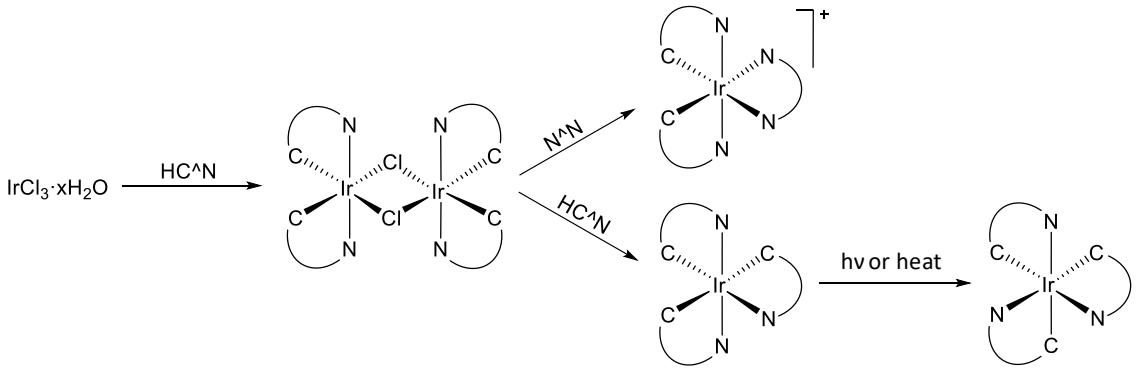

Scheme 1.2. *Synthetic scheme of cationic and neutral octahedral iridium(III) complexes.*

The neutral tris-cyclometalated complexes have some important drawbacks; the existence of the two isomers in the product, the often harsh conditions needed in their synthesis, and the difficulty encountered in the purification processes. In contrast, milder conditions are used to obtain charged complexes with neutral bidentate N^N ligands and usually present good performance. Furthermore, their cationic nature is helpful for the purification process. For instance, cationic bis-cyclometalated iridium(III) complexes containing two phenylpyridines and 2,2'-bipyridine or 1,10-phenanthroline as ancillary ligands have been extensively applied in different light-emitting devices. These complexes show intense phosphorescence at room temperature, and they have been widely investigated as phosphors in the construction of low energy consumption devices like organic light-emitting diodes (OLEDs) and light-emitting electrochemical cells (LECs).[72,73] In addition, their simple synthetic procedures, allows their photophysical properties to be modified by adjustment of the ancillary ligands.

The origin and features of the photoluminescent properties owned by these bis- and tris-cyclometalated Ir(III) complexes will be further detailed in the next section, followed by the introduction of several photoluminescent cation chemosensors based on these Ir(III) octahedral structures.

1.4.1 Ir(III) photoluminescence

The general molecular orbitals (MO) expected for an octahedral transition-metal complex are shown below (**Figure 1.45**). The overlapping of the ligands and metals atomic orbitals of matching symmetry and comparable energy form the molecular orbitals. When the atomic orbitals' wave functions are combined, they generate an

equal number of bonding and antibonding orbitals. The orbitals are labelled as a_{1g}, t_{1u}, e_g and t_{2g}, where the names correspond to the degeneracy and the symmetry of the orbitals.

In an octahedral d^6 complex, the degenerated d-orbitals in the octahedral ligand field are destabilized and divided by the splitting Δ0 energy. The energy between the three orbitals t_{2g} and the two orbitals e_g depends on the metals' oxidation state, the atomic number and the field strength of the ligand. Octahedral iridium complexes show large Δ0 values due to the high oxidation state of the metal and the size of its 5d orbitals. Additionally, cyclometalated aromatic ligands form strong bonding interactions with transition metals, increasing this energy gap.

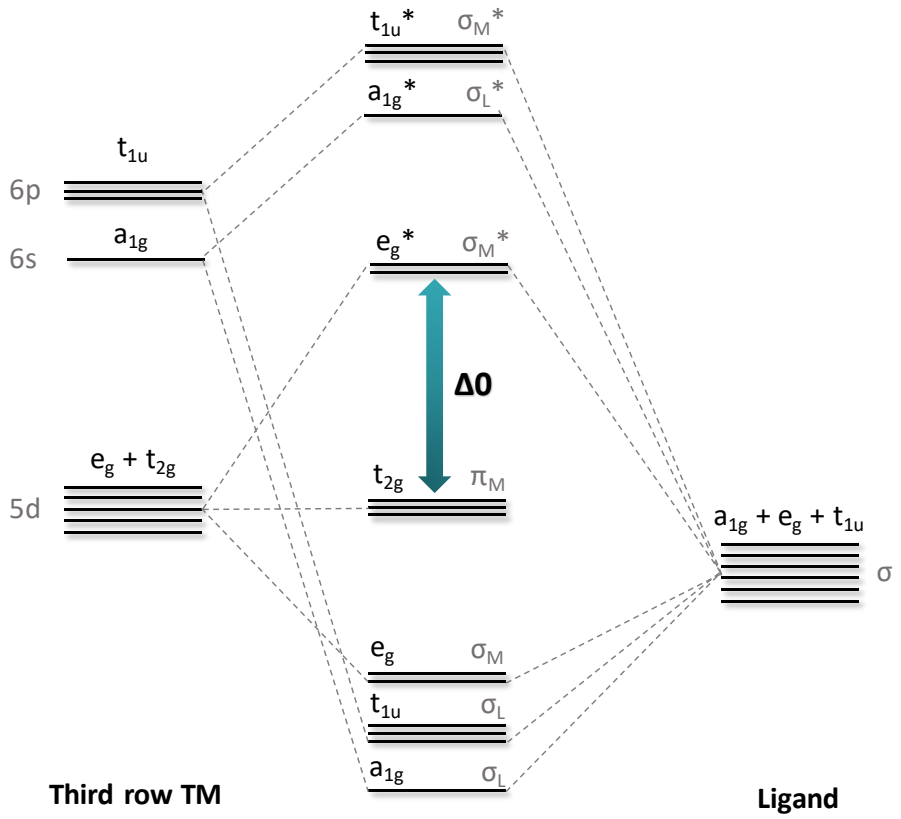

Figure 1.45. *Molecular Orbital diagram based on an octahedral transition-metal complex.*

In the ground electronic configuration of an octahedral complex of a d^n metal ion, molecular orbitals of types a_{1g}, t_{1u} and e_g are completely filled, while n electrons reside in the orbitals of types t_{2g} and e_g*. Due to the large Δ0 energy splitting, in the ground state, in a d^6 iridium complex the three orbitals t_{2g} will be full and the e_g empty.

The molecular orbital diagram shown in **Figure 1.45** is based on an ideal homoleptic octahedral symmetry diagram and involving merely σ donating ligands, thus the t_{2g} is just influenced by the metal. Nevertheless, for most octahedral coordinated complexes, the symmetry is lower than C3. As a result, the orbitals of the t_{2g} and e_g manifolds are no longer degenerate and are split into the d_n and d_n* orbitals, although they will still be proximate in energy. Additionally, when the π interactions are present Δ0 energy is further altered, relying on the π-donating or π-accepting ability of the ligands. Not only that, additional orbitals centered in the ligands, ppy and bpy, will be accessible. Ultimately, for the archetypal neutral $[Ir(ppy)_3]$ and the cationic $[Ir(ppy)_2(bpy)]^+$ complex the diagrams shown in **Figure 1.46** could be represented, with the split d_n and d_n* orbitals in grey, with a large Δ0 and the π and π* orbitals of the ligands, for ppy in blue and red and bpy in green.

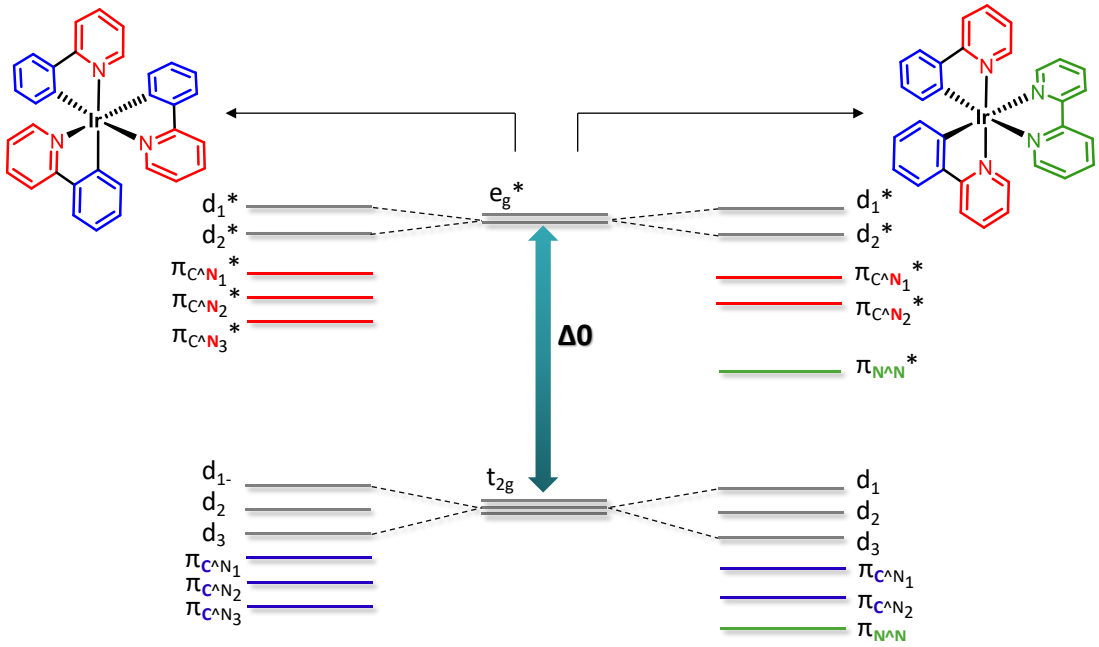

Figure 1.46. *Illustration of the molecular orbital energy level.*

Considering these simplified molecular orbital diagrams, the lowest unoccupied molecular orbital, LUMO, of these compounds will have a π* character, that will reside, in the case of $[Ir(ppy)_3]$, in the pyridine moiety of the ppy and in $[Ir(ppy)_2(bpy)]^+$ in the bipyridine ancillary ligand. When considering the excitation of the molecule, the following electronic transitions can be distinguished, according to the localization and nature of these orbitals (**Figure 1.47**): metal-centered (MC), ligand-centered (LC), metal-

to-ligand (MLCT), ligand-to-metal (LMCT) or ligand-to-ligand (LLCT) charge transfers. Note that this description is an oversimplification, as in this organometallic compounds one cannot make a distinction between metal and ligand orbitals. Some MO will have mixed d-ligand nature, they are better described as $d\pi_{Ir}$ and $d\sigma_{Ir}$*.

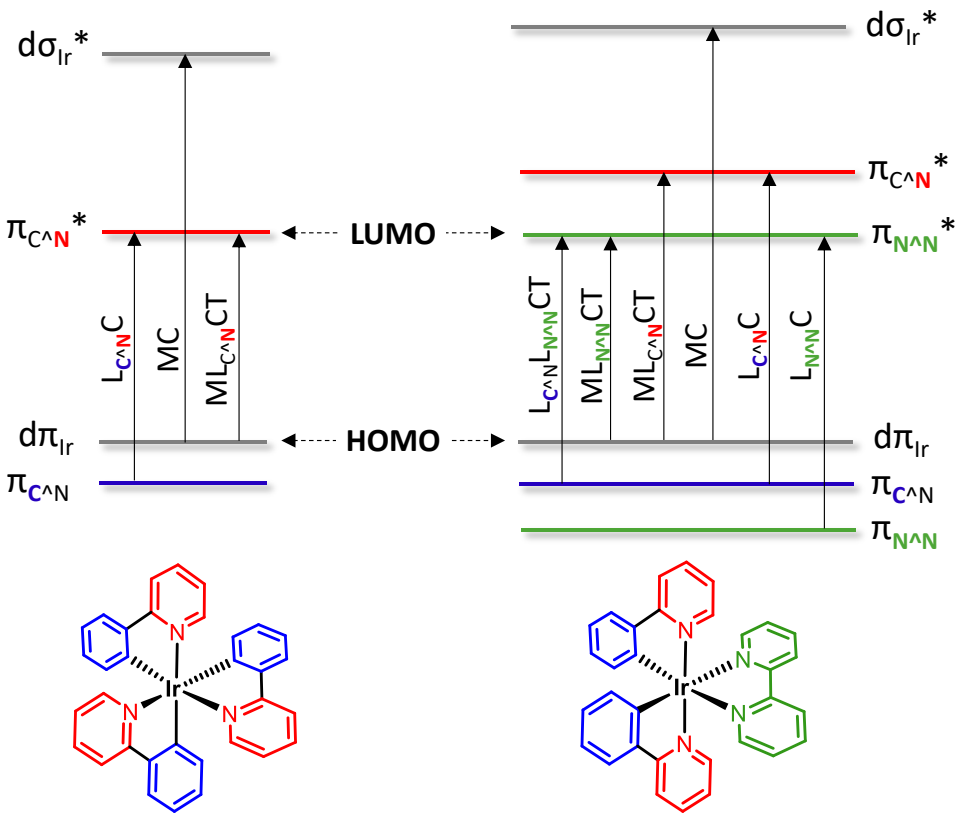

Figure 1.47. *Energy diagram of the possible electronic transitions.*

Because of the ligand-field stabilization energy (LFSE) in these complexes, the higher ionic charge of the metal, and the large size of the d orbitals, MC non-emissive states are not thermally accessible. In particular, by passing from a second-row Ru(II) to a third-row Ir(III) transition element the LFSE is further enhanced, thanks to the higher electric charge of the metal ion and to the presence of anionic cyclometalating ligands, typically used with Ir(III) centers. Thus, the non-emissive MC transition is avoided.

In addition to depicted spin-allowed transitions, the strong SOC of the Ir(III) center, enables a non-zero transition probability to overcome the spin restriction of singlet to/from triplet transitions. It is noted that the one-electron spin−orbit coupling constant of iridium(III) (4430 cm^{-1}) is greater than that of ruthenium(II) (990 cm^{-1}).[74]

As represented in the energy diagram in **Figure 1.47**, the highest occupied molecular orbital, HOMO, orbital is located mainly in the metal center, while the lowest unoccupied molecular orbital, LUMO, is mainly located in the pyridine ring of the ligands. When there is an absorption of a photon, the transition of an electron from the HOMO to LUMO is promoted, creating a singlet excited state. Due to the nature of HOMO and LUMO orbitals, the transitions ^{1}MLCT the ^{1}LC are observed.

This is represented in **Figure 1.48**, a simplified Jablonski diagram for the neutral archetypal complex [Ir(ppy)$_3$]. Due to the high spin-orbit coupling, there is a rapid relaxation from the singlet excited state to a lower lying ^{3}MLCT. As previously mentioned, phosphorescence always occurs from triplet levels ^{3}MLCT or ^{3}LC. In the case of the archetypal [Ir(ppy)$_3$] the emissive triplet state has been assigned to the ^{3}MLCT.[75] Finally, when it relaxes to the ground state (S_0), which is also a formally forbidden transition, phosphorescent light is emitted.

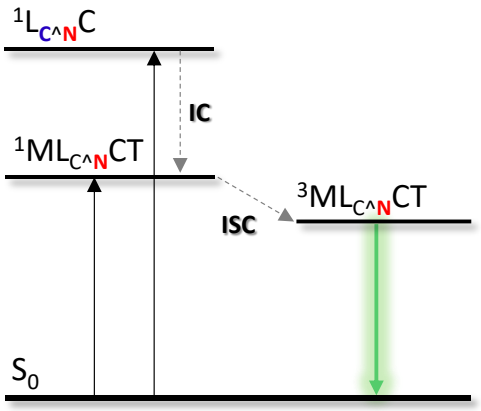

Figure 1.48. *Simplified Jablonski diagram of the fac-[Ir(ppy)$_3$].*

This results in the absorption and emission spectra for the archetypal *fac*-Ir(ppy)$_3$ shown in **Figure 1.49**.[76] The absorption at room temperature shows the ^{1}MLCT at lower energies and ^{1}LC, π-π*, at wavelengths above 300 nm. If the absorption spectra is recorded at low temperatures, excitation band of the directly ^{3}MLCT can be defined. The direct excitation to a triplet state involves also a spin-forbidden transition; it is less probable that a triplet state will form when the molecule absorbs radiation. However, the mixings between the different states by configuration interaction or spin-orbit coupling can be significant, due to the high density of states within corresponding

ranges. The emission spectrum at room temperature shows a broad band at around 520 nm, which at low temperature shows a double character, coming from vibronic states of ^{3}MLCT.

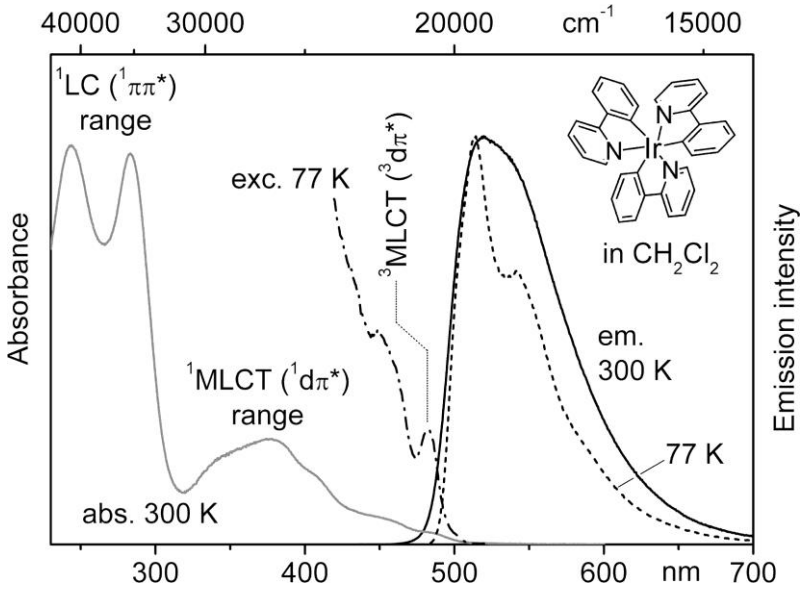

Figure 1.49. *Emission, absorption, and excitation spectra of fac-[Ir(ppy)$_3$] in CH_2Cl_2 ($c \approx 2 \times 10^{-5}$ M) measured at ambient temperature and 77 K. Emission spectra: λ_{exc} = 373 nm. Excitation spectrum: λ_{det} = 530 nm.*[75]

The meridional isomers of the tris-cyclometalates exhibit photophysical characteristics different from those of their facial analogues. For example, the ^{1}MLCT band shapes in the meridional isomer are less sharply defined and have lower extinctions than those in the facial isomer. Greater differences exist in the luminescent behavior. Unlike the highly structured emission displayed by *fac*-isomers, the *mer*-isomers display broader, red-shifted luminescence.[77]

In the case of the archetypal cationic [Ir(ppy)$_2$(bpy)]$^+$, **Figure 1.50**, the diagram is more complicated compared to the neutral *fac*-Ir(ppy)$_3$. Many excitation transitions to singlet manifolds are differentiated. After excitation, if ^{1}LLCT is accessed, it rapidly relaxes to the triplet manifold, low-lying states ^{3}LLCT and ^{3}MLCT, possibly indirectly via the ^{1}MLCT states. Partly is relaxed to ^{3}LLCT, responsible for the blue emission band. Another portion goes to ^{3}MLCT states lying at lower energies, responsible of the green and orange emissions.[78]

Often, to describe $[Ir(C^N)_2(N^N)]^+$ complexes, this diagram is simplified by defining the $^1ML_{C^N}L_{N^N}CT$ and $^3ML_{C^N}L_{N^N}CT$, as metal/ligand-to-ligand charge transfer excited states. Therefore, the less energetic absorption could be defined as a metal-ligand to ligand charge transfer, ^{1}MLLCT, a mixture of ^{1}MLCT and ^{1}LLCT.[79] Consequently, due to an effective intersystem-crossing (ISC), the emission originates from a ^{3}MLLCT state. Thus, the HOMO comprises a mixture of Ir d orbitals and the π-system of the phenyl rings of the ppy ligands, while LUMO, has primarily π*-character localized on the ancillary bipyridine ligand. In the case of the archetypal cationic complex, the high energy ^{3}LC does not participate in the emission.

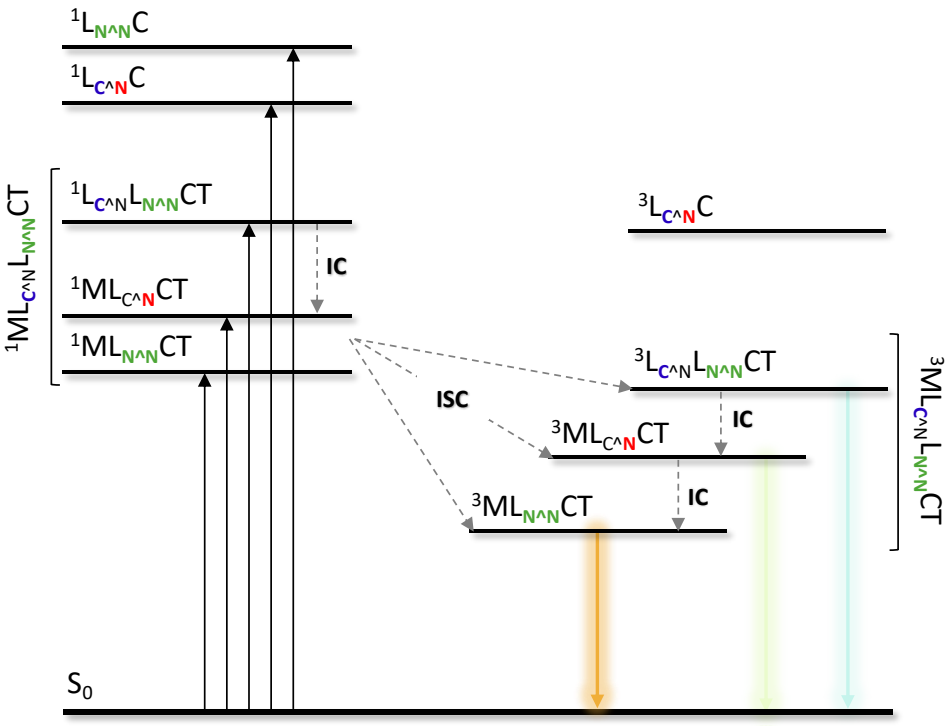

Figure 1.50. *Simplified Jablonski diagram of the fac-$[Ir(ppy)_2(bpy)]^+$.*

These electronic transitions result in the absorption and emission spectra in **Figure 1.51**. The absorption spectrum show the transitions of ^{1}ILCT centered in the ppy and bpy ligands of high energy and less intense bands in the lower energy region 300-500 nm assigned to the singlet and triplet MLLCT. The emission originated from a ^{3}MLCT centered at 600 nm at room temperature, is hypsochormically shifted to 500 nm at 77K, due to the rigidochromic effect.[78]

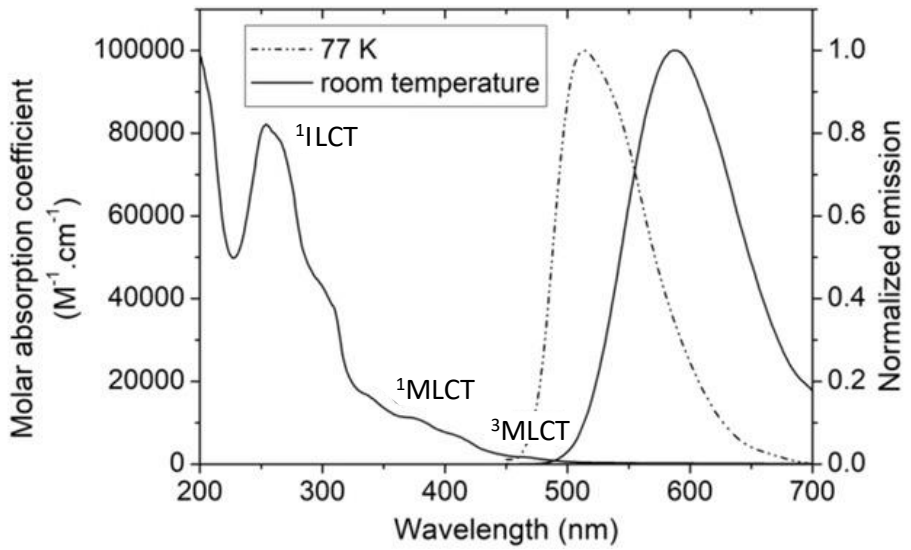

Figure 1.51. *Absorption and emission spectra of $[Ir(ppy)_2(bpy)]^+$ in MeCN at room temperature (solid lines) and in 4 : 1 ethanol/methanol glass at 77 K (dashed line).*[80]

Eventually, the color of the emission is related to the energy gap between the HOMO and LUMO orbitals of the complexes, so stabilization or destabilization of these orbitals causes changes in the color. As a general rule for $Ir(C^N)_2(N^N)^+$ compounds, substituents on the phenyl rings will impact mainly the HOMO level, while substituents on the N-coordinated ring impact the LUMO.[81] For instance, when electron donor groups are substituents on the ancillary ligand, the HOMO will destabilize and the HOMO-LUMO gap increases. If the electron donating group is strong enough, a less commonly encountered situation occurs, where the π of the bipyridyl ligand gets destabilized, lowering the transition energy of the diimine intra-ligand charge transfer.[82]

Cyclometalated Ir(III) complexes have attracted great interest due to their numerous advantages compared to organic fluorophores. It has been previously described the efficient tuning of the emission color with slight modifications in their structures.[83] The modular nature of inorganic synthesis allows the facile modification of these metal complexes. Besides, the excited states of transition-metal complexes are highly sensitive to both, the nature of the metal center as well as the character of the auxiliary ligands. For these reasons, the structural design and optimization of their luminescent properties becomes conveniently accessible.

As mentioned before, the lifetime of luminescent organometallic species is typically longer compared to the lifetime of organic fluorophores. Transition metal complexes

usually decay within a time range between hundreds of nanoseconds up to microseconds, whereas spin-allowed fluorescence from organic species typically occurs within few nanoseconds. In this context, the long-lived phosphorescence of these complexes could be useful to be distinguished from a fluorescent background, by using time resolved emission spectroscopy (TRES). This method involves setting a time gate between the excitation and the acquisition larger that the fluorescence decay time, to record only long-lived phosphorescent signals. The employment of this technique is introduced in some examples in the next section.

1.4.2 Iridium chemosensors

Over the last decades, transition metal complexes have received increasing interest in a number of fields such as optoelectronics, photochemistry, bio imaging, etc.[84] In recent years, they also have emerged as versatile chemosensors for different target analytes, including metal cations. By incorporating specific metal ion receptors, various iridium(III) complex sensors have been developed, based on different mechanisms.

Some reviews of heavy-metal chemosensors have been published in recent years.[85–87] In a transition metal complex-based sensor the metal center works as the signaling unit, i.e. luminescence source, while one or more of the ligands will include the selective receptor system to bind the cation.

In the context of this thesis, in the following section just photoluminescent iridium-based cation sensors will be discussed. The reported structures are divided into cationic and neutral iridium complexes, that respond as off/on, on/off and ratiometric chemosensors. The majority of structures found in the literature are cationic entities with pyridine and crown ether-based receptor sites. Sensors for the cationic analytes highlighted in the periodic table in **Figure 1.52** have been found in the literature.

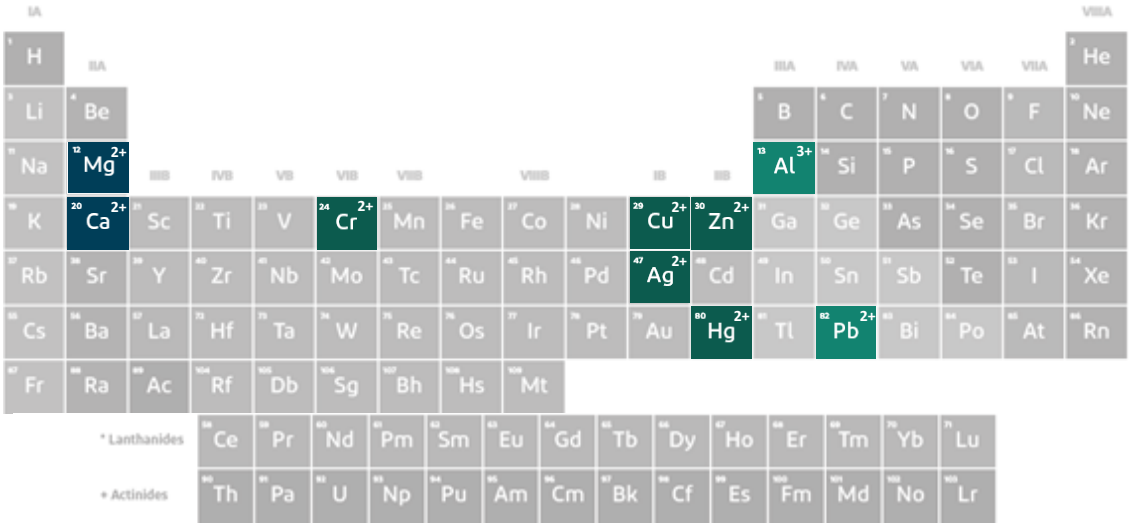

Figure 1.52. *Periodic table with the cationic analytes highlighted introduced in the next sections.*

1.4.2.1 Cationic

Even though most of the iridium-based sensors bear the receptor unit on the ancillary ligand Nabeshima et al. reported an iridium based Mg^{2+} sensor, bearing two aza-15-crown-5 ether phenylpyridines appended on the cyclometalating ligands (**Figure 1.53**).[88] The free complex is non-emissive, due to PET from the nitrogen atom of the aza-crown ether to the iridium(III) center. It becomes emissive in the blue-green region upon cation coordination. The emission was attributed, similarly to the general iridium cationic archetypes, to a mixed excited-state containing ^{3}IL and ^{3}MLCT transitions. The Mg^{2+}-bound aza-crown ethers anchored on the phenyl part of the cyclometalating ligands act like withdrawing substituents, inducing a stabilization of the HOMO and a subsequent blue shift of 51 nm compared to the crownless analogue reported structure. The stoichiometry of the host-guest system was assessed as 1:2.

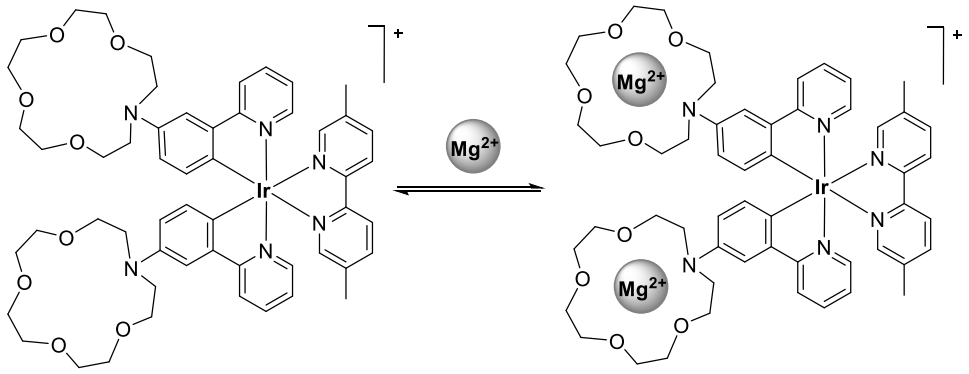

Nabeshima 2010

Figure 1.53. *Cationic Ir(III) system for Mg^{2+} sensing, reported by Nabeshima et al.*[88]

In 2016, Ma et al. described an off/on iridium chemosensor for Al^{3+} ion detection (**Figure 1.54**).[89] The structure contained an o-phenolsalicylimine cation receptor linked to an N^N ancillary ligand and two ppy ligands. In the presence of Al^{3+} ions, it suffered a 13.5-fold luminescence enhancement at 573 nm. The LUMO residing in the ancillary ligand was influenced by the cation interaction with the receptor, which activated the phosphorescence emission characterized a microsecond lifetime. The long lifetime luminescence of the complex was exploited by TRES measurements and was concluded to be potentially employed in a strongly autofluorescent biological sample.

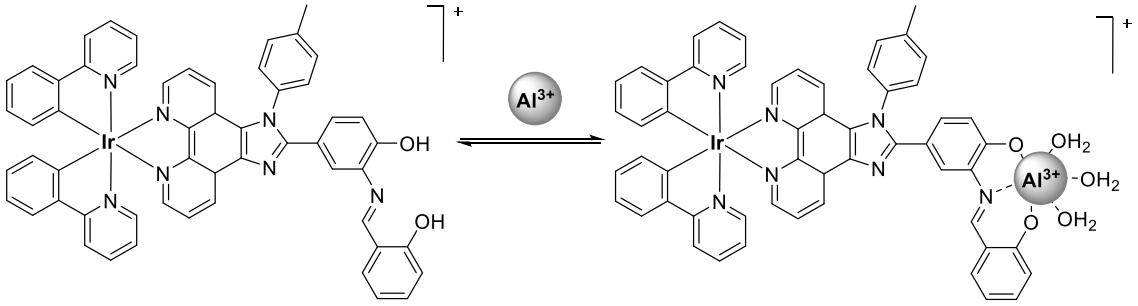

Ma 2016

Figure 1.54. *Cationic Ir(III) system for Al^{3+} sensing, reported by Ma et al.*[89]

Chen et al. published in the same paper four cationic structures capable of detecting Zn^{2+} and Cu^{2+} (**Figure 1.55**).[90] The free complexes display a low-energy absorption band with the maximum at 410-430 nm ascribed to an intraligand charge transfer (ILCT) transition from the HOMO(π) residing on the receptor end fragment to the LUMO (π*) localized on the bpy region. Thus, the complexes relax from a non-emissive or very low

emissive ^{3}ILCT transition energy excited state in their free state. Once the binding sites are bound to the specific metal ion, the HOMO switched to the ppy and the metal center, and highly luminescent ^{3}LLCT and ^{3}MLCT states are populated as the lowest energy excited states, resulting in a significant luminescence enhancement. Particularly high binding constants were reported for these complexes, $1.5 \cdot 10^8$ M^{-1} for the Zn^{2+} sensor and $1.7 \cdot 10^7$ M^{-1} for the Cu^{2+} sensor. Emission enhancements of 30 and 20-fold were recorded for Zn^{2+} and Cu^{2+} sensors, respectively.

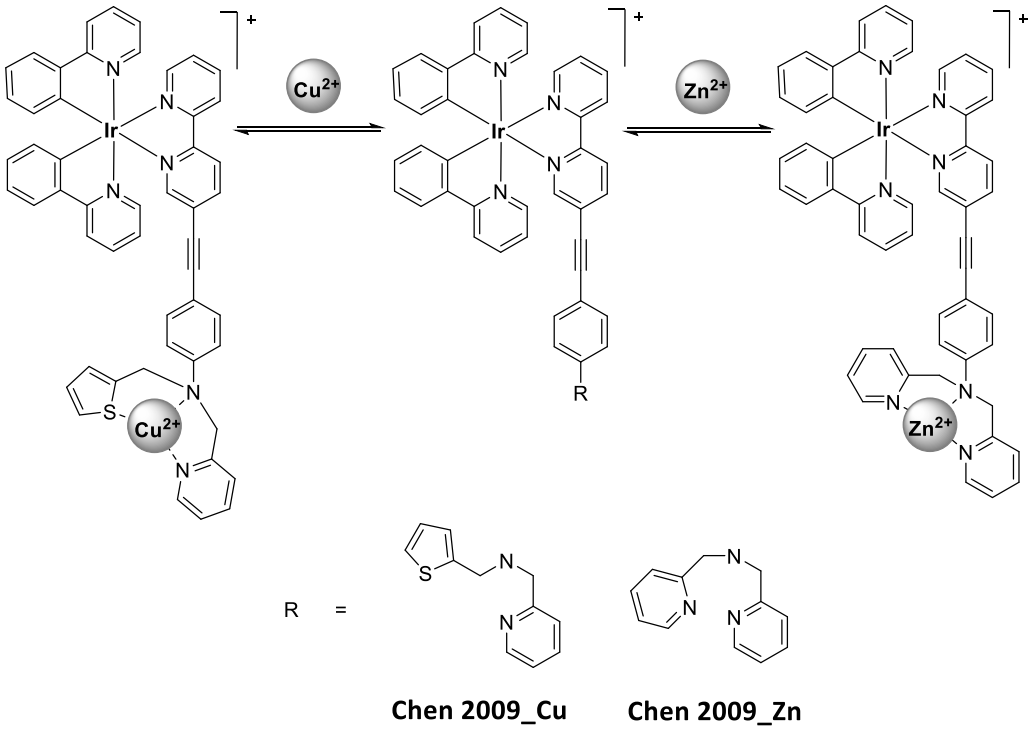

Figure 1.55. *Cationic Ir(III) system for Cu^{2+} and Zn^{2+} sensing, reported by Chen et al.*[90]

To date, the sensing of Cu^{2+}, together with Zn^{2+} cation, has been the most reported among the cationic iridium chemosensors. All the on/off cationic iridium-based structures found in the literature have been described for Cu^{2+} sensing. As it can be noticed in the following examples, several pyridyl containing receptors are designed to bind Cu^{2+}. In 2012, Yang et al. reported phenanthroline bearing sensor for Cu^{2+} sensing (**Figure 1.56**).[91] The luminescence centered at 600 nm in the orange region, attributed to the emission state of ^{3}MLCT, was quenched upon dication coordination. The host-guest 1:1 stoichiometry and proposed binding mode with a coordinated nitrate was confirmed by HRMS.

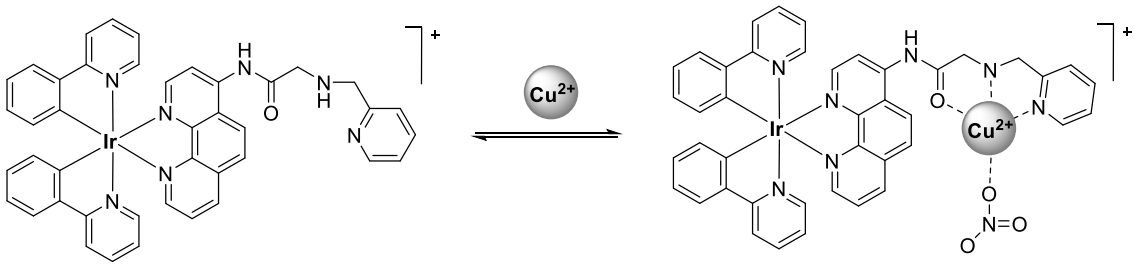

Yang 2012

Figure 1.56. *Cationic Ir(III) system for Cu^{2+} sensing, reported by Yang et al.*[91]

In 2013, Hyun et al. described a similar structure with the ancillary ligand based on a bipyridine with two receptor sites (**Figure 1.57**).[92] The emission spectrum showed the maximum at 589 nm in 50% MeCN in water, attributed to the ^{3}MLCT transition. The relative emission intensities, I_0/I, were 17.9 for Cu(II) and the host-guest stoichiometry was measured to be 1:2 by Job plot based on the emission spectrum.

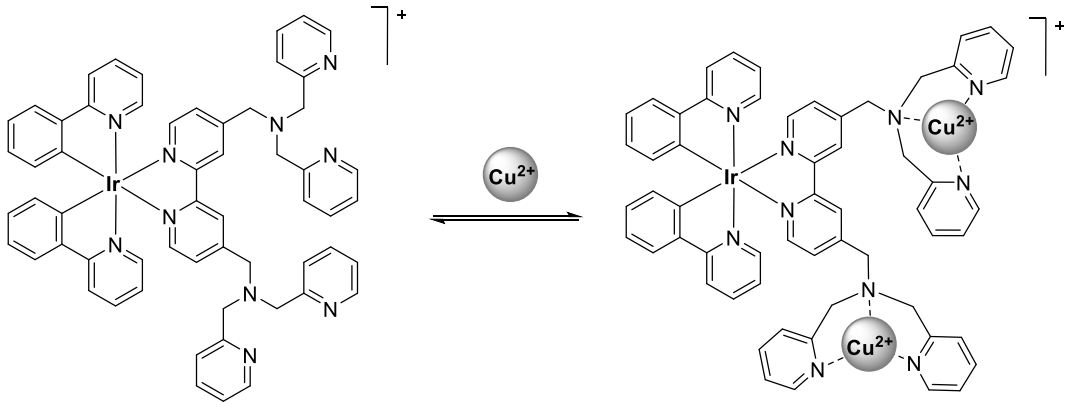

Hyun 2013

Figure 1.57. *Cationic Ir(III) system for Cu^{2+} sensing, reported by Hyun et al.*[92]

With the same receptor site, Zhang et al. designed two iridium complexes with different cyclometalating ligands, employing coumarin and benzothiazole-based ligands (**Figure 1.58**).[93] The complexes exhibited green emission with a maximum main peak at 529 nm and a small shoulder peak at 567 nm in methanol solution at room temperature, with different quantum yields of 0.06 and 0.3, and lifetimes of 1.8 and 1.1 μs, for **A** and for **B**, respectively. The phosphorescence quenching upon binding to Cu^{2+} ions was demonstrated to be reversible, testing with the addition of an aqueous of EDTA disodium. In 2017, same authors published another article based on a very similar structure, with comparable results.[94]

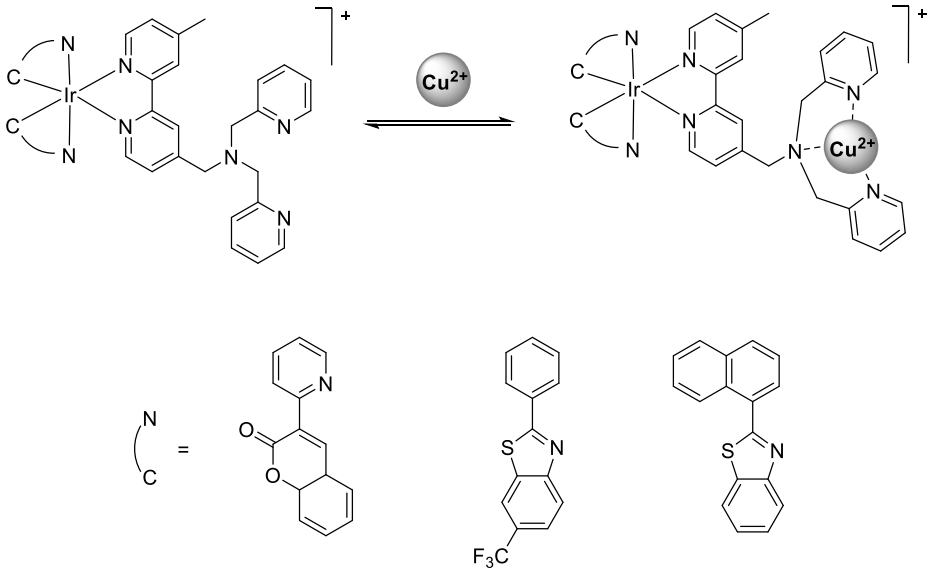

Zhang 2019_A **Zhang 2019_B** **Zhang 2017**

Figure 1.58. *Cationic Ir(III) system for Cu^{2+} sensing, reported by Zhang et al.*[93]

The last on/off sensor was reported by Leung et al., an iridium(III) complex-based chemosensor bearing the 5,6-bis(salicylideneimino)-1,10-phenanthroline ligand receptor for Cu^{2+} (**Figure 1.59**).[95] The emission of the free sensor at 560 nm, attributed to the ^{3}MLCT, was quenched upon cation chelation, while a highly sensitive and selective color change from colorless to yellow could be observed. The free complex showed an efficient quantum yield of 0.39 and a long lifetime luminescence of 4.8 µs.

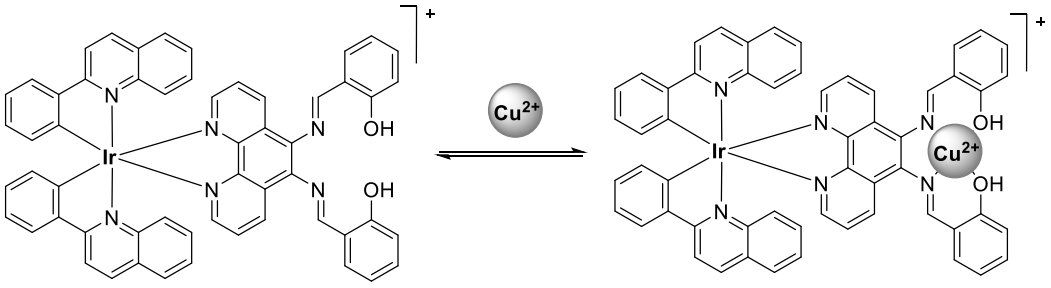

Leung 2014

Figure 1.59. *Cationic Ir(III) system for Cu^{2+} sensing, reported by Leung et al.*[95]

On the other hand, most of the ratiometric cationic iridium sensors have been described for Zn^{2+} detection. In 2011, Lippard et al. described an iridium sensor consisting of a zinc-binding di(2-picolyl)amine unit on a phenanthroline ancillary ligand and two 2-(2,4-difluorophenyl)pyridine ligands (**Figure 1.60**).[96] As a result, the sensor exhibited an

almost quenched slight dual emission in the blue and yellow regions in its zinc-free state, while zinc addition triggered a selective turn-on of the yellow phosphorescence. The quantum yield increased from 0.02 to 0.58. In the free state, the quenching mechanism of the phosphorescence was claimed to be based on PET. When the cation interacts with the electron lone-pair of nitrogen atom of the amine, this mechanism is no longer operative and the ^{3}MLCT is activated. In 2013, the same group further investigated the PET mechanism on these complexes and similar ones.[97]

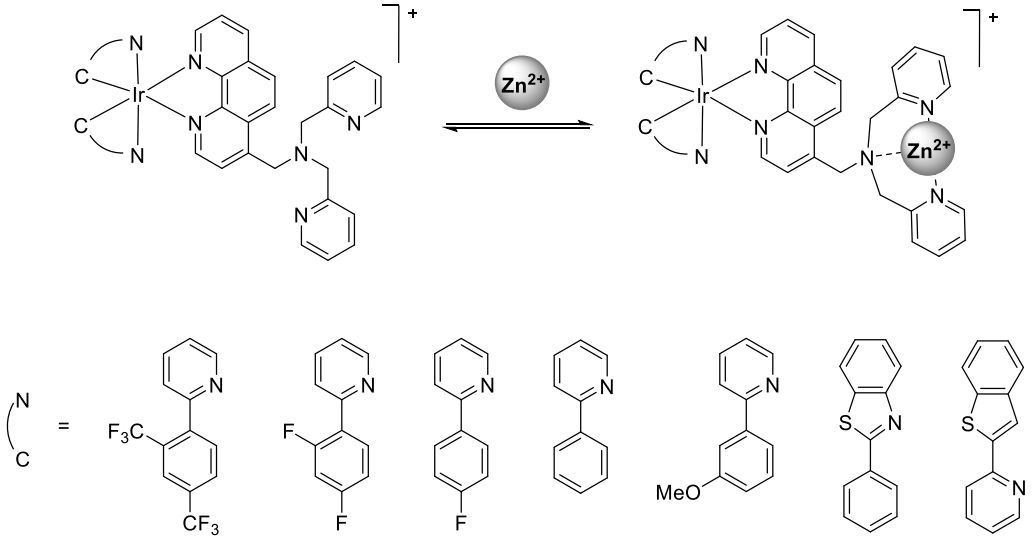

Lippard 2013

Figure 1.60. *Cationic Ir(III) system for Zn^{2+} sensing, reported by Lippard et al.*[96]

Substantially comparable structures have been described as Zn^{2+} chemosensors, based on $[Ir(ppy)_2(N^N)]^+$ systems bearing a similar receptor unit with pyridines. For instance, in the complexes reported by Lo et al. the binding unit di-2-picolylamine is directly appended in 5 position of a phenanthroline (**Figure 1.61**).[98] The emission of the complex is described as ^{3}MLCT mixed with some ^{3}ILCT (n-π*) element, which could be viewed as metal-perturbed ^{3}IL. Upon zinc binding, they suggest a substantial suppression of ^{3}ILCT character and the subsequent prevalence of ^{3}MLCT character in their emissive states, producing a ratiometric answer.

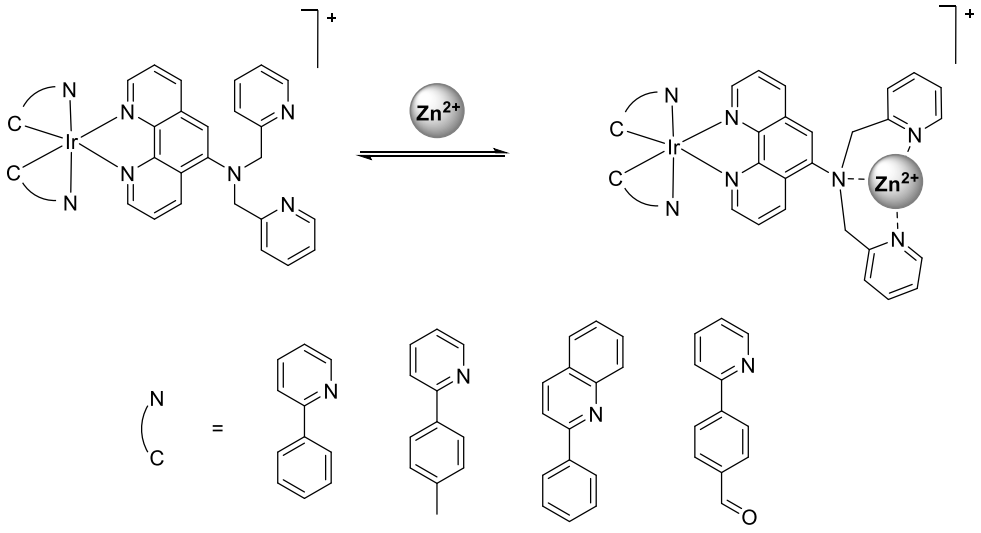

Lo 2011

Figure 1.61. *Cationic Ir(III) system for Zn^{2+} sensing, reported by Lo et al.*[98]

In the complex presented by Guerchais et al. the ancillary ligand is based on a bipyridyl unit and the same receptor is appended with a conjugated system as spacer (**Figure 1.62**).[99] A similar phenomena is observed. The free complex shows a non-emissive behavior in solution at RT. Nevertheless, when the emission was recorded at 77 K, the complex emitted brightly, displaying a highly structured spectrum deep into the red region. It showed an exceptionally long lifetime of 67 μs, which meant that the radiative rate constant is very low. The emission was assigned to ^{3}ILCT character localized on the styryl-substituted bpy ligand, with relatively low metal participation; triplet excited states, in which the metal plays only a minor role, are expected to have longer radiative lifetimes owing to less efficient ISC pathways. The triplet radiative rate constant was so low that, at RT, the excited state was essentially fully deactivated by the faster E–Z isomerization process of the stilbene-like spacer, resulting in no emission. This emission at 77 K blue-shifted upon Zn^{2+} binding.

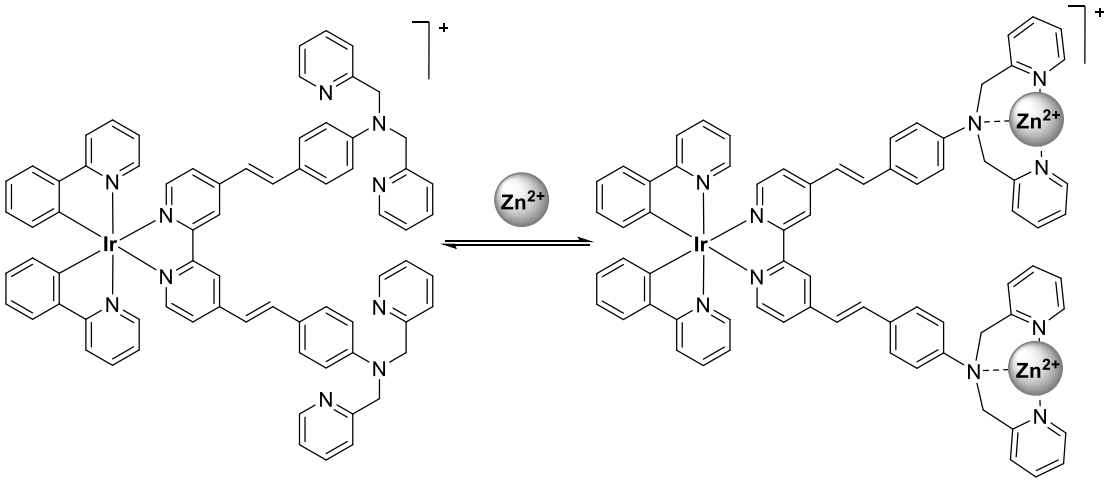

Guerchais 2010

Figure 1.62. *Cationic Ir(III) system for Zn^{2+} sensing, reported by Guerchais et al.*[99]

Wong et al. described an iridium cationic sensor with a visual ratiometric response (**Figure 1.63**).[100] Upon the addition of Zn^{2+} ions to the complex in solution, a pronounced luminescence color change from blue to green was observed, presenting a red shift of 60 nm, which was attributed to the suppression of PET upon complexation. By DFT calculations, the emission band of the free specie, at 425 nm, was assigned to a mixing of n(amine) → π*(phen) and dπ(Ir) → π*(phen) charge transfer transitions, while the emission band at 475 nm of the Zn^{2+}-bound specie, was attributed to the dπ(Ir) → π*(phen) charge transfer transition. Besides, a luminescence enhancement of 6-fold was observed. The practical application of the complex for imaging Zn^{2+} ions in live zebrafish was successfully demonstrated.

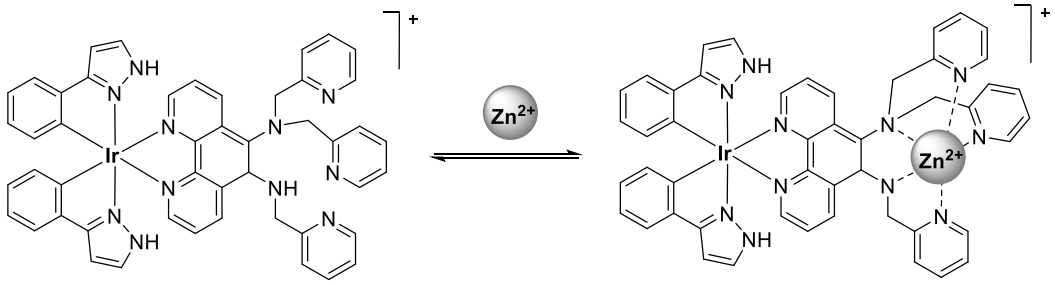

Wong 2014

Figure 1.63. *Cationic Ir(III) system for Zn^{2+} sensing, reported by Wong et al.*[100]

Ratiometric iridium cationic structures to detect other cations, such as Cr^{3+} or Al^{3+}, have also been reported. In 2012, the first phosphorescent probe for chromium ion was

developed by Nam et al., based on a cyclometalated Ir(III) complex bearing two 2-(2,4-difluorophenyl)pyridine and 1,10-phenanthroline ligands (**Figure 1.64**).[101] The Cr^{3+} ion responsive bis(2-(2-(methylthio)ethylthio)ethyl)amino receptor was introduced at the 4-position of the phenanthroline ligand. The interaction between cation and receptor produced a double-stage phosphorescence ratiometric response in MeCN. The first stage was prompt and reversible green-to-orange phosphorescence change, from 515 to 557 nm, the first reversible phosphorescence change that involves modulation of PET and the MLCT transition state. The quantum yield showed an increment from 0.016 to 0.13. In a second step, in the Cr-bound state, the Cr(III) center evokes a biomimetic oxidation reaction by activating molecular oxygen to cleave the [Cr(BTTA)] ionophore. This biomimetic oxidative cleavage produced the second phosphorescence ratiometric response.

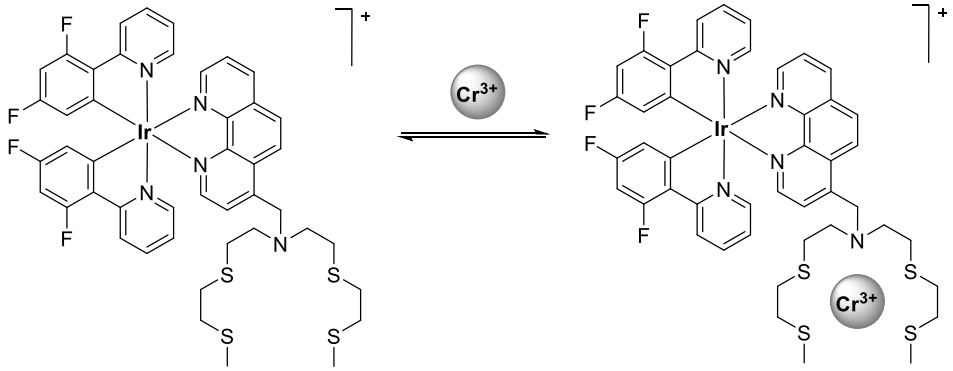

Nam 2012

Figure 1.64. *Cationic Ir(III) system for Cr^{3+} sensing, reported by Nam et al.*[101]

Lin et al. reported an aza-dithia-dioxa crown-ether-appended iridium(III) complex for Ag^{+} sensing (**Figure 1.65**).[102] A gradual emission enhancement and a red shift of in the emission maxima were observed upon cation addition. The free complex showed a double-shaped maximum, attributed to the excited states ^{3}LC and ^{3}MLCT, mainly dominated by ^{3}LC. The luminescence enhancement of the complex was rationalized by a weakening of the electron donating ability of the nitrogen of the crown ether moiety upon Ag^{+} complexation, altering its photophysical properties. The lower energy emission was explained by the stabilization of the LUMO energy level. Interestingly, the titration revealed how the double-shaped maximum gradually merged into one single maximum,

which was described as a change of the dominating ^{3}LC emission in the metal-free form to a dominating ^{3}MLCT emission in the metal-bound form.

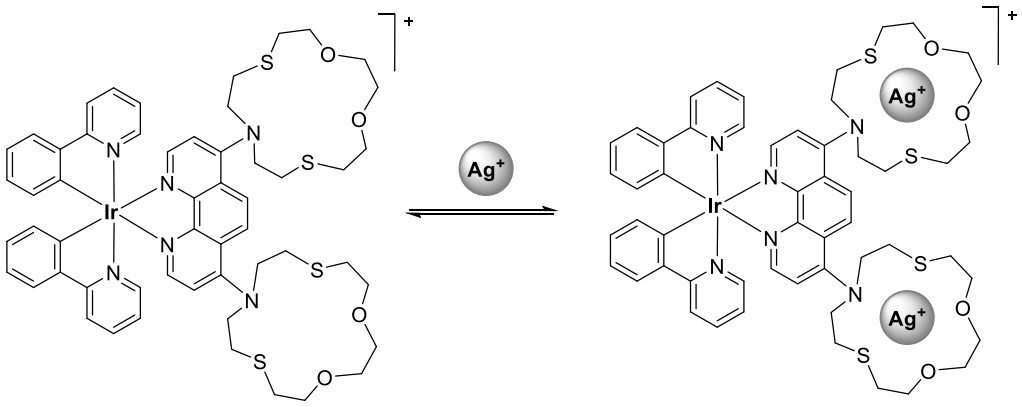

Lin 2007

Figure 1.65. *Cationic Ir(III) system for Ag^+ sensing, reported by Lin et al.*[102]

This last structure exemplified for cationic iridium structures resembles the first example in **Figure 1.53**. However, in this case, the crown receptors are appended in the N^N ancillary ligand. Thus, upon cation interaction, the LUMO is modified, while in the first introduced example the HOMO was affected when cation binding occurred.

1.4.2.2 Neutral

Although most of the iridium-based cation sensors reported to date are cationic structures, some neutral complexes have also been described in the literature.

A phosphorescent cyclometalated heteroleptic Ir(III) complex with two ppy and an ancillary ligand of 4-azacrownpicolinate was described by Hyun et al. with an on/off response (**Figure 1.66**).[103] The electron donating ability of the tertiary amino group of the azacrown ether moiety in Ir(III) complex was responsible for the enhancement of its phosphorescence intensity in aqueous MeCN media. The dramatic decrease in the phosphorescence emission of the iridium probe in presence of Hg^{2+} was attributed to the decreased electron donating ability of the amino group of the azacrown ether through the effective complexation of Hg^{2+} with the azacrown ether ring and the possible heavy atom effect exerted by the resulting complexed Hg^{2+}.

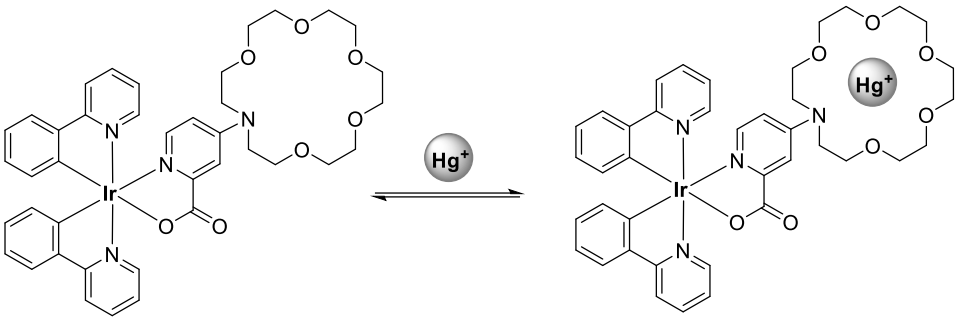

Hyun 2011

Figure 1.66. *Neutral Ir(III) system for Hg^{+} sensing, reported by Hyun et al.*[103]

In 2007, another on/off system was reported by Chi et al., to the best of our knowledge, the only iridium based Pb^{2+} sensor (**Figure 1.67**).[104] A 3,5-di(pyridyl)pyrazole moiety is attached to the heteroleptic Ir(III) complex, making the complex neutral and thus, theoretically, improving the binding of the cation analyte. In its free state, the HOMO and LUMO resided predominantly on the ancillary ligand. They conclude the emission quenching effect is due to the pyrazolate directly linked with Pb^{2+}, provoking the intersystem crossing to another lower-lying triplet state for the host molecule via an enhanced spin–orbit coupling. Consequently, the emission intensity could be quenched due to a smaller T_1– S_0 energy gap.

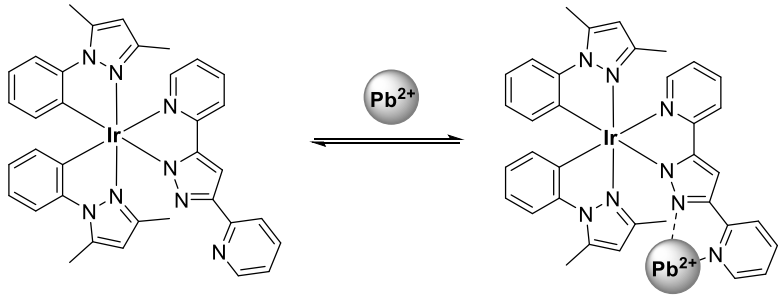

Chi 2007

Figure 1.67. *Neutral Ir(III) system for Pb^{2+} sensing, reported by Chi et al.*[104]

A very similar structure bearing a crown receptor was described as a ratiometric sensor. The cation probe bearing a central Ir(III) element and 1-aza-15-crown-5-ether substituted pyridyl pyrazolate as the chelate was introduced by Chou et al. (**Figure 1.68**).[105] It presented a yellow-green emission at ~560 nm in both solution and solid state at room temperature. A blue shift and emission enhancement in spectral properties upon metal Ca^{2+} were observed, from 560 to 520 nm. The complex quantum

yield gave a value of 0.22 that was unaltered upon cation binding. The lifetime of the emission lowered from 8.2 µs to 0.6 µs.

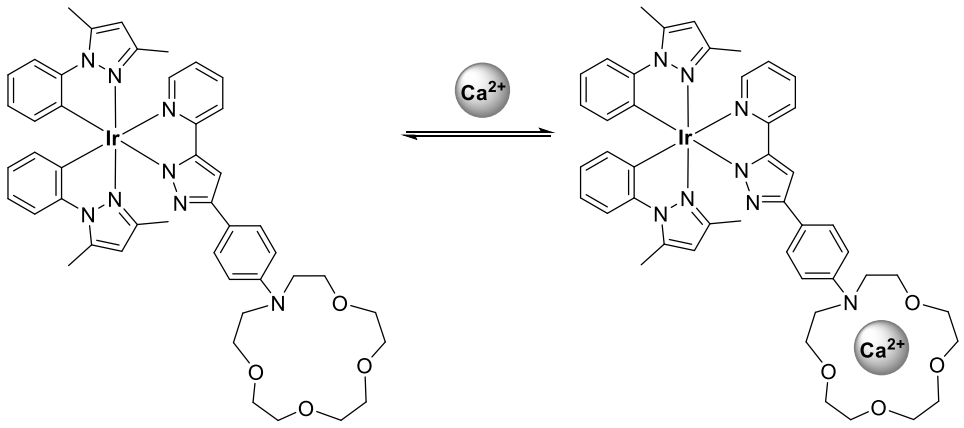

Chou 2016

Figure 1.68. *Neutral Ir(III) system for Ca^{2+} sensing, reported by Chou et al.*[105]

The mechanism was elucidated by DFT calculations based on an analogous crownless version and using H^+ as the analyte. The lowest triplet manifold exhibited predominantly a ^{3}ILCT transition, in which HOMO and LUMO are mainly located at the phenyl pyrazolate and pyridyl chromophores, respectively. In sharp contrast, upon protonation the transition switched greatly to ^{3}LLCT, from the phenyl pyrazole ligand to *p*-dialkylamino-phenyl pyrazolate. The assume that the differences in photophysical behavior between the crownless complex and H^+ could be applied to the described complex, thus changes of absorption and emission spectra during Ca^{2+} titration were rationalized by the swap of lowest transition from ^{3}ILCT to ^{3}LLCT in the complex. Interestingly, the same structure was tested for Ba^{2+}, Mg^{2+} and else. The complex gave an association constant of $4.2 \cdot 10^4$ M^{-1} for Ca^{2+} and $1.6 \cdot 10^5$ M^{-1} for Ba^{2+}. The quantum yield, lifetime and emission values were comparable for Ba^{2+} and Ca^{2+} bound sensor. However, the structure was only described for Ca^{2+} sensing.

The sensing performance was also tested in solid. A silica-based TLC plate was used as a solid support and soaked in a sensor containing MeCN solution. The plate was then dipped in Ca^{2+} containing water solution and vacuum dried. The emission changed from yellow of the Ca^{2+} free sensor to green emission upon Ba^{2+} binding.

In 2011, a Ir(III) complex was described by You et al. capable of detecting copper(II) reversibly and selectively in aqueous media (**Figure 1.69**).[106] The phosphorescent sensor based on a multichromophoric iridium(III) complex exhibited concomitant changes in its phosphorescence intensity ratio and phosphorescence lifetime in response to copper(II) ion. The iridium complex was described as a phosphorescent dual-emitter. The emission at 600 nm, centered in the 2-(20-benzo[b]thienyl)pyridine (btp) ligand, was quenched upon complexation with copper, while the green emission at 500 nm, centered in the ppy ligands, remained unaltered. Thus, a ratiometric signal was obtained based on dual emission, with green and red bands corresponding to the reference and probe signals, respectively. In addition, a decrease in phosphorescence lifetime of the red emission was monitored, which shortened from 4.6 to 2.5 μs, while the lifetime of the emission at 500 nm remained at 0.5 μs.

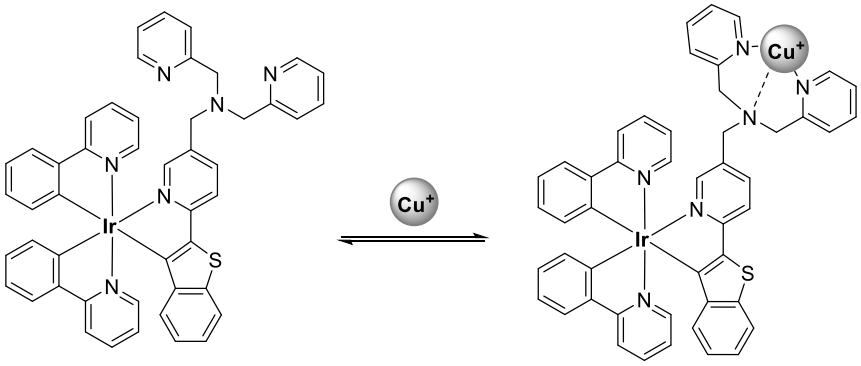

You 2011

Figure 1.69. *Neutral Ir(III) system for Cu^{2+} sensing, reported by You et al.*[106]

In 2019, Suzuki et al. described two iridium complexes capable of Al^{3+} sensing, with ppy and phen units as cyclometalating ligands (**Figure 1.70**).[107] Even though the third ligand is a bipyridine unit, the overall charge of the structure is neutral, due to the deprotonation of one of the phenolic oxygens. The ppy based structure, demonstrated to fold its emission 775 times after Al^{3+} chelation. Besides, the emission color blue shifted, from orange to green, with a 75 nm shift. When these Ir(III) complexes bound Al^{3+} cation, the complex rigidified and the quantum yields were 10-folded, achieving a quantum yield of 0.40. Before and after chelation the luminescence examined had a lifetime of 7 to 12 μs, which correlates with phosphorescence. In the free specie the HOMO-LUMO transition was attributed to a $^3\pi-\pi^*$ ILCT in the bipyridyl mixed with a

^{3}LLCT from the bipyridyl to the ppy ligands. In contrast, the emission of Al^{3+}-coordinated specie was assigned to the ^{3}MLCT from Ir to ppy orbitals and ppy to bipyridyl-Al^{3+} transitions.

The high selectivity obtained was attributed to the high affinities of the (O,O) atoms in 2,2'-bipyridine-3,3'-diol for hard metal ions and the increased strain of the seven-membered chelate ring due to the coordination of ligand to the Ir(III) center in each complex, which excluded large metal ions out of the chelate ring. The rigidity is one of the methods described for the augmentation of the phosphorescent quantum yields.[108]

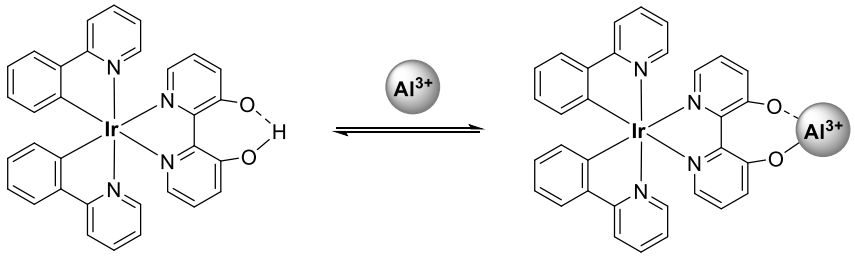

Suzuki 2019

Figure 1.70. *Neutral Ir(III) system for Al^{3+} sensing, reported by Suzuki et al.*[107]

1.5 SOLID STATE SENSING

As explained in the barium tagging section, barium tagging was proposed to lower the background signal for the NEXT experiment in the search of neutrinoless double beta decays. During this decay event, the formed electrons will lose energy by collisions with other Xe atoms and on the anodic side of the chamber, in the tracking plane (ETD), the silicon photomultipliers (SiPMs) will track the topology of this energy loss (**Figure 1.71**). On the opposite side, behind the transparent cathode the energy of the electrons will be quantified by the photomultipliers (PMTs) on the so-called energy plane. In this time-projection chamber (TPC) construction, the electric field that drifts the ionization electrons from the two emitted electrons towards the detector anode will cause the Ba^{2+} dication to drift towards the cathode.

In the proposed scheme, in this transparent cathodic site, there would be a monolayer of fluorescent sensors able to capture the Ba^{2+} cation.

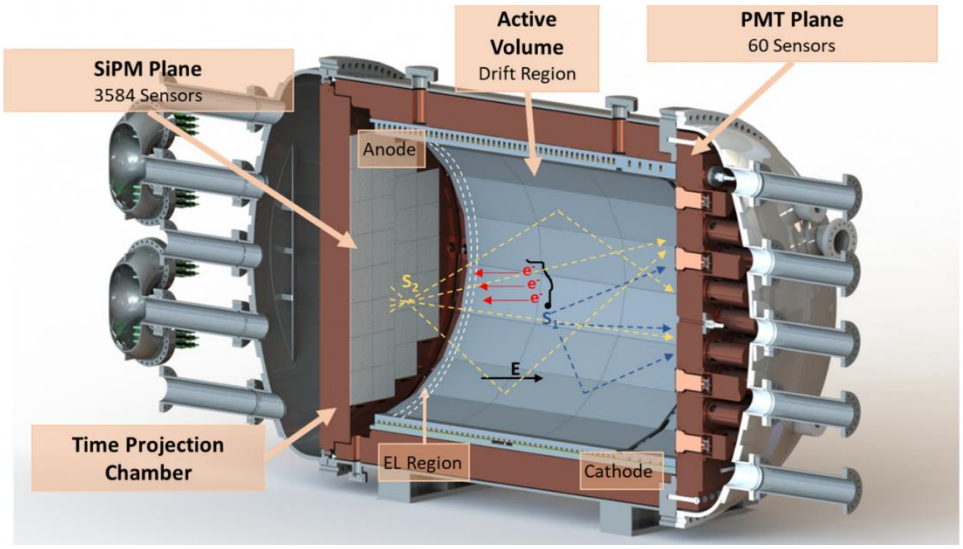

Figure 1.71. *Time Projection Chamber, reproduced from ref* 109.

The original proposal of Nygren in 2015,[11] of using a Ba^{2+} sensor based on fluorescent molecular indicator incorporated at the cathode of a HPXe-TPC, was further developed by the NEXT collaboration in the following papers.[12] In 2018, a first proof-of-concept study was published, identifying individual Ba^{2+} ions in aqueous medium by a transparent thin quartz plate with Fluo-3, a commercial indicator, suspended in polyvinyl alcohol (PVA).[13]

In 2019, Nygren et al. listed the requirements of a barium chemosensor suitable for Ba^{2+} tagging in ^{136}Xe-based 0νββ experiments.[14] The last two points were described as the ability to chelate ions at the gas-solid interface and its stability under a dry noble gas environment. These conditions depend sensitively on the form of the final coating, which was visualized and proposed as a self-assembled (SAM) and covalently tethered monolayer of chemical luminescent sensors on a thin transparent surface.

This stage remains quite a complex challenge, as most of the performance of sensors reported in literature are tested and described in solution or at solid-liquid interfaces. In this context, few chemosensors anchored in SAM to quartz or glass surfaces have been previously reported which will be introduced in this section.

Nesterov et al. have reported the only fluorescent ratiometric sensors described to date in a self-assemble monolayer mode. It is based on a chemodosimeter (sensing based on the analyte triggering a chemical modification of the sensor). The three systems show a similar structure,

with oligo(p-phenylene ethynylene)s (OPEs) terminated with a lower energy gap group and covalently immobilized on a surface to yield monolayer thin films. In 2009, to sense the analyte cysteine, an anthracene derivative was used as receptor (**Figure 1.72**).[110] The energy transfer from the OPE chain to the anthracene was efficient before the cysteine reaction, being the anthracene moiety the emissive unit. Upon the reaction of the aldehyde on the anthracene with cysteine, the HOMO-LUMO gap increased, changing the emission to higher wavelengths arising from the OPE moiety.

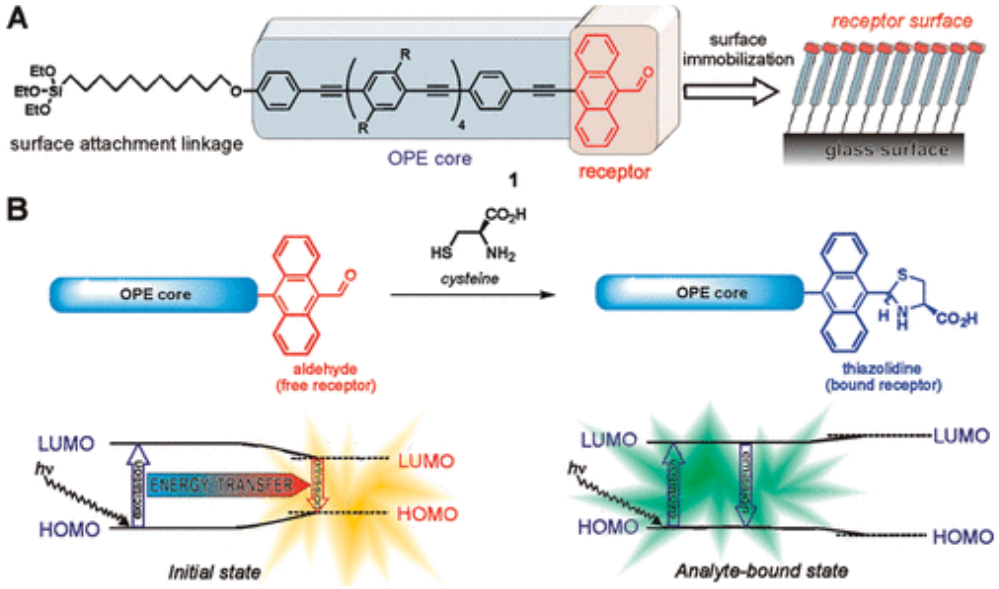

Figure 1.72. *Strategy employed by Nesterov et al. to anchor a chemodosimeter for cysteine on a glass surface. Reproduced from ref [110].*

In 2013, the same structure was described as pH and fluorine anion sensor, a self-assembled monolayer of OPE with a fluorescein receptor group.[111,112] The same mechanism was presented when encountering the fluorine anion. Since electronic coupling between the OPE and fluorescein chromophores is not very strong, the system displays two distinct emission bands. The relative intensity of the two emission bands can be controlled by changing efficiency of intramolecular energy transfer within the dyad through chemical perturbation of one of the dyad components (**Figure 1.73**). Thus, at low pH, fluorescein exists in the neutral lactone form with a higher HOMO-LUMO gap, and therefore fluorescent emission will predominantly originate from the OPE, a higher energy band. Increasing pH results in converting fluorescein into more delocalized anionic and dianionic isomers with a decreased HOMO-LUMO gap, facilitating the energy transfer to the fluorescein receptor, and raises the intensity of bathochromically shifted emission with concomitant decrease of the higher energy OPE emission.

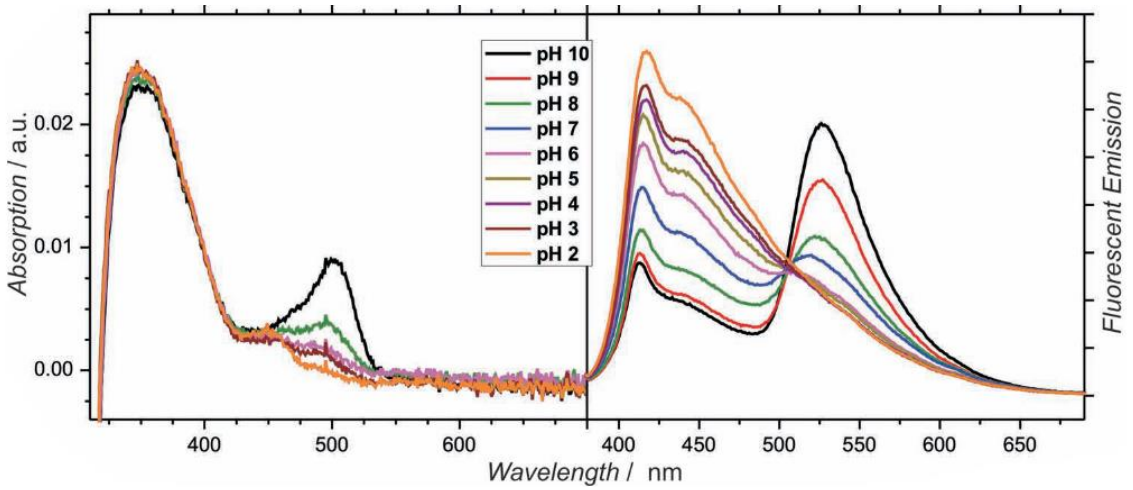

Figure 1.73. *Absorption and emission ratiometric response upon pH changing. Reproduced from ref* [112].

In 2014, a supported chemodosimeter for Hg^{2+} cation sensing was also reported by Palestino et al.[113] As shown in A in **Figure 1.74**, as a support, a porous silicon micro cavity (PSiMc) was used, and upon Hg^{2+} addition the shift and enhancement in the emission produced by the formation of metal-ligand coordination bonds, induces the spirolactam ring opening. The system produced a slight shift in the emission (B in **Figure 1.74**).

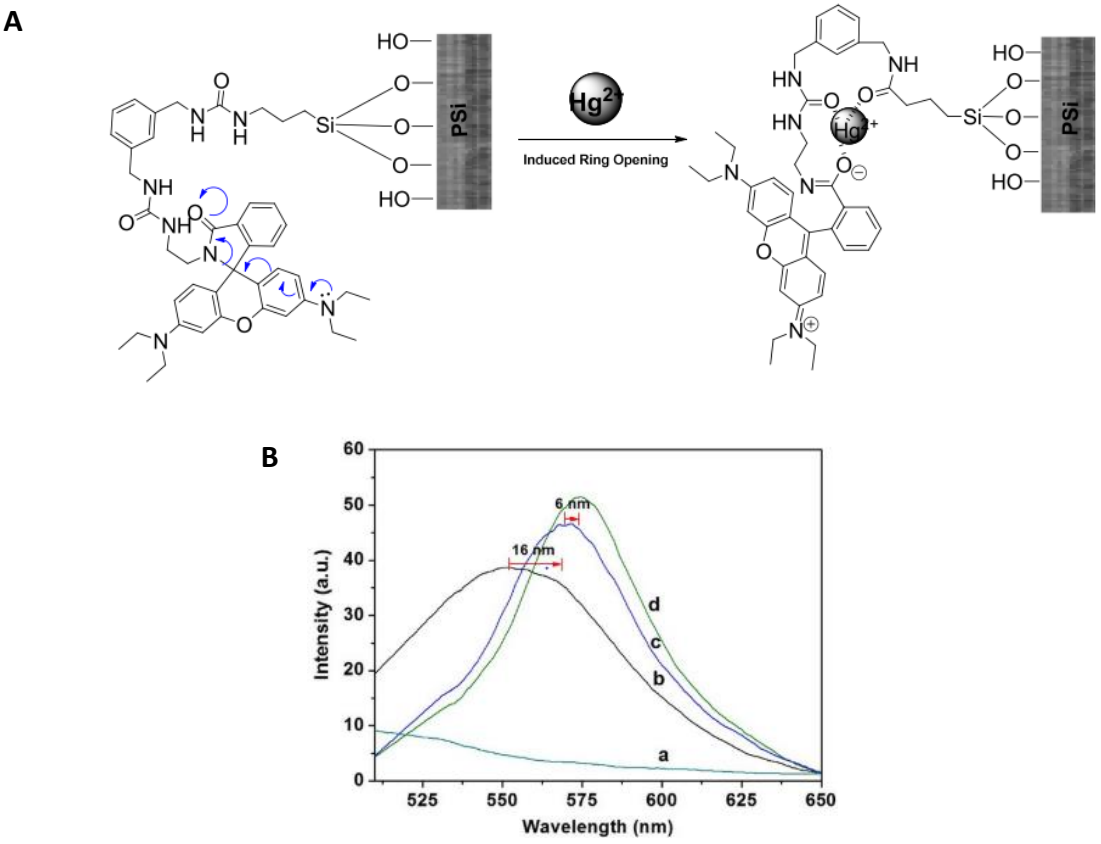

Figure 1.74. *A) Chemodosimeter strategy reported by Palestino et al. for Hg2+ sensing. B) Ratiometric response: b, starting material; c and d, with Hg^{2+} at different concentrations. Reproduced from ref* [113].

Aside from chemodosimeters, other SAM based fluorescent chemosensors have been reported, as “on-off” or “off-on” systems. In 1999, Reinhoudt described the selective binding of b-cyclodextrin to self-assembled dansyl monolayers on quartz and oxidized silicon wafers, detected by fluorescence spectroscopy (**Figure 1.75**).[114] The observed changes of the emission spectra, a slight turn on, were the result of molecular recognition rather than a specific binding of cyclic oligosaccharides to the dansyl monolayer.

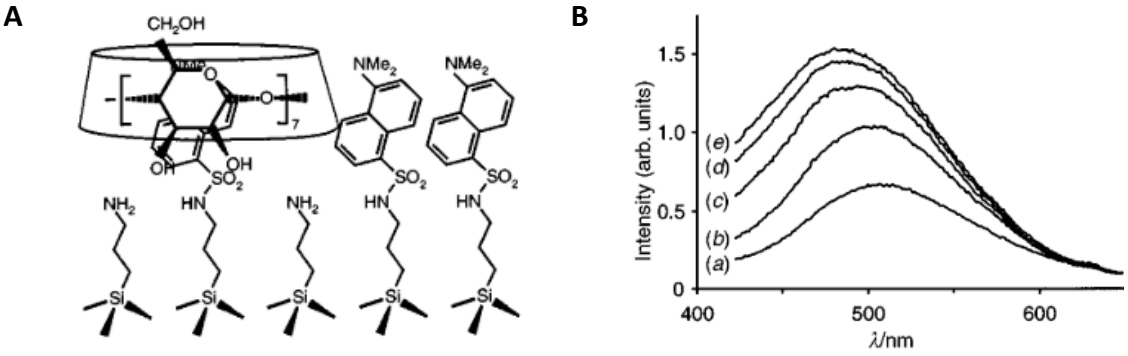

Figure 1.75. *A) “Off/on” sensor system for cyclodextrins. B) Off/on response upon cyclodextrin addition, a being the free sensor. Reproduced from ref* [114].

This recognition system was later employed by anchoring a calix[5]arene onto a surface to sense n-alkyl substrates, as represented in **Figure 1.76**, published by Gulino et al.[115,116] Using a silica surface the sensing performance was observed by XPS, UV-vis and fluorescence, were an emission enhancement was detected upon 1,5-pentanodiamina addition, for instance.

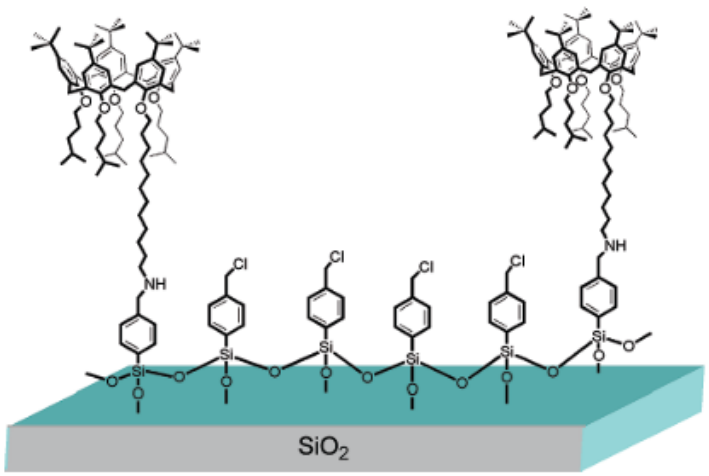

Figure 1.76. *Calix[5]arene based sensor system reported by Gulino et al fo alkyl sensing. Reproduced from ref* [115,116].

Cation chemosensors anchored onto a surface have also been reported. For instance, Wang et al. used a glass surface to immobilize a conjugated polymer film with phosphonate-functionalized polyfluorene as a luminescent sensor for Fe^{3+} cation (**Figure 1.77**).[117] The emission was quenched upon cation interaction by accessing the interior conjugated polymer film. Compared with the fluorescence quenching properties of the same polyfluorene in THF solution and in spin-casting film, both quenching constant and detection limit of the immobilized film were improved by an order of magnitude, which demonstrated the advantage of the immobilized film fluorescence sensor.

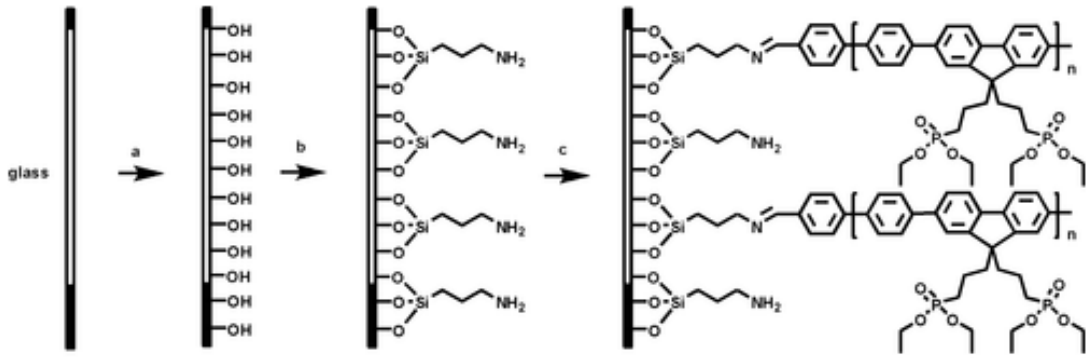

Figure 1.77. *The sensor system reported by Wang et al. based on glass immobilized phosphonate-functionalized polyfluorene for Fe^{3+} sensing. Reproduced from ref* [117].

In 2004, self-assembled monolayers on glass were used as a platform to sequentially deposit fluorophores and small molecules for ion sensing (**Figure 1.78**).[118] A library of luminescent sensing surfaces was introduce and the detection of several cations and

anions were evaluated with a combinatorial approach. By using this approach, based on cation-induced excimer formation, the need for complex receptor design was discarded.

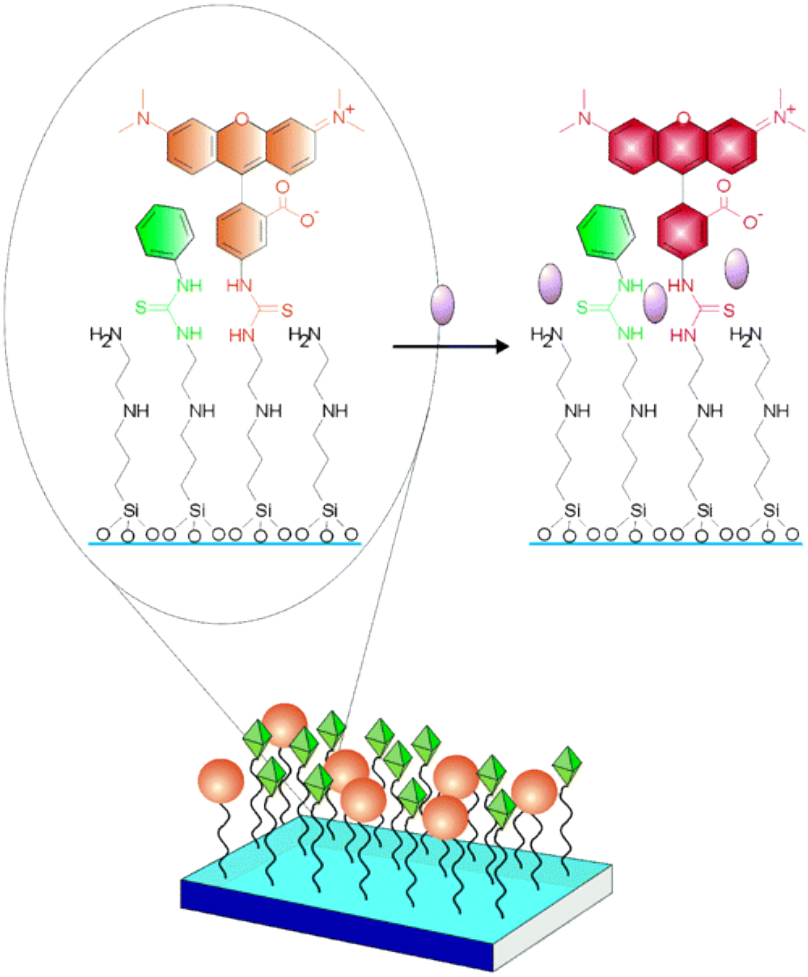

Figure 1.78. *Representation of the approach employed by Crego-Calama et al. for ion sensing. Reproduced from ref [118]. The bottom schematic depicts binding groups by octahedrons and fluorescent groups by orange spheres. The top schematic illustrates how an analyte (purple ovals) can interact with the layer due to its coordinating properties, and the interaction is reported by the fluorophore.*

Despite the fact that there are examples of sensors on the surface, as shown with the last examples, all of them operate in a solid-liquid interface and, most of them, are based on chemodosimeters. As far as we know, there are no examples of solid-gas sensors, aside from sensors for oxygen, based on the simple quenching of the triplet emission, or some sensors for reactive vapors, such as NH_3, HCl, NO, other VOCs.[119–121]

Thus, the transfer of the properties of a dissolution sensor to a solid-dry or solid-noble gas, as needed in the Ba^{2+}-tagging NEXT project, is not at all trivial and will still need a lot of R&D.

1.6 GENERAL OBJECTIVE

The general objective of this thesis is the synthesis of new sensors, composed by ligands based on the FBI structures bound to an iridium octahedral center. Eventually, the formation of self-assemble monolayers (SAM) of the best candidate will be optimized, and the study of the sensor on surface will be pursued. With this goal, the thesis is divided in three chapters and chronologically organized.

Chapter 2: Ligands

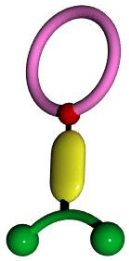

Develop **FBI**-based ligands as organic sensors to coordinate to Ir(III). Optimize their synthesis and measure their luminescent properties. Synthetize bipyridine-based Ba^{2+}-sensing ligands, as prototypes, for the optimization of the next objective.

Chapter 3: Iridium complexes

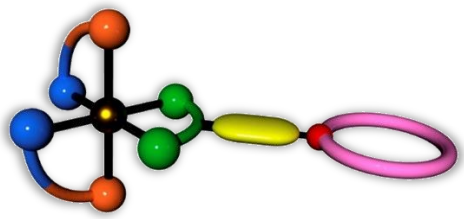

Coordinate **G3-FBI** ligands to simple Ir(III) complexes. Optimize the synthesis and measure their luminescent properties. Coordinate the prototype ligands. Optimize the synthesis and measure their luminescent properties.

Chapter 4: Functionalization and supporting

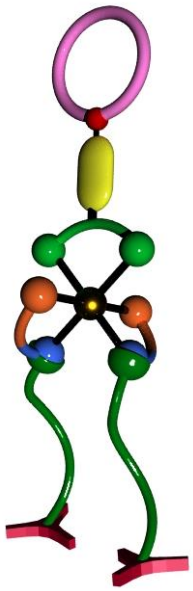

Functionalization of iridium and ruthenium complexes as luminescent models to optimize the anchoring procedures and luminescent behavior of upcoming supported sensors. Synthesize a derivative of the selected iridium complex and study the supporting. Characterize and measure its luminescent properties.

1.7 References

1 N. G. Cooper, *Los Alamos Science, Number 25 -- 1997: Celebrating the neutrino*, Los Alamos, NM, 1997.

2 Y. Fukuda, T. Hayakawa, E. Ichihara, K. Inoue, K. Ishihara, H. Ishino, Y. Itow, T. Kajita, J. Kameda, S. Kasuga, K. Kobayashi, Y. Kobayashi, Y. Koshio, M. Miura, M. Nakahata, S. Nakayama, A. Okada, K. Okumura, N. Sakurai, M. Shiozawa, Y. Suzuki,

Y. Takeuchi, Y. Totsuka, S. Yamada, M. Earl, A. Habig, E. Kearns, M. D. Messier, K. Scholberg, J. L. Stone, L. R. Sulak, C. W. Walter, M. Goldhaber, T. Barszczxak, D. Casper, W. Gajewski, P. G. Halverson, J. Hsu, W. R. Kropp, L. R. Price, F. Reines, M. Smy, H. W. Sobel, M. R. Vagins, K. S. Ganezer, W. E. Keig, R. W. Ellsworth, S. Tasaka, J. W. Flanagan, A. Kibayashi, J. G. Learned, S. Matsuno, V. J. Stenger, D. Takemori, T. Ishii, J. Kanzaki, T. Kobayashi, S. Mine, K. Nakamura, K. Nishikawa, Y. Oyama, A. Sakai, M. Sakuda, O. Sasaki, S. Echigo, M. Kohama, A. T. Suzuki, T. J. Haines, E. Blaufuss, B. K. Kim, R. Sanford, R. Svoboda, M. L. Chen, Z. Conner, J. A. Goodman, G. W. Sullivan, J. Hill, C. K. Jung, K. Martens, C. Mauger, C. Mc Grew, E. Sharkey, B. Viren, C. Yanagisawa, W. Doki, K. Miyano, H. Okazawa, C. Saji, M. Takahata, Y. Nagashima, M. Takita, T. Yamaguchi, M. Yoshida, S. B. Kim, M. Etoh, K. Fujita, A. Hasegawa, T. Hasegawa, S. Hatakeyama, T. Iwamoto, M. Koga, T. Maruyama, H. Ogawa, J. Shirai, A. Suzuki, F. Tsushima, M. Koshiba, M. Nemoto, K. Nishijima, T. Futagami, Y. Hayato, Y. Kanaya, K. Kaneyuki, Y. Watanabe, D. Kielczewska, R. A. Doyle, J. S. George, A. L. Stachyra, L. L. Wai, R. J. Wilkes and K. K. Young, *Phys. Rev. Lett.*, 1998, **81**, 1562–1567.

3 M. Agostini, G. R. Araujo, A. M. Bakalyarov, M. Balata, I. Barabanov, L. Baudis, C. Bauer, E. Bellotti, S. Belogurov, A. Bettini, L. Bezrukov, V. Biancacci, D. Borowicz, E. Bossio, V. Bothe, V. Brudanin, R. Brugnera, A. Caldwell, C. Cattadori, A. Chernogorov, T. Comellato, V. D'Andrea, E. V. Demidova, N. Di Marco, E. Doroshkevich, F. Fischer, M. Fomina, A. Gangapshev, A. Garfagnini, C. Gooch, P. Grabmayr, V. Gurentsov, K. Gusev, J. Hakenmüller, S. Hemmer, R. Hiller, W. Hofmann, J. Huang, M. Hult, L. V. Inzhechik, J. Janicskó Csáthy, J. Jochum, M. Junker, V. Kazalov, Y. Kermaïdic, H. Khushbakht, T. Kihm, I. V. Kirpichnikov, A. Klimenko, R. Kneißl, K. T. Knöpfle, O. Kochetov, V. N. Kornoukhov, P. Krause, V. V. Kuzminov, M. Laubenstein, A. Lazzaro, M. Lindner, I. Lippi, A. Lubashevskiy, B. Lubsandorzhiev, G. Lutter, C. MacOlino, B. Majorovits, W. Maneschg, L. Manzanillas, M. Miloradovic, R. Mingazheva, M. Misiaszek, P. Moseev, Y. Müller, I. Nemchenok, K. Panas, L. Pandola, K. Pelczar, L. Pertoldi, P. Piseri, A. Pullia, C. Ransom, L. Rauscher, S. Riboldi, N. Rumyantseva, C. Sada, F. Salamida, S. Schönert, J. Schreiner, M. Schütt, A. K. Schütz, O. Schulz, M. Schwarz, B. Schwingenheuer, O. Selivanenko, E. Shevchik, M. Shirchenko, L. Shtembari, H. Simgen, A. Smolnikov, D. Stukov, A. A. Vasenko, A. Veresnikova, C. Vignoli, K. Von Sturm, T. Wester, C. Wiesinger, M. Wojcik, E. Yanovich, B. Zatschler, I. Zhitnikov, S. V. Zhukov, D. Zinatulina, A. Zschocke, A. J. Zsigmond, K. Zuber and G. Zuzel, *Phys. Rev. Lett.*, 2020, **125**, 252502.

4 O. Azzolini, J. W. Beeman, F. Bellini, M. Beretta, M. Biassoni, C. Brofferio, C. Bucci, S. Capelli, V. Caracciolo, L. Cardani, P. Carniti, N. Casali, D. Chiesa, M. Clemenza, I. Colantoni, O. Cremonesi, A. Cruciani, A. D'Addabbo, I. Dafinei, F. De Dominicis, S. Di Domizio, F. Ferroni, L. Gironi, A. Giuliani, P. Gorla, C. Gotti, G. Keppel, M. Martinez, S. Nagorny, M. Nastasi, S. Nisi, C. Nones, D. Orlandi, L. Pagnanini, M. Pallavicini, L. Pattavina, M. Pavan, G. Pessina, V. Pettinacci, S. Pirro, S. Pozzi, E. Previtali, A. Puiu, C. Rusconi, K. Schäffner, C. Tomei, M. Vignati and A. S. Zolotarova, *Phys. Rev. Lett.*, 2022, **129**, 111801.

5 G. Anton, I. Badhrees, P. S. Barbeau, D. Beck, V. Belov, T. Bhatta, M. Breidenbach,

T. Brunner, G. F. Cao, W. R. Cen, C. Chambers, B. Cleveland, M. Coon, A. Craycraft, T. Daniels, M. Danilov, L. Darroch, S. J. Daugherty, J. Davis, S. Delaquis, A. Der Mesrobian-Kabakian, R. Devoe, J. Dilling, A. Dolgolenko, M. J. Dolinski, J. Echevers, W. Fairbank, D. Fairbank, J. Farine, S. Feyzbakhsh, P. Fierlinger, D. Fudenberg, P. Gautam, R. Gornea, G. Gratta, C. Hall, E. V. Hansen, J. Hoessl, P. Hufschmidt, M. Hughes, A. Iverson, A. Jamil, C. Jessiman, M. J. Jewell, A. Johnson, A. Karelin, L. J. Kaufman, T. Koffas, R. Krücken, A. Kuchenkov, K. S. Kumar, Y. Lan, A. Larson, B. G. Lenardo, D. S. Leonard, G. S. Li, S. Li, Z. Li, C. Licciardi, Y. H. Lin, R. MacLellan, T. McElroy, T. Michel, B. Mong, D. C. Moore, K. Murray, O. Njoya, O. Nusair, A. Odian, I. Ostrovskiy, A. Piepke, A. Pocar, F. Retière, A. L. Robinson, P. C. Rowson, D. Ruddell, J. Runge, S. Schmidt, D. Sinclair, A. K. Soma, V. Stekhanov, M. Tarka, J. Todd, T. Tolba, T. I. Totev, B. Veenstra, V. Veeraraghavan, P. Vogel, J. L. Vuilleumier, M. Wagenpfeil, J. Watkins, M. Weber, L. J. Wen, U. Wichoski, G. Wrede, S. X. Wu, Q. Xia, D. R. Yahne, L. Yang, Y. R. Yen, O. Y. Zeldovich and T. Ziegler, *Phys. Rev. Lett.*, 2019, **123**, 161802.

6 A. Gando, Y. Gando, T. Hachiya, A. Hayashi, S. Hayashida, H. Ikeda, K. Inoue, K. Ishidoshiro, Y. Karino, M. Koga, S. Matsuda, T. Mitsui, K. Nakamura, S. Obara, T. Oura, H. Ozaki, I. Shimizu, Y. Shirahata, J. Shirai, A. Suzuki, T. Takai, K. Tamae, Y. Teraoka, K. Ueshima, H. Watanabe, A. Kozlov, Y. Takemoto, S. Yoshida, K. Fushimi, T. I. Banks, B. E. Berger, B. K. Fujikawa, T. O'Donnell, L. A. Winslow, Y. Efremenko, H. J. Karwowski, D. M. Markoff, W. Tornow, J. A. Detwiler, S. Enomoto and M. P. Decowski, *Phys. Rev. Lett.*, 2016, **117**, 082503.

7 M. Goeppert-Mayer, *Phys. Rev.*, 1935, **48**, 512–516.

8 W. Rodejohann, *Int. J. Mod. Phys. E*, 2011, 20, 1833–1930.

9 M. K. Moe, *Phys. Rev. C*, 1991, **44**, R931.

10 C. Chambers, T. Walton, D. Fairbank, A. Craycraft, D. R. Yahne, J. Todd, A. Iverson, W. Fairbank, A. Alamre, J. B. Albert, G. Anton, I. J. Arnquist, I. Badhrees, P. S. Barbeau, D. Beck, V. Belov, T. Bhatta, F. Bourque, J. P. Brodsky, E. Brown, T. Brunner, A. Burenkov, G. F. Cao, L. Cao, W. R. Cen, S. A. Charlebois, M. Chiu, B. Cleveland, M. Coon, M. Côté, W. Cree, J. Dalmasson, T. Daniels, L. Darroch, S. J. Daugherty, J. Daughhetee, S. Delaquis, A. Der Mesrobian-Kabakian, R. DeVoe, J. Dilling, Y. Y. Ding, M. J. Dolinski, A. Dragone, J. Echevers, L. Fabris, J. Farine, S. Feyzbakhsh, R. Fontaine, D. Fudenberg, G. Gallina, G. Giacomini, R. Gornea, G. Gratta, E. V. Hansen, M. Heffner, E. W. Hoppe, J. Hößl, A. House, P. Hufschmidt, M. Hughes, Y. Ito, A. Jamil, C. Jessiman, M. J. Jewell, X. S. Jiang, A. Karelin, L. J. Kaufman, D. Kodroff, T. Koffas, S. Kravitz, R. Krücken, A. Kuchenkov, K. S. Kumar, Y. Lan, A. Larson, D. S. Leonard, G. Li, S. Li, Z. Li, C. Licciardi, Y. H. Lin, P. Lv, R. MacLellan, T. Michel, B. Mong, D. C. Moore, K. Murray, R. J. Newby, Z. Ning, O. Njoya, F. Nolet, O. Nusair, K. Odgers, A. Odian, M. Oriunno, J. L. Orrell, G. S. Ortega, I. Ostrovskiy, C. T. Overman, S. Parent, A. Piepke, A. Pocar, J. F. Pratte, D. Qiu, V. Radeka, E. Raguzin, T. Rao, S. Rescia, F. Retière, A. Robinson, T. Rossignol, P. C. Rowson, N. Roy, R. Saldanha, S. Sangiorgio, S. Schmidt, J. Schneider, A. Schubert, K. Skarpaas, A. K. Soma, G. St-Hilaire, V. Stekhanov, T. Stiegler, X. L. Sun,

M. Tarka, T. Tolba, T. I. Totev, R. Tsang, T. Tsang, F. Vachon, B. Veenstra, V. Veeraraghavan, G. Visser, J. L. Vuilleumier, M. Wagenpfeil, Q. Wang, J. Watkins, M. Weber, W. Wei, L. J. Wen, U. Wichoski, G. Wrede, S. X. Wu, W. H. Wu, Q. Xia, L. Yang, Y. R. Yen, O. Zeldovich, X. Zhang, J. Zhao, Y. Zhou and T. Ziegler, *Nature*, 2019, **569**, 203–207.

11 D. R. Nygren, in *Journal of Physics: Conference Series*, IOP Publishing, 2015, vol. 650, p. 012002.

12 B. J. P. Jones, A. D. McDonald and D. R. Nygren, *J. Instrum.*, , DOI:10.1088/1748-0221/11/12/P12011.

13 A. D. McDonald, B. J. P. Jones, D. R. Nygren, C. Adams, V. Álvarez, C. D. R. Azevedo, J. M. Benlloch-Rodríguez, F. I. G. M. Borges, A. Botas, S. Cárcel, J. V Carrión, S. Cebrián, C. A. N. Conde, J. Díaz, M. Diesburg, J. Escada, R. Esteve, R. Felkai, L. M. P. Fernandes, P. Ferrario, A. L. Ferreira, E. D. C. Freitas, A. Goldschmidt, J. J. Gómez-Cadenas, D. González-Díaz, R. M. Gutiérrez, R. Guenette, K. Hafidi, J. Hauptman, C. A. O. Henriques, A. I. Hernandez, J. A. Hernando Morata, V. Herrero, S. Johnston, L. Labarga, A. Laing, P. Lebrun, I. Liubarsky, N. López-March, M. Losada, J. Martín-Albo, G. Martínez-Lema, A. Martínez, F. Monrabal, C. M. B. Monteiro, F. J. Mora, L. M. Moutinho, J. Muñoz Vidal, M. Musti, M. Nebot-Guinot, P. Novella, B. Palmeiro, A. Para, J. Pérez, M. Querol, J. Repond, J. Renner, S. Riordan, L. Ripoll, J. Rodríguez, L. Rogers, F. P. Santos, J. M. F. Dos Santos, A. Simón, C. Sofka, M. Sorel, T. Stiegler, J. F. Toledo, J. Torrent, Z. Tsamalaidze, J. F. C. A. Veloso, R. Webb, J. T. White and N. Yahlali, *Phys. Rev. Lett.*, , DOI:10.1103/PhysRevLett.120.132504.

14 P. Thapa, I. Arnquist, N. Byrnes, A. A. Denisenko, F. W. Foss, B. J. P. Jones, A. D. McDonald, D. R. Nygren and K. Woodruff, *Sci. Rep.*, 2019, **9**, 1–13.

15 A. Hulanicki, S. Glab and F. Ingman, *INTERNATIONAL UNION OF PURE AND APPLIED CHEMISTRY ANALYTICAL CHEMISTRY DIVISION COMMISSION ON GENERAL ASPECTS OF ANALYTICAL CHEMISTRY"? CHEMICAL SENSORS DEFINITIONS AND CLASSIFICATION*, 1991, vol. 63.

16 K.-C. Yan, A. Steinbrueck, A. C. Sedgwick and T. D. James, *Front. Sensors*, 2021, **2**, 9.

17 P. R. Dongare and A. H. Gore, *ChemistrySelect*, 2021, 6, 5657–5669.

18 D. Wu, A. C. Sedgwick, T. Gunnlaugsson, E. U. Akkaya, J. Yoon and T. D. James, *Chem. Soc. Rev.*, 2017, 46, 7105–7123.

19 A. W. Czarnik, in *Fluorescent Chemosensors for Ion and Molecule Recognition*, 1991, vol. 87, pp. 1–9.

20 M. Montalti, A. Credi, L. Prodi and M. T. Gandolfi, *Handbook of Photochemistry*, CRC Press, 2006.

21 A. P. Demchenko, *J. Fluoresc.*, 2010, 20, 1099–1128.

22 S. K. Behera, S. Y. Park and J. Gierschner, *Angew. Chemie - Int. Ed.*, 2021, 60, 22624–22638.

23 A. P. De Silva, T. S. Moody and G. D. Wright, *Analyst*, 2009, 134, 2385–2393.

24 D. Escudero, *Acc. Chem. Res.*, 2016, **49**, 1816–1824.

25 A. F. Chaudhry, M. Verma, M. Thomas Morgan, M. M. Henary, N. Siegel, J. M. Hales, J. W. Perry and C. J. Fahrni, *J. Am. Chem. Soc.*, 2010, **132**, 737–747.

26 R. Misra and S. P. Bhattacharyya, *Intramolecular Charge Transfer*, Wiley-VCH Verlag GmbH & Co. KGaA, 2018.

27 J. Wang, X. Qian and J. Cui, *J. Org. Chem.*, 2006, **71**, 4308–4311.

28 D. Bourassa, C. M. Elitt, A. M. McCallum, S. Sumalekshmy, R. L. McRae, M. T. Morgan, N. Siegel, J. W. Perry, P. A. Rosenberg and C. J. Fahrni, *ACS Sensors*, 2018, **3**, 458–467.

29 P. Ning, J. Jiang, L. Li, S. Wang, H. Yu, Y. Feng, M. Zhu, B. Zhang, H. Yin, Q. Guo and X. Meng, *Biosens. Bioelectron.*, 2016, **77**, 921–927.

30 X. Meng, S. Wang, Y. Li, M. Zhu and Q. Guo, *Chem. Commun.*, 2012, **48**, 4196–4198.

31 W. Li, Z. Liu, B. Fang, M. Jin and Y. Tian, *Biosens. Bioelectron.*, 2020, **148**, 111666.

32 L. Wu, C. Huang, B. P. Emery, A. C. Sedgwick, S. D. Bull, X. P. He, H. Tian, J. Yoon, J. L. Sessler and T. D. James, *Chem. Soc. Rev.*, 2020, 49, 5110–5139.

33 H. Xu, C. Zhu, Y. Chen, Y. Bai, Z. Han, S. Yao, Y. Jiao, H. Yuan, W. He and Z. Guo, *Chem. Sci.*, 2020, **11**, 11037–11041.

34 X. Chen, Y. Ma, H. Chen, F. Wang, S. Kambam, Y. Wang and C. Mao, *Dye. Pigment.*, 2014, **102**, 301–307.

35 G. v. Bünau, *Berichte der Bunsengesellschaft für Phys. Chemie*, 1970, **74**, 1294–1295.

36 B. Valeur and I. Leray, *Coord. Chem. Rev.*, 2000, **205**, 3–40.

37 J. Rodríguez-Lavado, A. Lorente, E. Flores, A. Ochoa, F. Godoy, P. Jaque and C. Saitz, *RSC Adv.*, 2020, **10**, 21963–21973.

38 L. J. Ma, Q. Liang, R. Feng, Z. Lv, F. Cui, L. Li, L. Yang, H. Liu and F. Sun, *J. Photochem. Photobiol. A Chem.*, , DOI:10.1016/j.jphotochem.2020.113086.

39 J. Luo, Z. Xie, Z. Xie, J. W. Y. Lam, L. Cheng, H. Chen, C. Qiu, H. S. Kwok, X. Zhan, Y. Liu, D. Zhu and B. Z. Tang, *Chem. Commun.*, 2001, **18**, 1740–1741.

40 M. H. Chua, H. Zhou, Q. Zhu, B. Z. Tang and J. W. Xu, *Mater. Chem. Front.*, 2021, 5, 659–708.

41 Y. Li, Y. Liu, H. Zhou, W. Chen, J. Mei and J. Su, *Chem. - A Eur. J.*, 2017, **23**, 9280–9287.

42 M. Gao, Y. Li, X. Chen, S. Li, L. Ren and B. Z. Tang, *ACS Appl. Mater. Interfaces*, 2018, **10**, 14410–14417.

43 Y. Nakahara, T. Kida, Y. Nakatsuji and M. Akashi, *Chem. Commun.*, 2004, **4**, 224–225.

44 Y. Nakahara, T. Kida, Y. Nakatsuji and M. Akashi, *Org. Biomol. Chem.*, 2005, **3**, 1787–1794.

45 S. I. Kondo, T. Kinjo and Y. Yano, *Tetrahedron Lett.*, 2005, **46**, 3183–3186.

46 M. Licchelli, A. O. Biroli and A. Poggi, *Org. Lett.*, 2006, **8**, 915–918.

47 M. Yuan, W. Zhou, X. Liu, M. Zhu, J. Li, X. Yin, H. Zheng, Z. Zuo, C. Ouyang, H. Liu, Y. Li and D. Zhu, *J. Org. Chem.*, 2008, **73**, 5008–5014.

48 S. I. Kondo, T. Takahashi, Y. Takiguchi and M. Unno, *Tetrahedron Lett.*, 2011, **52**, 453–457.

49 P. Saluja, N. Kaur, N. Singh and D. O. Jang, *Tetrahedron Lett.*, 2011, **52**, 6705–6708.

50 P. N. Basa, A. Bhowmick, M. M. Schulz and A. G. Sykes, *J. Org. Chem.*, 2011, **76**, 7866–7871.

51 Y. X. Wu, J. Cao, H. Y. Deng and J. X. Feng, *Spectrochim. Acta - Part A Mol. Biomol. Spectrosc.*, 2011, **82**, 340–344.

52 S. P. Gromov, S. N. Dmitrieva, A. I. Vedernikov, N. A. Kurchavov, L. G. Kuz'Mina, S. K. Sazonov, Y. A. Strelenko, M. V. Alfimov, J. A. K. Howard and E. N. Ushakov, *J. Org. Chem.*, 2013, **78**, 9834–9847.

53 L. Zhao, D. Sui and Y. Wang, *J. Lumin.*, 2015, **162**, 81–86.

54 Q. Zhang and K. Duan, *Heterocycl. Commun.*, 2018, **24**, 141–145.

55 A. K. K. Bhasin, P. Chauhan and S. Chaudhary, *Sensors Actuators, B Chem.*, 2019, **294**, 116–122.

56 K. Chaichana, N. Phutlaprungrueang, L. Chaicharoenwimolkul, M. Promkatkaew and S. Kongsriprapan, *Spectrochim. Acta - Part A Mol. Biomol. Spectrosc.*, 2019, **207**, 118–122.

57 P. Ravichandiran, S. A. Subramaniyan, A. P. Bella, P. M. Johnson, A. R. Kim, K. S. Shim and D. J. Yoo, *Anal. Chem.*, 2019, **91**, 10095–10101.

58 C. J. Pedersen, *J. Am. Chem. Soc.*, 1967, 89, 2495–2496.

59 P. Thapa, N. K. Byrnes, A. A. Denisenko, F. W. Foss, B. J. P. Jones, J. X. Mao, K. Nam, C. A. Newhouse, D. R. Nygren, A. D. McDonald, T. T. Vuong and K. Woodruff, .

60 P. Thapa, N. K. Byrnes, A. A. Denisenko, J. X. Mao, A. D. McDonald, C. A. Newhouse, T. T. Vuong, K. Woodruff, K. Nam, D. R. Nygren, B. J. P. Jones and F. W. Foss, *ACS Sensors*, 2021, **6**, 192–202.

61 I. Rivilla, B. Aparicio, J. M. Bueno, D. Casanova, C. Tonnelé, Z. Freixa, P. Herrero, C. Rogero, J. I. Miranda, R. M. Martínez-Ojeda, F. Monrabal, B. Olave, T. Schäfer, P. Artal, D. Nygren, F. P. Cossío and J. J. Gómez-Cadenas, *Nature*, 2020, **583**, 48–54.

62 V. Boekelheide and R. J. Windgassen, *J. Am. Chem. Soc.*, 1958, 80, 2020.

63 É. Lévesque, W. S. Bechara, L. Constantineau-Forget, G. Pelletier, N. M. Rachel, J. N. Pelletier and A. B. Charette, *J. Org. Chem.*, 2017, **82**, 5046–5067.

64 S. Sanivarapu, N. Vaddiraju and L. Velide, *Med. Chem. Res.*, 2019, **28**, 1461–1470.

65 A. S. Jorgensen, P. Jacobsen, L. B. Christiansen, P. S. Bury, A. Kanstrup, S. M. Thorpe, L. Narum and K. Wassermann, *Bioorganic Med. Chem. Lett.*, 2000, **10**, 2383–2386.

66 M. Aginagalde, Y. Vara, A. Arrieta, R. Zangi, V. L. Cebolla, A. Delgado-Camón and F. P. Cossío, *J. Org. Chem.*, 2010, **75**, 2776–2784.

67 E. V. Babaev and I. A. Shadrin, *Molecules*, 2021, 26, 2050.

68 M. Alfonso, E. Garrido, F. Sancenón and R. Martínez-Máñez, in *Comprehensive Coordination Chemistry III*, Elsevier, 2021, vol. 1–9, pp. 181–203.

69 M. Chavarot, S. Ménage, O. Hamelin, F. Charnay, J. Pécaut and M. Fontecave, *Inorg. Chem.*, 2003, **42**, 4810–4816.

70 J. Ma, X. Zhang, X. Huang, S. Luo and E. Meggers, *Nat. Protoc.*, 2018, **13**, 605–632.

71 E. Meggers, *Chem. - A Eur. J.*, 2010, 16, 752–758.

72 C. Sahin, I. Oner and C. Varlikli, *RSC Adv.*, 2014, **4**, 46831–46839.

73 I. González, P. Dreyse, D. Cortés-Arriagada, M. Sundararajan, C. Morgado, I. Brito, C. Roldán-Carmona, H. J. Bolink and B. Loeb, *Dalt. Trans.*, 2015, **44**, 14771–14781.

74 K. Nozaki, *J. Chinese Chem. Soc.*, 2006, **53**, 101–112.

75 T. Hofbeck and H. Yersin, *Inorg. Chem.*, 2010, **49**, 9290–9299.

76 T. Hofbeck and H. Yersin, *Inorg. Chem.*, 2010, **49**, 9290–9299.

77 A. B. Tamayo, B. D. Alleyne, P. I. Djurovich, S. Lamansky, I. Tsyba, N. N. Ho, R. Bau and M. E. Thompson, *J. Am. Chem. Soc.*, 2003, **125**, 7377–7387.

78 S. H. Wu, J. W. Ling, S. H. Lai, M. J. Huang, C. H. Cheng and I. C. Chen, *J. Phys. Chem. A*, 2010, **114**, 10339–10344.

79 F. Monti, A. Baschieri, L. Sambri and N. Armaroli, *Acc. Chem. Res.*, 2021, **54**, 1492–1505.

80 R. Bevernaegie, S. A. M. Wehlin, B. Elias and L. Troian-Gautier, *ChemPhotoChem*, 2021, **5**, 217–234.

81 M. S. Lowry and S. Bernhard, *Chem. - A Eur. J.*, 2006, **12**, 7970–7977.

82 S. Ladouceur, D. Fortin and E. Zysman-Colman, *Inorg. Chem.*, 2010, **49**, 5625–5641.

83 K. Hasan, A. K. Bansal, I. D. W. Samuel, C. Roldán-Carmona, H. J. Bolink and E. Zysman-Colman, *Sci. Rep.*, 2015, **5**, 1–16.

84 *Iridium(III) in Optoelectronic and Photonics Applications*, Wiley, 2017.

85 D. L. Ma, S. Lin, W. Wang, C. Yang and C. H. Leung, *Chem. Sci.*, 2017, **8**, 878–889.

86 V. Guerchais and J. L. Fillaut, *Coord. Chem. Rev.*, 2011, **255**, 2448–2457.

87 D. L. Ma, S. Y. Wong, T. S. Kang, H. P. Ng, Q. Bin Han and C. H. Leung, *Methods*, 2019, 168, 3–17.

88 J. Brandel, M. Sairenji, K. Ichikawa and T. Nabeshima, *Chem. Commun.*, 2010, **46**, 3958–3960.

89 W. Wang, Z. Mao, M. Wang, L. J. Liu, D. W. J. Kwong, C. H. Leung and D. L. Ma, *Chem. Commun.*, 2016, **52**, 3611–3614.

90 N. Zhao, Y. H. Wu, H. M. Wen, X. Zhang and Z. N. Chen, *Organometallics*, 2009, **28**, 5603–5611.

91 H. Yang, Y. Zhu, L. Li, Z. Zhou and S. Yang, *Inorg. Chem. Commun.*, 2012, **16**, 1–3.

92 Y. W. Chin, K. D. Yoon and J. Kim, *Bull. Korean Chem. Soc.*, 2013, **34**, 653–656.

93 T. Yu, Y. Wang, Z. Zhu, Y. Li, Y. Zhao, X. Liu and H. Zhang, *Dye. Pigment.*, 2019, **161**, 252–260.

94 T. Yu, Q. Yang, Z. Zhu, Y. Zhao, X. Liu, C. Wei and H. Zhang, *J. Organomet. Chem.*, 2017, **853**, 42–48.

95 D. L. Ma, H. Z. He, D. S. H. Chan, C. Y. Wong and C. H. Leung, *PLoS One*, 2014, **9**, e99930.

96 Y. You, S. Lee, T. Kim, K. Ohkubo, W. S. Chae, S. Fukuzumi, G. J. Jhon, W. Nam and S. J. Lippard, *J. Am. Chem. Soc.*, 2011, **133**, 18328–18342.

97 H. Woo, S. Cho, Y. Han, W. S. Chae, D. R. Ahn, Y. You and W. Nam, *J. Am. Chem. Soc.*, 2013, **135**, 4771–4787.

98 P. K. Lee, W. H. T. Law, H. W. Liu and K. K. W. Lo, *Inorg. Chem.*, 2011, **50**, 8570–8579.

99 J. C. Araya, J. Gajardo, S. A. Moya, P. Aguirre, L. Toupet, J. A. G. Williams, M. Escadeillas, H. Le Bozec and V. Guerchais, *New J. Chem.*, 2010, **34**, 21–24.

100 D. L. Ma, H. Z. He, H. J. Zhong, S. Lin, D. S. H. Chan, L. Wang, S. M. Y. Lee, C. H. Leung and C. Y. Wong, *ACS Appl. Mater. Interfaces*, 2014, **6**, 14008–14015.

101 Y. Han, Y. You, Y. M. Lee and W. Nam, *Adv. Mater.*, 2012, **24**, 2748–2754.

102 M. Schmittel and H. Lin, *Inorg. Chem.*, 2007, **46**, 9139–9145.

103 Y. Li, U. C. Yoon and M. H. Hyun, *Bull. Korean Chem. Soc.*, 2011, **32**, 122–126.

104 M. L. Ho, Y. M. Cheng, L. C. Wu, P. T. Chou, G. H. Lee, F. C. Hsu and Y. Chi, *Polyhedron*, 2007, **26**, 4886–4892.

105 M. L. Ho, F. M. Hwang, P. N. Chen, Y. H. Hu, Y. M. Cheng, K. S. Chen, G. H. Lee, Y. Chi and P. T. Chou, *Org. Biomol. Chem.*, 2006, **4**, 98–103.

106 Y. You, Y. Han, Y. M. Lee, S. Y. Park, W. Nam and S. J. Lippard, *J. Am. Chem. Soc.*, 2011, **133**, 11488–11491.

107 Y. Suzuki, I. Mizuno, Y. Tabei, Y. Fujioka, K. Shinozaki, T. Sugaya and K. Ishihara, *Inorg. Chem.*, 2019, **58**, 9663–9671.

108 Y. You and S. Y. Park, *J. Chem. Soc. Dalt. Trans.*, 2009, 1267–1282.

109 R. Esteve Bosch, J. Rodríguez Ponce, A. Simón Estévez, J. M. Benlloch Rodríguez, V. Herrero Bosch and J. F. Toledo Alarcón, *Sensors*, 2022, **22**, 5197.

110 J. R. Acharya, H. Zhang, X. Li and E. E. Nesterov, *J. Am. Chem. Soc.*, 2009, **131**, 880–881.

111 B. G. Imsick, J. Raj Acharya and E. E. Nesterov, *Chem. Commun.*, 2013, **49**, 7043–7045.

112 B. G. Imsick, J. R. Acharya and E. E. Nesterov, *Adv. Mater.*, 2013, **25**, 120–124.

113 M. De la Cruz-Guzman, A. Aguilar-Aguilar, L. Hernandez-Adame, A. Bañuelos-Frias, F. J. Medellín-Rodríguez and G. Palestino, *Nanoscale Res. Lett.*, 2014, **9**, 1–9.

114 S. Flink, F. C. J. M. Van Veggel and D. N. Reinhoudt, *Chem. Commun.*, 1999, 2229–

2230.

115 F. Lupo, C. Capici, G. Gattuso, A. Notti, M. F. Parisi, A. Pappalardo, S. Pappalardo and A. Gulino, *Chem. Mater.*, 2010, **22**, 2829–2834.

116 D. A. Cristaldi, I. Fragalà, A. Pappalardo, R. M. Toscano, F. P. Ballistreri, G. A. Tomaselli and A. Gulino, *J. Mater. Chem.*, 2012, **22**, 675–683.

117 X. Wu, B. Xu, H. Tong and L. Wang, *Macromolecules*, 2010, **43**, 8917–8923.

118 L. Basabe-Desmonts, J. Beld, R. S. Zimmerman, J. Hernando, P. Mela, M. F. García Parajó, N. F. Van Hulst, A. Van Den Berg, D. N. Reinhoudt and M. Crego-Calama, *J. Am. Chem. Soc.*, 2004, **126**, 7293–7299.

119 M. Singh, N. Kaur, G. Drera, A. Casotto, L. Sangaletti and E. Comini, *Adv. Funct. Mater.*, 2020, **30**, 2003217.

120 A. M. Andringa, M. J. Spijkman, E. C. P. Smits, S. G. J. Mathijssen, P. A. va. Hal, S. Setayesh, N. P. Willard, O. V. Borshchev, S. A. Ponomarenko, P. W. M. Blom and D. M. de Leeuw, *Org. Electron.*, 2010, **11**, 895–898.

121 Y. Chang, N. Tang, H. Qu, J. Liu, D. Zhang, H. Zhang, W. Pang and X. Duan, *Sci. Rep.*, 2016, **6**, 1–12.

Chapter 2

G3 FBI and bipyridine based ligands

In this chapter the 3rd generation **FBI**- and bipyridine-based ligands will be introduced. Their synthetic development and photophysical characterization as Ba^{2+} sensors will be detailed.

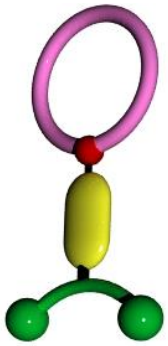

2.1 INTRODUCTION

As discussed in the general introduction, the ambitious goal of NEXT demands a highly sensitive indicator. It must be capable of showing a clear signal for a single barium cation in a 100 Kg ^{136}Xe gas pressure-chamber, anchored on a transparent solid support (cathode) and be active in an ultra-dry environment. So far, **G1 FBI** demonstrated to be an appropriate organic sensor for Ba^{2+} and has exhibited certainly promising results in a dry environment. Nonetheles, due to the demanding sensing abilities required for the compound, it is fundamental to continue searching and studying new barium sensors. In this context, it seems reasonable to design compounds based on the **FBI** structure and its characteristic mode of interaction.

2.2 G3 LIGANDS

2.2.1 Design

As described in the introduction, the 1st Generation Fluorescent Bicolour Sensor (**G1 FBI**) molecule interacts in a specific manner with the Ba^{2+} cation where the rotating aryl group and the exposed nitrogen of the indazole have key roles, as deduced from DFT calculations (**Figure 2.1**).

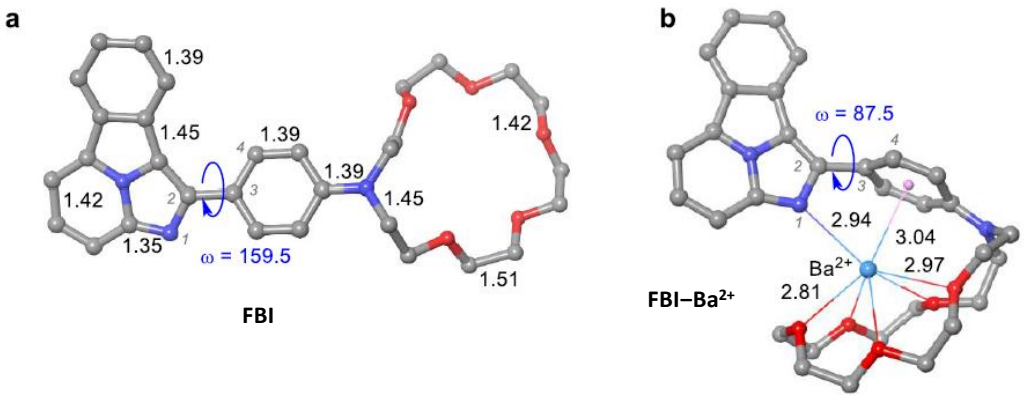

Figure 2.1. *First–generation* ***FBI*** *and its spatial conformation of the free and barium(II) chelated form.*[1]

The original idea was to cyclometalate the **G1 FBI** molecule as a third ligand to an iridium biscyclometalated $[Ir(ppy)_2]^+$ center (Hppy = 2-phenylpyridine), and investigate how the coordination to a metal center could affect the response of the sensor to Ba^{2+}. This cyclometalation to Ir(III) would occur through coordination to the exposed nitrogen of

the indolizine core and cyclometalation of the rotating aryl unit through one of the carbon atoms in ortho position to the indolizine. This coordination pattern would cause the loss of the characteristic features of the **FBI**, as it would block the potential interaction of the nitrogen of the indazole with Ba^{2+} and the rotation of the aryl group, with the subsequent loss of the expected bicolour response to Ba^{2+}.

The 3rd generation of **FBI**s was designed to overcome this problem. They were conceived to coordinate to the metal center while partially maintaining the original features of **FBI** (**Figure 2.2**). Similarly to their predecessor, they contain an indolizine fluorescent core (in blue) and an aza–crown ether connected to a phenylene spacer (red and green, respectively) to function as Ba^{2+} receptor site and rotating aryl, respectively. Yet, another aromatic spacer was inserted in between these two components (dashed) to be used as an additional coordination site to the metal center. Thus, the final objective was based on the synthesis and characterization of the new designed **FBI** ligands and their iridium complexes, together with their photophysical study.

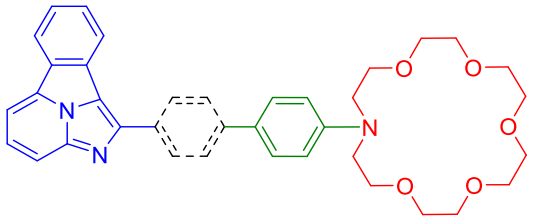

Figure 2.2. *Illustration of the general structure of the* ***G3 FBI*** *family.*

Hence, the 3rd Generation Fluorescent Bicolour Indicators (**G3 FBI**) ligands involved in this thesis, together with the study of their photochromic behavior are presented in this chapter. These three molecules, labeled as **G3a**, **G3b**, and **G3c** (shown in **Figure 2.3**), were synthesized and fully characterized.

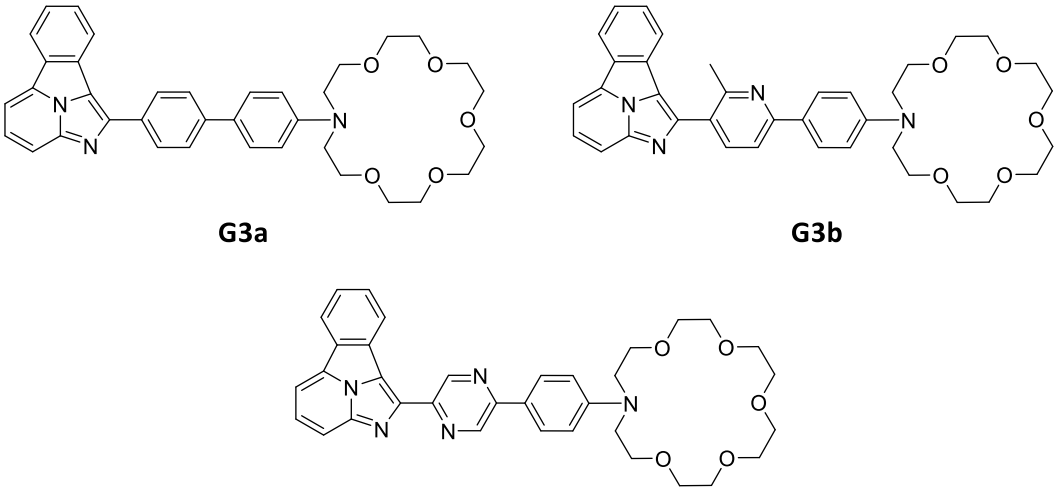

Figure 2.3. *The three 3rd generation* ***FBI*** *structures synthesized in this project.*

In the figure below (**Figure 2.4**) the characteristic components of these three molecules are emphasized, together with the proposed coordination/cyclometalation points to the Ir(III) center.

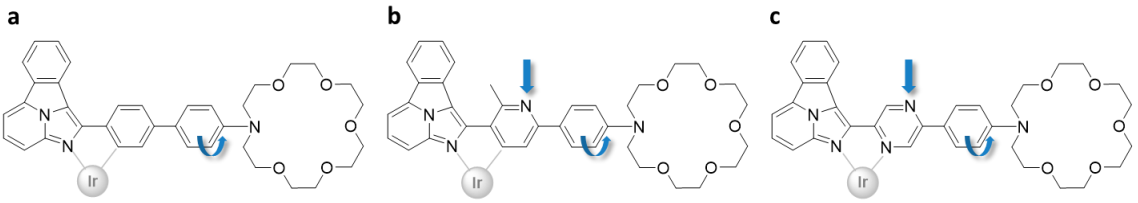

Figure 2.4. *Structure of* ***G3 FBI****s and illustration of their expected iridium joining mode and key structural features.*

The **G3a** was designed to have a second phenyl group between the indazole and the rotating aryl unit (a in **Figure 2.4**). This addition would permit the free rotation of the phenyl–crown component, while the new intermediate phenyl would be cyclometalated to the iridium. In this case, the final compound would not have the exposed nitrogen to interact with the Ba^{2+}.

In **G3b** (b in **Figure 2.4**), a methylpyridine was inserted between the indazole and the rotating aryl unit. This would allow the compound to maintain the free rotating aryl unit, already present in **G3a**, and, after cyclometalation, the pyridine nitrogen would mimic the exposed nitrogen of the imidazole in **G1 FBI**. In addition, **G3b** has a methyl group appended in the ortho position to the nitrogen. This methyl was not intentionally

incorporated in the original design, but the commercially available starting product caused the final compound structure to have it in the final structure. Nevertheless, in principle it would not interfere with the Ba^{2+} sensing mechanism, and could prevent cyclometallation occurring through this position, which would reduce the participation of this nitrogen in the sensing process (**Figure 2.5**).

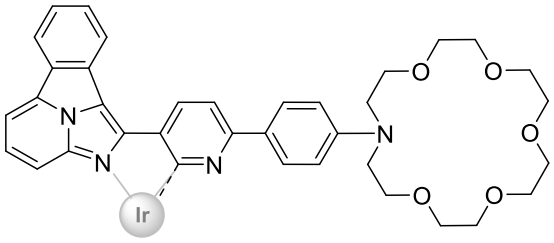

Figure 2.5. *Illustration of the hindrance produced by the methyl group for the cyclometalation to iridium(III).*

Ligand **G3c** (c in **Figure 2.4**), not only contains the aryl rotating unit and an exposed nitrogen to interact with Ba^{2+}(as in already described for **G3b**) , but a change in the coordination mode was intended. **G3c** was designed to be a neutral N–N chelating. With this modification, we aimed to avoid the harsh conditions often required for the iridium C–N cyclometalation and use instead a N–N coordination, which usually requires milder conditions.

In summary, three new **G3 FBI** ligands were synthesized: two were intended to act as C–N monoanionic ligands (**G3a** and **G3b**) upon coordination to iridium, and one as a neutral N–N bidentate (**G3c**). In the former, coordination would occur through the exposed N–atom of the indolizine core and cyclometalation of the adjacent aromatic ring through the C in ortho to the indolizine, whereas in the latter it would be through the N–atom of the indolizine and the N on the heterocyclic aromatic spacer.

2.2.2 Synthetic procedures

2.2.2.1 G3a

The first approach for the synthesis of **G3a** was based on a seven-step route, described in **Scheme 2.1**, which involved the synthesis of the boronic fragment **3** and halogenated **5**, and their subsequent Suzuki Miyaura C–C coupling to form intermediate **6**. Finally, this compound should render **G3a** through a 8+2 cycloaddition reaction.

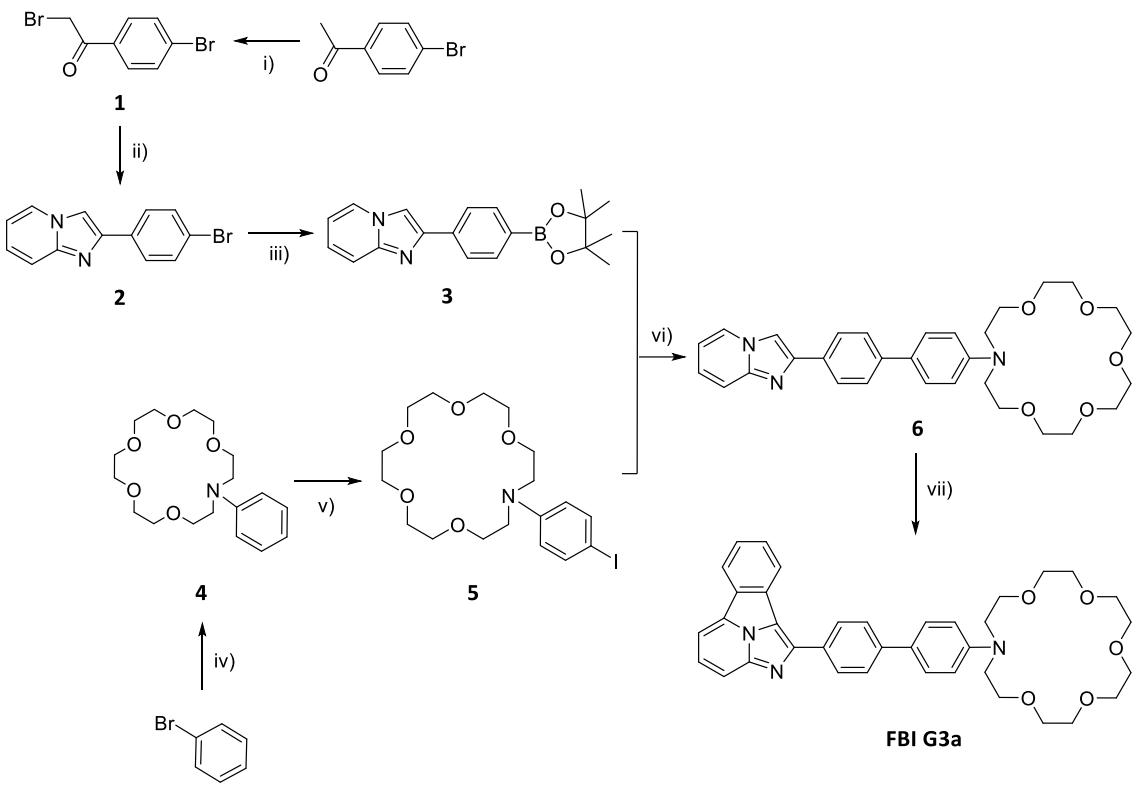

Scheme 2.1. *Synthetic route toward ligand* ***G3a****. i)* Br_2 *(1 equiv.),* $CHCl_3$*. ii) 2–aminopyridine (1.1 equiv.), EtOH, 82 °C. iii)* $(Bpin)_2$ *(1.5 equiv.),* $Pd(PPh_3)_4$ *(5 mol %), NaOAc (5 equiv.), DMSO, 80 °C. iv) 1–aza–18–crown–6 (1 equiv.),* $Pd_2(dba)_3$ *(2 mol %), DavePhos (6 mol %),* ^tBuONa *(1.5 equiv.), toluene, 110 °C. v) NIS (1.05 equiv.),* NH_4OAc *(0.1 equiv.), MeCN. vi)* $Pd(PPh_3)_4$ *(5 mol %),* Na_2CO_3 *(5 equiv.), DME/*H_2O *(3:1, v/v), 80 °C. vii)* $Pd(OAc)_2$*, XPhos, o–dibromide benzene,* K_2CO_3*, DMF, 160 °C.*

Compound **2** was synthesized in two steps starting from the commercially available 4-bromoacetophenone, using the previously reported procedure described by Rivilla et al. for the formation of the **G1 FBI**s.[1] The boronic adduct **3** was obtained by reacting compound **2** with $(Bpin)_2$ catalyzed with Pd(0) in DMSO and NaOAc as the base.[2] The formation of the boronic compound was confirmed by ^1H NMR, based on the observation of an aliphatic singlet at 1.34 ppm and the low–field shift of the *para*–substituted aromatic system when compared to the ^1H NMR spectra of **2** (**Figure 2.6**). To isolate the product, H_2O is added and the formed precipitate is filtered. The garnet product was used in the next step without further purification.

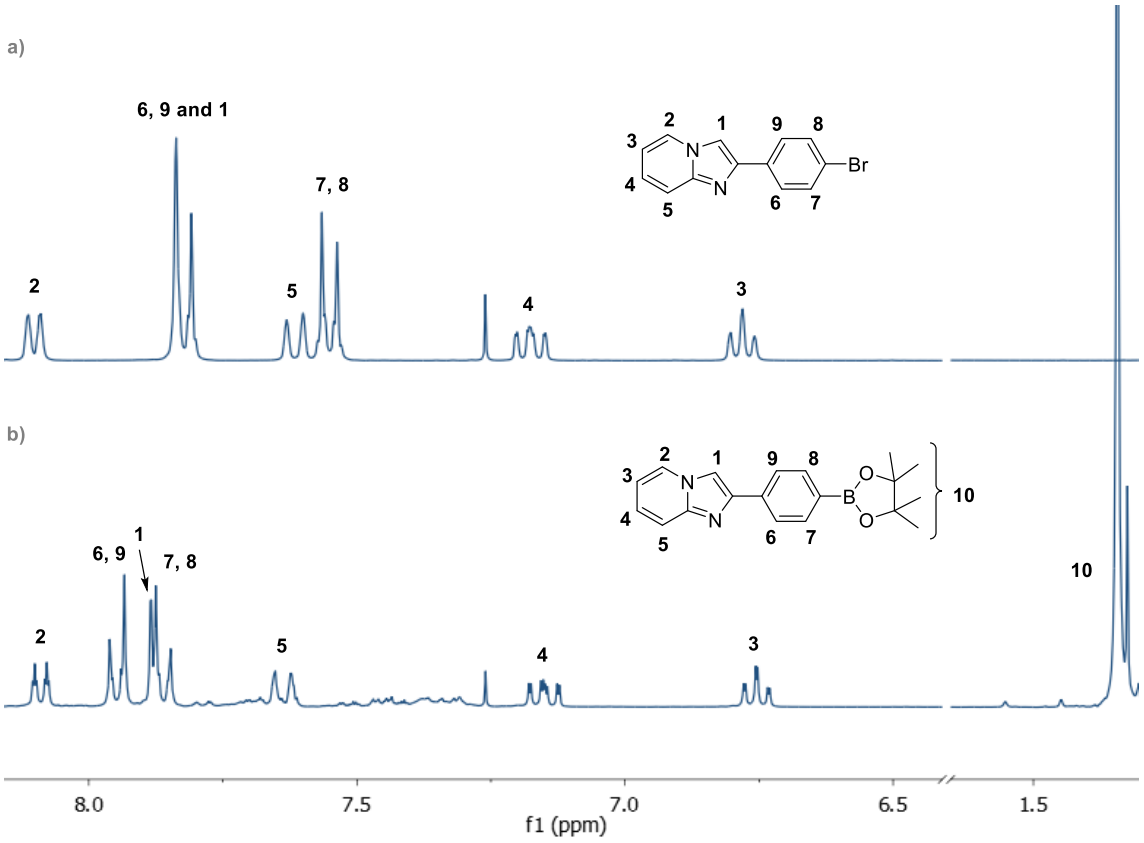

Figure 2.6. *^{1}H NMR spectra of a) **2** and b) **3** and their assigned structures ($CDCl_3$, 300 MHz).*

To obtain synthon **4**, bromobenzene was coupled with 1–aza–18–crown–6, using toluene as a solvent. This cross coupling reaction was performed using $Pd_2(dba)_3$/DavePhos as catalyst and ^{t}BuONa as a base.[3] The reaction proceeded at 110 °C, and after completion of the reaction, the mixture was filtered and the evaporation of the solvent from the filtrate yielded a brown oil that was used in the next step without further purification. Compound **4** was later iodinated in MeCN at room temperature to form synthon **5**, based on a procedure reported by Reddy et al.[4] The generation of 4-iododerivate occurred in quantitative yield and was used in the next step without purification. The ^{1}H NMR pattern (**Figure 2.7**) showed the change in the aromatic region, from a doublet and two triplets for compound **4** to the AA'BB' spin system expected for compound **5**, together with the aliphatic signals of the aza–crown fragment.

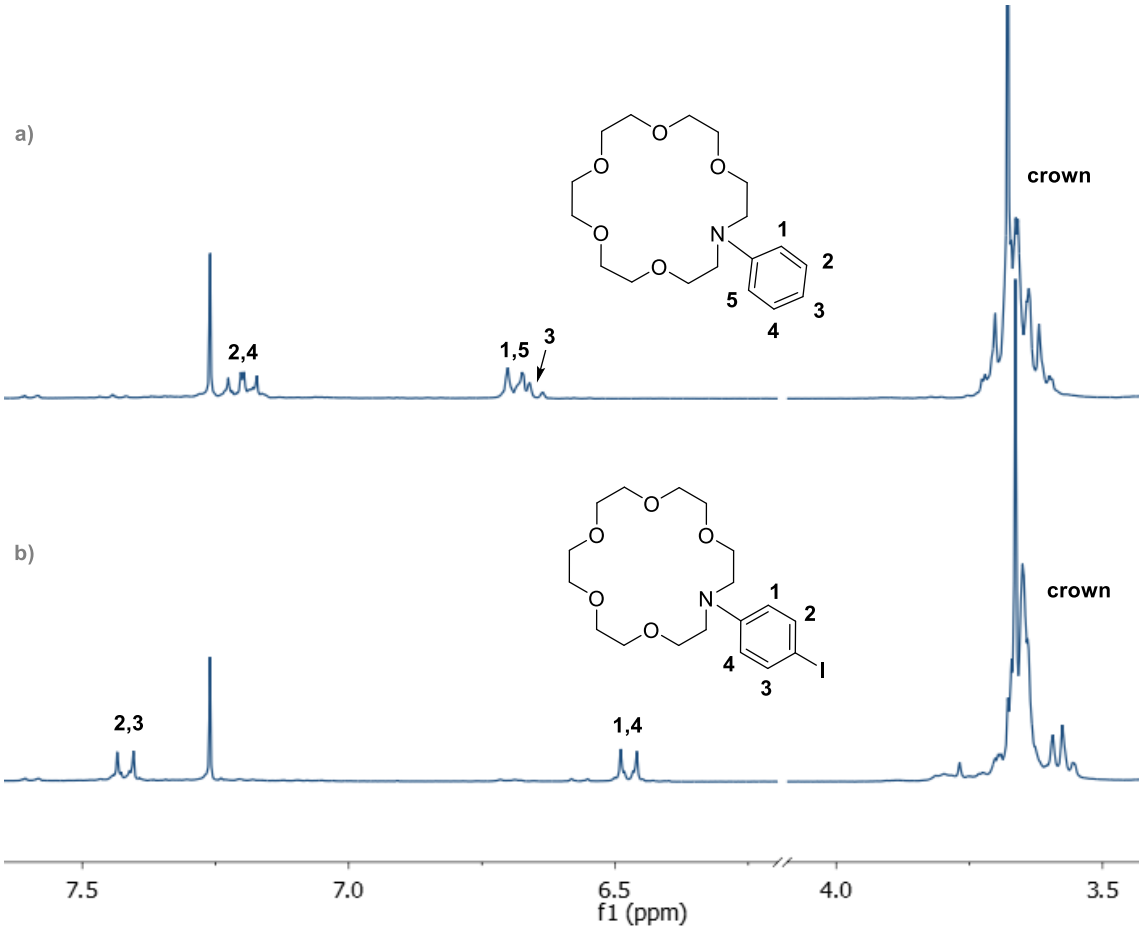

Figure 2.7. *^{1}H NMR spectra of a) compound **4** and b) compound **5** and their assigned structures ($CDCl_3$, 300 MHz).*

The Suzuki–Miyaura coupling of the boronic adduct **3** and halogenated **5** to obtain compound **6** was performed under standard conditions: in a solvent mixture of DME/H_2O (3:1, v/v) at 80 °C, catalyzed by $Pd(PPh_3)_4$ in basic conditions. The formation of **6** was confirmed by ^{1}H NMR spectroscopy of an aliquot of the reaction mixture. However, due to the low conversions inferred from the ^{1}H NMR spectra of aliquots of this reaction, even at extended reaction times, the purification of the product was not attempted. Instead, another synthetic route was envisaged to reach the same intermediate **6**. This alternative route was initially proposed for the synthesis of **G3b**, to circumvent the C–C cross–coupling that was expected to be problematic in the case of the pyridine, present in the intermediate for the synthesis of **G3b**. Indeed, the lack of reactivity of pyridine derivatives in Suzuki–Miyaura cross–coupling reactions to form the corresponding boronic esters under standard conditions, and the lack of stability of

these derivatives, is well documented in the literature. Often specific reaction conditions and co–catalysts are required for each pyridinic substrate.[5,6]

In this case, the strategy relied on the utilization of a starting material that already contained the fused biphenyl fragment, present in between the indolizine core and the crown. This synthetic pathway was intended to improve the yield of **6**, by avoiding the C–C coupling and reducing the overall number of steps from six to three. The alternative second route is depicted in **Scheme 2.2**.

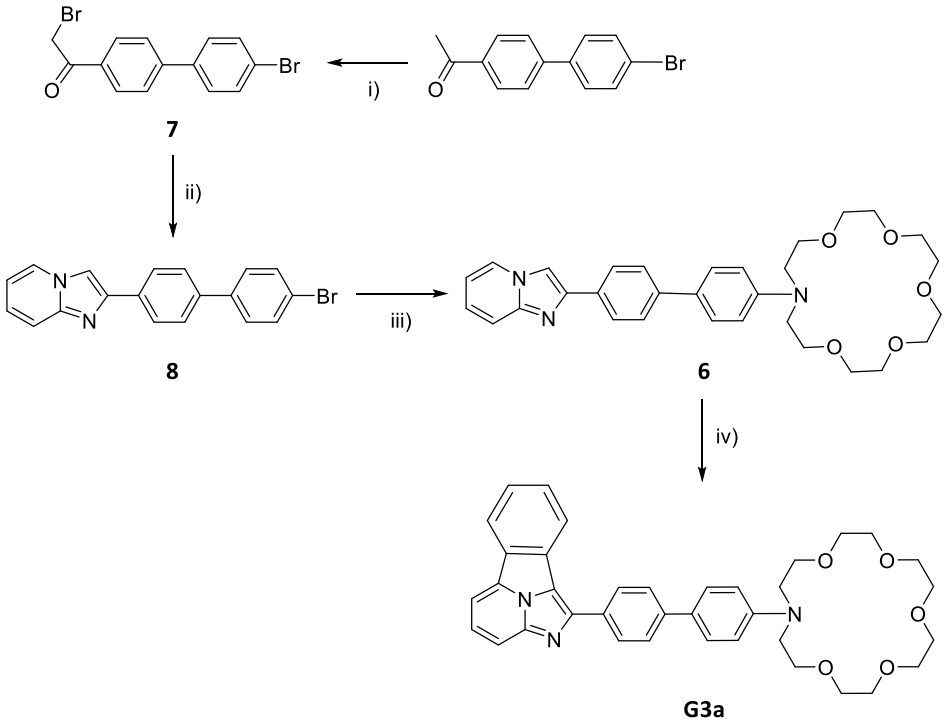

Scheme 2.2. *Alternative synthetic route towards ligand **G3a**. i) Br_2 (1 equiv.), $CHCl_3$. ii) 2–aminopyridine (1.1 equiv.), $NaHCO_3$ (1.5 equiv.), EtOH, 80 °C. iii) 1–aza–18–crown–6 (1 equiv.), $Pd_2(dba)_3$ (4 mol %), DavePhos (12 mol %), ^tBuONa (1.5 equiv.), toluene, 115 °C. iv) $Pd(OAc)_2$, XPhos, o–dibromide benzene, K_2CO_3, DMF, 160 °C.*

The synthetic route started with the bromination of the commercially available 1–(4'–bromo–[1,1'–biphenyl]–4–yl)ethan–1–one to obtain compound **7**. As described in the literature, $CHCl_3$ was used as the solvent and almost quantitative yields were reached.[7]

The reaction progress was followed by ^1H NMR analysis of aliquots of the reaction mixture, shown in **Figure 2.8**. The relative integrations of the characteristic $–CH_3$ acetyl group of the reactant at 2.6 ppm (highlighted in green) and the methylene hydrogens of the desired compound **7** at 4.5 ppm (highlighted in orange) were measured. After 40

min of reaction (c in **Figure 2.8**) another peak at 6.7 ppm was noticed (highlighted in pink), which was assigned to **7'**, product of a double bromination in the acetyl group.

The formation of by–product **7'** was minimized if the reaction time was controlled not to exceed the tested 40 minutes at a 5 g scale. When CH_2Cl_2 was used as the solvent, to lower the toxicity and experimental cost of the process, the formation of **7'** could not be controlled. Despite the presence of this by-product, that lowers the overall yield, the next step was performed without further purification, as the double brominated by–product **7'** should not interfere in the next reaction.

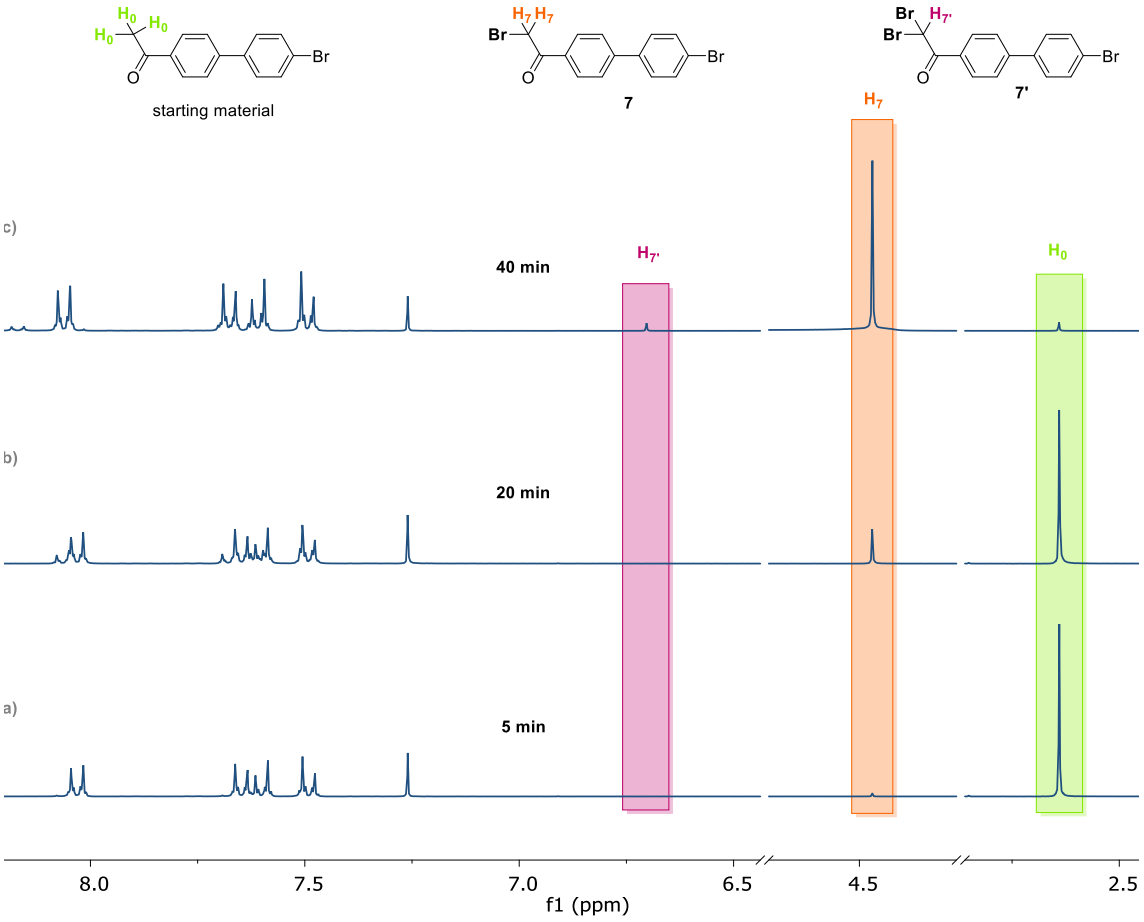

Figure 2.8. *a) ^{1}H NMR of the reaction to form compound **7** after 5 minutes, b) ^{1}H NMR of the reaction to form compound **7** after 20 minutes, and c) ^{1}H NMR of the reaction to form compound **7** after 40 minutes ($CDCl_3$, 300 MHz).*

The condensation of compound **7** with 2–aminopyridine yielded compound **8**. The reaction proceeded in refluxing EtOH, and it was initially tested without any base obtaining a yield of 30–40%. Upon the addition of sodium bicarbonate, the yield improved to 80%. For purification of **8**, the column chromatography that was necessary

in the initial attempts was eluded, by running the reaction with an excess of 2–aminopyridine. Using this procedure, **8** was obtained by simple filtration of the reaction mixture. The white solid obtained was washed with H_2O and vacuum–dried.

Compound **6** was synthesized by reacting 1–aza–18–crown–6 with compound **8** in toluene, catalyzed by Pd(0), and using ^{t}BuONa as the base, following the same procedure described before for **4**. The reaction crude was filtered through a celite pad and the filtrate was evaporated and triturated again with Et_2O to remove any unreacted starting products, giving the pure product in 60% yield. The product formation and its purity were confirmed by ^{1}H NMR spectra (**Figure 2.9**). The incorporation of the aza–crown ether is confirmed by the shift in the spectra of the doublet from 7.51 ppm present in **8** to 6.76 ppm, which corresponds to two of the protons of the *para*–substituted aromatic system directly bound to the aza–crown ether. The signals corresponding to the aliphatic protons of the aza–crown ether appear at 3.45 ppm.

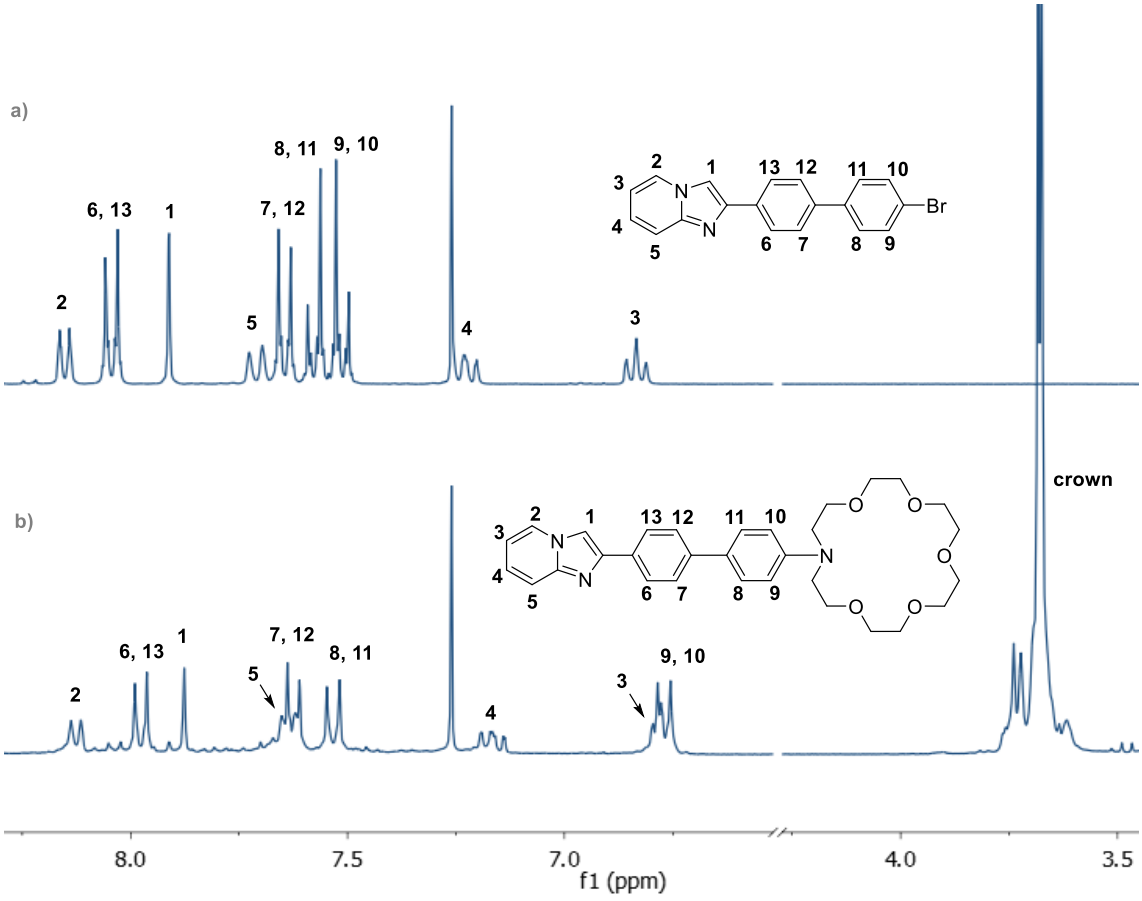

Figure 2.9. *^{1}H NMR spectrum of compounds **8** (a) and **6** (b), with their respective assigned structures ($CDCl_3$, 300 MHz).*

The last step to obtain **G3a** is based on the so-called [8+2] cycloaddition, described in the introduction. As explained, the 8+2 reaction is employed for the formation of the benzocyclazine, to form the fluorophore core of **FBI**. Nevertheless, before proceeding with the [8+2] reaction of compound **6** to obtain the final **G3a**, a model reaction was tested on compound **8**, to confirm the viability of the product and have a ^{1}H NMR spectra to be used for comparative purposes (**Scheme 2.3**). The reaction was carried out under microwave irradiation, with 2–(trimethylsilyl)phenyl triflate as the benzyne precursor, CsF, and 18–crown–6.[8]

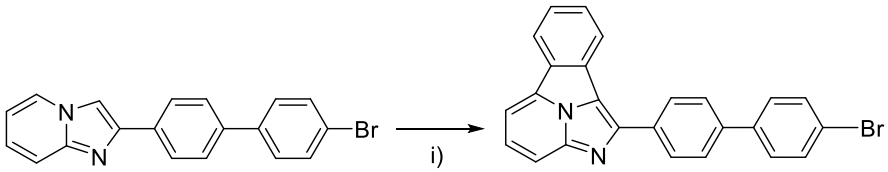

8 **9**

Scheme 2.3. *Microwave assisted cycloaddition tested for compound **8**. i) MW, 30 min, 100W, 220 °C max, CsF, 18–crown–6, 2–(trimethylsilyl)phenyl triflate.*

The crude product was purified by column chromatography, using a mixture hexane:EtOAc (1:1, v/v) as the eluent. The ^{1}H NMR spectrum of the purified product **9**, with the tentative assignment to the structure, compared with that of the starting reactant, is shown in **Figure 2.10**.

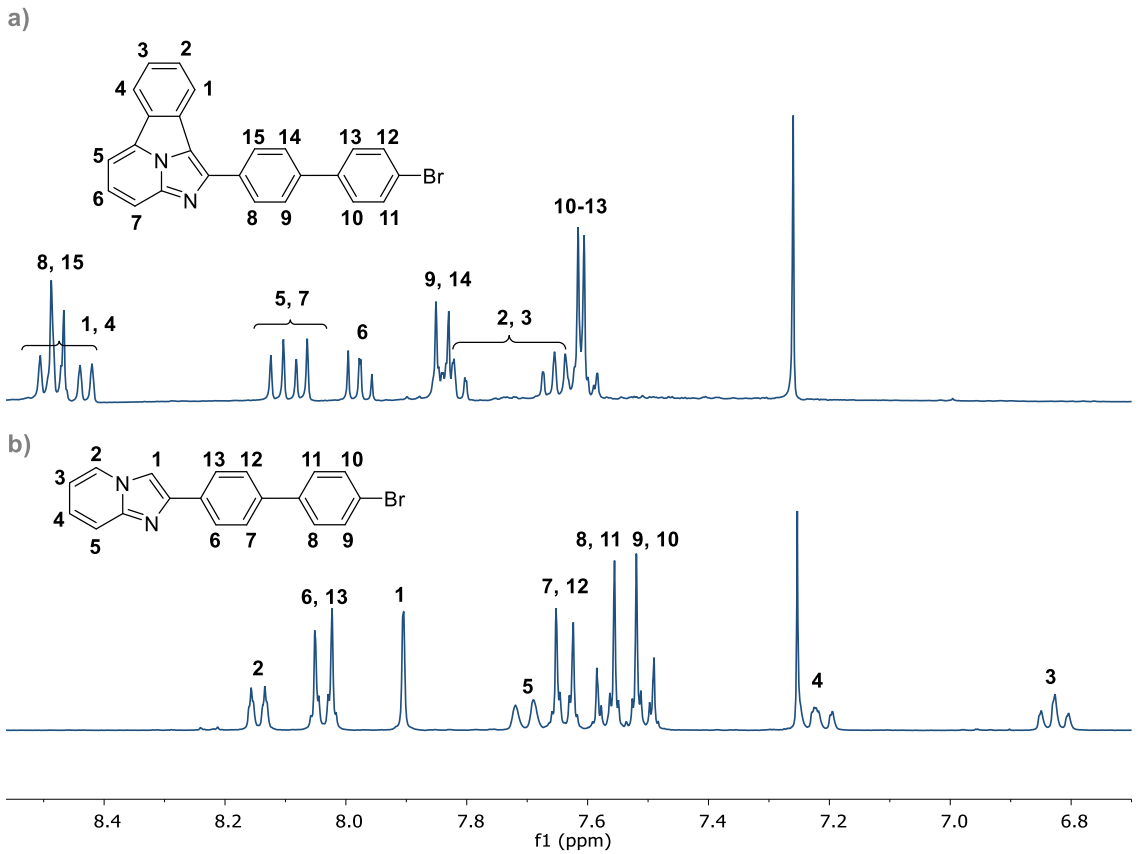

Figure 2.10. *^{1}H NMR of compounds a) **9** and b) **8**, with their assigned structures ($CDCl_3$, 300 MHz).*

With the confirmation of the feasibility of the product **9** and the ^{1}H NMR spectrum for comparison, the [8+2] cycloaddition to compound **6** to obtain **G3a** was attempted. In this case, the reaction was carried out in refluxing DMF at 160 °C, with K_2CO_3, $Pd(OAc)_2$, XPhos, and o–dibromide benzene as benzyne precursor. As described in the literature, when the reaction is catalyzed at high temperatures, the yields for the cyclazine formation are higher, compared to MW conditions.[9] After 30 minutes of reaction, a clear yellow emission color was observed under UV–irradiation of the reaction mixture (initially it was a blue–emitting mixture), which indicated the formation of the fluorophore. When the reaction finished, the solvent was evaporated under vacuum, yielding a brown sticky solid. The ^{1}H NMR spectrum of the crude revealed some signals that could be assigned to the desired compound (a in **Figure 2.11**). For instance, the observation of signals at 8.4–8.5 ppm, similar to those observed for compound **9**, was considered proof of the occurrence of the cycloaddition.

The purification of the crude started with an initial chromatographic column, using a mixture of AcOEt and hexanes as eluents, which yielded a compound of higher purity,

as observed in b in **Figure 2.11**. The ^{1}H NMR spectra presented a spectroscopic pattern compatible with the one expected for compound **G3a**. Again, it was similar to the one observed for compound **9**, which differs in the signals of the doublet corresponding to the phenyl next to de Br or crown, which shifts from 7.61 ppm for **9** to 6.82 ppm for **G3a**. Likewise, this shift was previously detected for fragment **6** in **Figure 2.9**.

However, the obtained fraction still contained some impurities that could obstacle the complete characterization of the **G3a**. Therefore, the product was further purified by a centrifugal thin–layer chromatography, in this case, using CH_2Cl_2 and MeOH as eluents. The spectrum obtained from this purification method is shown in c in **Figure 2.11**, which confirmed the purity of **G3a**. The identity and purity of the **G3a** were further demonstrated by ^{13}C NMR, COSY, HSQC, and HR–MS spectroscopies. Unfortunately, due to the tedious purification procedure, the overall yield obtained for pure compound **G3a** ended up being 5%.

Once compound **G3a** structure was confirmed and characterized, its luminescent properties were measured, which will be discussed in the next section.

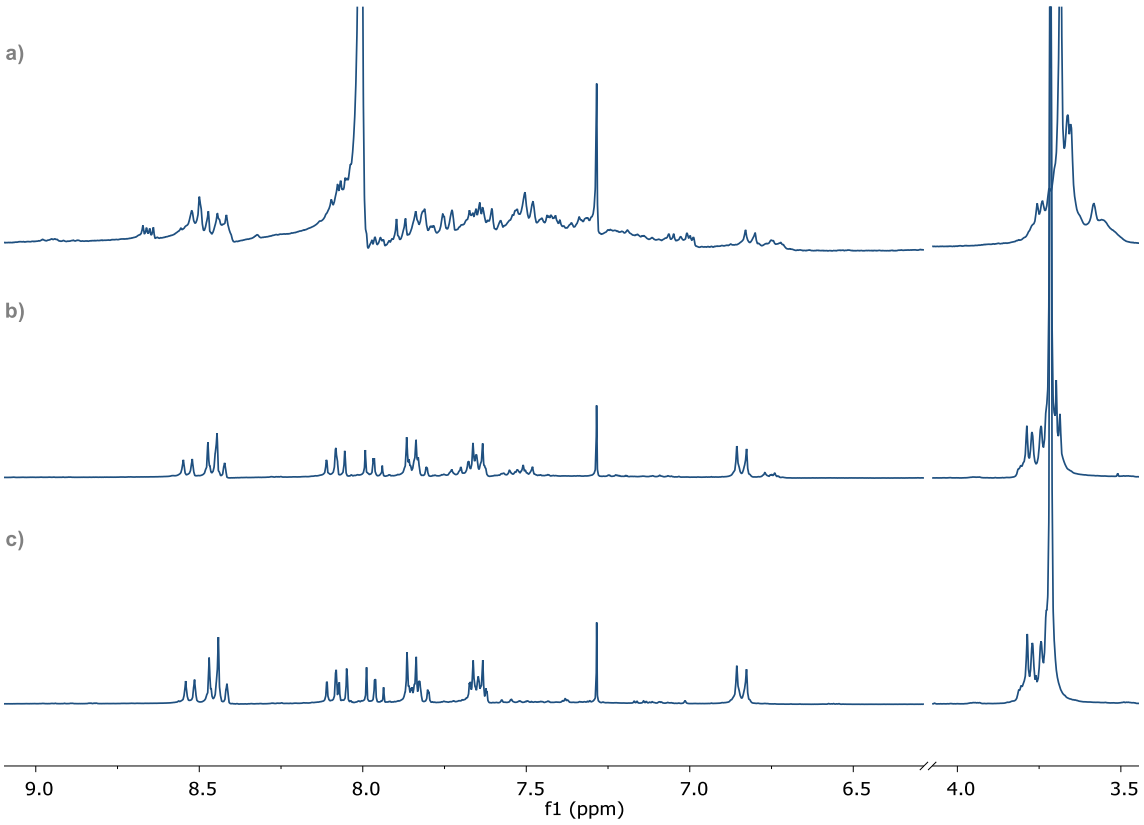

Figure 2.11. *^{1}H NMR spectra of the synthesis of **G3a**. a) the first aliquot of the crude, b) the product from the first chromatographic column, and c) pure **G3a**, after the centrifugal thin–layer chromatography ($CDCl_3$, 300 MHz).*

2.2.2.2 G3b

Once **G3a** was obtained, a similar synthetic pathway was followed for the synthesis of **G3b** (**Scheme 2.4**).

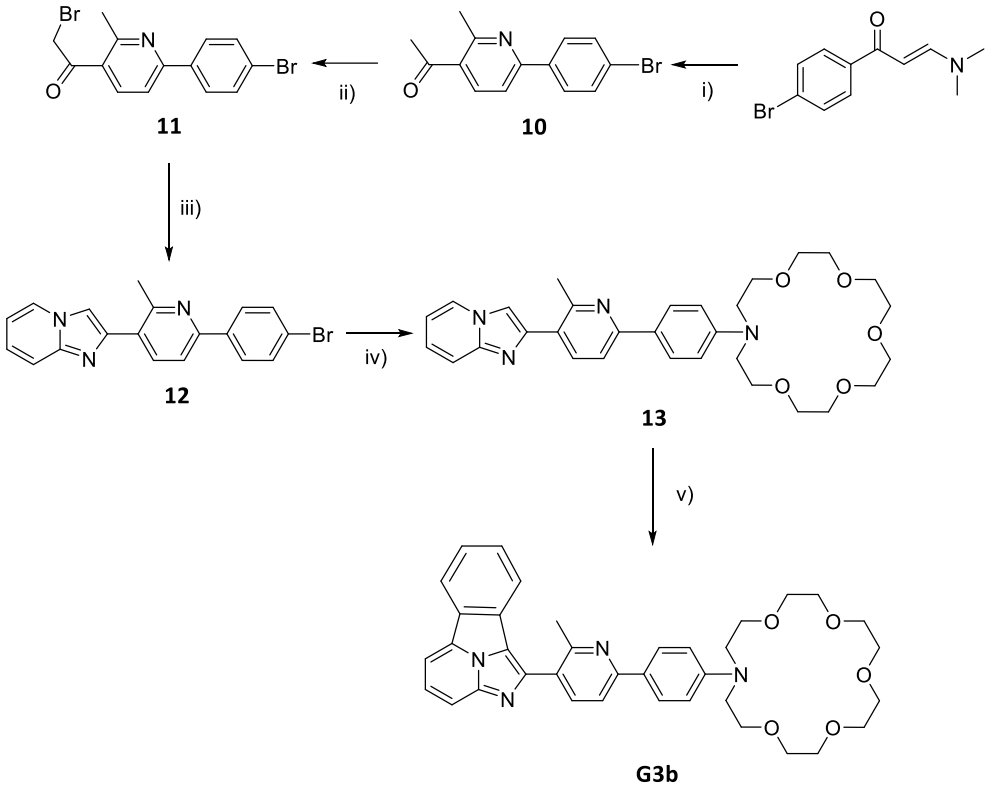

Scheme 2.4. *Synthetic pathway for the* ***G3b****. i) acetyl acetone (1.1 equiv.), NH_4OAc (6 equiv.), glacial AcOH, 120 °C. ii) Br_2 (1 equiv.), HBr (1 equiv.), glacial AcOH, 75 °C. iii) 2–aminopyridine (1.1 equiv.), $NaHCO_3$ (1.5 equiv.), EtOH, 80 °C. iv) 1–aza–18–crown–6 (1 equiv.), $Pd_2(dba)_3$ (4 mol %), DavePhos (12 mol %), ^tBuONa (1.5 equiv.), toluene, 115 °C. v) $Pd(OAc)_2$, XPhos, o–dibromide benzene, K_2CO_3, DMF, 160 °C.*

In this case, (E)–1–(4–bromophenyl)–3–(dimethylamino)prop–2–en–1–one was employed as starting material, due to its low cost compared to commercially available compound **10**.

Compound **10** was synthesized by reacting the starting product with acetyl acetone and NH_4OAc in glacial acetic acid, following the procedure described by Kumar et al.[10] The reaction was heated at 120 °C for four hours and the resulting mixture was dropped into ice–cold H_2O where a precipitate formed. The precipitate was filtered to obtain **10** as a pale yellowish solid in 72% yield. The ^1H NMR spectrum was in agreement with the data reported in the literature and, given the purity of the product, it was decided to use it in the next step without further purification.

Compound **10** was brominated to obtain compound **11**. Initially, this reaction was attempted in $CHCl_3$, as described before for the bromination of **G3a**. However, the reaction did not progress due to the lack of solubility of the starting material. Therefore,

an alternative procedure, described by Bavetsias et al. using 48% aqueous HBr in glacial acetic acid, was attempted.[11] Br_2 was added over a solution of **10** in aq. HBr/glacial acetic acid, and then the reaction was stirred at room temperature for 1 h, and eventually heating at 75 °C for 90 minutes. Upon completion of the reaction period, THF was added to the mixture and stirred overnight, while a precipitate started forming. The product was extracted from the mixture by basification with $NaHCO_3$ and extraction with EtOAc, to give almost quantitative yields.

The ^{1}H NMR spectrum of the crude product showed the expected spectroscopic pattern of **11** (b in **Figure 2.12**), with no starting material. The characteristic signal assigned to the protons of the brominated acetyl group was detected at 4.42 ppm (highlighted in green). Likewise in the reaction to form compound **7**, some other signals were observed assigned to the double brominated **11'** species, which was recognized with the appearance of a peak at 6.61 ppm (highlighted in pink). Compound **11** could be obtained as a pure species by simple filtration of the precipitate formed upon THF addition instead of performing the neutralization and extraction. This workup gave pure compound **11**, as confirmed by ^{1}H NMR spectroscopy (c in **Figure 2.12**), with 70% yield.

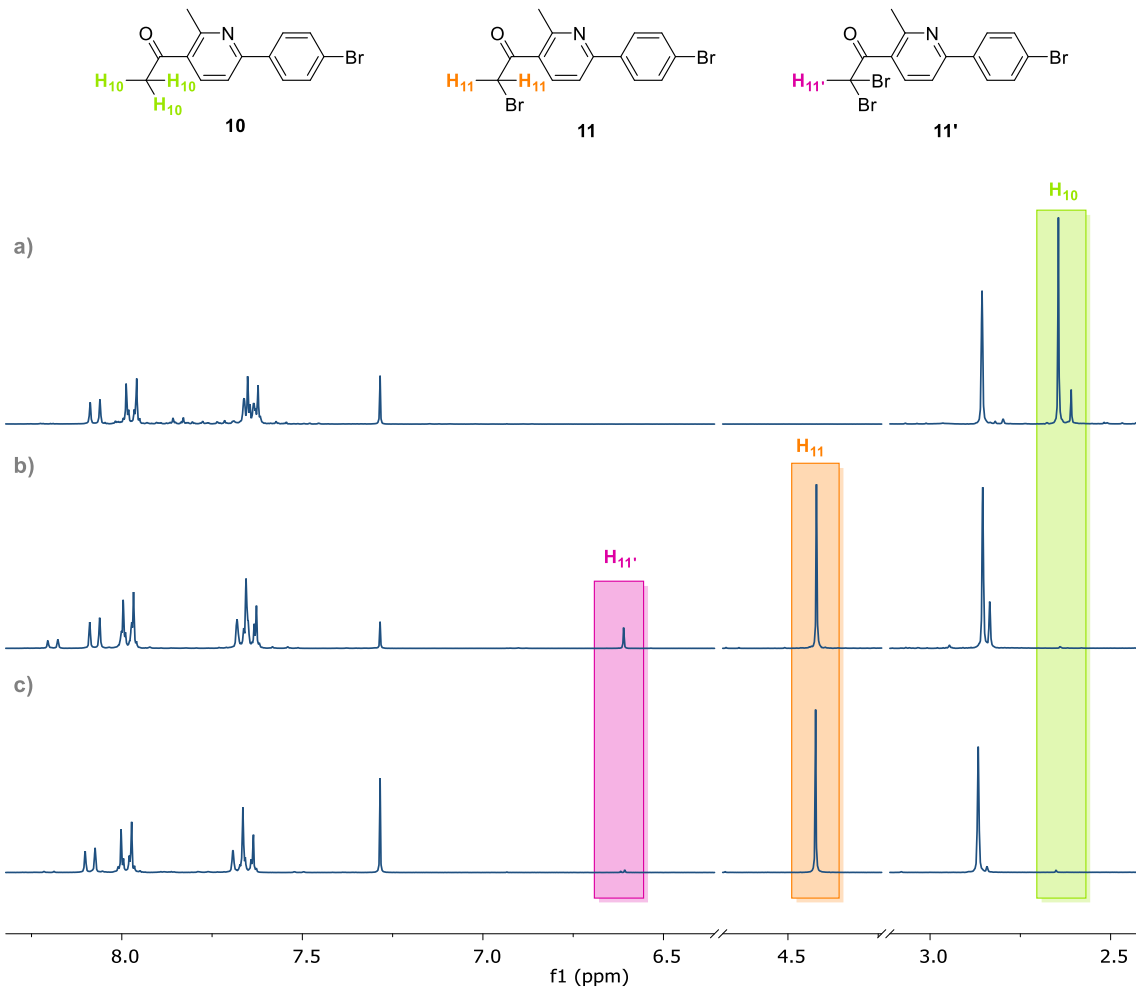

Figure 2.12. *The structures of compound **10**, monobromide **11** and dibromide **11'**. ^{1}H NMR spectra of a) **10**, b) crude in the reaction to obtan **11** and c) purified compound **11**, with the aliphatic proton signals shadowed ($CDCl_3$, 300 MHz).*

The condensation of **11** with 2–aminopyridine in an EtOH reflux with $NaHCO_3$ yielded compound **12**. When reaction finished, it was cooled down, and the formed precipitate was filtered and washed with H_2O, yielding pure product **12** as confirmed by ^{1}H NMR spectroscopy (a in **Figure 2.13**). In this case, the yields oscillated from 60 to 80%.

For the addition of the aza–crown–ether to obtain **13**, the same reaction conditions previously described for **6** were attempted. **12** was coupled with 1–aza–18–crown–6 yielding compound **13**, using toluene as a solvent. This cross coupling reaction was performed using $Pd_2(dba)_3$/DavePhos as catalyst and ^{t}BuONa as a base. However, in this case, longer reaction times were required (72 h). After this period, the mixture was filtered over a celite pad and the filtrate was evaporated and triturated with Et_2O. The residue was analyzed by ^{1}H NMR spectroscopy to confirm its identity and purity (b in

Figure 2.13). As described before for derivative **6**, the high–field shift of one aromatic signal from 7.60 ppm to 6.77 ppm, and the presence of the aliphatic hydrogens of the aza–crown ether were considered evidences of the addition of the aza–crown ether. The extension of the reaction time from 16 h to 72 h, improved the yield up to 75%.

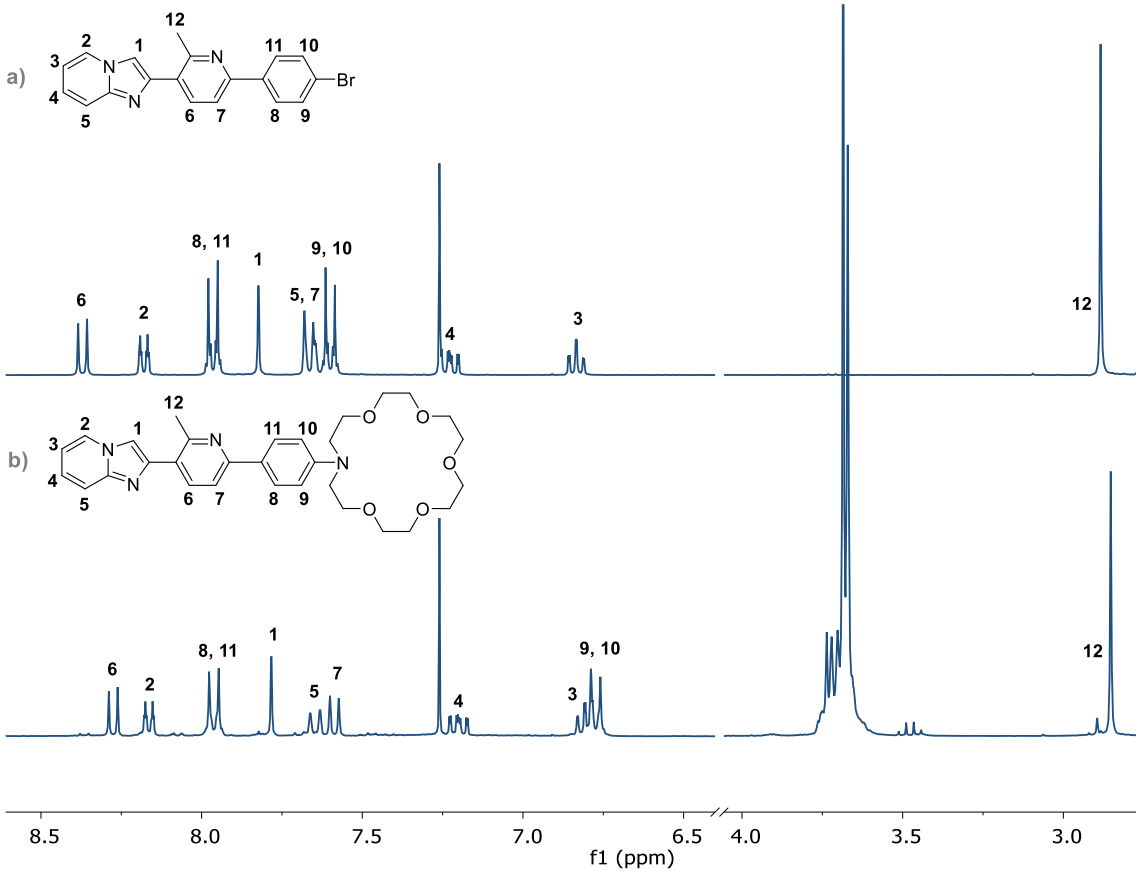

Figure 2.13. *^{1}H NMR of compound a)* ***12*** *and b)* ***13****, and their assigned structures ($CDCl_3$, 300 MHz).*

The conditions for the cycloaddition [8+2] described before for **G3a** were also replicated for the last step of the synthesis of **G3b**. The reaction was carried out in refluxing DMF at 160 °C, with K_2CO_3, $Pd(OAc)_2$, XPhos, and o–dibromide benzene as benzyne precursor. After completion of the reaction, DMF was removed under vacuum, and the crude was purified by two subsequent centrifugal thin–layer chromatography on silica: first one starting with CH_2Cl_2 and changing to 10% MeOH in CH_2Cl_2 as the eluent; and, the second one, less polar, with from in CH_2Cl_2 to 1% MeOH in CH_2Cl_2. In this manner, the desired **G3b** was obtained, in 3% yield. In **Figure 2.14**, the ^{1}H NMR of the pure compound **G3b** is shown. The identity and purity of the **G3b** were further demonstrated by COSY and HR–MS spectroscopies.

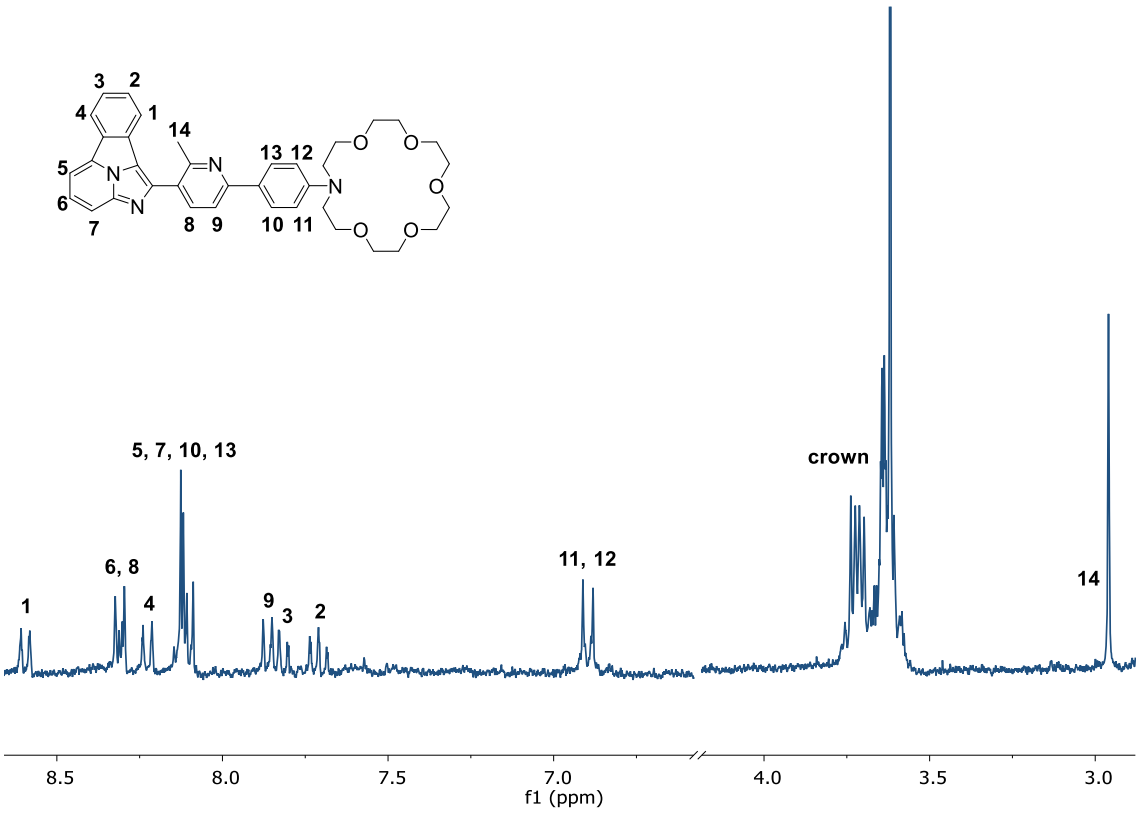

Figure 2.14. *^{1}H NMR spectrum of pure **G3b** ligand and its assigned structure ($CDCl_3$, 300 MHz).*

2.2.2.3 G3c

G3c was, chronologically, the last derivative synthesized. As the corresponding 4–bromophenyl pyrazine derivative was not commercially available, an alternative methodology was developed based on a Suzuki–Miyaura coupling of a chloropyrazine derivative and a 4–pinacolboronic ester of the phenyl aza-crown ether adduct **17**, by that time developed in Prof. Cossio's lab. The entire synthetic route is described in **Scheme 2.5**.

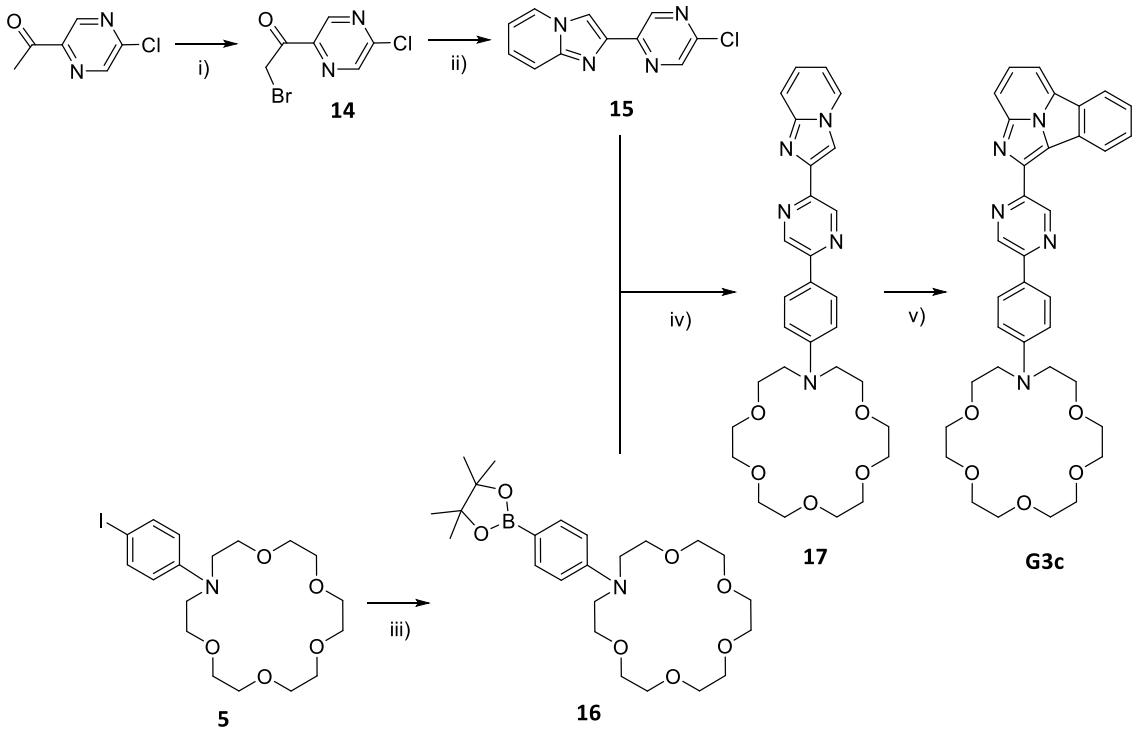

Scheme 2.5. *Synthetic pathway for the formation of* ***G3c****. i) Br_2 (1 equiv.), AcOH. ii) 2–aminopyridine (1.1 equiv.), $NaHCO_3$ (1.5 equiv.), EtOH, 80 °C. iii) $(Bpin)_2$ (1.1 equiv.), $PdCl_2(dppf)_2$ (3 mol %), KOAc (3 equiv.), DMSO. iv) $Pd(PPh_3)_4$ (5 mol %), Na_2CO_3 (5 equiv.), DME/H_2O (3:1, v/v). v) 18–crown–6 (2 equiv.), K_2CO_3 (2 equiv.), 2–(trimethylsilyl)phenyl triflate (2 equiv.), acetone.*

As described in **Scheme 2.5**, the first step was the monobromination of the acetyl group of the starting 1–(5–chloropyrazin–2–yl)ethan–1–one. Based on a procedure described in a patent,[12] Br_2 was added over a solution of the reactant in a mixture 48% aqueous HBr/AcOH (1:4, v/v) and the reaction was stirred at 60 °C for 2 h. The resulting mixture was neutralized $NaHCO_3$ and extracted with EtOAc, yielding an orange/brown solid after evaporation of the solvent. ^{1}H NMR spectrum of the product is shown in a in **Figure 2.15**. The signals observed corresponded to two similar compounds. In the aromatic region, two sets of two doublets were observed and two singlets were distinguished in the aliphatic area of the spectra at 4.7 ppm (highlighted in orange), assigned to two types of mono brominated acetyl signals. It was concluded that the chlorine atom present in the reactant had partially been exchanged with the bromine atom during the reaction, yielding two different products, **14** and **14Br**. It could also be observed that the aliphatic signal at 2.72 ppm of the unreacted starting compound also showed two singlets instead of one (highlighted in green), which was in agreement with the chlorine partial exchange in the reactant.

Based on these results, the reaction time was extended to 4 h, using the same reaction conditions, to get the complete replacement of the chlorine atom with the bromine. However, the ^{1}H NMR spectrum of the crude (b in **Figure 2.15**) showed the presence of 4 species in the aromatic region and at 7.34 ppm began to show two other singlets (shadowed in pink), which were assigned to the double brominated acetyl groups of **14'** and **14'Br**.

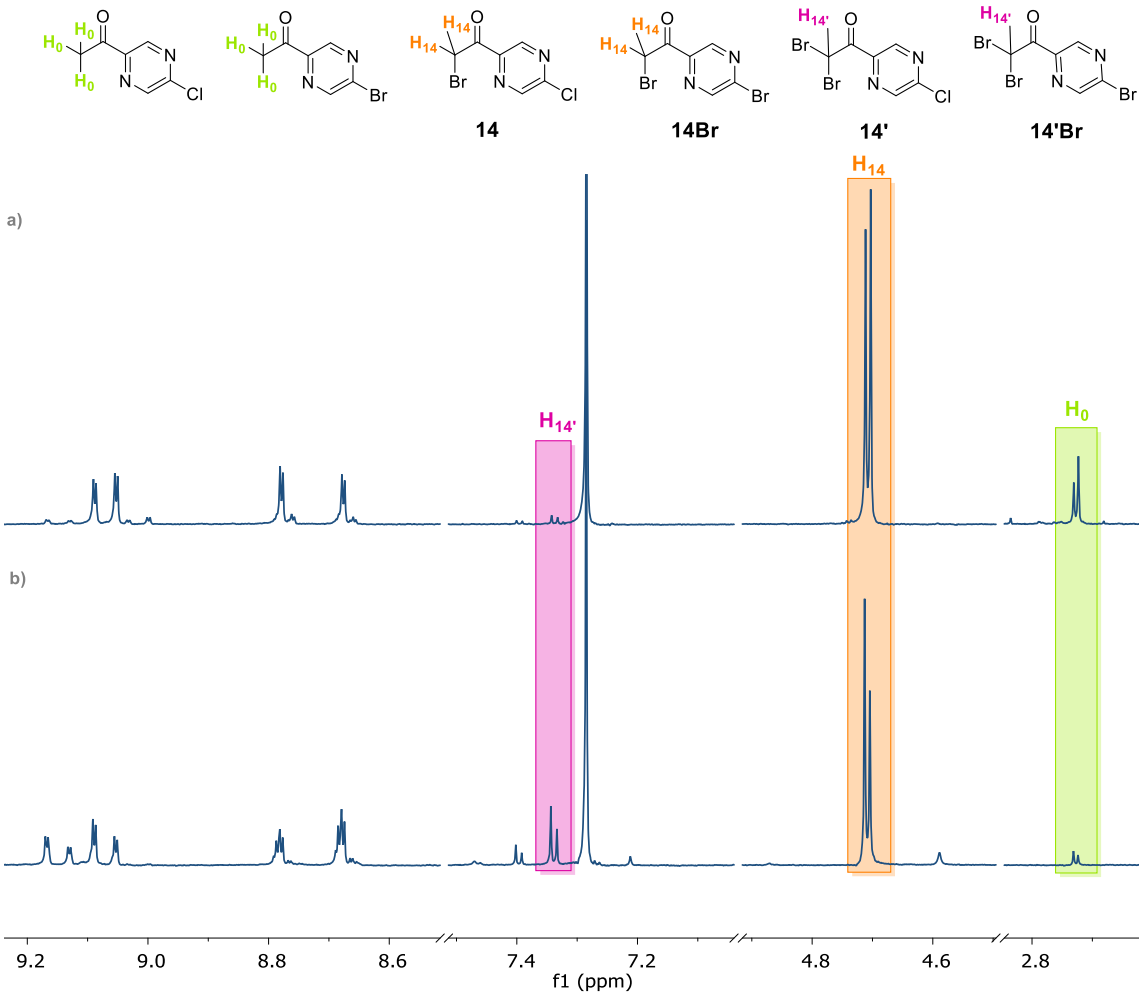

Figure 2.15. *^{1}H NMR spectrum of the monobromination reaction of 1–(5–chloropyrazin–2–yl)ethan–1–one to form compound **1**, a) when the reaction was heated at 60 °C for 2h. b) when the reaction was heated at 60 °C for 4h ($CDCl_3$, 300 MHz).*

Another attempt was made following the procedure described by Lopes et al.[13] In this case, Br_2 is added dissolved in AcOH to the reactant previously dissolved in AcOH, without HBr. The solution was stirred at 40 °C for 16 h and during that time, a precipitate formed. The solid was filtered and analyzed by ^{1}H NMR. The spectrum showed again the two monobrominated species **14** and **14Br**.

In view of these results, the obtention of the isolated product **14** or **14Br** was discarded, and it was decided to continue with the synthesis of **15**, using the mixture of **14** and **14Br**. This mixture was reacted with 2–aminopyridine using the same conditions as for the synthesis of **8** and **12**, in an EtOH reflux with Na_2CO_3. The precipitate formed was filtered and washed with H_2O and Et_2O. The solid obtained was analyzed by ^1H NMR spectrum (**Figure 2.16**). The formation of the indolizine core was confirmed by the appearance of the singlet at 8.28 ppm, together with the two triplets and two doublets corresponding to the 3 and 4, and 2 and 5 protons, respectively, represented in the structures in the same **Figure 2.16**. As expected, two sets of signals were observed in the spectra, which was more evident in the ones assigned to the protons of the pyrazine (6 and 7 in the structures **15** and **15Br**) and the singlet of the indolizine, which confirmed the partially exchanged chlorine atom for bromine in the previous step.

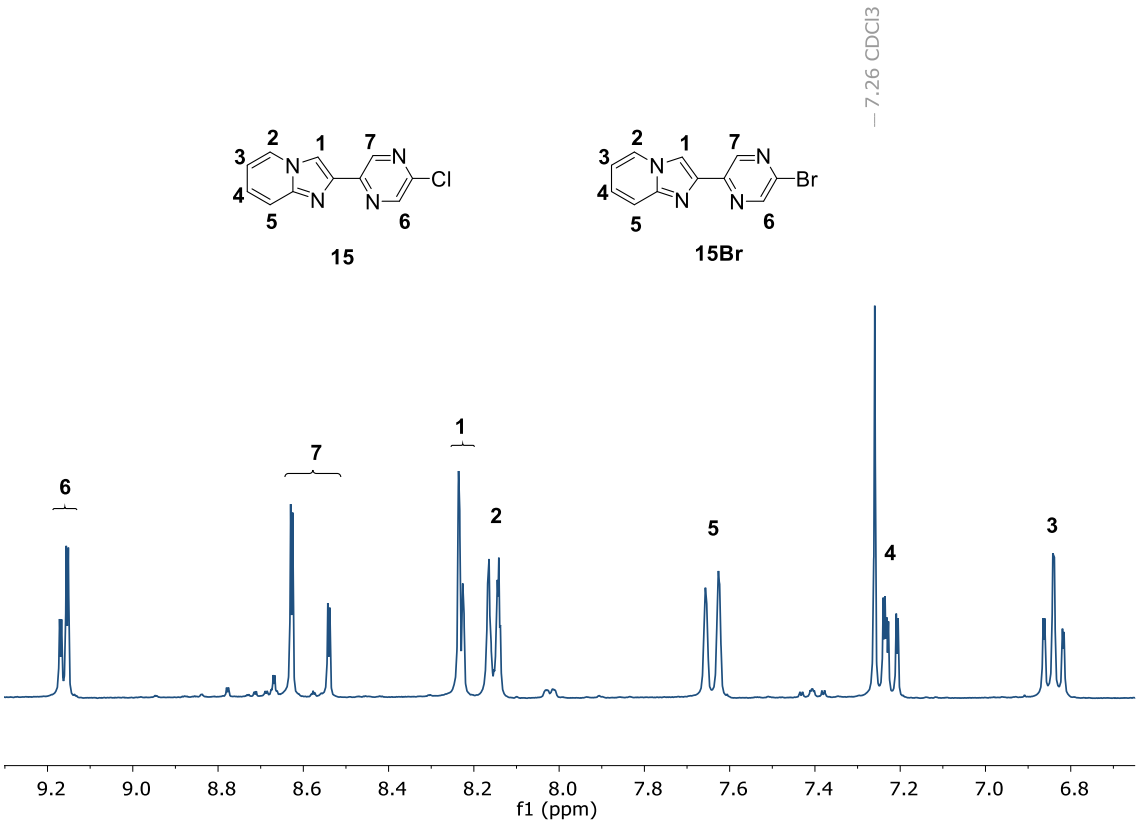

Figure 2.16. *^1H NMR spectrum of the mixture of the species **15** and **15Br** and their assigned structures. ($CDCl_3$, 300 MHz).*

Simultaneously, the synthesis of the boronic synthon **16** was carried out, following the procedure optimized at Prof. Cossio's lab. Compound **5**, previously described for the synthesis of **G3a**, was reacted with $(Bpin)_2$ using $PdCl_2(dppf)_2$ as catalyst in DMSO at 80

°C, with KOAc as the base 16 h. H_2O was added to the resulting mixture and it was extracted with CH_2Cl_2, to give a thick brown oil in quantitative yield after solvent evaporation. The formation of **16** was confirmed by ^1H NMR, shown in **Figure 2.17**, by comparison with the spectra of the starting compound **5** by a clear shift of the aromatic signals and the presence of the aliphatic peak at 1.35 ppm corresponding to the pinacol group.

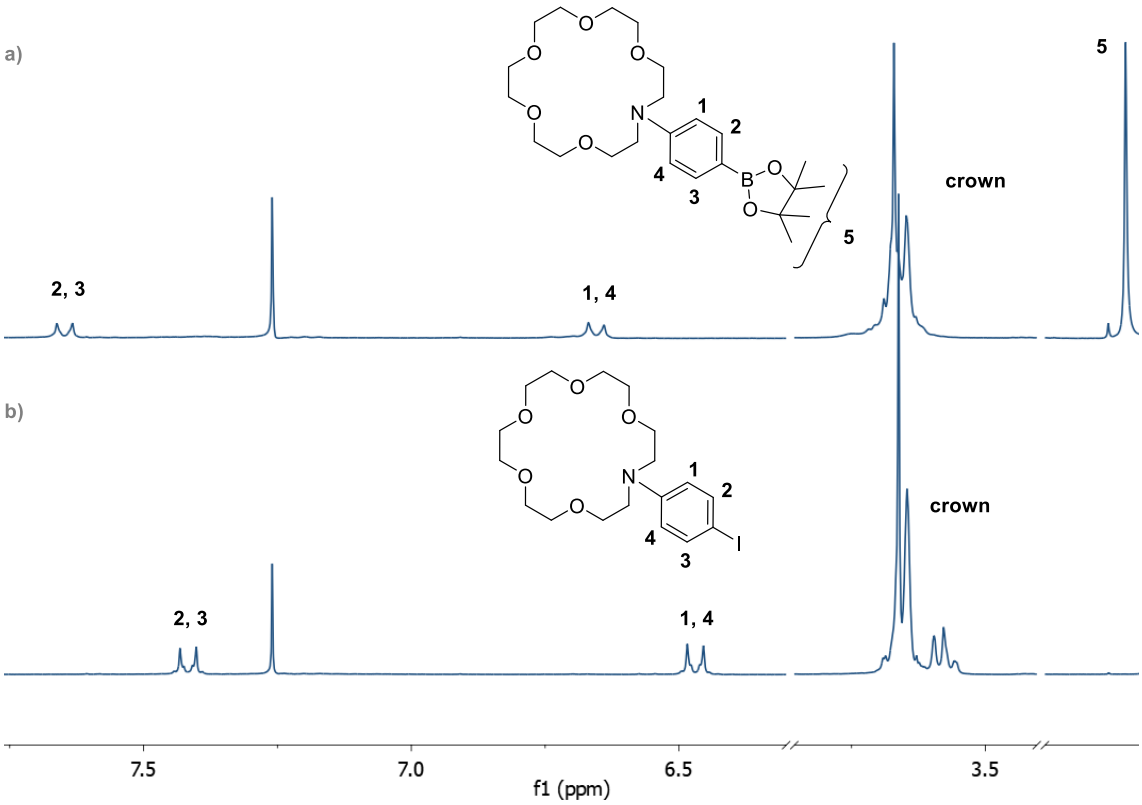

Figure 2.17. *^1H NMR spectrum of compounds a) **16** and b) **5**, with their assigned structures ($CDCl_3$, 300 MHz).*

The formation of **17**, relied on the C–C cross–coupling of fragments **15** and **16**. Although **15** was obtained as a mixture of two compounds, the cross–coupling was attempted with the mixed product **15** and **15Br**, as both the chloride and bromide derivatives should be reactive in cross–coupling processes.

Thus, for the synthesis of **17**, the Suzuki–Miyaura reaction was proceeded under standard conditions. The mixed compounds **15** and **15Br** were reacted with **16** in a solvent mixture of DME/H_2O, catalyzed by $Pd(PPh_3)_4$ and using Na_2CO_3 as the base.[14] The mixture was refluxed for 16 h, and the formation of a bright yellow–emitting material

under UV irradiation was indicative of the reaction progress. After this time, the solvent was evaporated, and the crude was analyzed by ^{1}H NMR (a in **Figure 2.18**).The spectrum showed almost no signal of the reactants, which meant that **15** and **15Br**, both reacted with **16**, and new signals could be detected. CH_2Cl_2 was added to the crude and the mixture was filtered to remove the salts formed. The solvent of the filtrate was removed under vacuum and the residue was purified by chromatographic column, using a mixture of CH_2Cl_2 and MeOH as eluent. The fraction emitting in green was collected and identified as the pure product **17**, with a 50% yield. Unfortunately, when the reaction was scaled–up to 3 mmol, the yield dropped to 30%. The ^{1}H NMR spectrum (b in **Figure 2.18**) showed three sharp singlets, at 9.33, 8.90, and 8.19 ppm assigned to the pyrazine and the singlet of the indolizine core, the rest of the aromatic indolizine protons and the AA'BB' spin system and the signals of the azacrown–ether were also clearly distinguished.

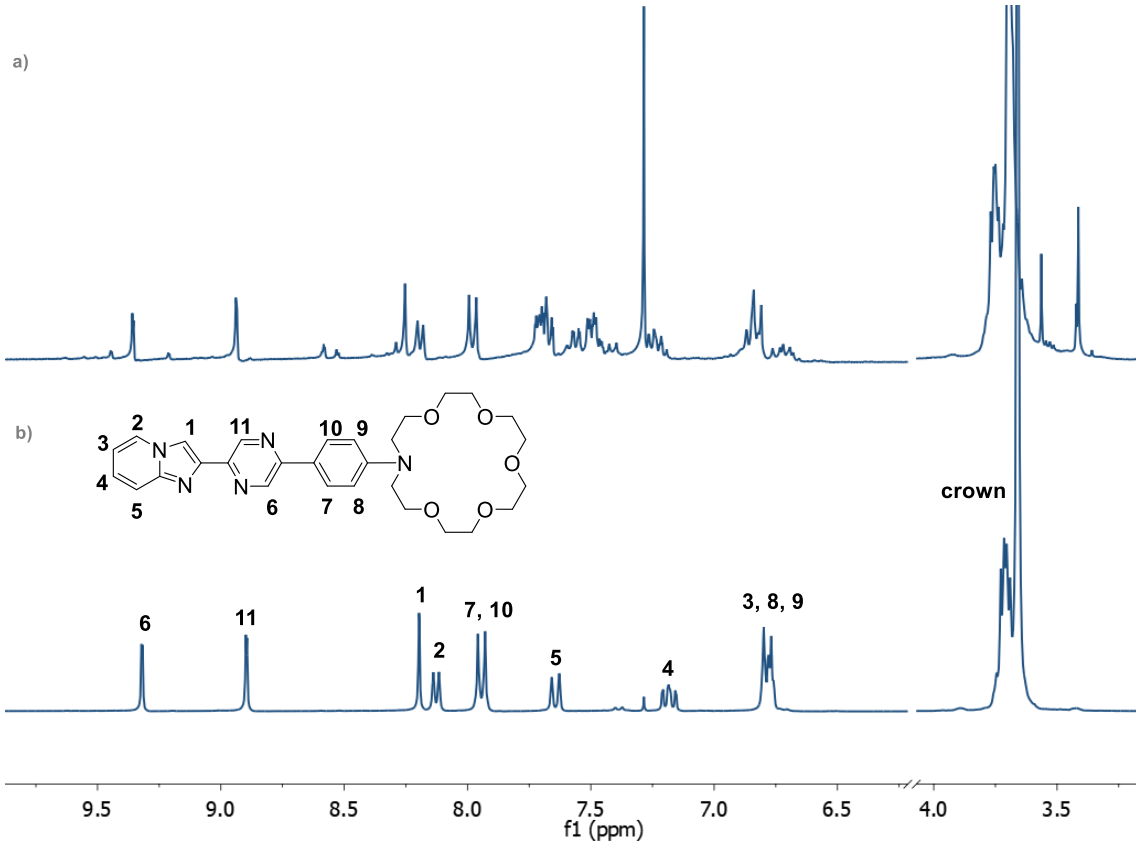

Figure 2.18. *^{1}H NMR spectrum of a) the reaction crude and b) purified compound **17**, with the assigned structure ($CDCl_3$, 300 MHz).*

The last step for the synthesis of **G3c** was the [8+2] reaction. In this case, the conditions used were different from those used to obtain **G3a** and **G3b**, and a method developed by Semwal et al. for the synthesis of benzo[a]imidazo[5,1,2–cd]indolizines, with metal–free conditions was attempted.[15] According to these authors, almost quantitative yields could be obtained for a simple benzo cyclazine synthesis.

Thus, compound **17** was dissolved in acetone and 2 equiv. of K_2CO_3, 18–Crown–6, and 2–(trimethylsilyl)phenyl triflate, as the benzyne precursor, were added. The reaction was heated at 45 °C for 24 h. ^{1}H NMR of the crude is shown in c in **Figure 2.19**. Due to the complexity of the spectrum pattern, to check the conversion, the decrease of signal corresponding to the singlet of the indolizine (highlighted in grey) was followed. The spectrum showed that a new compound started forming, but the conversion appeared to be too low compared to the starting compound **17** (d in **Figure 2.19**). Therefore, the same reaction was repeated but the temperature was adjusted to 70 °C (in a small pressure reactor) and the reaction was left for 48 h. The ^{1}H NMR of the aliquot of the reaction showed a better conversion, but it was concluded that it was still too low for a practical synthesis (b in **Figure 2.19**). To improve the conversion, to the same reaction 2 equiv. of the benzyne precursor were added and the reaction was left for 96 h at 75 °C. After this time, and aliquot of the reaction showed the ^{1}H NMR shown in a in **Figure 2.19**, and the reaction was stopped.

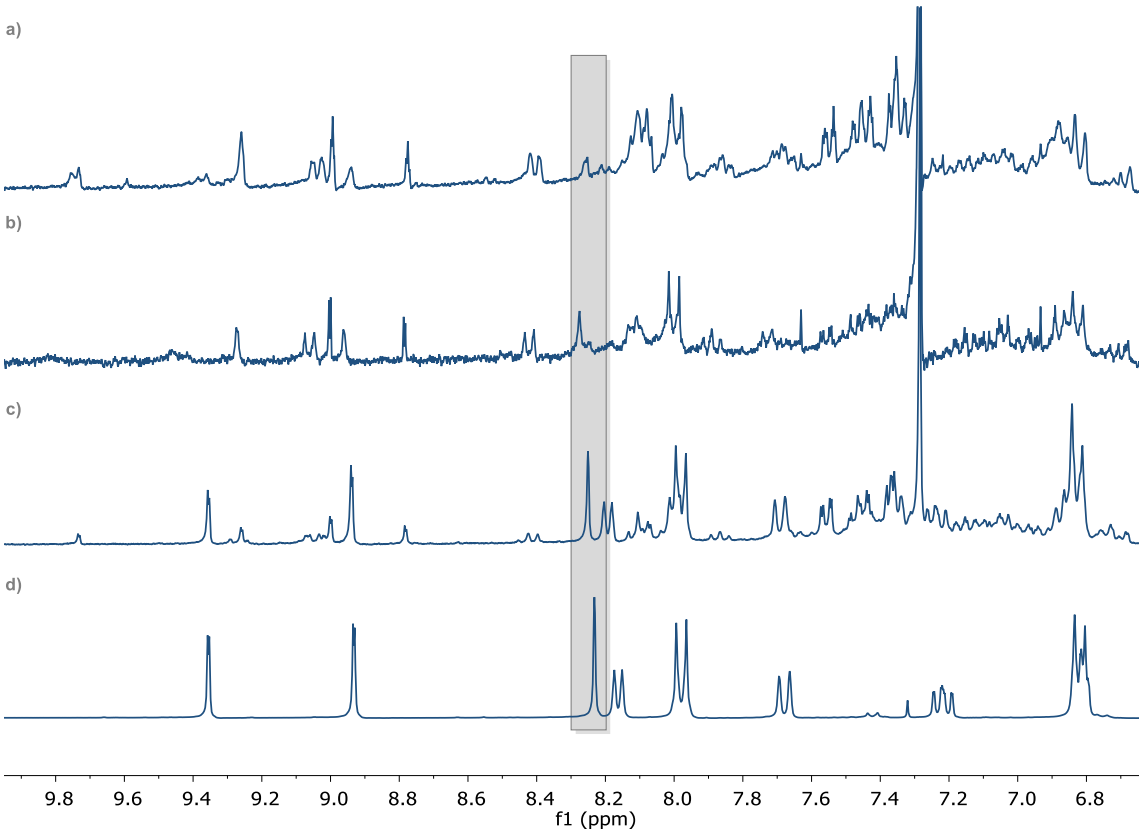

Figure 2.19. *^{1}H NMR spectrum of a-c) aliquots of the reaction in the synthesis of **G3c** and d) the starting compound **17** ($CDCl_3$, 300 MHz).*

The purification of the product was achieved by chromatographic column using CH_2Cl_2 as eluent and changing the polarity with MeOH from 0.5% to 5%. The final product was obtained as an orange solid with a 10% yield and its identity and purity were confirmed by ^{1}H NMR, ^{13}C NMR, COSY, HSQC, and HR–MS spectroscopies. The assigned structure of **G3c** and the ^{1}H NMR spectrum is shown in **Figure 2.20**.

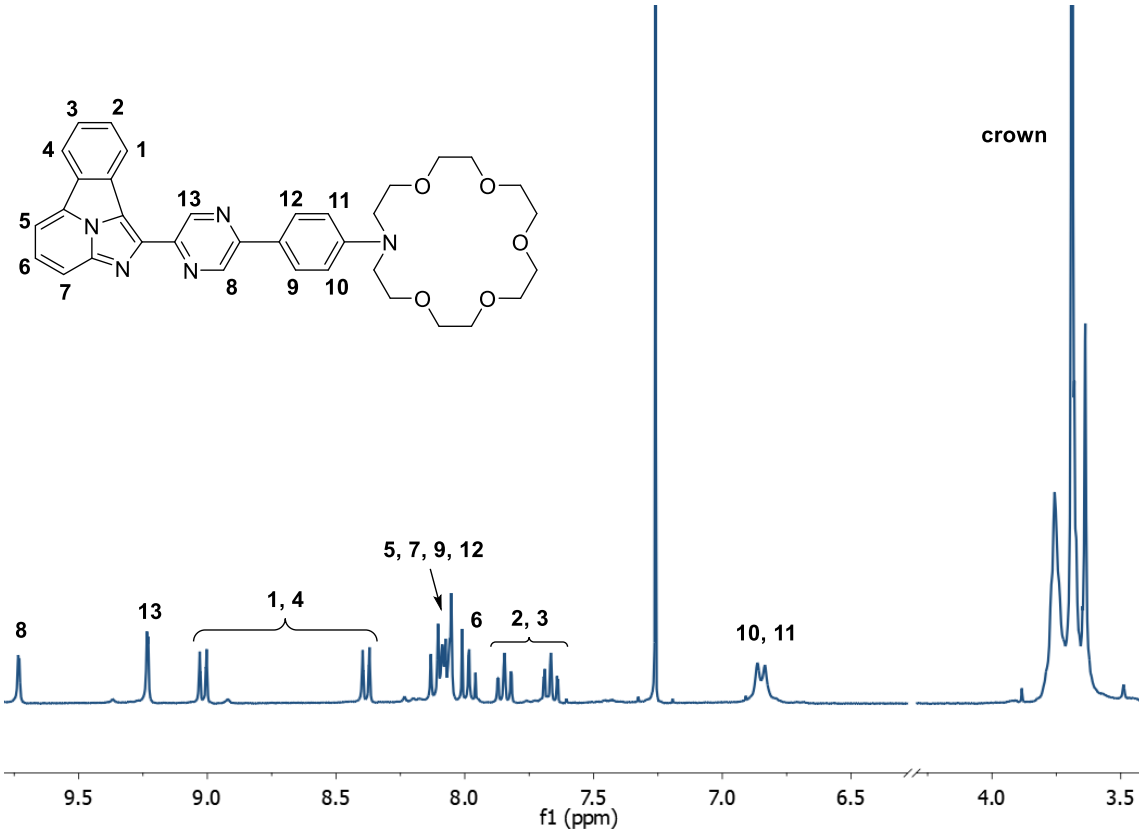

Figure 2.20. *^{1}H NMR spectrum of pure **G3c** ligand and its assigned structure ($CDCl_3$, 300 MHz).*

2.2.3 Photophysical properties

2.2.3.1 Absorption and emission of free ligands

Normalized absorption and emission spectra of **G3** ligands in MeCN solutions are shown in **Figure 2.21**, and the most relevant data are collected in **Table 2.3**. All the compounds show strong absorption bands in the UV region of the spectra associated to π → π* transitions of aromatic units. They are red–shifted compared to the absorption bands of bare benzene or pyridine. This bathochromic shift could be explained by the presence of multiple conjugated aromatic rings with an appended tertiary amine (azacrownether). Both the extended conjugation and the participation of the nitrogen lone–pair in the π–sytem contribute to lower the energy of these transitions. At lower energies (370–500 nm) they also present multiple bands characteristic of the chromophoric annulated benzo[a]imidazo[5,1,2–cd]indolizine core, as described before for this type of derivatives.[15–18] These bands are less resolved in the case of **FBI G3b**.

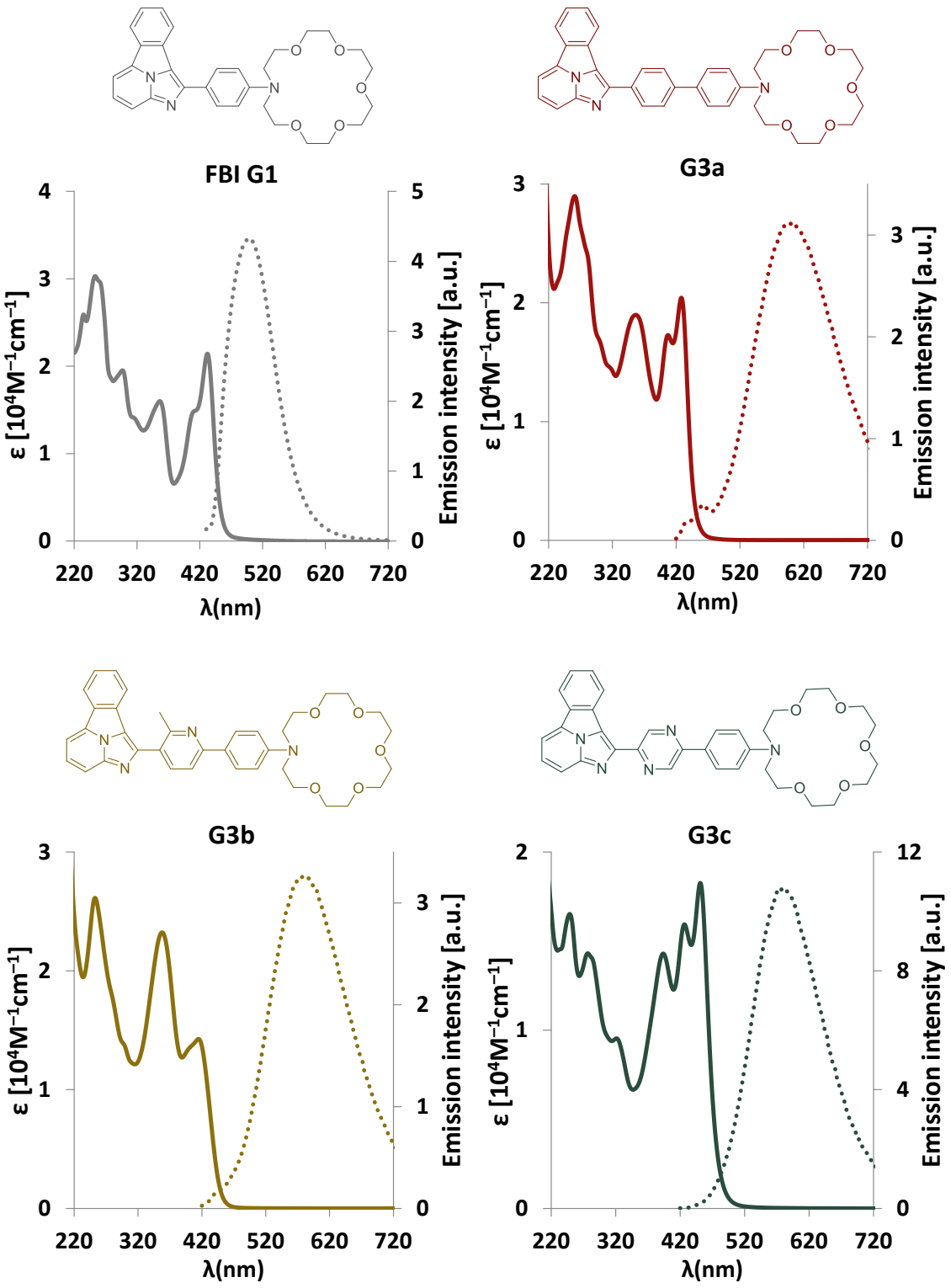

Figure 2.21. *Normalized absorption (solid lines) and emission (dotted lines) spectra of* ***FBI*** *compounds* ***G1***, ***G3a***, ***G3b***, *and* ***G3c***.

Unbound **G3** derivatives are strongly emissive. They present fluorescent emissions ($\tau \approx$ 3.4 ns) in the visible area of the spectra with maxima around 580–600 nm, and relatively high quantum yield values (≥74%). This emission is around 100 nm red-shifted compared

to the original **FBI G1**, probably due to the presence of additional aromatic conjugated rings. This red–shifted emission is reflected in the very large stokes shifts measured for these compounds, which is, in principle, beneficial for their use as fluorescent sensors.

Table 2.3. *Absorption and emission data of* ***FBI G3*** *compounds in MeCN.*

	absorption	emission			
	λ_{max} [nm] (ε [$10^4 M^{-1}cm^{-1}$])[a]	λ_{max} [nm][b]	Φ [%] [b]	τ [ns][c,d]	Stokes shift [cm^{-1}]
G3a	261 (2.87), 356 (1.96), 407 (1.79), 428 (2.1)	600	76.9	3.4	6698
G3b	252 (2.88), 357 (2.65), 414 (1.61)	580	74.7	3.4	6913
G3c	250 (2.55), 277 (2.33), 394 (2.32), 428 (3.75), 451 (3.11)	580	85.5	3.5	4932

MeCN solutions. a) Based on linear regression of the measured absorption of 6 concentrations in the range 10^{-4} M–10^{-6}M. b) Excitation at 368 nm. c) excitation EPLED 340 nm, TCSPC, 10 MHz, 5000 counts. d) All χ^2 values were between 1.0-1.1.

2.2.3.2 Effect of Ba^{2+}

The interaction of the different sensors with Ba^{2+} was analyzed by UV–vis absorption and emission spectroscopies. For **G3a** and **G3b**, $5 \cdot 10^{-5}$ M solutions of the free sensor were titrated using aliquots of concentrated $Ba(ClO_4)_2$ solutions prepared in MeCN. At this concentration, in both cases, 1 equivalent of Ba^{2+} sufficed to reach stable spectra assigned to the chelated form of the sensors (see a more detailed explanation below). The absorption and emission spectra are shown in **Figure 2.22**, and relevant data are collected in **Table 2.4**. In the case of **G3c**, $5 \cdot 10^{-6}$ M solution of the free sensor was titrated using aliquots of concentrated $Ba(ClO_4)_2$ solutions prepared using $5 \cdot 10^{-6}$ M solutions of the free **G3c**. For **G3c**, at this concentration, 5 equivalents of Ba^{2+} were necessary to obtain a complete chelation.

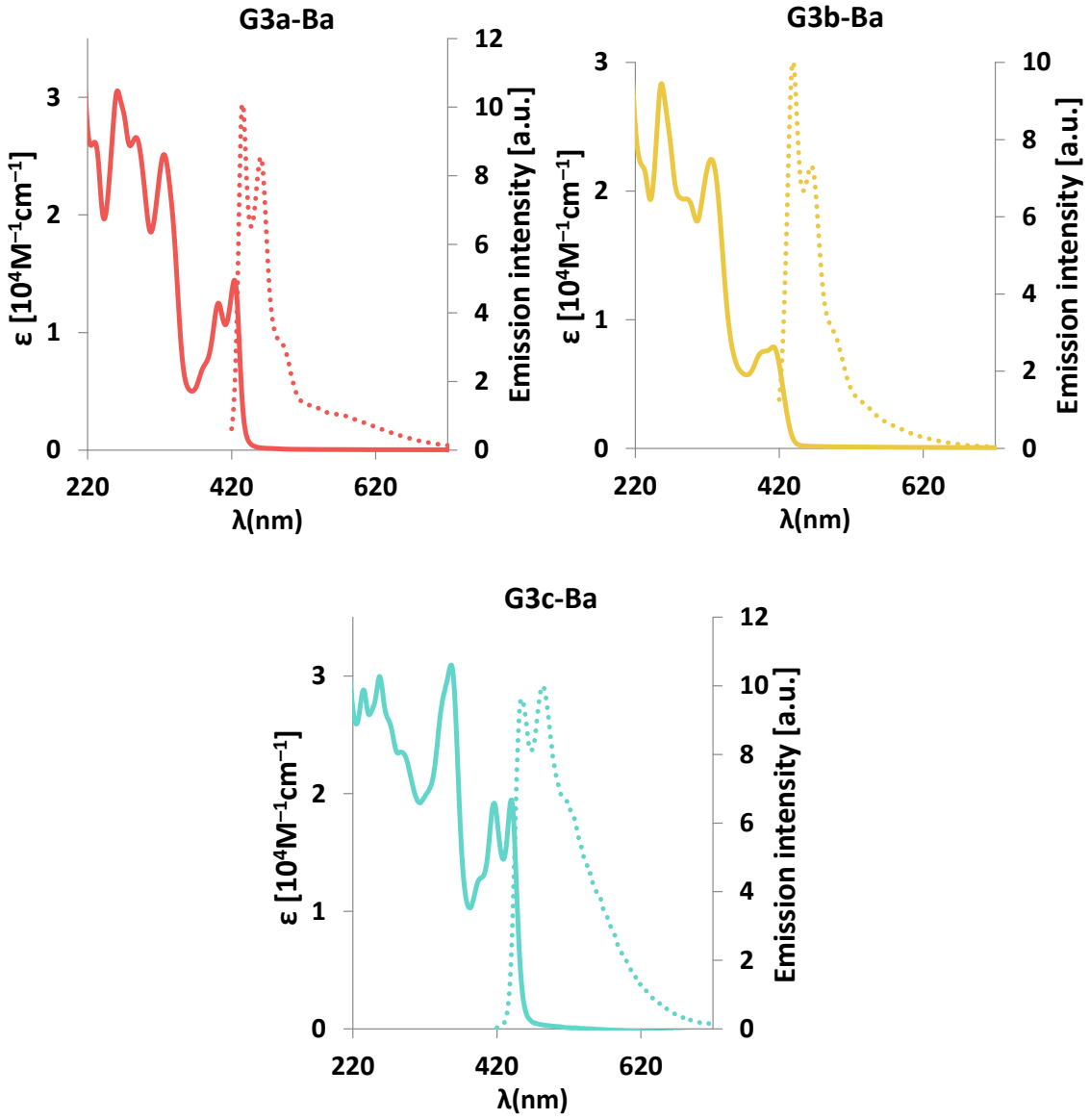

Figure 2.22. *Normalized absorption (solid lines) and emission (dotted lines) spectra of compounds* Ba^{2+}*-bound* ***G3a***, ***G3b***, *and* ***G3c*** in MeCN.

The emission spectra of the Ba^{2+}–chelated molecules show blue–shifted emission if compared to the free **FBI G3** sensors. Due to the slight hypsochromic shift observed in the less energetic transitions of the UV–vis spectra, eventually **FBI G3** chelated sensors present smaller Stokes–shift values compared to the free sensors. The bound sensors present structured emissions, as already observed for the parent **FBI G1** compound.[1] The Ba^{2+}–bound **FBI G3** sensors are less emissive and have slightly longer lifetimes than the free molecules.

Table 2.4. *Absorption and emission data of* ***I G3-Ba^{2+}*** *compounds in MeCN.*

	absorption	emission			Stokes shift [cm^{-1}]
	λ_{max} [nm] (ε [10^{4}M^{-1}cm^{-1}])[a]	λ_{max} [nm][b]	Φ [%] [b]	τ [ns][c,d]	
G3a–Ba	261 (2.86), 287 (2.58), 326 (2.43), 402 (1.23), 424 (1.42)	434 ,460	72.8	3.8	543
G3b–Ba	256 (2.99), 325 (2.49), 412 (0.86)	440, 462	71.5	3.8	1545
G3c–Ba	257 (2.41), 356 (2.54), 416 (1.72),440 (1.76)	461, 483	61.7	4.0	1035

MeCN solutions. a) Based on linear regression of the measured absorption of 6 concentrations in the range 10^{-4} M–10^{-6}M. b) Excitation at 368 nm. c) excitation EPLED 340 nm, TCSPC, 10 MHz, 5000 counts. d) All χ^2 values were between 1.0-1.2.

The UV–vis spectra of the titration experiments (**Figure 2.23**) show clear isosbestic points, which is consistent with the sensors forming supramolecular 1:1 assemblies (**FBI G3 → FBI G3–Ba^{2+}**). The most characteristic features observed along the titration are the slight hypo– and hypsochromic shift of the bands assigned to π → π* transitions of the annulated benzo[a]imidazo[5,1,2–cd]indolizine core, and the clear blue–shift of the band in the region 350–400 nm, tentatively assigned to π → π* transitions of the aromatic spacers. This hypsochromic shift upon interaction with Ba^{2+} could be explained by two effects: a loss of conjugation between the aromatic rings and the fluorescent indolizine core and a decrease in the participation of the lone-pair of the nitrogen in the conjugated system, now compromised in the formation of a dative bond to the Ba^{2+} centre.

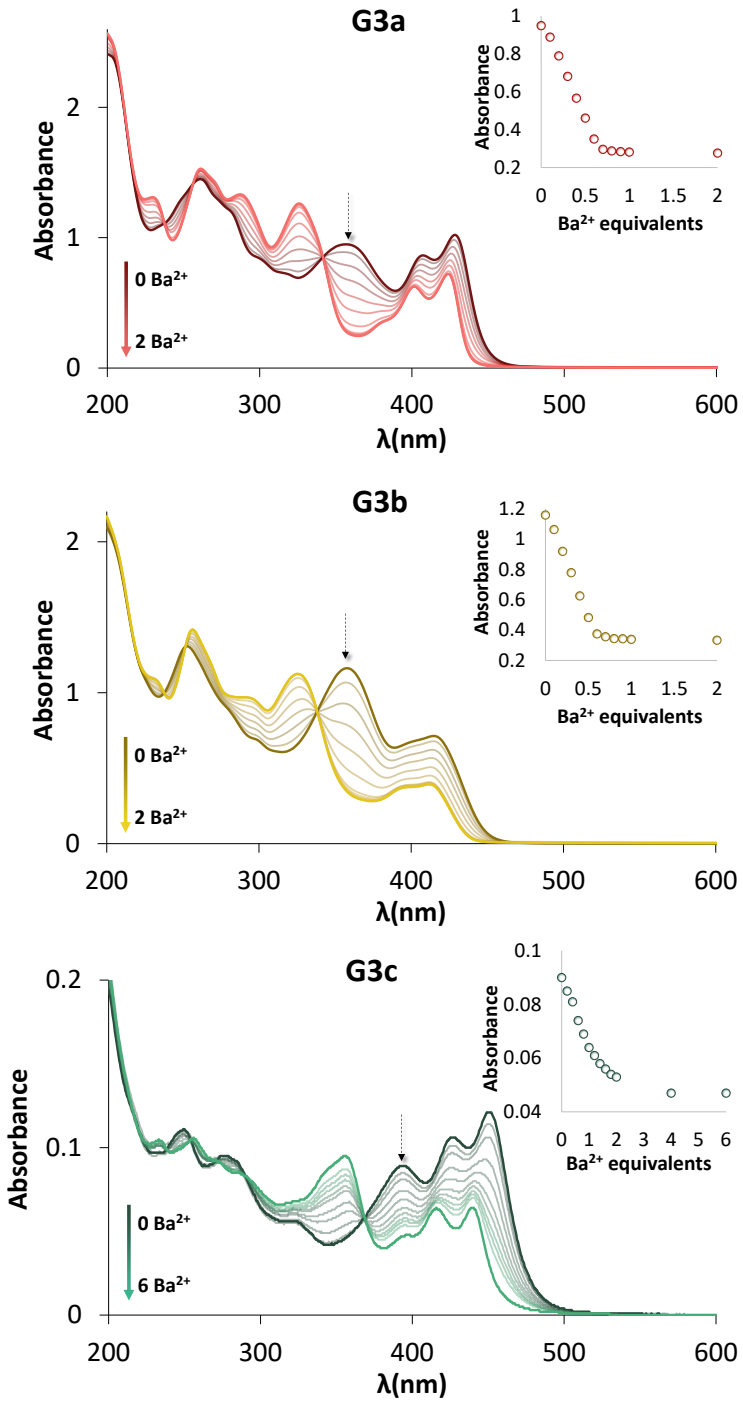

Figure 2.23. *UV–vis absorption spectra of titration experiments in MeCN at $5{\cdot}10^{-5}$ M for **G3a** and **G3b**, and at $5{\cdot}10^{-6}$ M for **G3c**. The inset plot shows the titration curve at the absorption maximum of the free compounds, indicated with an arrow.*

Both effects are in agreement with DFT calculations of the bound molecules, conducted by the group of Prof. F.P. Cossío (**Figure 2.24**). In the case of **G3a**, the interaction of the nitrogens lone pair can be observed, while in the case of **G3b** and **G3c**, with a pyridine in next to the rotating aryl unit, the nitrogen of the pyridine is interacting with the Ba^{2+}, thus breaking the planarity and losing the conjugation. The optimized structure for the

Ba^{2+} bound species reveals a large molecular torsion of the aza-crown ether with respect to the free compounds, so that a molecular cavity is formed when the metal cation creates a π-complex between the Ba^{2+} metallic centre and the rotating phenyl group.

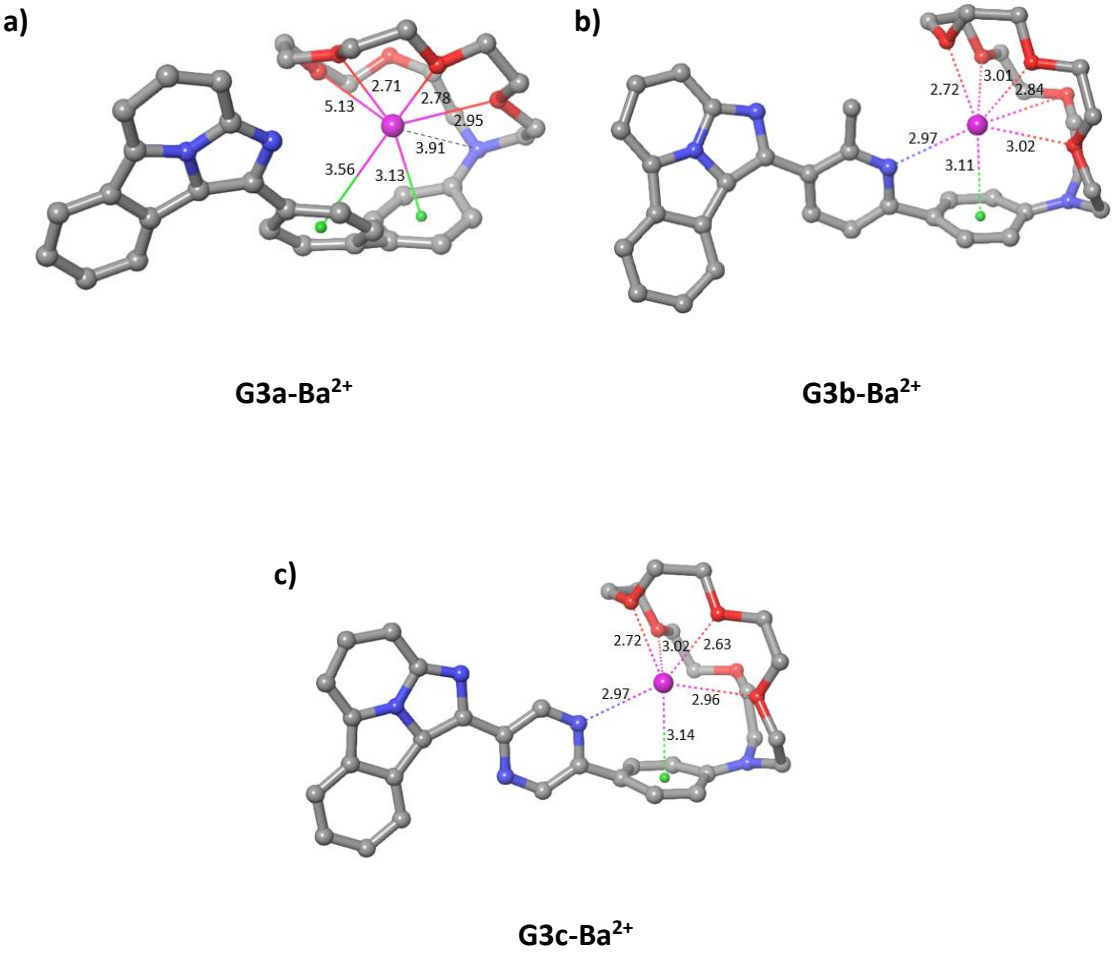

G3a-Ba^{2+} **G3b-Ba^{2+}**

G3c-Ba^{2+}

Figure 2.24. *DFT-derived gas-phase structures of a) Ba^{2+}-bound **G3a**, b) Ba^{2+}-bound **G3b** and c) Ba^{2+}-bound **G3c**. Bond distances are given in Å.*

The UV–Vis titration experiments data were attempted to fit with the software Bindfit.[19–21] Unfortunately, the data of **G3a** and **G3b** did not show a good fit when assuming a 1:1 Host:Guest ratio. In the case of **G3c**, a K_a value of $5.5 \cdot 10^5 \pm 0.9\%$ M^{-1} was obtained. In the inset plots in **Figure 2.23** shows the evolution of the absorption maxima of the free **G3** sensors against barium equivalents. **G3a** and **G3b** showed the complete chelation before reaching 1 equivalent of Ba^{2+}, which was attributed to impurities (probably residual silica) present in the samples.

Figure 2.25 show the Job's plots of **G3** compounds, showing a maximum at 0.5 molar fraction of Ba^{2+} in the three cases, indicating that **G3** compounds capture only one Ba^{2+} cation per molecule, a 1:1 stoichiometry, thus forming the complex **G3-Ba^{2+}**.

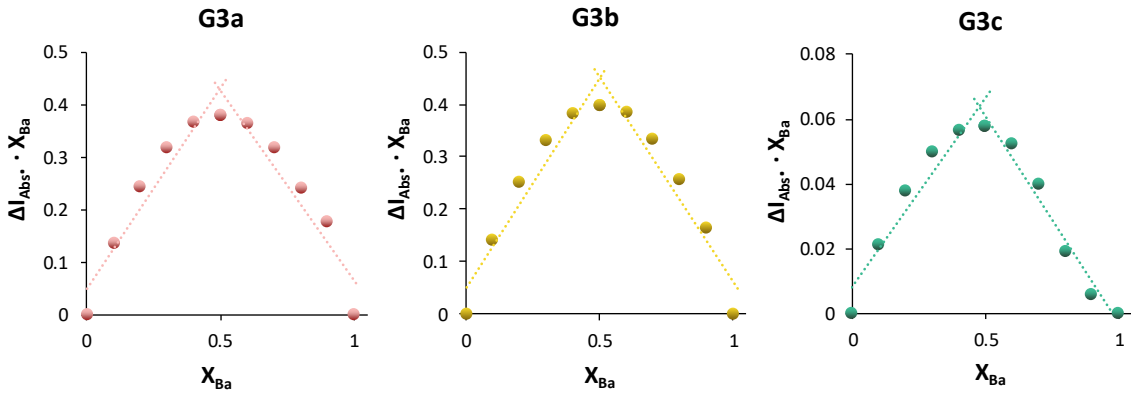

Figure 2.25. *Job's plot of the **G3** with $Ba(ClO_4)_2$ interaction, ΔI, variation in the measured emission; X_{Ba}, molar fraction of Ba^{2+}. Represented at 260, 250 and 420 nm wavelength for **G3a**, **G3b** and **G3c** respectively.*

2.2.3.3 Free vs Chelated emission

For comparative purposes, **Figure 2.26** shows the emission spectra of the free and Ba^{2+}–bound FBI sensors. In comparison with **FBI G1** they present much larger $\Delta\lambda$, being **G3a** the one presenting the largest bicolour character. As already inferred from the corresponding quantum yield values, they also show slightly decreased total emission upon chelation when measured at the isosbestic point deduced from UV-vis tritrations (at which both free and chelated sensors show identical absorptivity). Ideally, a bicolour indicator should have a large $\Delta\lambda$ and more intense emission upon chelation. Nevertheless, the relative intensity could be modulated by exciting the compounds at a wavelenght where the bound sensor presents better molar absorptivity than the free one (i.e. 320 nm). Therefore, one can conclude that, according to their photophysical properties, **G3a** would be a potentially good ratiometric sensor for Ba^{2+}.

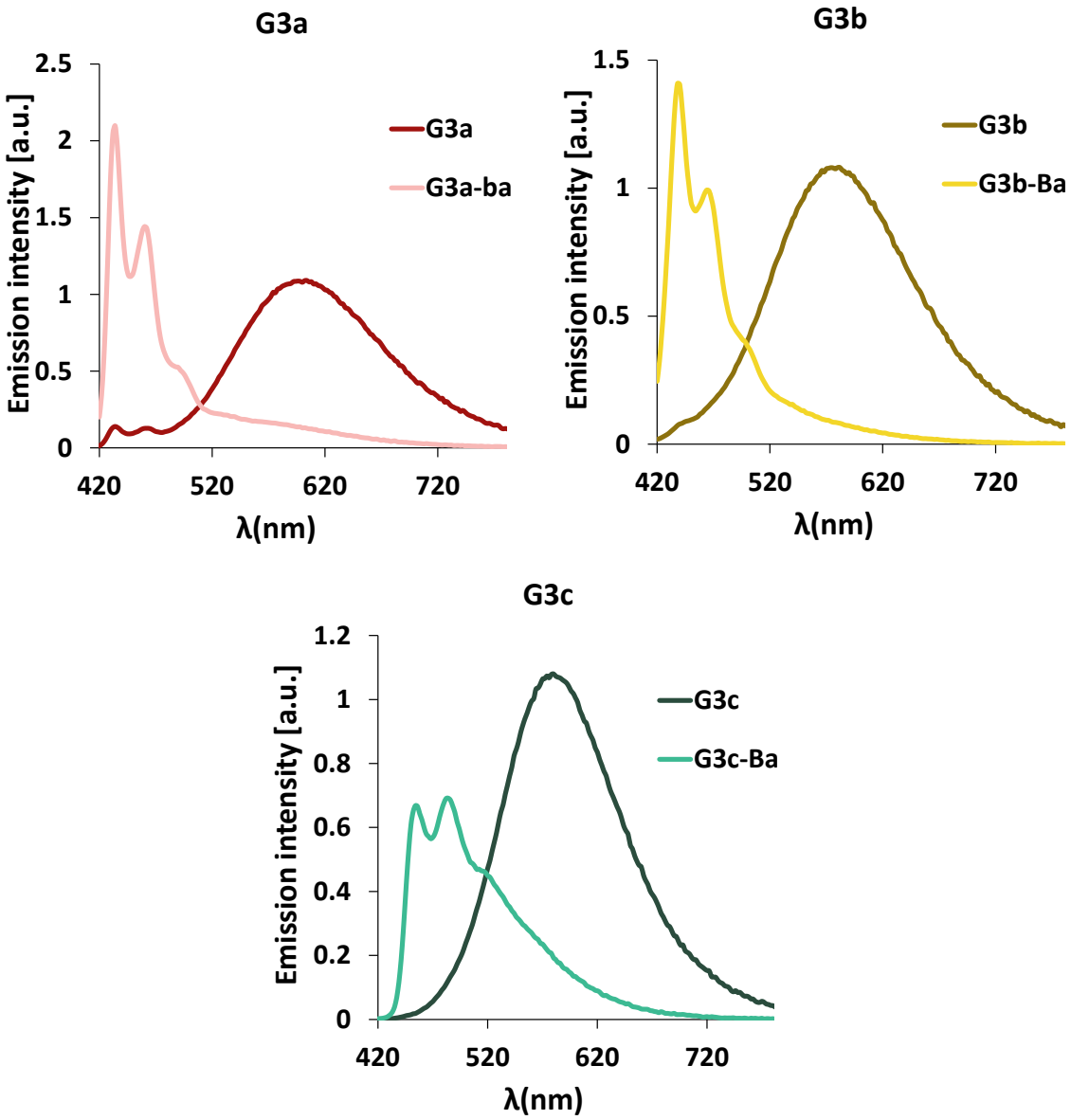

Figure 2.26. *Emission spectra of free and Ba^{2+}–bound **G3** compounds in MeCN at $5 \cdot 10^{-5}$ M.*

However, if the intention is to discriminate the emission signal of a single chelated molecule over the emission of any unchelated molecule, a wavelength measuring zone where the emission of the free sensor is null is needed. Therefore, even if **G3a** showed the biggest $\Delta\lambda$ upon chelation, the residual emission in the region 420–480 nm, due to decomposition or impurities, would hinder the experiment. Furthermore, **G3c** would be a more suitable candidate in this context.

2.2.3.4 Selectivity

To determine the selectivity of the sensors, the interaction of the **G3** compounds with other cation analytes was studied. To solutions of free **G3**, at $1 \cdot 10^{-5}$ M, 1 equivalent and

saturated solutions of the corresponding perchlorate salts in MeCN were added, and their absorption and emission spectra were measured (see supporting). The diagram in **Figure 2.27** shows the fluorescence response in the chelated region of the spectra after the addition of 1 equivalent of the corresponding salt. The three compounds behave similarly to the tested cations, responding with up to 15 fold increased emission to Ba^{2+} and Sr^{2+}. Gratifyingly Na^{+}, Mg^{2+} and K^{+} did not show any interaction with the proves. Therefore, we can conclude that the three sensors show good selectivity for Ba^{2+}, and Sr^{2+}, which is in agreement with the selectivity reported for **FBI.**

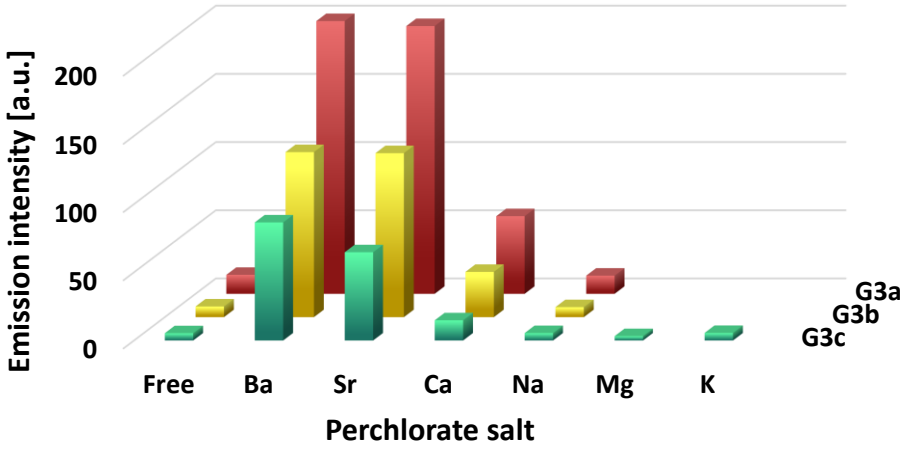

Figure 2.27. *Emission response of **G3** compounds with 1 equivalent of perchlorate salts in MeCN. Excited at 405 nm and emission measured at the maxima of the chelated specie.*

2.3 PROTOTYPE LIGANDS

2.3.1 Synthetic procedure

While the synthesis and purification of **G3** ligands was carried out, three different and simpler **L1**, **L2** and **L3** ligands were synthesized, illustrated in **Figure 2.28**.

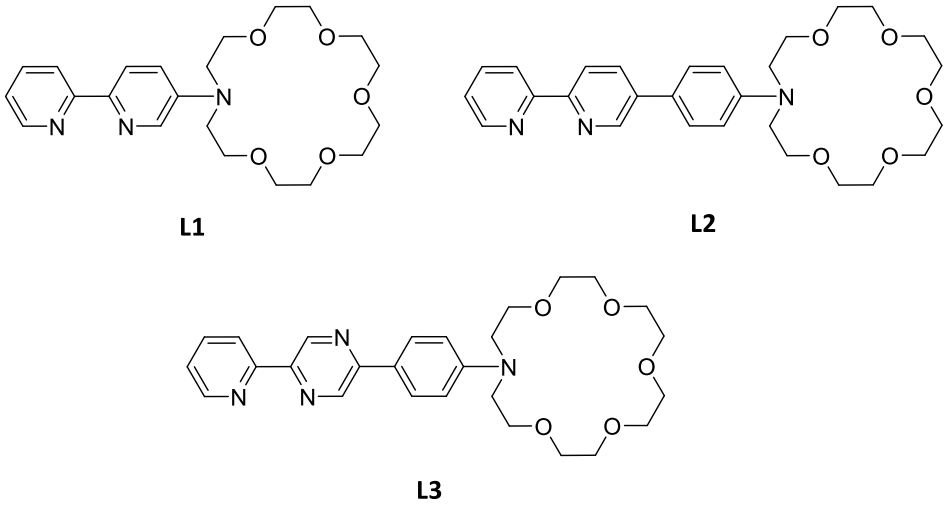

Figure 2.28. *Structure of* ***L1****,* ***L2*** *and* ***L3*** *ligands.*

In comparison to **G3–FBI** ligands, the lack of the cyclazine core made their synthesis and characterization simpler. Furthermore, their bipyridine–based structure was expected to simplify the coordination to iridium, compared to the C^N type ligands **G3a** and **G3b**. Therefore, these ligands were initially intended to be used as prototypes to optimize the synthesis and characterization of the complexes and their procedure for the eventual anchoring on a surface.

Each one was designed to be a **G3** analogous. **L1** ligand is the analog to the original **G1 FBI**; **L2** is analog to **G3a**, with the additional rotating phenyl group; and **L3** ligand is analog to **G3b** or **G3c**, with the nitrogen capable of interacting with the Ba^{2+}. Their synthetic route is described in the **Scheme 2.6**.

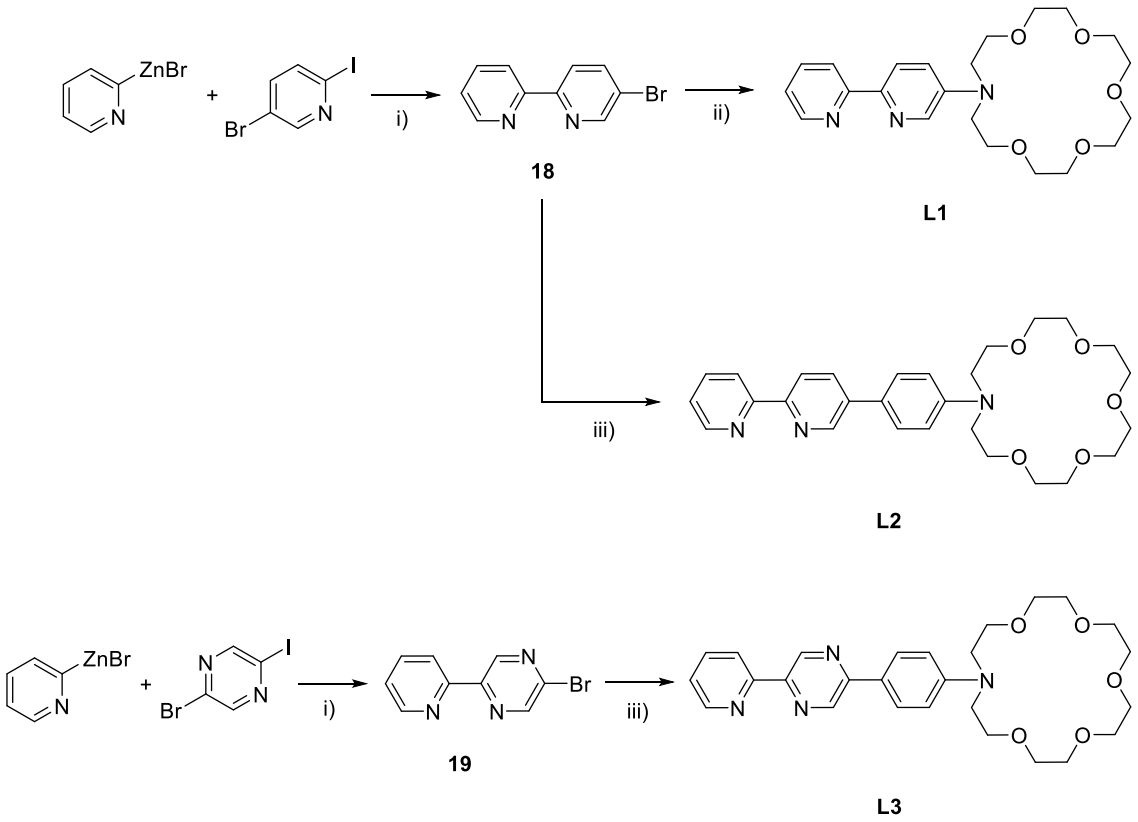

Scheme 2.6. *Synthetic pathway for the prototype ligands* ***L1***, ***L2*** *and* ***L3.*** *i) 1 mol % $Pd(PPh_3)_4$, THF. ii) 1–aza–18–crown–6 (1 equiv.), $Pd_2(dba)_3$, DavePhos, ^tBuONa, toluene, 115 °C. iii)* ***17****, $Pd(PPh_3)_4$, Na_2CO_3, DME/H_2O (3:1, v/v), 80 °C.*

The synthesis of **L1** was achieved in two steps. The synthesis of **18** was based on the procedure described by Rieke et al. where the coupling of two different pyridines was accomplished by cross-coupling using 1 mol% of $Pd(PPh_3)_4$ in THF.[22] In this manner, numerous asymmetric bipyridines were obtained at room temperature. The reaction was left for 48 h and at 70 °C instead of 24 h at room temperature described in the publication as the ^1H NMR spectrum of the aliquote at 24 h still showed the signals of the reactants. After this time, aq. EDTA/Na_2CO_3 was added to the mixture. The product was extracted with CH_2Cl_2, obtaining **18** in 85% yield as a white-brownish solid. ^1H NMR spectroscopy confirmed the identity of the resultant product (b in **Figure 2.29**).

For the incorporation of the aza–crown ether, in a second step, the conditions used for the synthesis of **6** and **12** were reproduced. **18** was coupled with 1-aza-18-crown-6-ether yielding **L1**, using toluene as a solvent, with $Pd_2(dba)_3$/DavePhos as catalyst and ^tBuONa as the base. The reaction crude was purified by column chromatography, using CH_2Cl_2 as eluent and increasing gradually the polarity with MeOH. The ^1H NMR of the product,

shown in **Figure 2.29** confirmed the structure and purity of compound **L1**. A similar spectroscopic pattern to the reactant was observed, but the signals corresponding to the pyridine next to the crown, assigned in the structure as 6 and 7, were up–field shifted compared to the reactant. The crowns' signals could also be observed around 3.70 ppm.

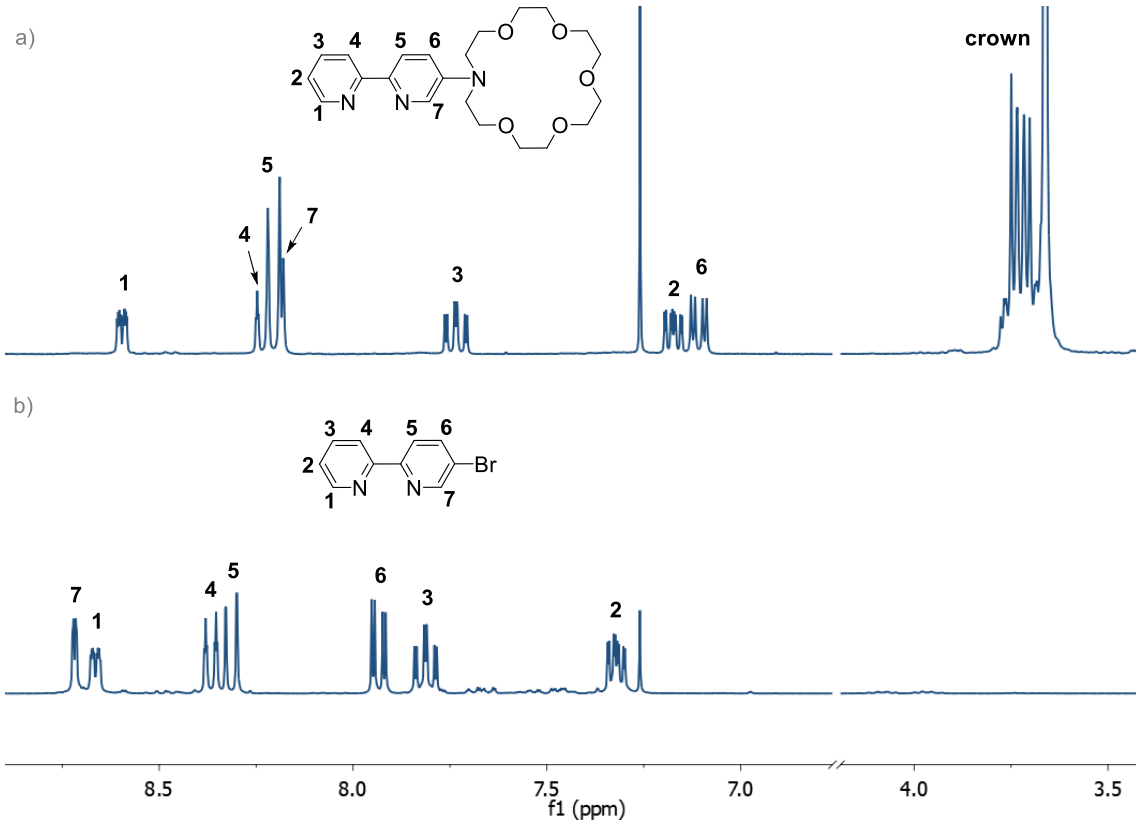

Figure 2.29. *^{1}H NMR spectrum of a) L1 and b) **18**, with their respective assigned structures ($CDCl_3$, 300 MHz).*

For the synthesis of **L2**, the same intermediate **18** was coupled with the pinacol protected and crown containing synthon **16**, that was previously synthesized as described in the synthetic procedure for **G3c**. Under standard conditions, **18** and **16** were reacted in a solvent mixture of DME/H_2O, catalyzed by $Pd(PPh_3)_4$ and using Na_2CO_3 as the base, to obtain **L2**. The reactioncrude was purified directly by column chromatography, using CH_2Cl_2 as eluent and gradually increasing polarity with MeOH.

The ^{1}H NMR spectrum of the product (**Figure 2.30**) showed a similar pattern compared to the spectrum of the bipyridine reactant, with slight differences in the shift of proton 11 and the completely overlapped signals of protons 4 and 5, as assigned in the

structure. As expected, an the AA'BB' spin system assigned to the phenyl unit bond to the crown and the aza–crown ethers aliphatic signals could be observed.

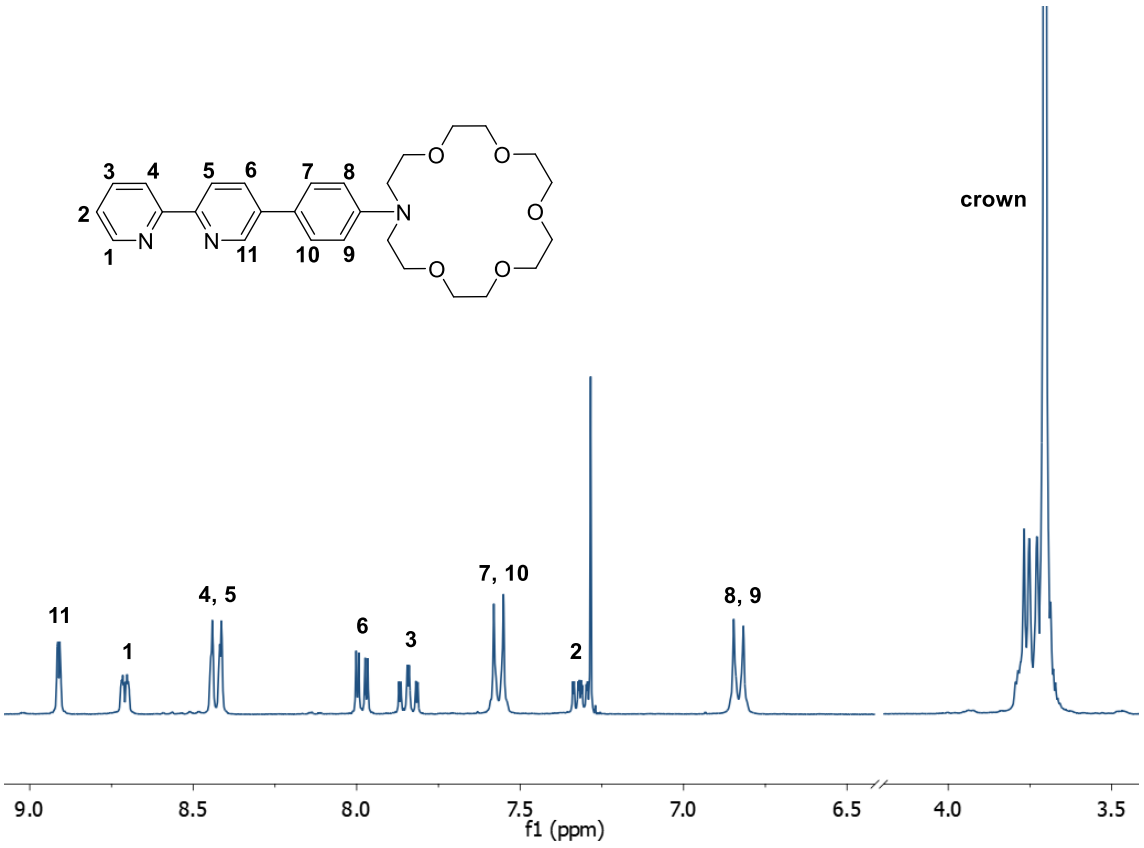

Figure 2.30. *^{1}H NMR spectrum of **L2** and its completely assigned structure ($CDCl_3$, 300 MHz).*

The last designed model ligand **L3**, was synthesized analogously to **L2**. First the asymmetric bipyridine **19** was synthesized by reacting 2–bromo–5–iodopyrazine with 2–pyridinylzinc bromide, in THF and catalyzed by $Pd(PPh_3)_4$. When the reaction finished, the product was directly purified by column chromatography. The ^{1}H NMR spectrum of purified **19** (a in **Figure 2.31**) showed two singlets corresponding to the pyrazine and the pattern of two doublets (one of them overlapped with the pyrazine) and two triplets of the pyridine.

The coupling between **19** and **16** was proceeded in a solvent mixture of toluene/H_2O/EtOH (5:5:1, v/v/v), with $Pd(PPh_3)_4$ and Na_2CO_3. The reaction was refluxed at 80 °C for 48 h, the formation of **L3** could be noticed by the progressive green emission of the reaction mixture under UV irradiation. The purification step of the reaction crude

was carried out by column chromatography, simmilarly as described before for compound **L2**, which produced **L3** as a yellowish solid in a 61% yield.

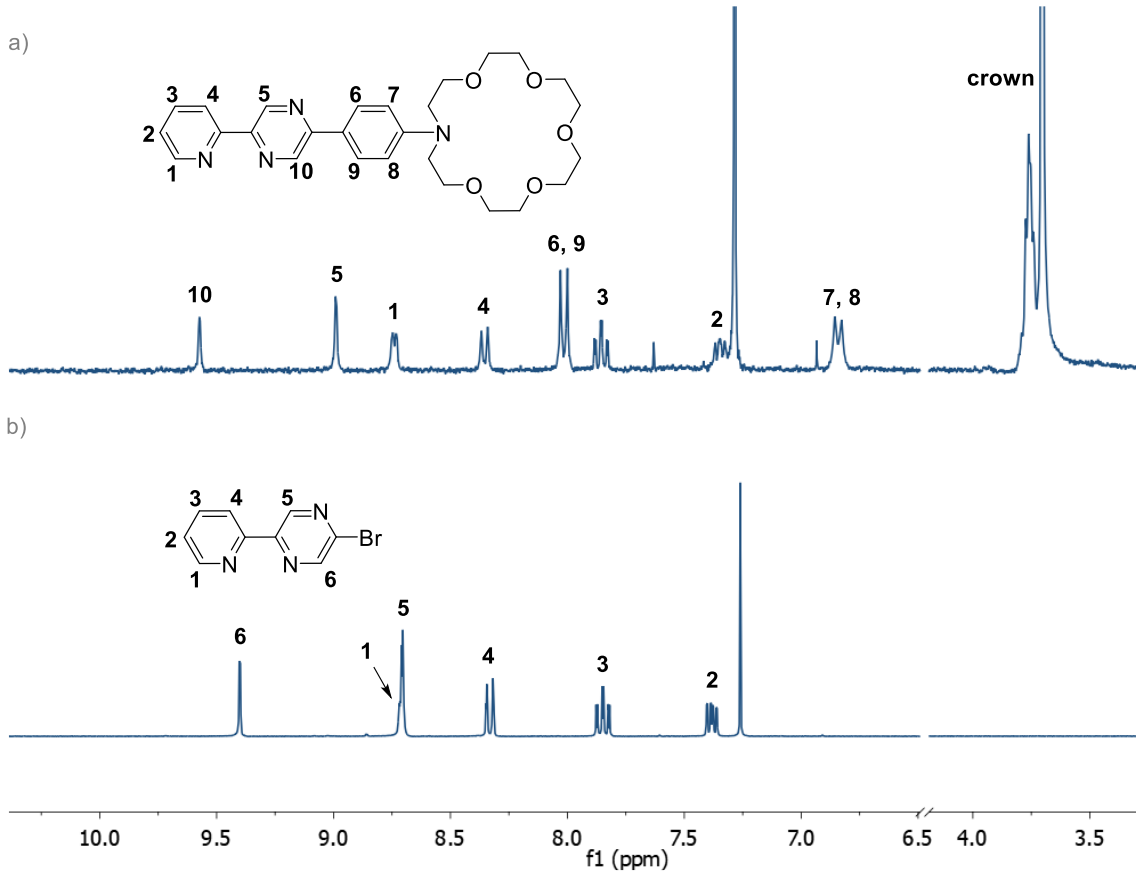

Figure 2.31. *^{1}H NMR spectrum of a)* ***L3*** *and b)* ***19****, with their respective assigned structures ($CDCl_3$, 300 MHz).*

The identity and purity of the three compounds **L1**, **L2** and **L3** was further by ^{13}C NMR, COSY, HSQC, and HR–MS spectroscopy.

2.3.2 Photophysical properties

2.3.2.1 Free L ligands

The photophysical and photochemical properties of **L1**, **L2** and **L3** were examined. **Figure 2.32** shows the absorption and normalized emission spectra of the ligands in MeCN. The absorption spectra present bands in the UV region associated to π → π* transitions of the aromatic units. **L1** and **L2** show a single band between 300-400 nm. **L2** maxima is red-shifted compared to **L1**, due to the additional phenyl ring between the bipyridine unit and the crown. **L3** absorption spectrum shows three bands between 250 and 450

nm. The three ligands emit as a single band between 400 and 530 nm. As espected, the emission of the **L1** is blue-shifted compared to the ligands with more extended conjugation. The most relevant data is summarized in **Table 2.5.** Absorption and emission data of **L1-L3** compounds in MeCN.

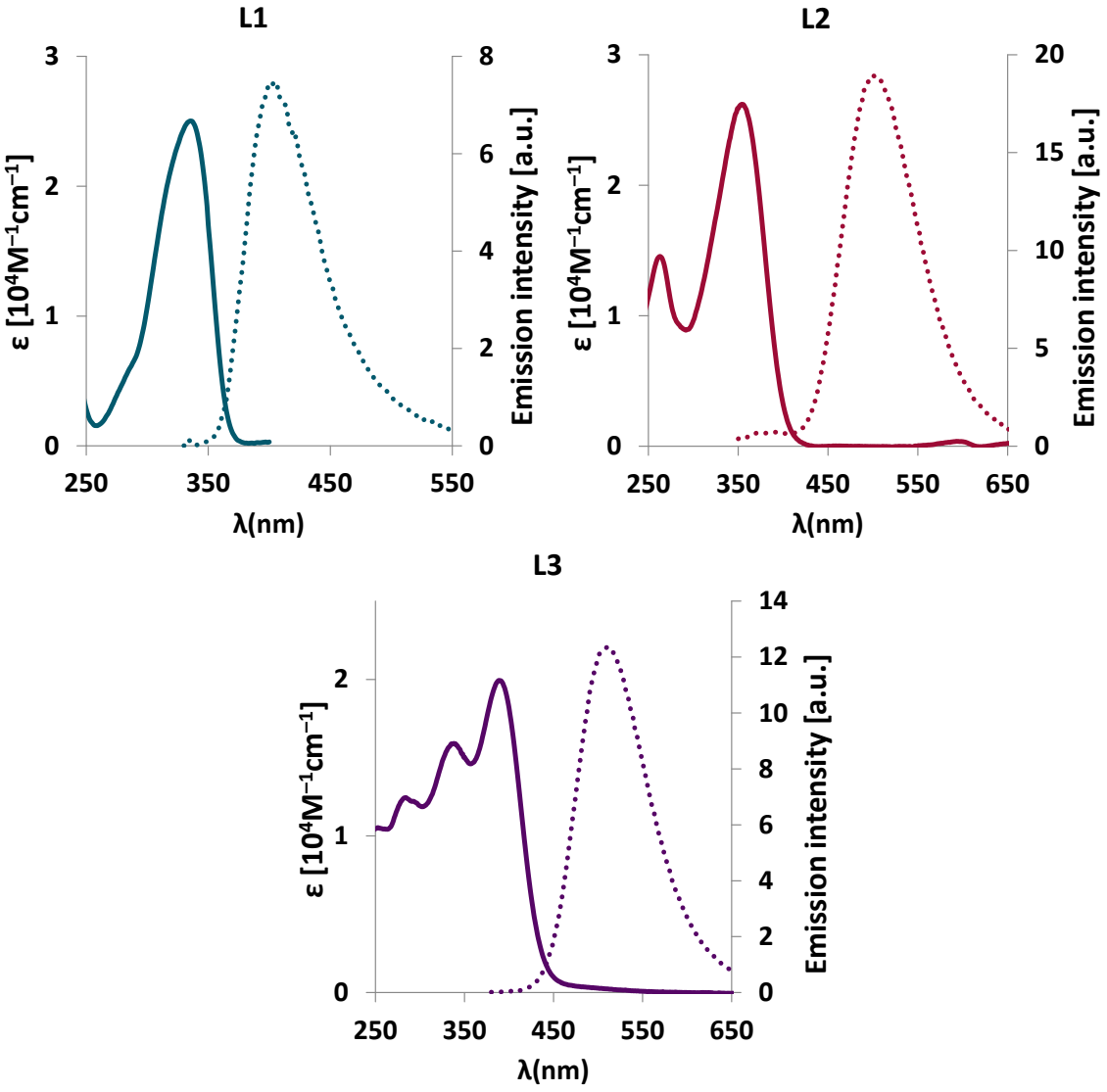

Figure 2.32. *Absorption (left) and normalized emission (right) spectra of the free ligands **L1**, **L2** and **L3**.*

2.3.2.2 Ba^{2+} chelation

Titration studies were performed for the three ligands in MeCN and followed by UV-vis spectroscopy (**Figure 2.33**). The best concentrations to obtain the binding constant were optimized starting from solutions of the free ligands at $5 \cdot 10^{-6}$ M and adding aliquots of concentrated solutions of $Ba(ClO_4)_2$ prepared in solutions of the ligand at the selected

concentration (to avoid dilution of the total concentration of the sensor during the titration).

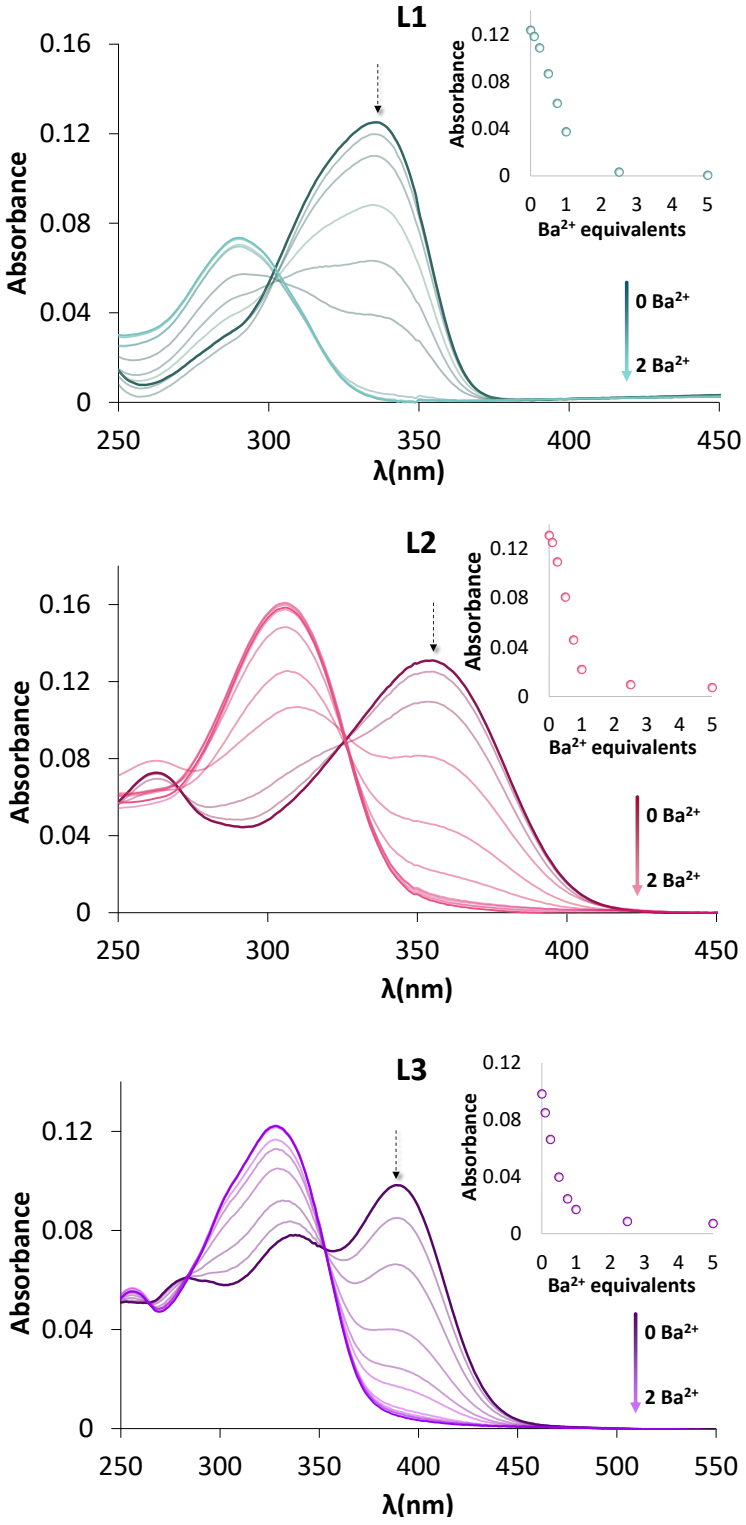

Figure 2.33. *UV–vis absorption spectra of titration experiments in MeCN at $5 \cdot 10^{-6}$ M.*

The most characteristic aspect presented in the UV-vis spectra is the hypsochromic shift of the band at longer wavelengths. This could be explained by loss of conjugation in the ligands, due to the lower participation of the nitrogens lone pair in the crown with the rest of the aromatic moiety. The isosbestic points present in the three ligands spectra together with the Job's plots (**Figure 2.34**), are indicative of the 1:1 stoichiometry of the ligands and the Ba^{2+} cation.

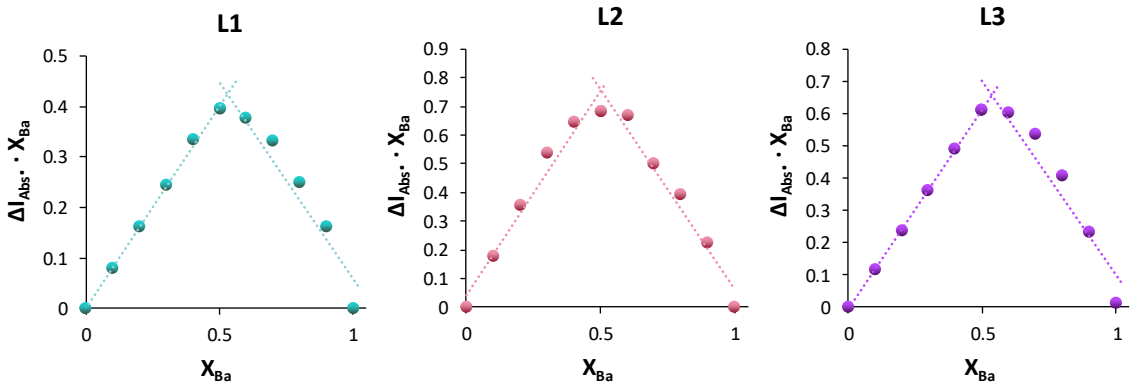

Figure 2.34. *Job's plot of the **L** ligands with $Ba(ClO_4)_2$ interaction, ΔI, variation in the measured emission; X_{Ba}, molar fraction of Ba^{2+}. Represented at 260, 304 and 335 nm wavelength for **L1**, **L2** and **L3** respectively. Experiments in MeCN at $1 \cdot 10^{-4}$ M.*

Table 2.5. *Absorption and emission data of **L1**-**L3** compounds in MeCN.*

	K_{ass} ± error %	absorption	emission		Stokes shift [cm^{-1}]
		λ_{max} [nm] (ε [$10^4 M^{-1}cm^{-1}$])[a]	λ_{max} [nm][b]	τ [ns] (contribution)[c,d]	
L1	$3.97 \cdot 10^5$ ± 4%	235 (0.66), 335 (2.50)	404	2.7	5098
L1–Ba		248 (0.58), 290 (1.46)	386	1.23 (76%) 2.68 (24%)	8576
L2	$5.05 \cdot 10^6$ ± 2%	263 (1.45), 355 (2.62)	498	2.8	8089
L2–Ba		306 (3.17)	478	2.46	11759
L3	$1.23 \cdot 10^6$ ± 2%	284 (1.25), 338 (1.59), 389 (1.99)	526	3.5	6695
L3–Ba		255 (1.12), 328 (2.45)	500	3.3	10488

MeCN solutions. a) Based on the measured absorption of $2.5 \cdot 1^{-5}$ M solutions. b) Excitation at corresponding isosbestic point. c) excitation EPLED 340 nm, TCSPC, 20 MHz, 10000 counts. d) All χ^2 values were between 1.0-1.2.

Emission of the ligands was also studied for comparative purposes, shown in **Figure 2.35**. The three compounds show a sharp single emission and suffer a slight hypsochormic

shift upon chelation with Ba^{2+}, attributed to the loss of conjugation. However, this shift is not enough to use them as ratiometric sensors as isolated molecules.

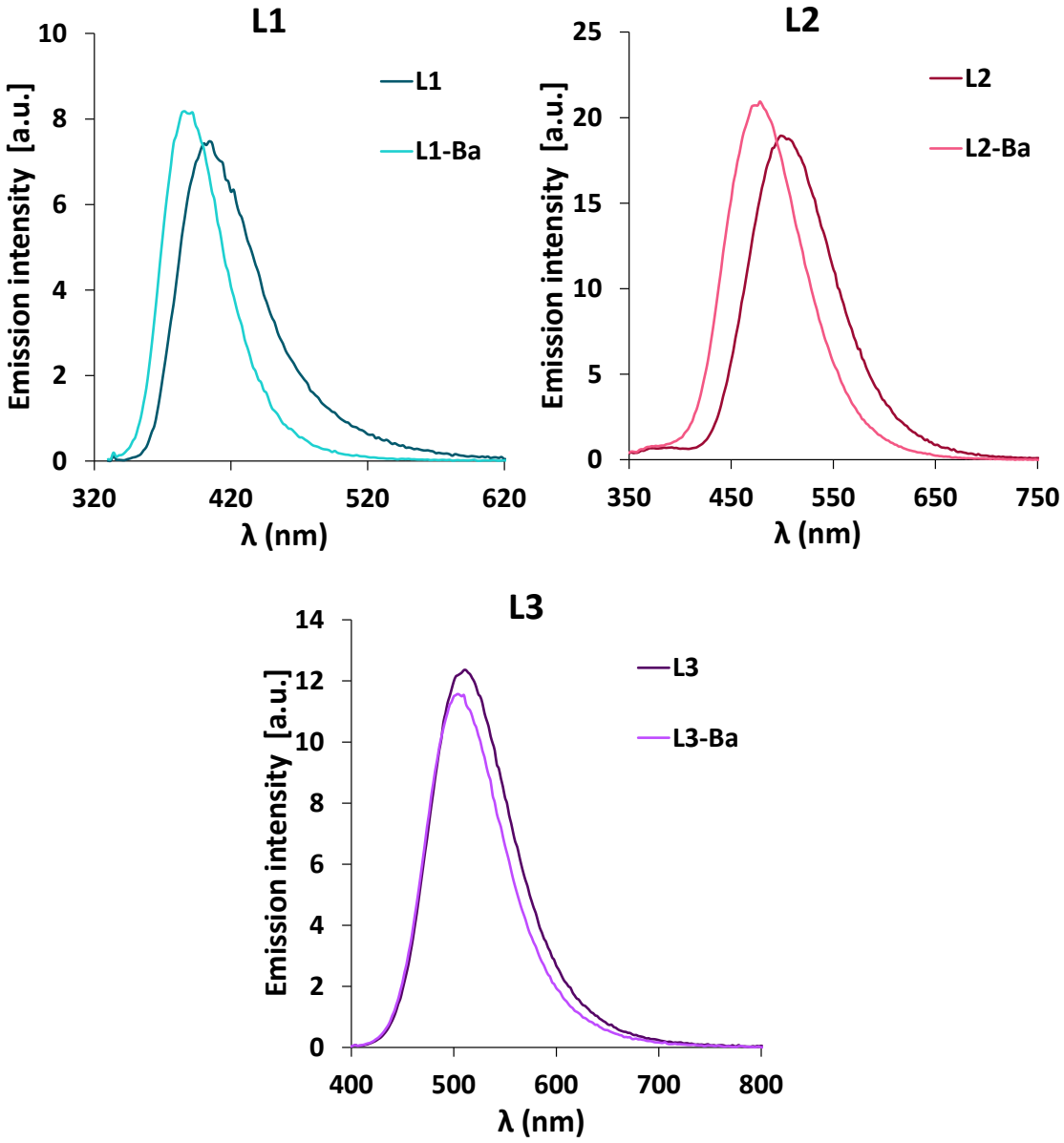

Figure 2.35. *Emission spectra of ligands **L1**-**L3**, in their free and Ba^{2+}-chelated form, excited at corresponding isosbestic point.*

2.4 References

1 I. Rivilla, B. Aparicio, J. M. Bueno, D. Casanova, C. Tonnelé, Z. Freixa, P. Herrero, C. Rogero, J. I. Miranda, R. M. Martínez-Ojeda, F. Monrabal, B. Olave, T. Schäfer, P. Artal, D. Nygren, F. P. Cossío and J. J. Gómez-Cadenas, *Nature*, 2020, **583**, 48–54.

2 L. Tian, S. Gao, R. Wang, Y. Li, C. Tang, L. Shi and J. Fu, *Chemical Communications*, 2019, **55**, 5347–5350.

3 X. X. Zhang and S. L. Buchwald, *Journal of Organic Chemistry*, 2000, **65**, 8027–8031.

4 B. Das, K. Venkateswarlu, A. Majhi, V. Siddaiah and K. R. Reddy, *Journal of Molecular Catalysis A: Chemical*, 2007, **267**, 30–33.

5 L. C. Campeau, S. Rousseaux and K. Fagnou, *Journal of the American Chemical Society*, 2005, **127**, 18020–18021.

6 X. A. F. Cook, A. de Gombert, J. McKnight, L. R. E. Pantaine and M. C. Willis, *Angewandte Chemie - International Edition*, 2021, 60, 11068–11091.

7 A. P. Kourounakis, C. Charitos, E. A. Rekka and P. N. Kourounakis, *Journal of Medicinal Chemistry*, 2008, **51**, 5861–5865.

8 A. J. Stasyuk, M. Banasiewicz, B. Ventura, M. K. Cyrański and D. T. Gryko, *New Journal of Chemistry*, 2014, **38**, 189–197.

9 H. Wang, C. Chen, Z. Huang, L. Yao, B. Li and J. Peng, *Synthesis (Germany)*, 2015, **47**, 2457–2466.

10 P. V Sowmya, B. Poojary, B. C. Revanasiddappa, M. Vijayakumar, P. Nikil and V. Kumar, *Research on Chemical Intermediates*, 2017, **43**, 7399–7422.

11 V. Bavetsias, R. M. Lanigan, G. F. Ruda, B. Atrash, M. G. McLaughlin, A. Tumber, N. Y. Mok, Y. V. Le Bihan, S. Dempster, K. J. Boxall, F. Jeganathan, S. B. Hatch, P. Savitsky, S. Velupillai, T. Krojer, K. S. England, J. Sejberg, C. Thai, A. Donovan, A. Pal, G. Scozzafava, J. M. Bennett, A. Kawamura, C. Johansson, A. Szykowska, C. Gileadi, N. A. Burgess-Brown, F. Von Delft, U. Oppermann, Z. Walters, J. Shipley, F. I. Raynaud, S. M. Westaway, R. K. Prinjha, O. Fedorov, R. Burke, C. J. Schofield, I. M. Westwood, C. Bountra, S. Müller, R. L. M. Van Montfort, P. E. Brennan and J. Blagg, *Journal of Medicinal Chemistry*, 2016, **59**, 1388–1409.

12 2015.

13 S. M. M. Lopes, J. S. Novais, D. C. S. Costa, H. C. Castro, A. M. S. Figueiredo, V. F. Ferreira, T. M. V. D. Pinho e Melo and F. de C. da Silva, *European Journal of Medicinal Chemistry*, 2018, **143**, 1010–1020.

14 D. Blakemore, in *RSC Drug Discovery Series*, Royal Society of Chemistry, 2016, vol. 2016-Janua, pp. 1–69.

15 R. Semwal, A. Joshi, R. Kumar and S. Adimurthy, *New Journal of Chemistry*, 2020, **44**, 20530–20534.

16 M. Aginagalde, Y. Vara, A. Arrieta, R. Zangi, V. L. Cebolla, A. Delgado-Camón and F. P. Cossío, *Journal of Organic Chemistry*, 2010, **75**, 2776–2784.

17 A. J. Stasyuk, M. Banasiewicz, B. Ventura, M. K. Cyrański and D. T. Gryko, *New Journal of Chemistry*, 2014, **38**, 189–197.

18 R. V. Prajapati, V. D. Prajapati, V. B. Purohit, J. R. Avalani, R. D. Kamani, N. H. Sapariya, S. C. Karad and D. K. Raval, *ChemistrySelect*, 2022, **7**, e202201436.

19 D. Brynn Hibbert and P. Thordarson, *Chemical Communications*, 2016, **52**, 12792–12805.

20 Supramolecular.org - Binding Constant Calculators | Supramolecular, http://supramolecular.org/, (accessed 19 December 2022).

21 P. Thordarson, *Chemical Society Reviews*, 2011, **40**, 1305–1323.

22 S. H. Kim and R. D. Rieke, *Tetrahedron Letters*, 2009, **50**, 5329–5331.

Chapter 3

Iridium complexes with G3 FBI and bipyridine based ligands

In this chapter, the synthetic attempts to coordinate **G3 FBI** and **L** ligands to simple Ir(III) complexes will be described. The photophysical characterization of the obtained complexes will be discussed, together with their adequacy as Ba^{2+} sensors.

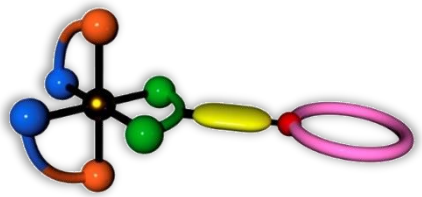

3.1 INTRODUCTION

In the previous chapter, the synthesized **G3** family and the prototype ligands were presented. These ligands were intended to coordinate to iridium(III) centers and study the barium(II) sensing behavior of the complexes compared to that of the free ligands. The novel complexes synthesis and their photophysical performance are described in this chapter.

3.2 SYNTHESIS

Six ligands were synthesized, as exposed in Chapter 2, three **G3** and three bipyridine-based ligands. Two of the **G3** ligands (**G3a** and **G3b**) are potential monoanionic C^N type chelators, while the **G3c** and prototype ligands are neutral N^N donors.

As the conditions for the coordination of C^N type ligands (through cyclometalation) and N^N ligands (by direct ligand substitution) are very different, they will be discussed separately.

1.1.1. Synthesis of neutral C^N iridium(III)-derivatives.

As described in the ligands synthesis section, the yields for **G3** compounds were low. Therefore, the cyclometalation reaction was initially attempted with the intermediates of their predecessor **G1 FBI**: the intermediate **I1** (a bromine derivative) and **I2** with the appended 1-aza-18-crown-6, depicted in **Scheme 3.1**, which were synthesized by the group of Prof. F.P. Cossío.

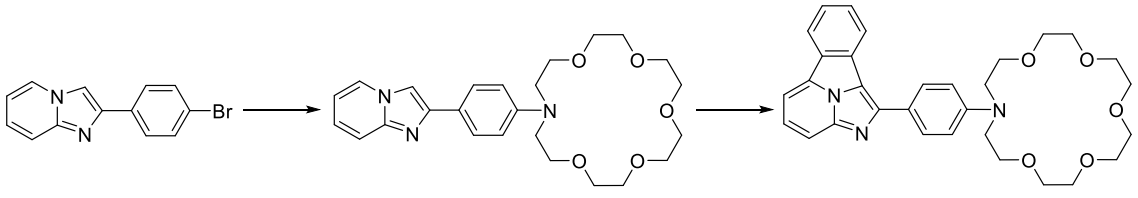

Scheme 3.1. *Intermediates in the synthesis of* ***FBI*** *used for the optimization of the cyclometalation reaction.*

The chloride-bridge iridium dimer $[Ir(ppy)_2(\mu\text{-}Cl)]_2$ was used as the metal precursor for the synthesis of tris-cyclometalated complexes. This dimer was first prepared following the Nonoyama method, shown in **Scheme 3.2**, by reacting $IrCl_3{\cdot}3H_2O$ with 2.5

equivalents of phenylpyridine in a mixture of 2-ethoxyethanol/H_2O (3:1, v/v).[1] The ^1H NMR of the product agreed with the spectroscopic information reported in the literature, and the yields upon repetition were all above 50%.

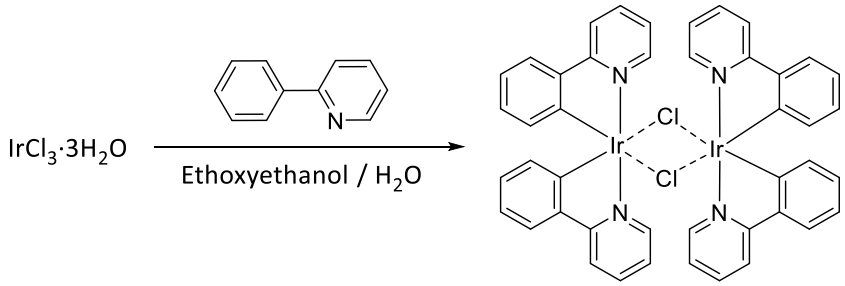

Scheme 3.2. *Synthesis of iridium dimer $[Ir(ppy)_2(\mu\text{-}Cl)]_2$*

The first attempts to introduce compounds **I1** and **I2** as third ligands were based on the most frequently applied route for the synthesis of meridional heteroleptic cyclometalated iridium(III) compounds, described by Thomson et al.[2] The dimeric precursor is reacted with an excess of cyclometalating ligand using glycerol or 2-ethoxyethanol as the solvent and K_2CO_3 as the base. In our case, the reaction was attempted in 2-ethoxyethanol and heated overnight under nitrogen at 110 °C. In both cases, the ^1H NMR spectrum of the crude did not reveal any signal that could be assigned to the corresponding cyclometalated complexes, but only signals related to the unreacted ligand and decomposed precursor were distinguished.

Given these results, it was decided to test an alternative synthetic procedure to obtain tris-cyclometalated heteroleptic Ir(III) complexes described in the literature.[3] In this paper, Crutchley et al. reported a two-step procedure, where first a silver salt is added as a halide abstractor forming a bis-solvated iridium intermediate. After removal of the precipitated AgCl salt from the reaction media, an excess of the ancillary ligand is added (2 equivalents per iridium metal center). Initially, they used 2-ethoxyethanol as solvent at elevated temperatures, obtaining the desired products with low yields. In a modified procedure, they changed the solvent to acetone and added Et_3N to facilitate the deprotonation of the 2-phenylpyridine ligand, which resulted in a yield improvement even at room temperature.

The cyclometalation of compound **I1** was attempted following this experimental procedure, resumed in **Scheme 3.3**. AgOTf was added to a suspension of iridium dimer in acetone. The mixture was stirred at 50 °C and after 12 h was filtered with a cannula. The filtrate was evaporated, and the ligand, acetone and Et_3N were added to the residue, under nitrogen. The mixture was refluxed under nitrogen for 12 h. The solvent was removed by rotary evaporator and the compound was purified by column chromatography in CH_2Cl_2 to obtain the desired complex in a moderate yield (20%). The formation of **C1** was confirmed by ^1H NMR spectroscopy.

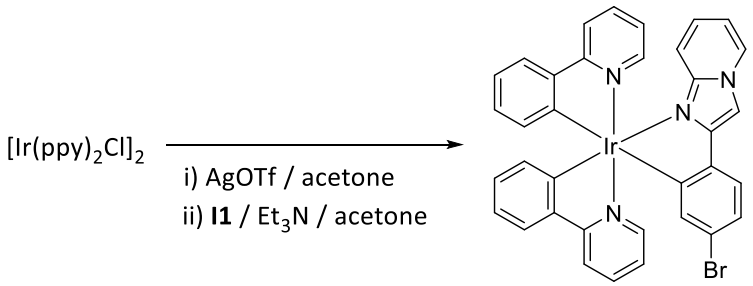

C1

Scheme 3.3. *Cyclometalation reaction of the iridium chloride-bridged dimer with **I1** ligand.*

Despite some signals overlapping, the ^1H NMR of the pure **C1** complex showed a spectroscopic pattern compatible with the expected cyclometalated product, compared with the ^1H NMR of **I1** in **Figure 3.36.** ^{1H} NMR spectrum of a) **I1** and b) iridium complex **C1** and with their partially assigned structures (CDCl3, 300 MHz). As expected, the number of signals reflects the C_1 symmetry of the compound. Concerning the phenylpyridyl fragment, the most characteristic signals of the spectra are two doublets at 6.10 and 6.47 ppm that correspond to the protons H1 and H1', and the other two doublets at 8.00 and 8.19 ppm, assigned to the protons next to the coordinated nitrogen H8 and H8'. The effective coordination of **I1** can be inferred from the shift in the singlet signal of H13 from 7.82 ppm to 7.69 ppm. Besides, the AA'BB' spins system present in the unbound **I1** (H14–H17) is not present in the spectrum of the complex, which is solid evidence that cyclometalation occurred at **C1**.

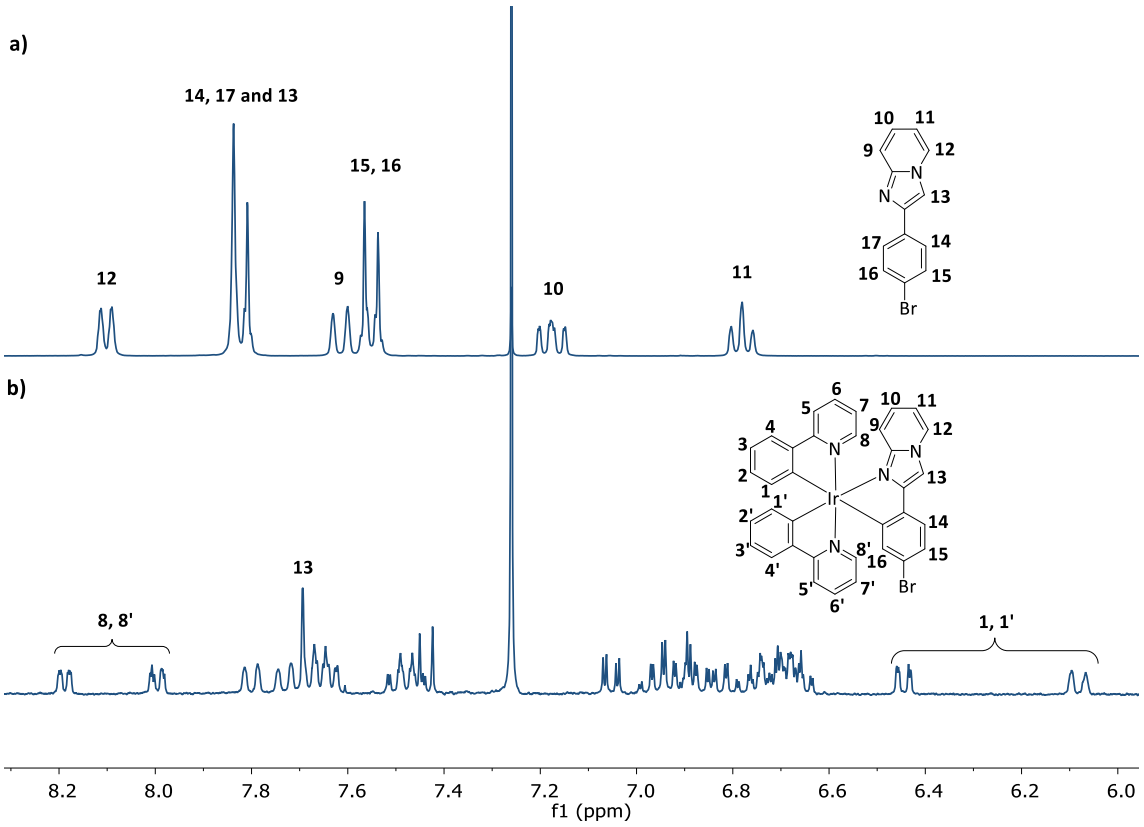

Figure 3.36. *^{1}H NMR spectrum of a) **I1** and b) iridium complex **C1** and with their partially assigned structures ($CDCl_3$, 300 MHz).*

Initially, the cyclometalation of **I2** was attempted using the same methodology. The reaction residue obtained after evaporation of the solvent at the end of the reaction was washed with EtOH and H_2O to remove the excess of ligand and Et_3N, and the residue was analyzed by ^{1}H NMR spectroscopy. The ^{1}H NMR spectrum showed two new sets of signals, which did not fit the spectroscopic pattern of the iridium precursor nor the one of the free ligand **I2** (**Figure 3.37**). One of them was compatible with the expected cyclometalated product **C2** due to some similarity to the spectrum of **C1** (indicated with arrows). Additionally, the presence of the characteristic signal of the aza-crown ether indicated that the **I2** ligand was present as a somehow coordinated ligand in the mixture. The remaining group of signals was tentatively assigned to a disolvated form of the iridium $[Ir(ppy)_2(solv)_2]^+$, because of the resemblance to the iridium dimer and the intermediate signals (indicated with asterisks). The presence of this iridium species was taken as an indication that the reaction did not reach the full conversion.

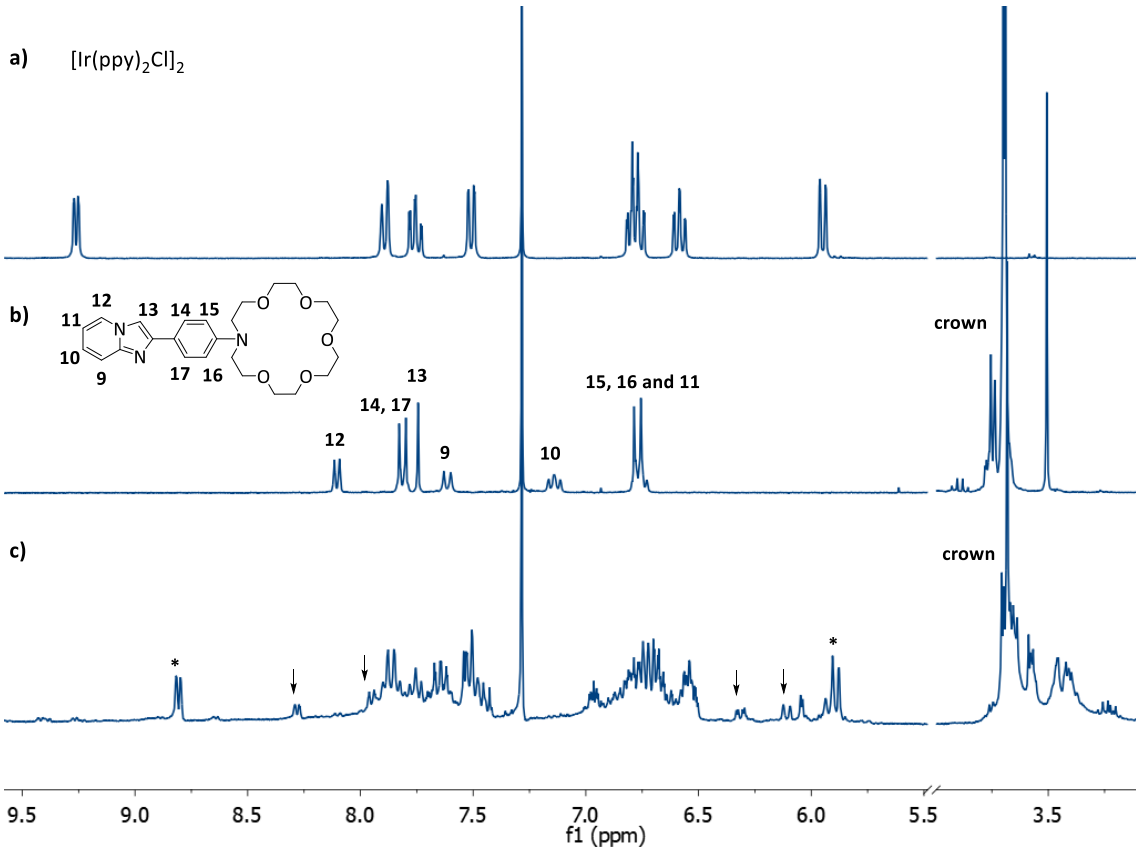

Figure 3.37. *Comparison of the ^{1}H NMR spectrum of a) iridium precursor, b) ligand* **l2** *and c) residue of the synthesis of* ***C2****. The asterisks mark the peaks assigned to the disolvated iridium species and the arrows indicate the peaks assigned to* ***C2*** *($CDCl_3$, 300 MHz).*

Several washings and crystallizations were assayed to remove the unwanted disolvated iridium compound, followed by a chromatographic column using CH_2Cl_2 as starting eluent and changing polarity to CH_2Cl_2 with 5% of MeOH. Unfortunately, **C2** could not be isolated from the impurities.

Because of the above-described difficulties encountered in separating the solvated iridium species from the final compound, the reaction conditions were modified to a two-step procedure to increase the conversion in the cyclometalation step (**Scheme 3.4**).

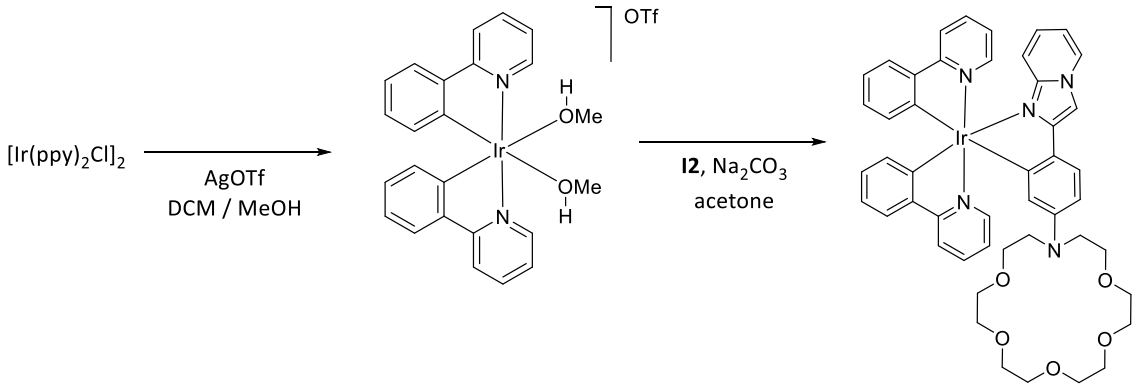

C2

Scheme 3.4. *Alternative two-step synthetic procedure for the formation of* ***C2****.*

Thus, based on paper reported by Yuan et al. for the monomeric intermediate formation, the solvent was changed to a mixture of a MeOH and CH_2Cl_2, and the intermediate iridium(III) disolvate $[Ir(ppy)_2(MeOH)_2]OTf$ was isolated (a in **Figure 3.38**).[4] This compound was reacted in a subsequent step with an excess of **I1** in refluxing acetone, using Na_2CO_3 as a base to avoid the loss of Et_3N by evaporation. After 16 h of reaction, the solvent of the mixture was removed, and the reaction crude was washed with EtOH and H_2O. The ^1H NMR of the obtained product is shown in b in **Figure 3.38**.

Although the signals in the ^1H NMR spectrum are not well defined due to the lack of solubility of the compound **C2** in $CDCl_3$, considering the similarity of the spectrum to the one of **C1**, it was concluded that the pattern corresponded to the desired **C2**. The signals at 8.27 and 7.95 ppm were assigned to the protons H8 and H8', next to the coordinated pyridines, and the signals at 6.50 and 6.10 ppm, to the protons 1 and 1', next to the cyclometalated carbon on the phenylpyridines. The singlet corresponding to the proton H13 on the ligand shifted from 7.74 ppm in the free ligand to 7.54 ppm after cyclometalation. Other deuterated solvents, such as CD_2Cl_2, acetone-d_6, DMSO-d_4, MeCN-d_3 and THF-d_8 were assayed to improve the quality of the spectrum without any success.

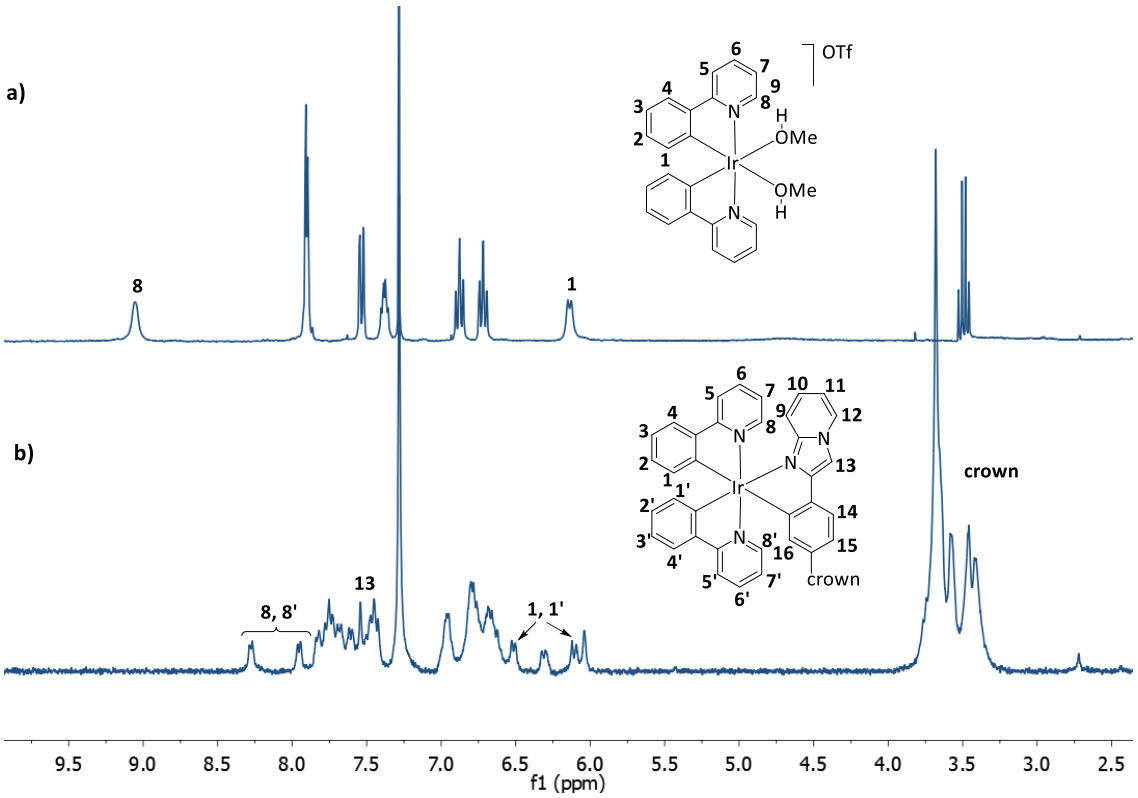

Figure 3.38. *^{1}H NMR of a) iridium monomeric intermediate and b) complex* ***C2,*** *with their partially assigned structures ($CDCl_3$, 300 MHz).*

With these results, an attempt to cyclometalate the definite **FBI** molecule was made under identical conditions. Unfortunately, the ^{1}H NMR of the crude just revealed signals assigned to the starting ligand and some decomposition of the iridium precursor. Since our objective with the **FBI** intermediates was simply to optimize the cyclometalation reaction conditions for **G3** compounds, no other attempts were made to cyclometalate the **FBI**.

Despite the discouraging results obtained with **FBI**, the reaction conditions were transferred to the cyclometalation of **G3** compounds. Likewise, the reaction was first pursued with **6** and **12,** the intermediate compounds of **G3a** and **G3b**, respectively (**Scheme 3.5**).

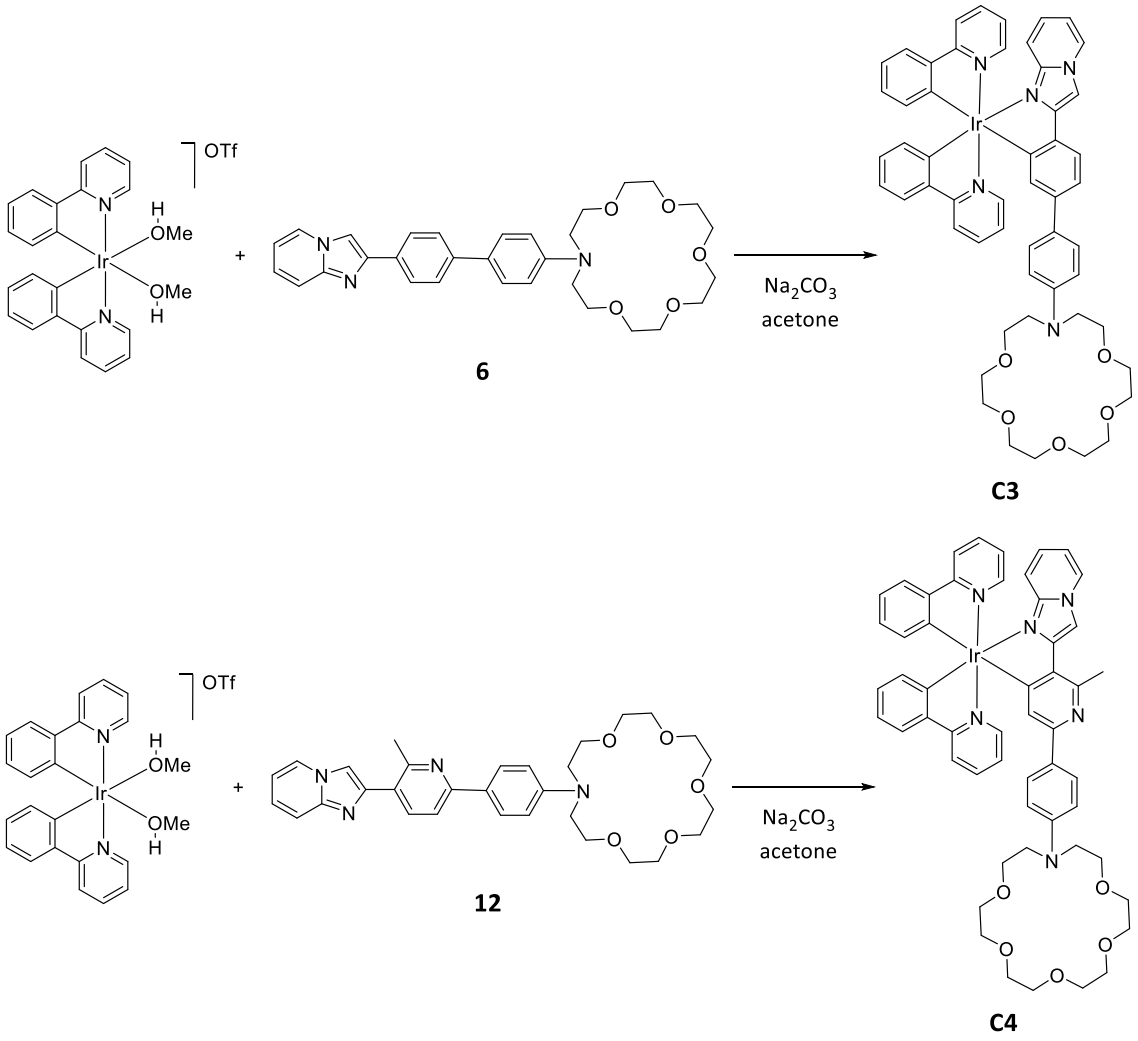

Scheme 3.5. *Intermediates **6** and **12** in the synthesis of **G3a** and **G3b**, respectively.*

Therefore, **6** was reacted with $[Ir(ppy)_2(MeOH)_2]OTf$ in refluxing acetone overnight, using Na_2CO_3 as the base. The ^1H NMR of the reaction crude obtained after solvent evaporation is compared to the one of the free ligand (**Figure 3.39**). In the spectrum, apart from the signals of unreacted **6**, new signals could be observed. The peaks at 8.28, 6.52 and 6.12 ppm (indicated with arrows) were assigned to the desired complex **C3**, due to their similarity to ones observed in the ^1H NMR spectrum of **C2**. However, some signals of an unidentified iridium decomposition product were again present in the spectrum.

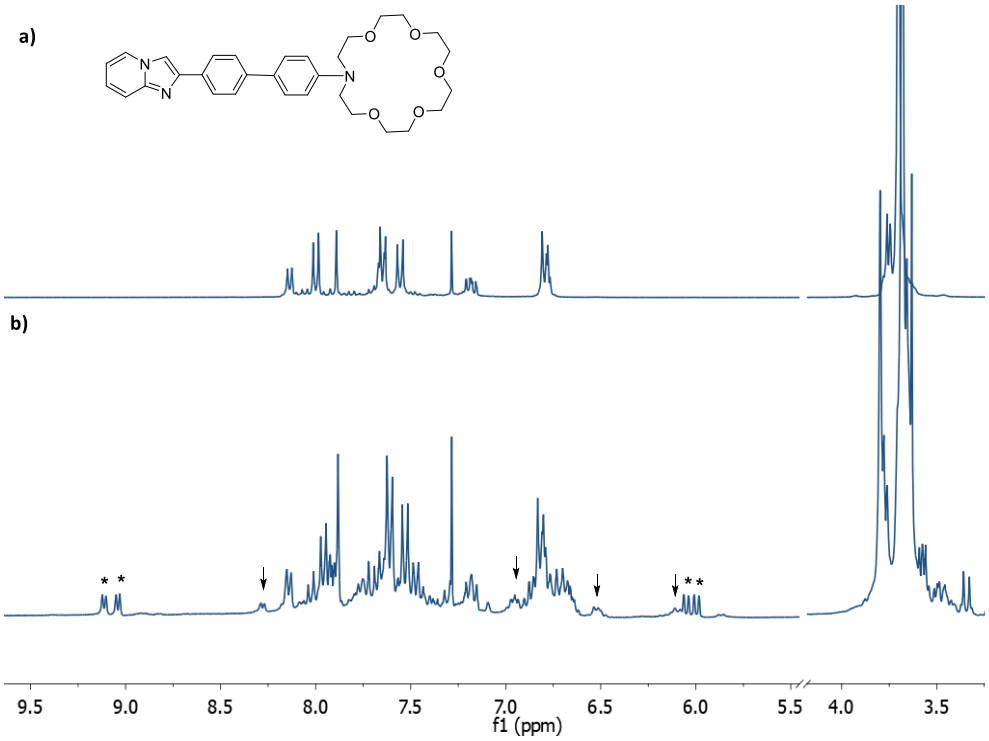

Figure 3.39. *^{1}H NMR spectrum of a) ligand **6** and b) crude of attempted **C3** synthesis ($CDCl_3$, 300 MHz).*

The same conditions were tested for the cyclometalation of **12** and the ^{1}H NMR spectrum of the reaction crude showed a similar pattern to the one observed for **C3** (**Figure 3.40**).

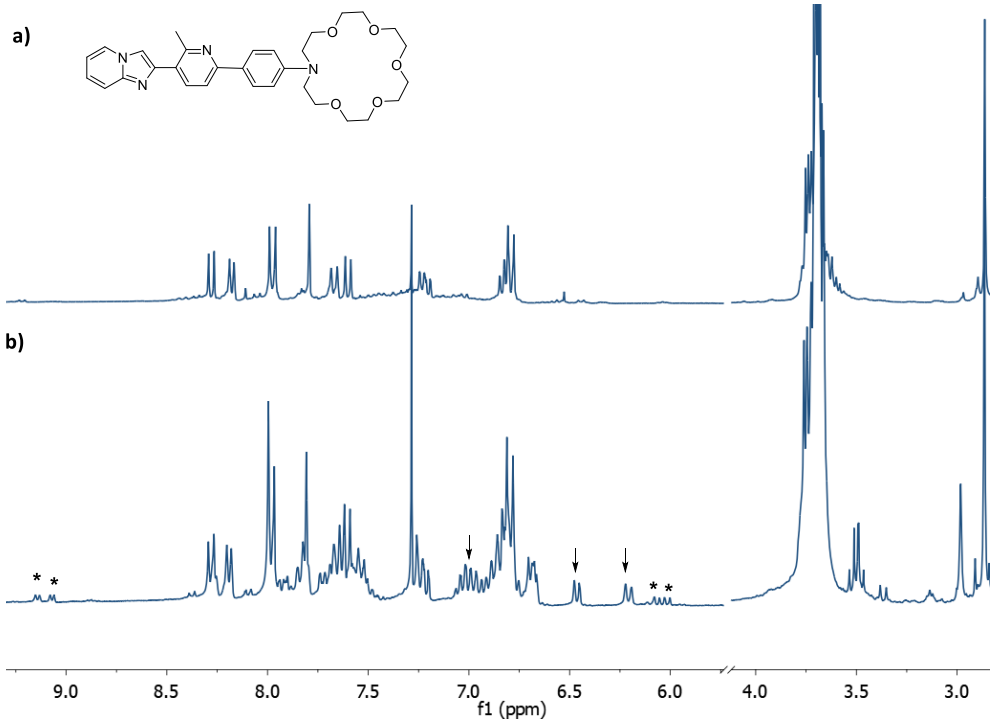

Figure 3.40. *^{1}H NMR spectrum of a) ligand **12** and b) crude of attempted **C4** synthesis ($CDCl_3$, 300 MHz).*

Extending the reaction time to two weeks (with analysis of reaction aliquots at different times) did not show any improvement in the conversion. For this reason, alternative reaction conditions were assayed.

In 2007, Mann published alternative synthetic routes for the cyclometalation of both phenylpyridine and pyridylthiophene ligands to Ir(III) metal centers forming both facial and meridional complexes under relatively mild conditions.[5] These routes involved the use of the bis-MeCN iridium(III) solvate $[Ir(ppy)_2(MeCN)_2]PF_6$ or the dimeric $[Ir(ppy)_2(\mu\text{-}OH)]_2$ intermediates as iridium precursors (**Scheme 3.6**).

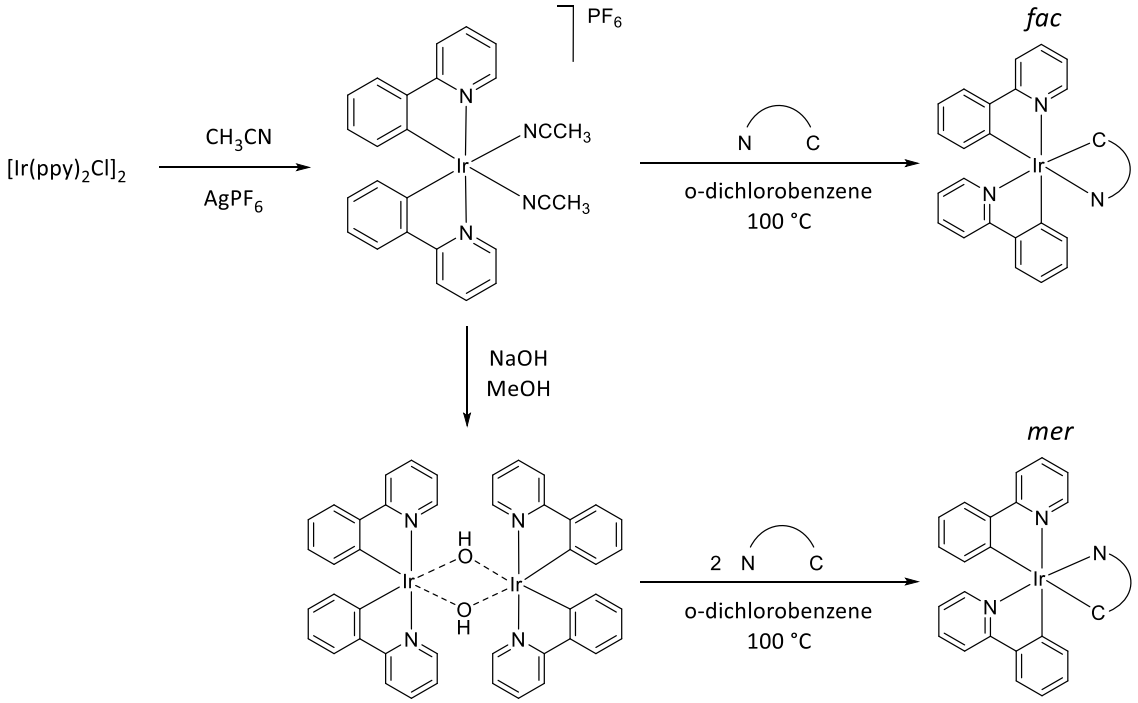

Scheme 3.6. *The synthetic scheme proposed by Mann et al. for facial and meridional complexes.*

Therefore, to test these routes, these iridium precursors were synthesized. $[Ir(ppy)_2(\mu\text{-}OH)]_2$ was synthesized following the procedure described by Bolink et al.[6] 2-phenylpyridine was reacted with $IrCl_3{\cdot}3H_2O$ in a refluxing 2-ethoxyethanol/H_2O mixture resulting in the in situ formation of the μ-dichloro-bridged dimer complex $[Ir(ppy)_2(\mu\text{-}Cl)]_2$ which was subsequently reacted under strongly basic conditions (aq. NaOH, reflux) to form the desired hydroxyl-bridged dimer as orange solid in good yield (55%) after further treatment with aq. NaOH in CH_2Cl_2.

For the bis-MeCN precursor, $[Ir(ppy)_2(\mu\text{-}Cl)]_2$ was refluxed in MeCN with a silver salt as a halide abstractor. The formed AgCl was removed from the reaction mixture by filtration through a celite pad, and the desired product was obtained by evaporation of the solvent from the filtrate. In our case, we synthesized the $[Ir(ppy)_2(MeCN)_2]OTf$ derivative.

With these precursors, Manns' routes were tested on NMR scale. $[Ir(ppy)_2(\mu\text{-}OH)]_2$ was reacted with **12** in o-dichlorobenzene at 100 °C. The reaction crude was analyzed by ^1H NMR, which showed no new signals that could be assigned to **C4**. Also, negative results were obtained when $[Ir(ppy)_2(MeCN)_2]OTf$ was reacted with **12** in acetone at room temperature.

Because of the low yields obtained for the synthesis of iridium(III) cyclometalated derivatives **C3** and **C4** with their unsuccessful isolation attempts, and considering that it was expected to be even more problematic in the case of derivatives of the definite **G3a** and **G3b**, the synthesis of these neutral Ir(III) derivatives was abandoned to follow with the synthesis of the cationic complexes.

1.1.1. Synthesis of cationic N^N iridium(III)-derivatives.

Cationic complexes were obtained using the most frequently employed procedure to synthesize biscyclometalated bipyridine iridium(III) complexes, consisting of the cleavage of the corresponding chloride-bridged dimer in the presence of two equivalents of the ligand in a refluxing mixture of CH_2Cl_2 and MeOH (2:1, CH_2Cl_2/MeOH).[7] This general synthetic route is described in **Scheme 3.7**.

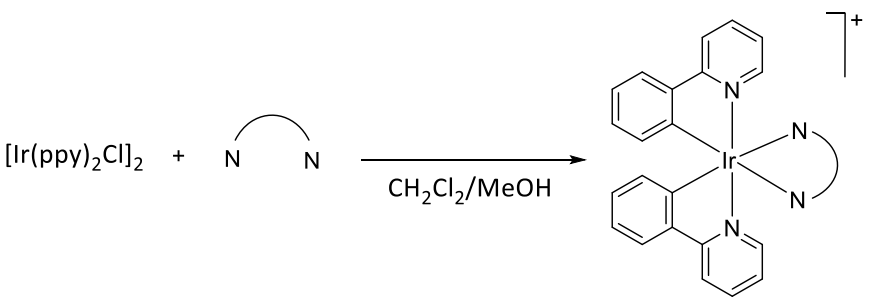

Scheme 3.7. *Synthetic procedure for the formation of cationic compounds* $[Ir(ppy)_2(N\text{^}N)]^+$.

The coordination of the prototype ligands **L1, L2** and **L3** and **G3c**, described in Chapter 2, was performed. Thus, following the procedure presented in **Scheme 3.7**, Ir(III) heteroleptic cationic complexes **C5**-**C8** decorated with two cyclometalated phenyl pyridine ligands and a N^N ligand were obtained under mild conditions and in good yields (>80%). Their chemical structure is shown in **Scheme 3.8**.

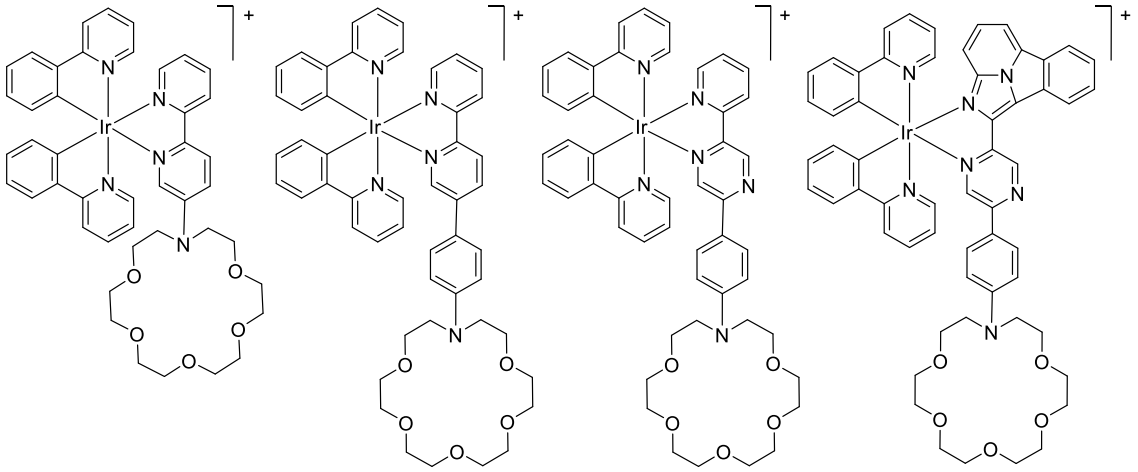

Scheme 3.8. *The iridium cationic complexes synthesized in this work (counterions are omitted).*

The formation and purity of each complex were established by 1D and 2D NMR experiments and mass spectroscopy.

To exemplify the NMR spectrum of the complexes **C5** to **C7**, the ^{1}H NMR spectra of complex **C6** are shown in **Figure 3.41** (full spectra and detailed synthetic procedures are compiled in the Supporting Information). Although the complexity of the spectra hampered its full assignment, the spectrum was consistent with the proposed structure. Taking into account its C_1 symmetry, for **C6** complex, up to 19 aromatic and 24 aliphatic (overlapped) different proton signals were expected in the ^{1}H NMR spectrum, and up to 50 carbon signals in the ^{13}C APT NMR spectrum.

In the ^{1}H NMR (**Figure 3.41**), the two overlapped doublets at 8.57 ppm were assigned to the protons next to the nitrogen in the phenylpyridines. The two doublets at 6.37 and 6.32 ppm correspond to the protons next to the cyclometalated phenyl on the phenylpyridines. The signals between 3.6-3.4 ppm correspond to the 24 protons present in the crown, the only aliphatic protons in the complex.

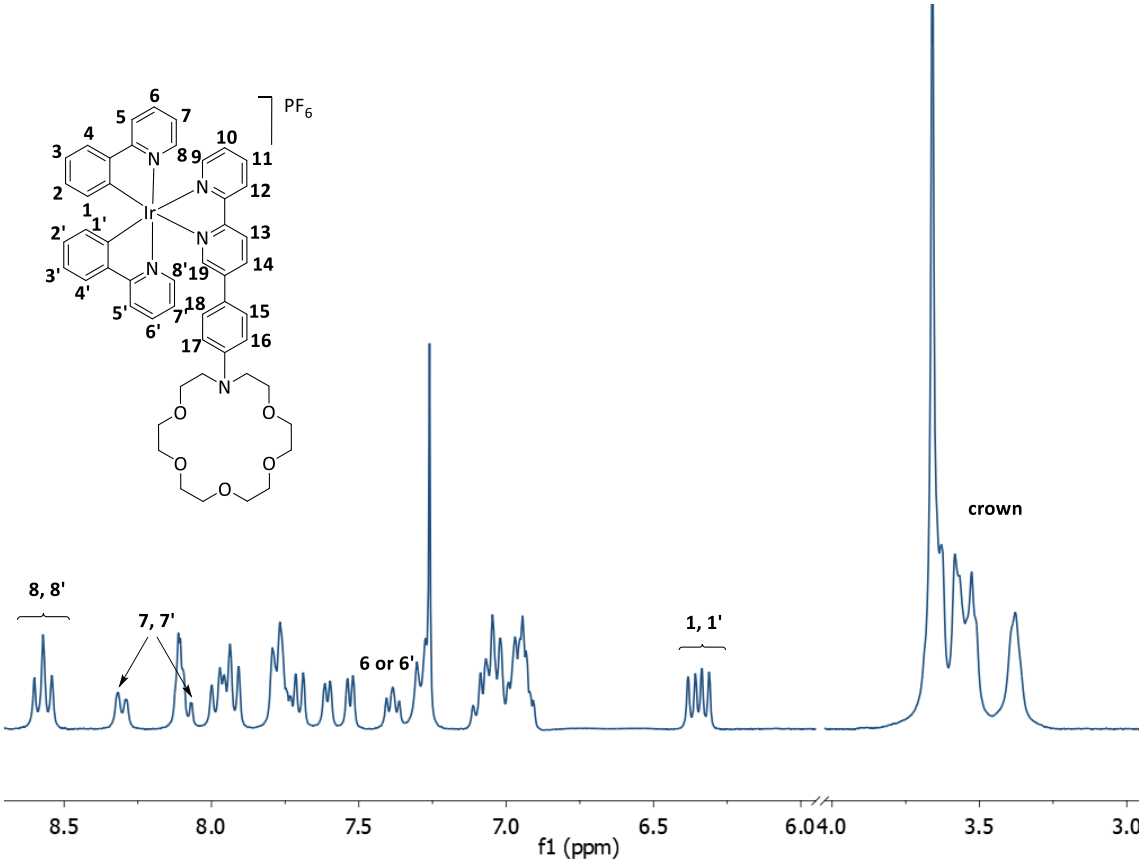

Figure 3.41. *^{1}H NMR spectrum of complex **C6** and the partially assigned structure ($CDCl_3$, 300 MHz).*

In the ^{13}C APT NMR spectrum (**Figure 3.42**), in CD_2Cl_2, in the upfield region of the spectrum the five peaks at 70.53, 70.37, 70.21, 68.54 and 56.23 ppm were assigned to the secondary carbons of the crown. The other eleven negative signals that are downfield corresponded to the quaternary carbons present in the complex. The positive signals were consistent with the 27 C-H carbons in the complex.

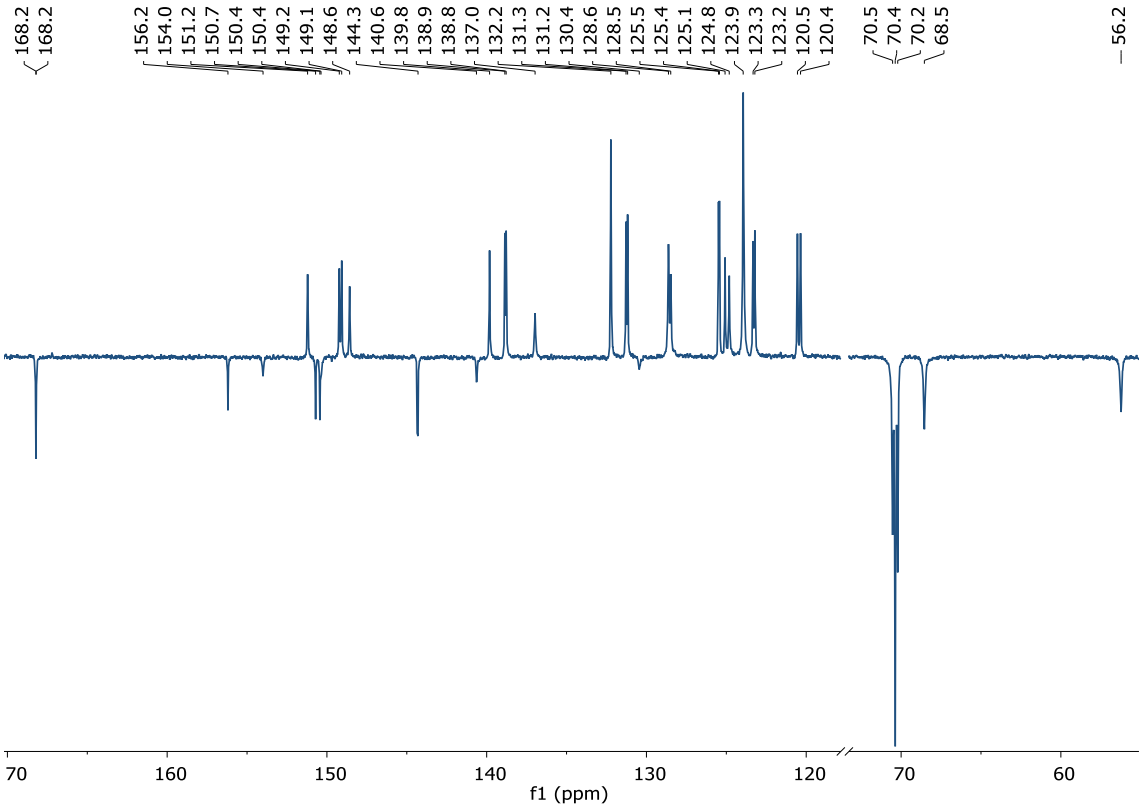

Figure 3.42. *^{13}C APT NMR of complex **C6** (CD_2Cl_2, 300 MHz).*

The structure of **C6** was further confirmed by single-crystal X-ray diffraction. Crystals were obtained by slow diffusion of CH_2Cl_2/pentane. Nevertheless, the poor quality of the sample did not allow us to obtain a properly refined structure. In any case, the expected structure of C6 can be seen in Figure X. The sample was measured under monochromatic Cu-Kα radiation (λ = 1.54184 Å), solving the structure in the monoclinic *P* 2_1/c space group. Apparently, the asymmetric unit consists of a cationic $[Ir(ppy)_2\mathbf{L2}]^+$ fragment and a PF_6^- counterion. Moreover, a water molecule seems to be stabilized by hydrogen bonds in the center of the crown-ether. Residual peaks were found in the refinement process, but we were unable to assign further possible solvent molecules. The crown-ether shows a large disorder due to the flexible nature of this group, and several restrains were needed in order to obtain a reliable model. The structure concluded by NMR is supported by the structure, having deprotonated phenyl groups trans to the bipyridine nitrogen atoms. Nonetheless, we cannot conclude this arrangement from the crystal structure, due to its poor quality.

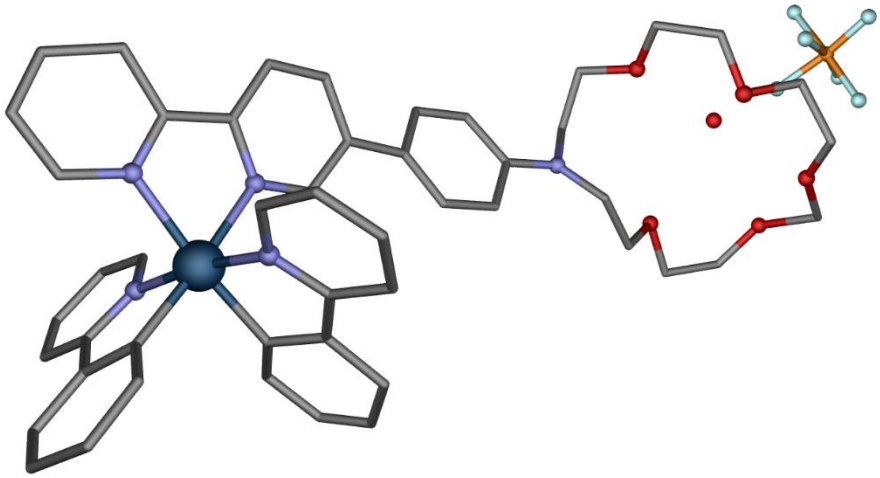

Figure 3.43. *Molecular structure of* ***C6*** *derived from single crystal X-ray diffraction.*

3.3 PHOTOPHYSICAL CHARACTERIZATION

In this section, the photophysical characterization of the cationic complexes will be described. For a better discussion, a different organization will be used compared to the photophysical scheme used in Chapter 2 for the ligands. The luminescent behavior of the isolated **C5**, **C6**, **C7** and **C8** compounds free and upon their interaction with Ba^{2+} cation was studied.

3.3.1 Absorption

Absorption spectra of free and Ba^{2+}-bound **C5**-**C8** complexes in MeCN solutions are shown in **Figure 3.44**, and the most relevant data of the complexes are summarized in **Errorea! Ez da erreferentzia-iturburua aurkitu.**.

In their free form, the four complexes show an absorption band below 300 nm correlated to spin-allowed ^{1}LC(ppy) $^1\pi \rightarrow \pi^*$ transitions. The bands at middle wavelengths (300–550 nm), are correlated to ^{1}ILCT(bpy) $^1\pi \rightarrow \pi^*$ transitions. Red-shifted absorption features are generally attributed to $d \rightarrow \pi^*$ MLCT transitions of an electron from a d orbital of the metal center to an antibonding π^* ligand orbital, corresponding to ^{1}MLCT and ^{3}MLCT transitions.[8] However, in $[(C\text{^}N)_2Ir(N\text{^}N)]^+$ complexes the latter are masked by the the intense ^{1}ILCT(bpy) transitions.[9–11]

Upon chelation with Ba^{2+}, the band attributed to ^{1}LC(ppy) transitions remained unaltered. In contrast, the band corresponding to the ^{1}ILCT(bpy) transitions appears blue-shifted. This result is not surprising considering that the interaction of the Ba^{2+} cation with the sensor occurs through the ancillary bipyridine ligand. The hypsochromic shift of this band upon interaction with Ba^{2+} could be explained, for **C6**-**C8**, by the loss of conjugation in the bpy ligand due to the decoupling of the free rotating aromatic unit and the bipyridyl fragment, together with the decrease in the participation in the π system of the electron lone pair of the nitrogen of the crown, for the four complexes (now compromised in the interaction with Ba^{2+}).

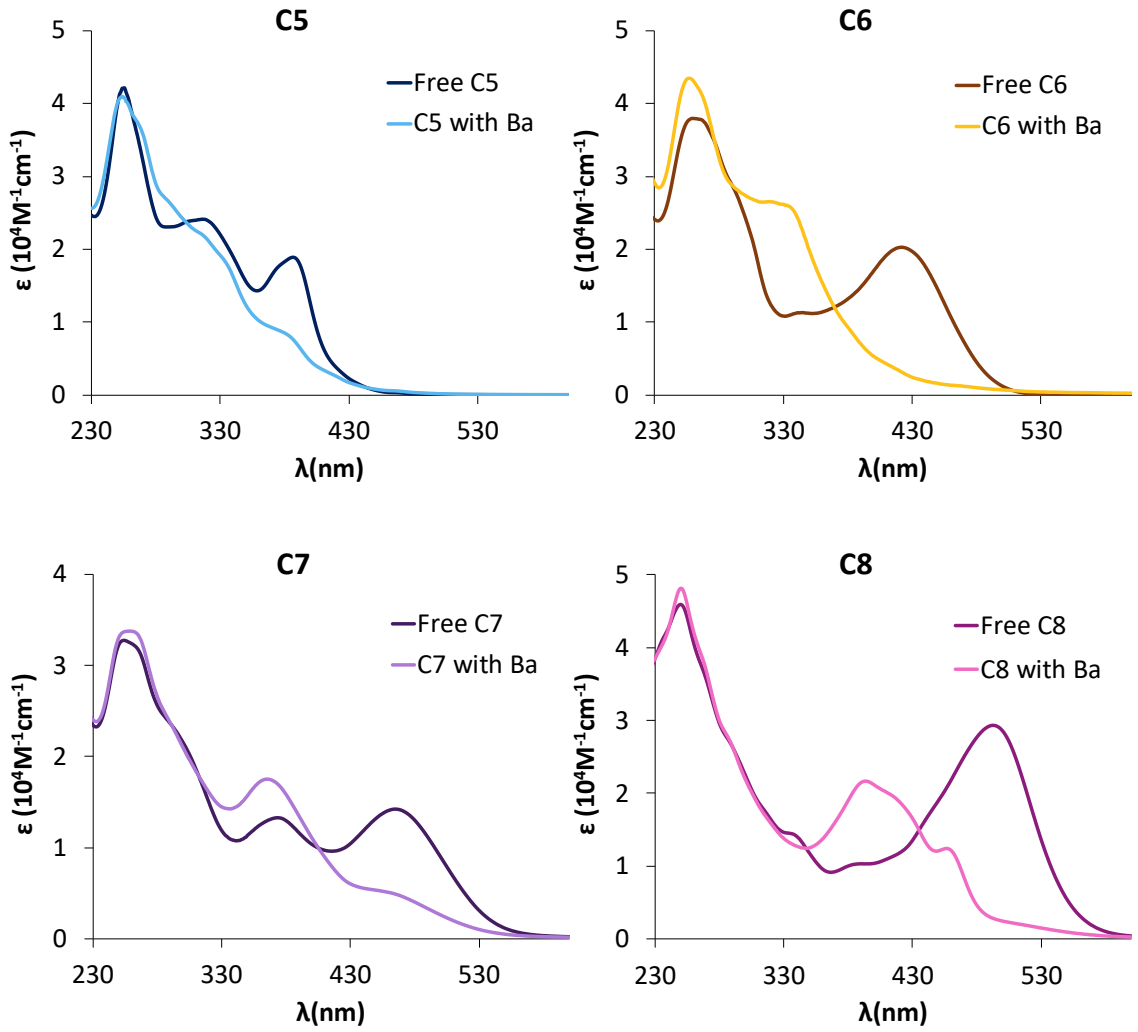

Figure 3.44. *Absorption spectra of free and chelated **C5**-**C8** complexes in MeCN.*

This phenomenon was confirmed for complex **C6** by DFT calculations performed by the group of Prof. F.P. Cossío (**Figure 3.45**). The optimized structure for the coordinated

species **C6**–Ba^{2+} reveals a large molecular torsion of the aza-crown ether with respect to the free **C6** compound, so that a molecular cavity is formed when the metal cation creates a π-complex between the Ba^{2+} metallic center and the phenyl group. The oxygen atoms of the aza-crown ether occupy five coordination positions with O–Ba contacts. Interestingly, the aromatic ring bound to the crown ether is oriented towards the center of the cavity, using its π-electrons to chelate the cation.

The dihedral angle is increased from 26.6° to 48.9°, by the phenyl group rotation and breaks the π-coordination with the rest of the fluorophore. Thus, the electronic structure may be affected by the molecular distortion upon metal coordination in **C6**–Ba^{2+}.

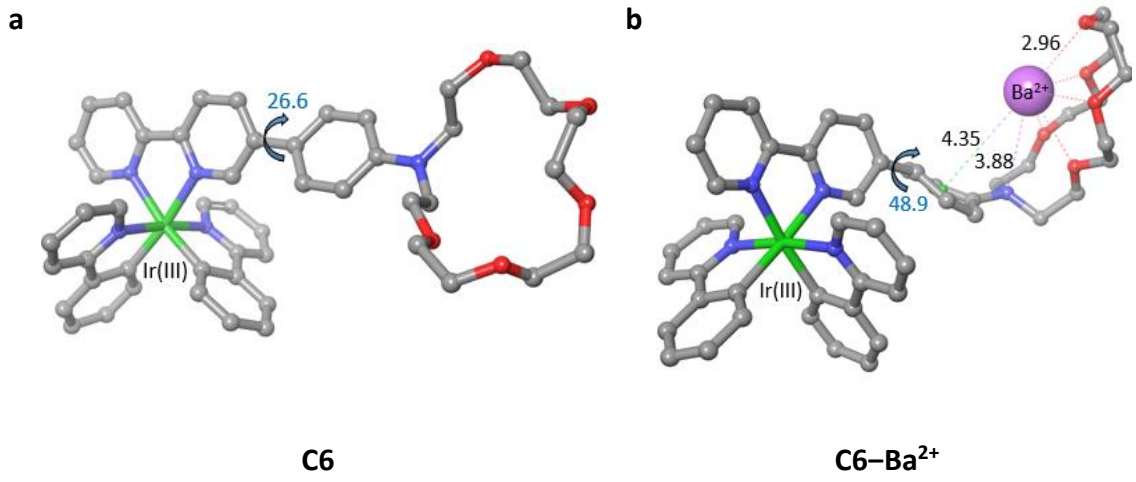

Figure 3.45. *DFT-derived gas-phase structures of a) C2 and b) **C2**–Ba^{2+}. Bond distances are given in Å. Dihedral angles ω formed by covalently bonded atoms 1–4 are given in degrees and in absolute values. (calculation done at ωB97X-D/6-311++G(p,d)&Lanl2DZ level of theory)*

3.3.2 Binding affinity

The strength of interaction of the sensors with Ba^{2+} was further studied. The binding affinity of the sensors for Ba^{2+} was calculated by binding experiments in solution. All the compounds were titrated using aliquots of concentrated $Ba(ClO_4)_2$ solutions and monitored by UV-vis spectroscopy. These solutions were prepared using the mother solution of the unbound complex as the solvent, to guarantee that the sensor concentration remains constant along the titration. Initially, all the titrations were conducted at $5 \cdot 10^{-6}$ M in MeCN. Then the titration was repeated at specific concentrations individually optimized for each sensor depending on the guessed value

of their individual binding constants, extracted from the initial titration, summarized on **Table 3.1**. The final titration plots are shown in **Figure 3.46**, with the experimental binding profile of selected wavelengths (indicated with an arrow). The binding constants were calculated by minimum squares optimization applying Nelder-Mead optimization procedure (using Bindfit) on the most relevant range of the spectra.[12–14]

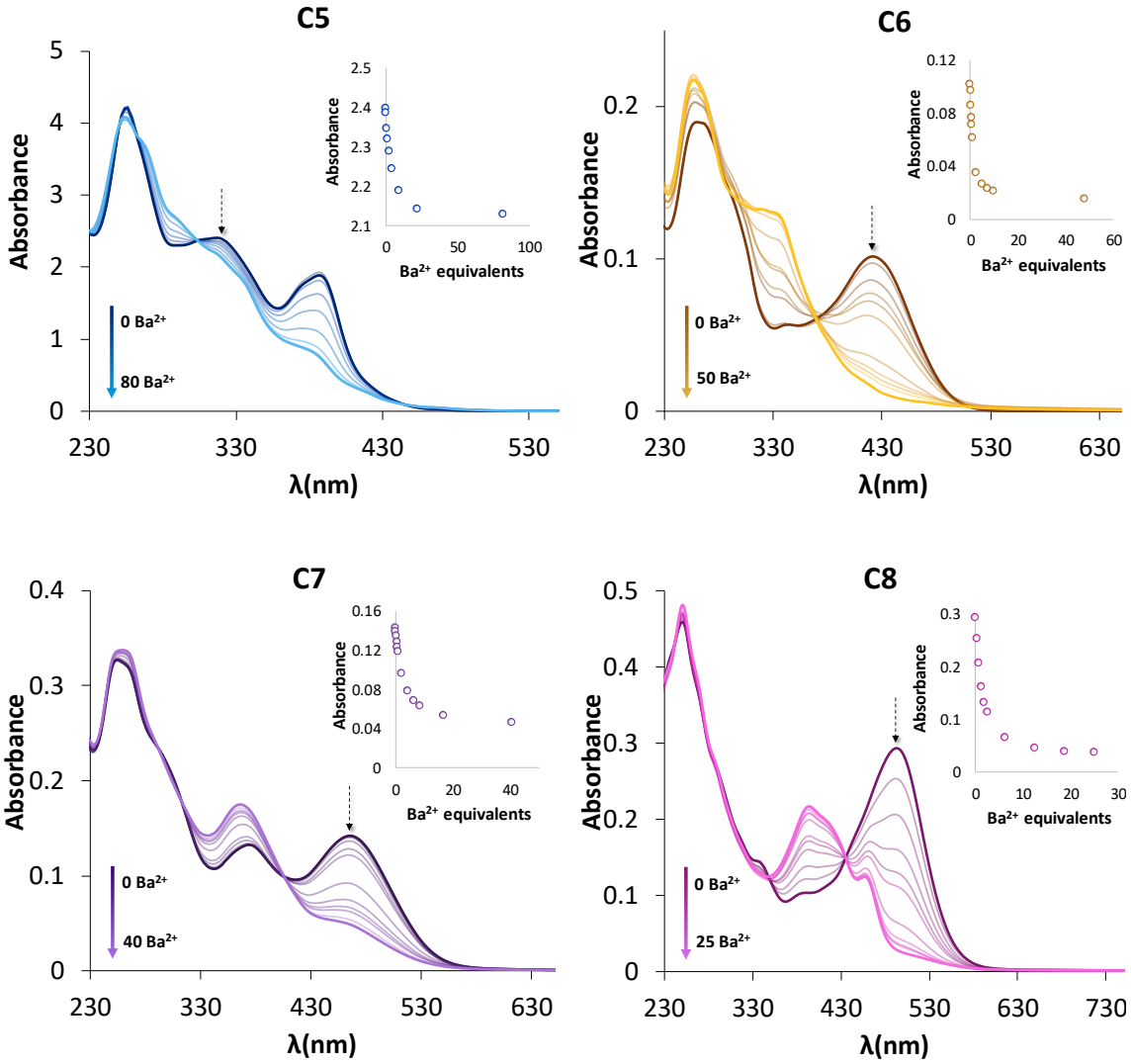

Figure 3.46. *UV–vis absorption spectra of titration experiments in MeCN at optimized concentrations of* ***C5***, ***C6***, ***C7*** *and* ***C8*** *with* $Ba(ClO_4)_2$. *The inset plot show the titration curve at the maxima of the free complexes (indicated with an arrow.*

Table 3.1 summarizes the binding constants obtained for each complex at the optimized concentrations. As a general remark, the four complexes present lower association constants compared to their respective ligands (described in Chapter 2). This result is not surprising, as the cationic nature of the compounds should produce an electronic

repulsion with the Ba^{2+} ion, therefore reducing the binding constant. Not surprisingly, the biggest decrease corresponds to the **C5** complex, whose K_a decreases from $4 \cdot 10^5$ M^{-1} of the ligand to $2 \cdot 10^3$ M^{-1} of the complex. This effect, which could be attributed to the steric impedance of Ba^{2+} to interact with the crown due to its proximity to the iridium coordination sphere, and the forced proximity of Ba^{2+} to the cationic metal center in the bound sensor. Even if **C7** was design to improve **C6** by having an extra nitrogen to interact with the Ba^{2+} cation, the binding constant of **C6** is higher than the **C7**. These binding values are comparable to other iridium sensors for cations reported in the literature (see Chapter 1).

Table 3.1. *Summary of the data for the K_a measurements and K_a results for each complex.*

	$\lambda_{isosbestic}$ (nm)	K_a (M^{-1})	Concentration (M)
C5	303	$2.1 \cdot 10^3 \pm 2\%$	$1 \cdot 10^{-4}$
C6	370	$4.3 \cdot 10^5 \pm 2\%$	$5 \cdot 10^{-6}$
C7	405	$4.6 \cdot 10^4 \pm 1\%$	$1 \cdot 10^{-5}$
C8	435	$1.3 \cdot 10^5 \pm 1\%$	$1 \cdot 10^{-5}$

The clear isosbestic points in the UV-vis spectra, resumed in **Table 3.1**, present for all the complexes, are indicative of the 1:1 stoichiometry formation between the sensors and Ba^{2+}. To support this statement, the method for continuous variation was performed. As explained in Chapter 1, same concentration solutions of stock solutions were prepared, one with each complex (host) and the second one with $Ba(ClO_4)_2$ (guest). From these solutions, eleven other solutions were prepared in MeCN. The molar fraction of the host varied from 0 to 1 and the remaining molar fraction corresponding to guest. Thus, in each solution there will be a molar fraction, X, of **G3** and a molar fraction (1-X) of Ba^{2+}. In **Figure 3.47** the Job's Plots of the four complexes are represented. All the complexes show a maximum at 0.5 molar fraction of Ba^{2+}, confirming the 1:1 stoichiometry already observed in the titration experiments.

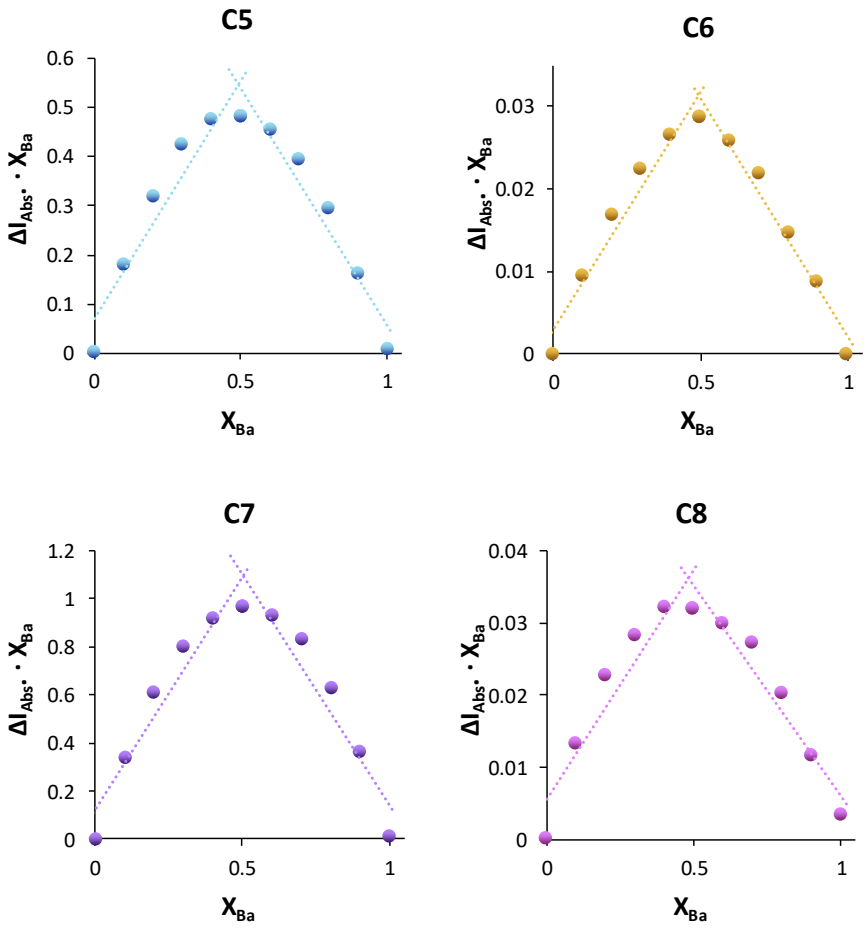

Figure 3.47. *Job's Plots of the **C5**-**C8** complexes. Plotted at 390, 421, 260 and 493 nm for **C5**, **C6**, **C7** and **C8**, respectively. Concentrations of $1 \cdot 10^{-4}$ and $5 \cdot 10^{-6}$ M were used for **C5** and **C7**, and **C6** annd **C8**, respectively.*

The interaction of Ba^{2+} with the complexes was further studied by ^{1}H NMR spectroscopy. In **Figure 3.48**, the spectrum of the free and Ba^{2+}-bound **C6** are shown as exemplification (The rest in SI). The most characteristic change occurred in the aliphatic region, were the signals corresponding to the crown ether appear unfolded upon Ba^{2+} addition, revealing two triplets at 3.25 and 3.68 ppm, due to the deshielding of the protons corresponding to the methylene group contiguous to the nitrogen atom. This phenomenon was also observed for the complexes **C5**, **C7** and **C8** (see supporting) and for FBI.[15] In the aromatic region, the main shift corresponded to the two doublets from 6.80 and 7.22 ppm in the free form to 7.31 and 7.43 ppm for the Ba^{2+}-bound form, respectively. This is congruent with the previously presented computational studies (**Figure 3.45**), explained by the deshielding of the para-phenyl group upon coordination with Ba^{2+}, associated with the formation of a π-cation complex.[16]

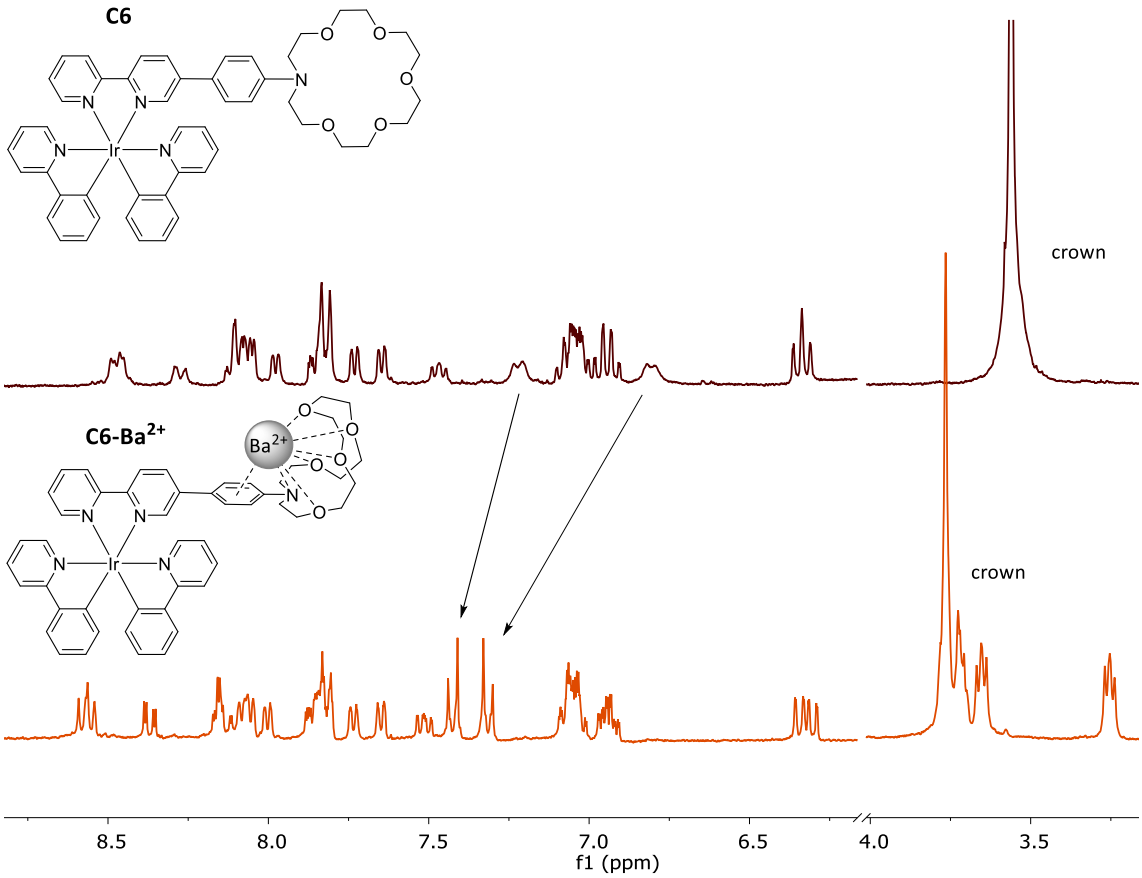

Figure 3.48. *^{1}H NMR of **C6** and Ba^{2+}-bound **C6** (CD_3CN, 300 MHz).*

3.3.3 Emission

Figure 3.49 shows the emission of the free and bound sensors in MeCN solutions registered under excitation at their corresponding isosbestic point (deduced from UV-vis titration experiments previously described). It is worth noticing that upon excitation at this point, at which both free and bound sensors present identical molar absorptivities, the emission intensities should be proportional to their respective quantum yields.

The four complexes show a ratiometric response for Ba^{2+}. At this wavelength of excitation, the main emission band of the **C5**, **C6** and **C7** free complexes resides in the region below 550 nm, which will be defined as the high energy band (HB), and the main emission of the bound species emits around 600–700 nm, a low energy band (LB). This emission change can be observed by "naked eye" (**Figure 3.50**).

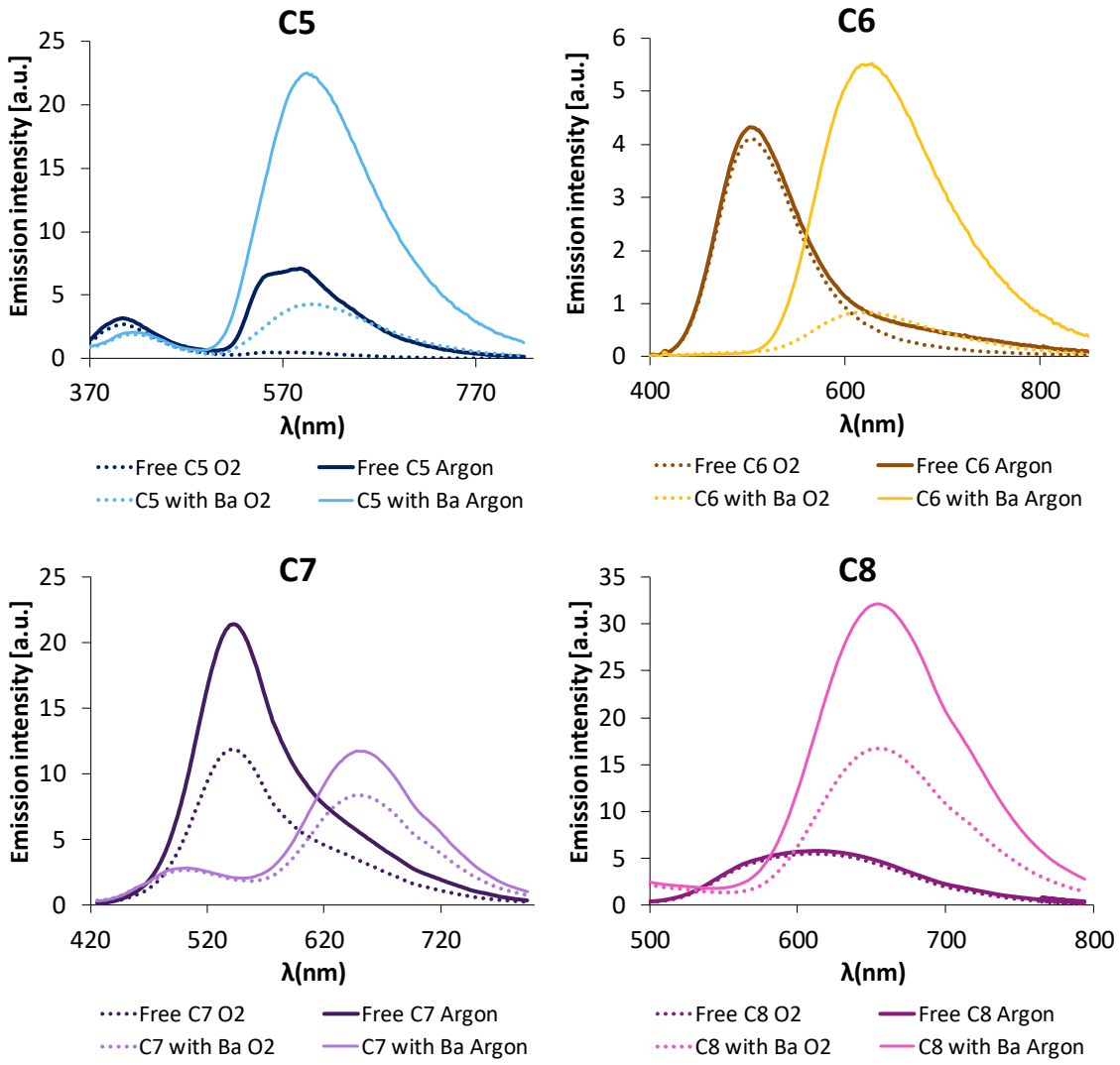

Figure 3.49. *Emission spectra of sensors **C5**-**C8** in MeCN ($1 \cdot 10^{-5}$ M) under excitation at the corresponding isosbestic point. Dotted line: aerated MeCN solutions. Continuous line: argon equilibrated MeCN solutions.*

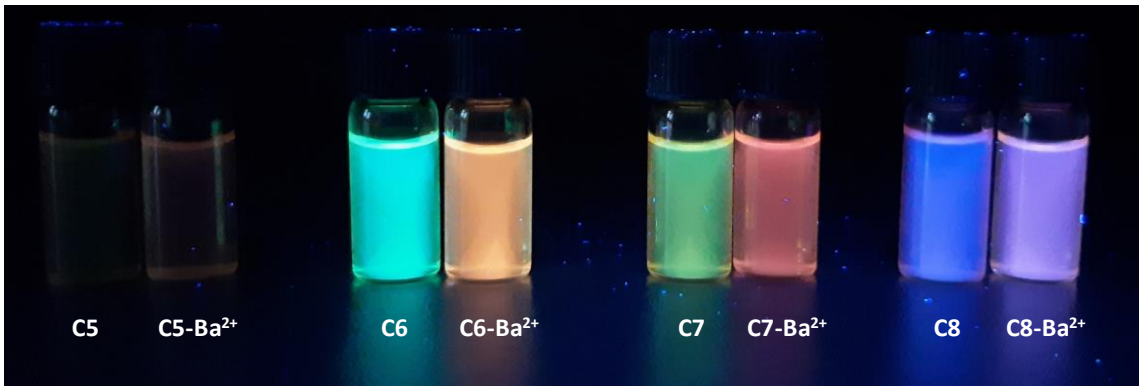

Figure 3.50. *Picture of complexes **C5**-**C8** in aereated MeCN, in their free and Ba^{2+}-bound form, under 365 nm UV-lamp.*

Table 3.2. *The most important photophysical data of the complexes **C5**, **C6**, **C7** and **C8**.*

	absorption	emission			Stokes shift [cm^{-1}]
	λ_{max} [nm] (ε [$10^4 M^{-1}cm^{-1}$])[a]	λ_{max} [nm][b]	Φ [%] [c]	τ [ns] (contribution)[d,e]	
C5	256 (4.05), 306 (2.40), 318 (2.40), 388 (1.85)	408 559	9	2.7 (1.00 %) 388 (4%), 6735 (96%)[b]	1330 7951
C5-Ba	256 (4.11), 320 (2.30), 338 (1.83), 387 (1.23)	408 600	21.4	2.7 (100%) 414(40%), 744(60%)	1330 9173
C6	263, (4.00), 293 (3.02), 349 (1.24), 424 (2.14)	502	4	2.8 (100%)	3832
C6-Ba	259 (4.13), 323 (2.67), 337 (2.59), 413 (0.34)	618	10	11 (12%), 121 (64%), 371 (24 %)	13405
C7	255 (3.66), 298 (2.53), 379 (1.31), 469 (2.12)	540	1.2	3.9 (100%)	2637
C7-Ba	255 (3.78), 290 (2.70), 365 (2.08), 567 (0.43)	512 650	2.9	4.0 (100%) 26.2 (17%), 342.6 (83%)	1655 6901
C8	251 (4.25), 340 (1.25), 385 (0.92), 496 (2.71)	610	0.83	6.41 (88%), 1420 (12%)	3832
C8-Ba	252 (4.29), 400 (1.97), 416 (0.18), 459 (1.14)	660	5.23	34 (12%), 486 (64%), 1534 (24%)	7596

MeCN solutions. a) Based on linear regression of the measured absorption of 6 concentrations in the range 10^{-4} M–10^{-6}M. b) Excitation at their corresponding isosbestic points. c) Φ Measured at the corresponding isosbestic point at 0.1 optical density in argon-equilibrated MeCN. d) Acquired on argon-equilibrated solutions using EPLED 340 nm, TCSPC mode at 10MHz or 20MHz for the HB and MCS mode at 10KHz or 20 KHz for the LB. e) All χ^2 values were between 1.0-1.2. f) Acquired at 340 nm using a micro-pulsed Xenon lamp at 100 Hz.

As it can already be intuited from the emission spectra of compounds free and Ba^{2+} bound complexes shown in **Figure 3.49**, the free and Ba^{2+}-bound complexes behave as dual emitters. This is especially evident in the spectra of the compounds **C5** and **C7**. To highlight this feature and investigate if **C6** and **C8** behaved in the same manner, the emission of the free and Ba^{2+}-bound sensors was registered under excitation at two additional wavelengths, at absorption maxima of the corresponding free and chelated compounds. For instance, the comparison of **C6** is shown in **Figure 3.51** (for the rest see **Figures S119**, **S137** and **S146**). The Ba^{2+}-bound **C6** shows a modest tail in the high-energy region when excited at 338 nm, while exciting at 422 nm the free **C6** manifests a second HB emission. As previously outlined, these complexes present a HB emission in the most

energetic region of the spectra between 350–500 nm (except **C8**), and an additional red-shifted LB at 550–800 nm. As it can be observed, exemplified for **C6** in **Figure 3.51**, the total and relative intensity of these two emission bands are strongly dependent on the excitation wavelength. It is worth noticing that the HB is the only one present with the compounds are excited at the emission maxima of the unbound sensors.

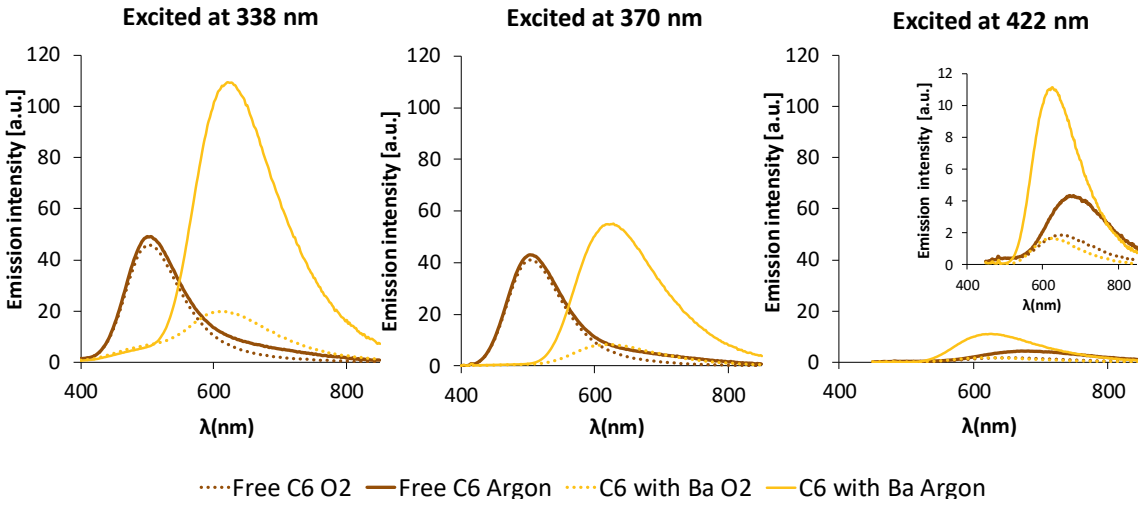

Figure 3.51. *Emission spectra of sensor **C6** in MeCN ($1 \cdot 10^{-5}$ M) excited at the absorption maxima of the bound sensor (left), of the free sensor (right) and at the corresponding isosbestic point (middle).*

The excitation spectra of free **C6** were also measured to confirm the dual character of the complex (**Figure 3.52**). These spectra confirm that **C6** behaves, in fact, as a dual emitter, as the normalized excitation spectra for both emissions (HB and LB) show coincident maxima in the region 320–380 nm.[17]

The possibility of compounds of the type $[Ir(C^N)_2(N^N)]^+$ acting as dual emitters is well reported in the literature since the earliest examples of this type of complexes.[18–20] This dual emission is generally attributed to the multi-component nature of the emitting triplet excited state.[21] Other iridium complexes as cation sensors displaying dual emission have also been reported.[22]

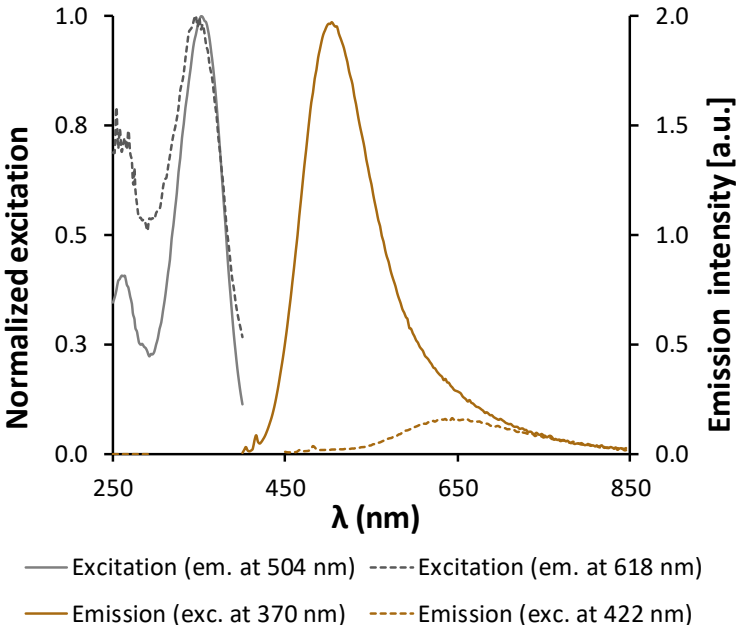

***Figure 3.52**. Excitation and emission spectra of free sensor **C2** in MeCN ($1 \cdot 10^{-6}$ M).*

Additional experiments also reveal the different nature of these two emissions. When the solutions were purged with argon, the intensity of the HB emission was not affected (except for the free **C7**), whereas a clear emission enhancement was observed for the red-shifted HB (**Figure 3.49**).

The phosphorescent nature of the LB of the Ba^{2+}-bound complexes and free **C5**, intuited from the oxygen-free experiments, was confirmed by lifetime measurements. Ba^{2+}-chelated compounds **C5**-**C8** showed lifetimes between 300–700 ns. These phosphorescent emissions have been widely reported for related iridium complexes.[4,23] On the contrary, the oxygen independence of the HB emission could indicate a fluorescent decay. The lifetime of the free compounds at the maxima of their emission band, and of the blue-shifted band of Ba^{2+}-bound **C5** and **C7** showed a monoexponential decay, with lifetimes of few nanoseconds, summarized in **Errorea! Ez da erreferentzia-i turburua aurkitu.**. The small values of the Stokes shift (e.g. 2600 cm^{-1}), the excited state lifetimes in a nanosecond domain (2–4 ns) and the independence of emission intensity in the presence of molecular oxygen point to the singlet nature of these emissions.

This is a rather rare result for biscyclometalated iridium(III) complexes, as in a typical octahedral iridium complex, the large spin–orbit coupling constant of the iridium(III) ion induces a very efficient of S → T intersystem crossing that makes $[Ir(C^N)_2(N^N)]^+$

complexes relax from triplet excited states. Thus, phosphorescence is the common relaxation pathway encountered for these compounds.

Nevertheless, few iridium biscyclometalated complexes with dual fluorescent/phosphorescent emission have been previously reported. However, the singlet–triplet dual emission in these complexes is reported mostly for hybrid systems, where an electronically independent remote fluorophore is attached to the complex via an appropriate spacer,[24,25] in a polymeric chain,[26–28] or coordinated in a monodentated fashion.[29,30] Some of these structures are exemplified in **Figure 3.53**.

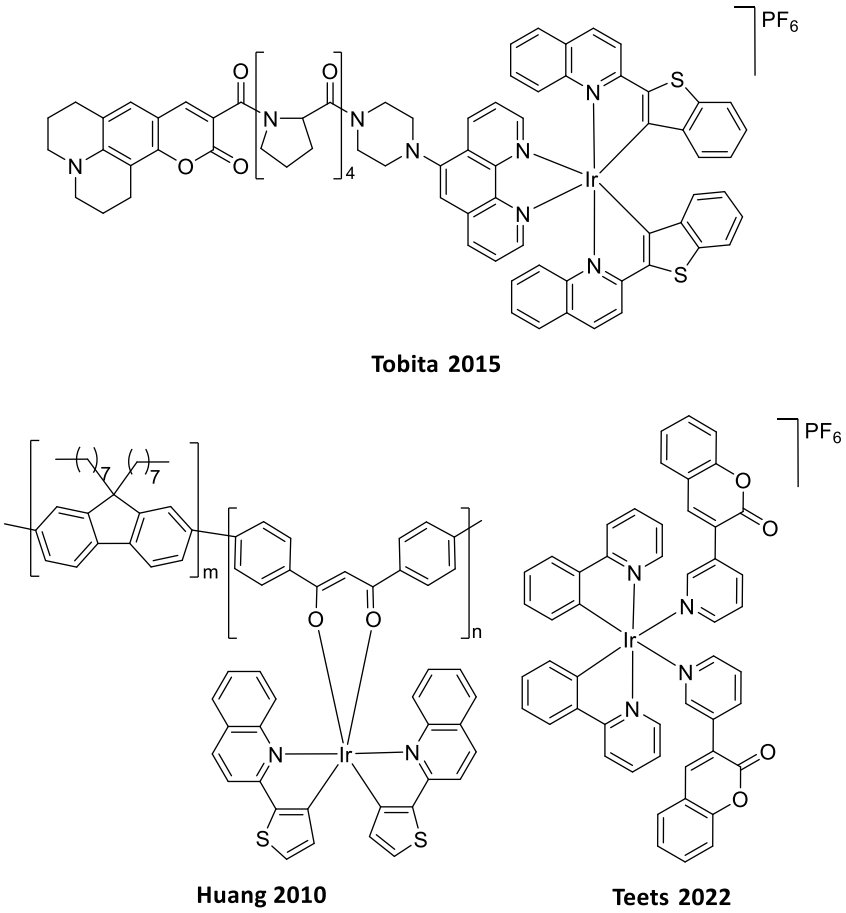

Figure 3.53. *Iridium biscyclometalated complexes reported in literature with dual fluorescent/phosphorescent emission.*

Fewer examples were found of relatively compact iridium complexes, which demonstrate independent singlet emission and a phosphorescent signal. In 2018, Grachova et al. reported an example of a dual fluorescent/phosphorescent compact iridium $[(ppy)_2Ir(bpy^*)]^+$, functionalized bipyridine with a pendant 5-(4-ethynylphenyl) fragment, which demonstrated to have very well-separated singlet–triplet dual emission

(**Figure 3.54**).[31] They studied a family of related compounds, and observed that the emission energy and the shape of the fluorescent band were not affected by the nature of the C^N ligand, concluding that the excited state responsible for fluorescence was the same for all complexes under study and, therefore, it was localized on the ancillary ligand. The emission was assigned to the metal-perturbed ππ* intraligand fluorescence, with nanosecond lifetime. Choudhury et al. described a NHC-Ir^{III} complex, showing the same behaviour (**Figure 3.54**).[32] The energy of the fluorescent band of the complex did not depend on the composition of the coordination sphere and the charge of the complexes, and showed the vibronic structure typical of π-π* electronic transitions.

In 2010, Zysman et al. introduced a biscyclometalated iridium complex with nanosecond emission lifetime at room temperature, however, the emission was not defined as fluorescence.[10] In the paper, a new family of $[(ppy)_2Ir(bpy^*)]^+$ (bpy*=5,5'-diarylbipyridines) was described, where the majority of these complexes emit, as expected, from an admixture of ligand-to-ligand charge-transfer ^{3}LLCT/^{3}MLCT states. These complexes showed lifetimes of 500-950 ns and, therefore were defined as phosphorescent. Exceptionally, the last structure presented in **Figure 3.54**, possessing NMe_2 groups, potent electron-releasing substituents, in the ancillary ligand, presented an only short-lived emission band (τ = 12 ns). However, based on DFT calculations, the 10 μs lifetime measured at 77 K and the ≈7000 cm^{-1} stokes shift observed for the emission, it was defined as phosphorescent relaxation of an ^{3}ILCT(bpy) transition.

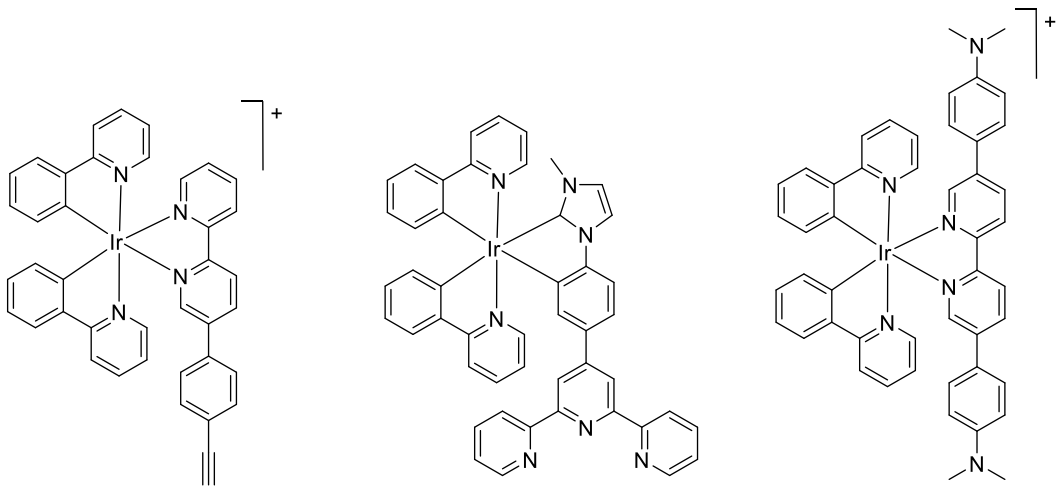

Figure 3.54. *Relatively compact iridium complexes with dual fluorescent/phosphorescent emission.*

It is worth noticing the resemblance between the structure introduced by Zysman et al. and that of compounds **C5**-**C7,** particularly to **C6**, with a 4-dialkylamino phenyl appended in 5 position to the 2,2'-bipyridine. However, the free complexes **C5**-**C7** show a smaller stokes shift of <3800 cm^{-1} compared to the reported complexes. Based on the resemblance with other dual emitters reported in the literature, the emissions at shorter wavelengths of nanosecond lifetimes observed in compounds **C5**-**C8** will be here defined as fluorescent. This description is additionally supported by comparing of the emission of the free compounds with the one of their respective ancillary ligands, which particularly concur in the case of **C5** and **C6** (**Figure 3.55**). This observation also supports the idea that the participation of the iridium in this transition is minimal not to say null, backing the singlet nature HB emissions of the complexes.

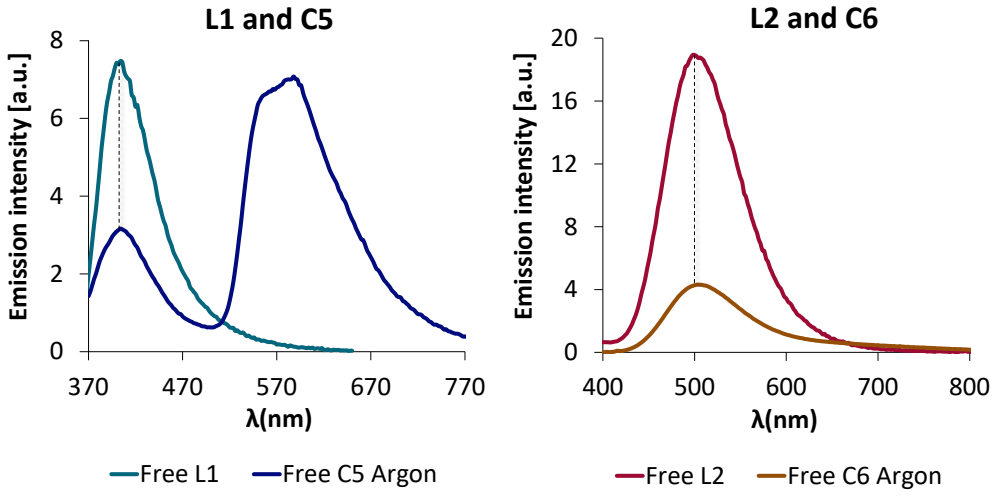

Figure 3.55. *Comparative emission spectra of **L1** with **C5** and **L2** with **C6**. Note the emission intensity is arbitrary.*

In this context, it is worth highlighting the case of compound **C6**, which upon excitation at the isosbestic point, in its free form showed an almost "pure" fluorescent emission whereas a red-shifted phosphorescence LB is observed upon interaction with Ba^{2+}. Even if this situation is very convenient for its use as a sensor, it is true that even in its free form, a phosphorescent component reveals when excited at lower energies than the isosbestic point.

In order to complement the characterization of **C6**, a two-dimensional excitation-emission map was measured under argon, for the free and Ba^{2+}-bound **C6**, shown in **Figure 3.56**. As mentioned before, for free **C6** the LB is hardly noticeable when excited

at 320–380nm, masked by the tailing of the HB emission. Nevertheless, it reveals an emission when the sample is excited in the region of highly energetic transitions (<280 nm) or in the visible part of the spectra (400-450 nm), as a very weak emission. The HB emission is very intense when exited at 320-380 nm, but it appears again activated when it is excited below 280 nm. This behaviour could also be observed in the excitation spectra illustrated in **Figure 3.52**. The **C6_Ba^{2+}** specie shows a single emission with the maximum at 600-650 nm, regardless the excitation wavelength, when excited below 400 nm. The emission reaches the maximum intensity when exciting the sample at 260 nm.

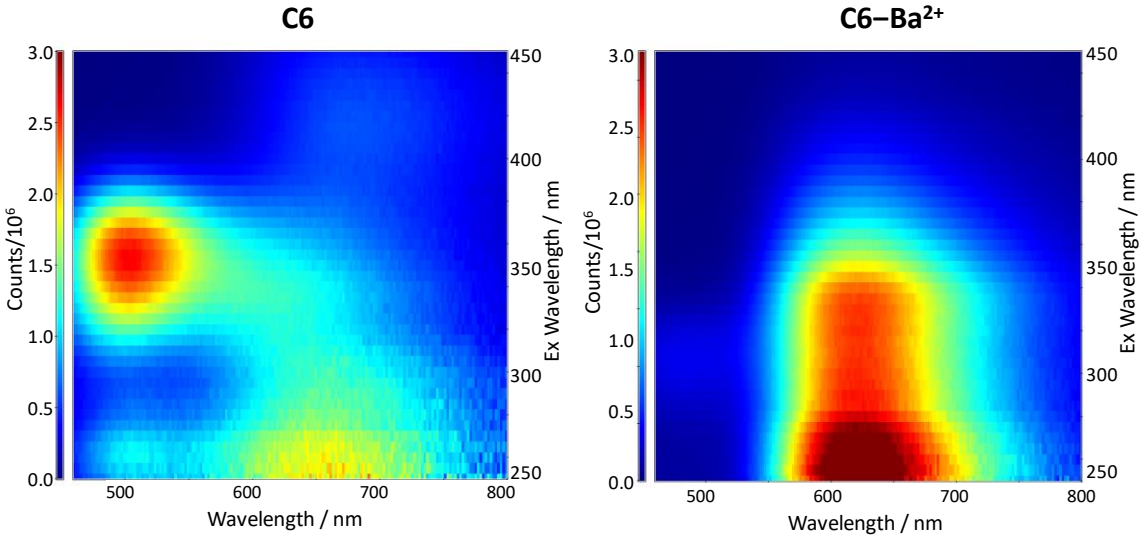

Figure 3.56. *Emission map of **C6** (left) and Ba^{2+}-bound **C6** (ight) in argoned MeCN $1{\cdot}10^{-5}$ M. Spectra displayed at different intensity scales to reveal the emission properties of the free sensor.*

The excitation-dependent emission behavior for the free **C6** is explained with the proposed Jablonski diagrams in **Figure 3.57**. When excited at the isosbestic point, 370 nm, a main emission is appreciated at 508 nm, with a residual band at around 650 nm. The band at 508 nm, HB band, is proposed to be the emissive relaxation from the ^{1}ILCT on the bipyridyl ligand, which has been defined as fluorescence. The residual emission, assigned to the ^{3}MLCT/^{3}LC state, could come from the direct excitation to the singlet MLLCT manifold and the relaxation to the ^{3}MLLCT/^{3}LC or the partial relaxation from the ^{1}ILCT to the ^{1}MLLCT to the triplet manifold. For the moment, the exact energy position of the ^{1}MLLCT is unknown (represented by the yellow arrow), and thus, the two processes could be possible.

If the complex is excited at lower wavelengths (<300 nm), two emissions are observed, the main band at 660 nm and another weak band at around 500 nm. For this dual

emission, another relaxation pathway is proposed, with the initial excitation to ^{1}MCT state. From here, the molecule relaxes by internal crossing to ^{1}MLLCT, mainly, and ^{1}LC a small portion. Thus, in the end, again, from ^{1}MLLCT relaxes to ^{3}MLLCT and shows the LB band and the weak HB arises from the relaxation from ^{1}ILCT.

Finally, if the sample is excited at low energies (>380 nm), the direct excitation and weak emission of the triplet manifold ^{3}MLLCT/^{3}ILCT is proposed.

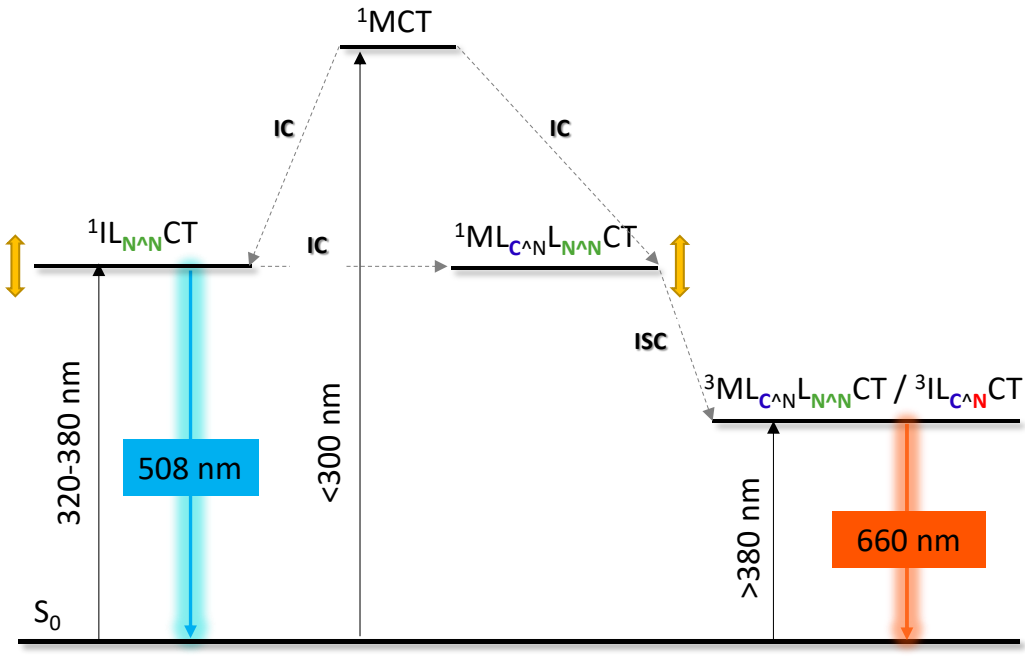

Figure 3.57. *Proposed Jablonski diagrams for* ***C6****, situation A and B.*

The Ba^{2+}-bound **C6** presents a similar absorption and emission spectra compared to the cationic $[Ir(ppy)_2(bpy)]^+$ complex. This effect can be explained by the fact that the lone-pair of the nitrogen is compromised in the interaction with Ba^{2+}, stabilizing the HOMO of the bipyridyl fragment. Due to this HOMO stabilization, the excitation to ^{1}ILCT is not accessible anymore. Therefore, as represented in **Figure 3.58**, the excitation occurs to the ^{1}MLLCT or ^{1}MCT state, depending on the excitation wavelength; with the subsequent inter crossing and the inter-system crossing to the triplet ^{3}MLLCT/^{3}ILCT. Thus, the single emission observed, regardless the excitation wavelength, is assigned to ^{3}MLLCT/^{3}ILCT.

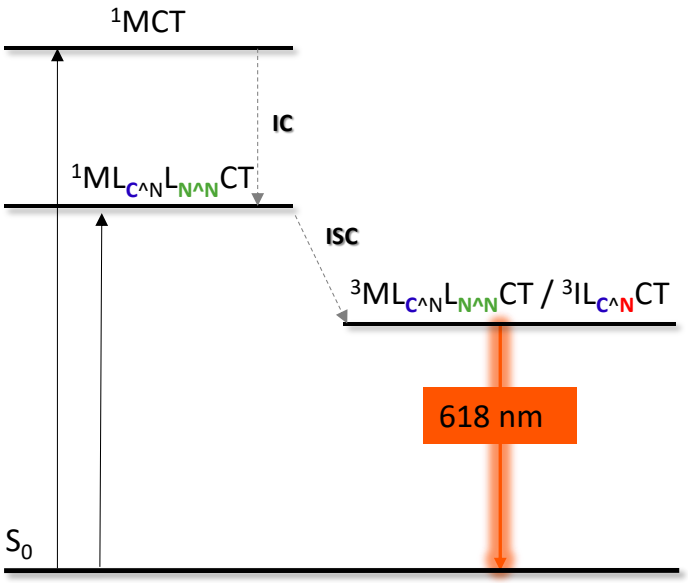

Figure 3.58. *Simplified Jablonski diagram proposed for Ba^{2+}-bound **C6** specie.*

Another anomaly, compared to the other complexes, was found for complex **C5**. In the case of unbound **C5**, upon excitation at the isosbestic point, in addition to the fluorescent band, the band at 560 nm was clearly observed (**Figure 3.49**). Lifetime measurements of this red-shifted emission showed a two-component lifetime, being dominant a long-lived decay of 6.7 µs (τ_1 = 388 ns (4%), τ_2 = 6735 (96%)). This long-lived emission is not observed in the bound sensor nor for the other Ba^{2+} bound complexes. The long-lived nature of this emission and its fine structure points to an emitting state with a dominant ^{3}LLCT character and a much less significant contribution from the ^{3}MLCT state.

Additionally, all the complexes showed slightly larger emission quantum yields upon Ba^{2+}-chelation compared to the unbound compounds, which is beneficial for their potential use as sensors.

Table 3.3 shows the data related to the sensing behavior of the complexes. When considering only the LB as the signaling emission, **C5** could be described as a modest phosphorescent off/on sensor, being the calculated discrimination factor more favorable in aerated solutions. **C7** could be discarded as off/on sensor, as the discrimination factor is very low in both, aerated and argoned solutions. **C8**, opposite to **C5**, works better in argoned environment, resulting in a discrimination factor of 6.25. In

general, in comparison to the **FBI** compound, the obtained f_λ values are lower. For **C6**, when considering only the emission at 618 nm as a signaling probe, due to the overlap of the tailing emission of the free sensor with the Ba^{2+}-bound **C6** emission, the calculated discrimination factors (f_λ) are also modest for this sensor.

Table 3.3. *Emission properties as sensors for Ba^{2+} of **C5**-**C8**.*

	Δλ (nm)	off/on		Ratiometric			
		f_λ (aerated)	f_λ (argoned)	I_{LB}/I_{HB} (aerated)	Variation factor (aereated)	I_{LB}/I_{HB} (argoned)	Variation factor (argoned)
C5	190	7.93	2.19	0.19	11.95	2.26	4.94
C5-Ba				2.27		11.13	
C6	129	0.27	5.13	0.15	68.87	0.21	308.90
C6-Ba				10.33		64.87	
C7	110	1.47	1.12	0.28	13.57	0.26	19.31
C7-Ba				3.80		5.02	
C8	40	3.14	6.25	0.73	2.55	0.76	2.45
C8-Ba				1.86		1.86	

Calculated at the emission maxima of the bound sensor. e) Calculated at the LB maxima of the bound sensors as $f_\lambda = (I_\lambda(\mathbf{C\text{-}Ba^{2+}}) - I_\lambda(\mathbf{C}))/I_\lambda(\mathbf{C})$, as described in reference[15]

As a ratiometric sensor, **C5** is more effective in aerated solutions compared to argon-equilibrated conditions. Upon Ba^{2+} binding, the I_{LB}/I_{HB} emission ratio for this compound increases by a factor of 12 in aerated solutions, whereas it reaches only a factor of 5 in argon-equilibrated samples.

C6 showed to perform best as a ratiometric indicator for Ba^{2+}. Even though the Δλ is larger for **C5**, the free **C6** showed a monocolor fluorescent emission centered at 502 nm leaving an almost emission free region at longer wavelengths, around 700 nm, where Ba^{2+}-bound **C6** shows an intense phosphorescent emission. The addition of Ba^{2+} to a solution of **C6** increases the I_{LB}/I_{HB} ratio by a factor of 69, attaining a factor of 309 in argon-equilibrated solutions. Indeed, most remarkably, upon Ba^{2+} binding there is a clear switch in the emission color (from green to red) in both aerated and argon-equilibrated solutions (**Figure 3.59**) and therefore, **C6** falls in a specific category of

ratiometric sensors, which can also be described as ratiometric probes based on two reversible signal changes,[33] or bicolor indicators.[15,34]

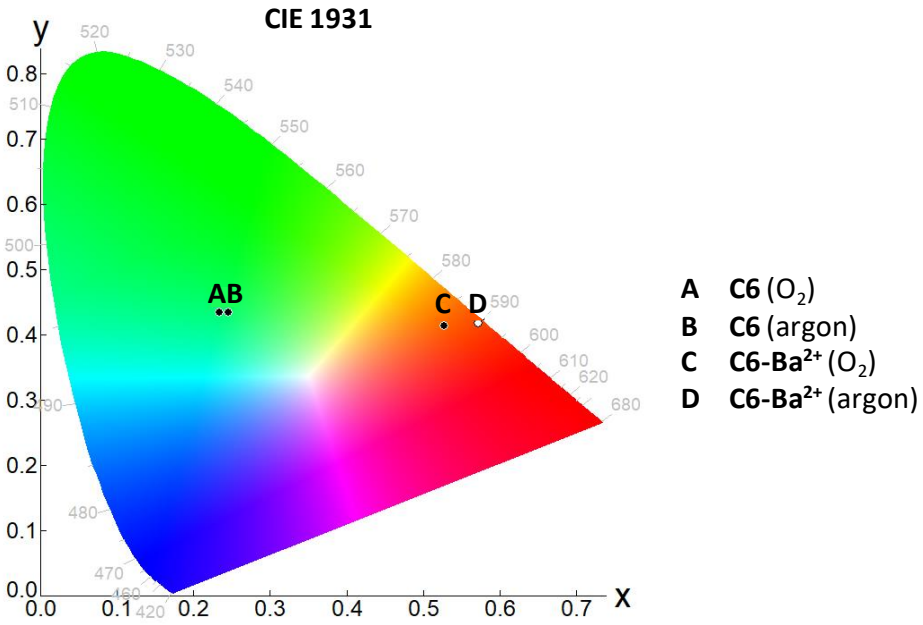

Figure 3.59. *Chromaticity map (Commission Internationale de l'Éclairage 1931 (CIE) coordinates) for* ***C6*** *sensor, based on emission spectra of MeCN 1·10^{-5} M solutions under excitation at 307 nm.*

These results clearly show that **C6** is a promising ratiometric indicator for Ba^{2+}. Nevertheless, the sensor required for barium tagging experiments needs an explicit off/on behavior in a xenon environment. In this context, **C6** and **C8** show to perform the best, and based on their Δλ, **C6** was chosen for time-resolved studies.

3.3.4 Selectivity

To determine the selectivity of the sensors, the interaction of the iridium sensors with other cation analytes was studied. For this purpose, 1 equivalent and concentrated solutions of perchlorate salts in MeCN were added to solutions of free complexes at 1·10^{-5} M, and their absorption and emission spectra were measured (see SI). **Figure 3.60** shows the fluorescence response when saturated salt solutions are added. As expected, the four complexes respond to barium and strontium.

In the case of **C5**, the fine shape of emission of the LB is changed upon Ba^{2+} and Sr^{2+} addition. For **C6**, similar to **C7** and **C8**, the phosphorescent band appears mainly when Ba^{2+}, Sr^{2+} and Ca^{2+} are added. This tendency is also supported by the absorption spectra

(see SI). **FBI** also showed the same intensity shift with Sr^{2+}. This is not a surprising result, as the 18-crown-6 ther has been described in the literature to uptake Ca^{2+} and Sr^{2+}.[35,36] A peculiar behavior was observed for Na^{+}, where the intensity of the HB of **C6** and **C7** increases upon cation addition, which happened also with K^{+} in the case of **C7**.

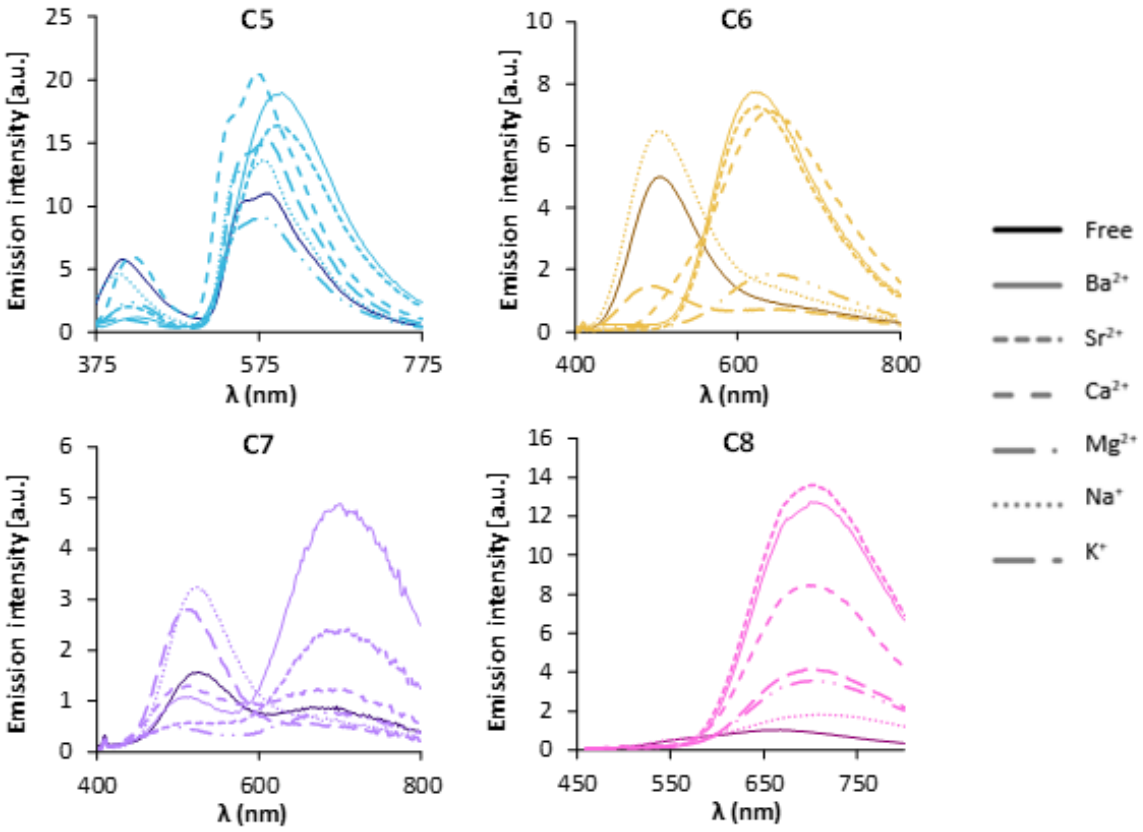

***Figure 3.60**. Emission response of complexes **C5-C8** with saturated solutions of perchlorate salts in MeCN. Excited at 405 nm and emission measured at the maxima of the chelated specie.*

In the final application, none of these ions is expected to be present. Nevertheless, they must be taken into account in preliminary studies because, for instance Ca^{2+}, Mg^{2+}, Na^{+} or K^{+} are very common cations as impurities in solvents, the most abundant cations present in water.

3.3.5 Time-resolved bicolor sensors

As described before, the emission wavelength difference of the free and Ba^{2+}-bound compounds made the sensors potential bicolour indicators. Nevertheless, the difference in the emissions lifetime found for the free and chelated complexes presented the opportunity to exploit an additional discrimination factor, the time.

As previously presented, and summarized in **Table 3.2**, the free sensor **C6** presents a purely fluorescent emission (τ = 2.7 ns, 502 nm) and the bound sensor a mixed fluorescent and phosphorescent decay (τ = 11 ns (12%), 121 ns (64%), 371 ns (24%), 618 nm) (**Figure 3.61**).

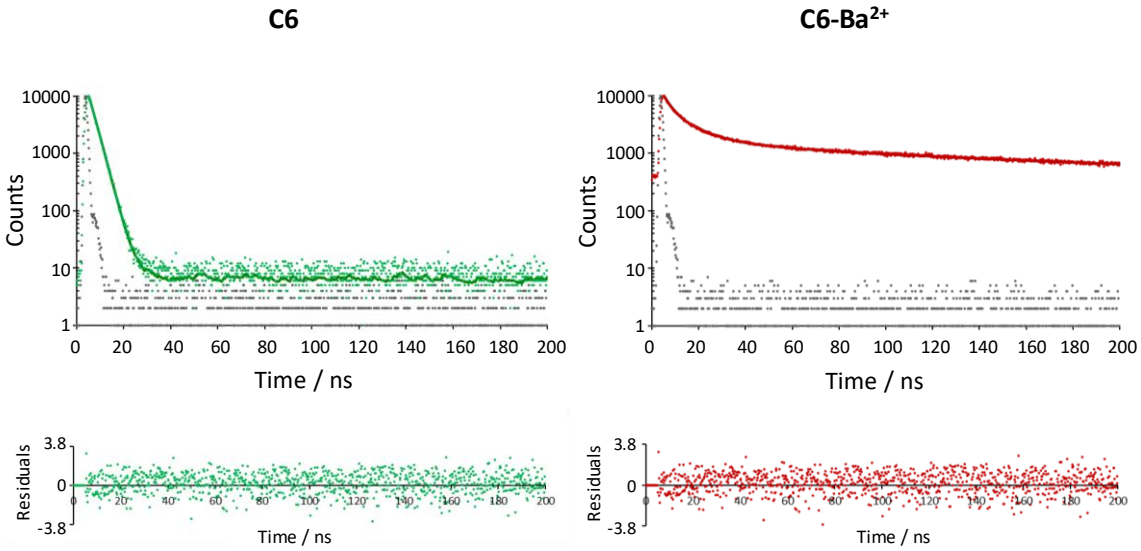

Figure 3.61. *Decay lifetimes of **C6** and Ba^{2+}-bound **C6**. Measurements acquired with an EPLED lamp excited at 340 nm, with 500 ns pulse. Lifetime measured at 502 nm for **C6** and at 618 for **C6**-Ba^{2+}.*

This lifetime difference makes it reasonable to assume that using a pulsed-light excitation and time-gated acquisition it should be possible to detect exclusively bound sensors from mixtures containing both components. This strategy is illustrated in **Figure 3.62**. If this delayed acquisition is combined with a color filter centered around 618 nm in the LB region, we should be able to increase outstandingly the current sensibility (discrimination factor) of the sensors.

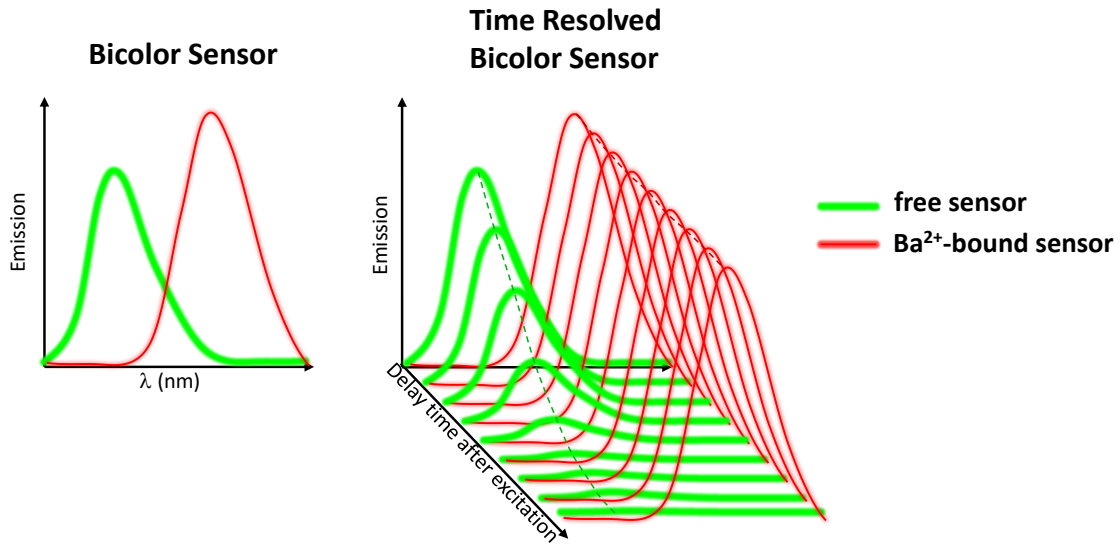

Figure 3.62. *Illustration of the strategy used for delayed acquisition.*

In order to demonstrate this hypothesis, a time-resolved emission spectrum (TRES) of **C6** and Ba^{2+}-bound **C6** was carried out (**Figure 3.63**). In a TRES experiment, a pulsed excitation source excites the sample, and the emission spectra are recorded at specified delay times after acquisition to create a 3D dataset that contains the spectral and time evolution of the emission. The TRES spectra of the **C6** samples were acquired by exciting with an EPL340 source and using MSC mode with a frequency of 100 KHz. The emission spectra were collected in the range 450-750 nm at different delay times within a temporal window of 5000 ns.

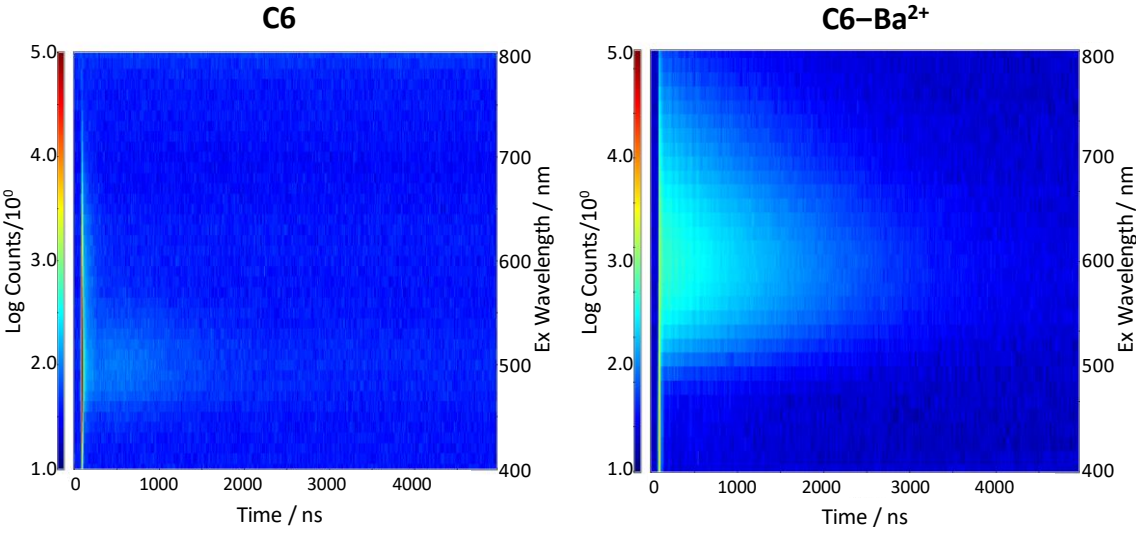

Figure 3.63. *Time-resolved emission spectrum of **C6** in the absence (c) and presence (d) of $Ba(ClO_4)_2$ (λ_{ex} = 370 nm) in MeCN in argon equilibrated solutions. Excited with an EPL340 source and using MSC mode with a frequency of 100 KHz. Collected in the range 450-750 nm, within a temporal window of 5000 ns.*

As expected, TRES of free **C6** shows an emission band with the most intense region between 450-550 nm, the HB emission, which decays in the first ns time, and after 1000 ns no emission is left. On the contrary, the Ba^{2+}-bound **C6** spectra, shows a band centered at 600 nm, the LB emission, shows longer-lived emissions, in agreement with the lifetimes measured at the corresponding emission maxima.

TRES experiments permit selectively displaying the total emission spectra (integrating all the individual spectra from 0 to 5000 ns) or simulate the emission spectra after applying a time-gated acquisition (for instance integrating the spectra from 250 to 5000 ns). The simulated total and time-gated spectra of the free and bound sensors are displayed in **Figure 3.64**. As expected, the total emission spectrum resembles that obtained in steady state emission experiments. On the contrary, in the delayed spectra, most of the fluorescent signal caused by the free sensor is removed (b in **Figure 3.64**). This demonstrates that if an acquisition is made with a delay after the excitation pulse it should be possible to detect chelated molecules with very high sensitivity due to removal of the free sensors signal.

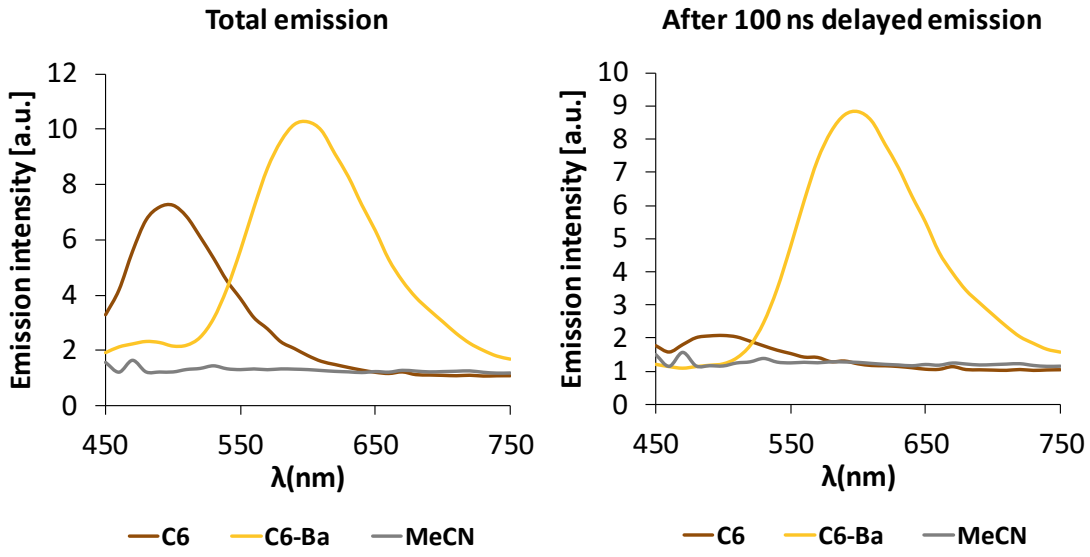

Figure 3.64. *Time-integrated spectra total (left) and 100 ns delayed from excitation (right), extracted from TRES experiments. Excitation EPLED-340 nm, MultiChannel Scaling (MSC), 100 KHz, stop condition 20 min.*

If the solvents emission is subtracted to **C6** and **C6**-Ba^{2+}, it could result in the increment by 3 orders of magnitude of the discrimination factor at the Ba^{2+}-bound **C6** maximum.

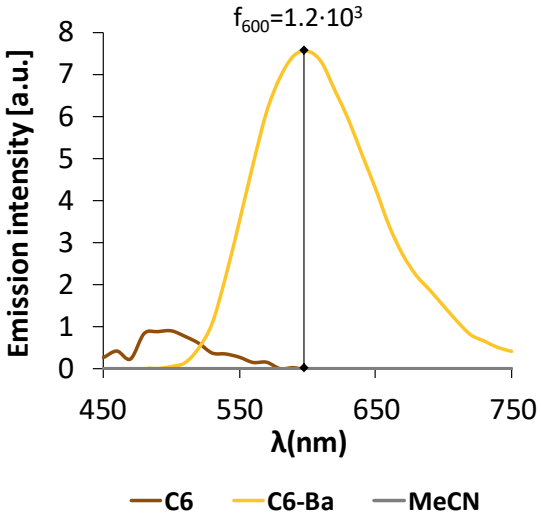

Figure 2.65. *Solvent emission subtracted summed emission spectra with 100 ns delay of* ***C6*** *and* ***C6****-Ba^{2+} in the TRES experiments.*

TRES technique is mostly exploited for biological applications, due to the frequent presence of endogenous fluorophores in sample matrices.[22,37–39] The use of TRES thus allows the phosphorescent response of the complex to the target analyte to be efficiently detected even in the presence of background fluorescence. In the context of barium-tagging, as the device would be constructed by a monolayer of free sensors and the emission proceeding from the single Ba^{2+}-bound molecule is needed to be discerned form the emissive background of unbound sensors, the strategy of the acquisition at delayed time, combined with a color filter rejecting the signal of the unbound sensor region, could derive in a potentially background free signal. In this framework, **C6** has shown promising results.

3.4 References

1 M. Nonoyama, *Bull. Chem. Soc. Jpn.*, 1974, **47**, 767–768.

2 A. B. Tamayo, B. D. Alleyne, P. I. Djurovich, S. Lamansky, I. Tsyba, N. N. Ho, R. Bau and M. E. Thompson, *J. Am. Chem. Soc.*, 2003, **125**, 7377–7387.

3 M. C. DeRosa, D. J. Hodgson, G. D. Enright, B. Dawson, C. E. B. Evans and R. J. Crutchley, *J. Am. Chem. Soc.*, 2004, **126**, 7619–7626.

4 Q. Li, X. Zhang, Y. Cao, C. Shi, P. Tao, Q. Zhao and A. Yuan, *Dalt. Trans.*, 2019, **48**, 4596–4601.

5 K. A. McGee and K. R. Mann, *Inorg. Chem.*, 2007, **46**, 7800–7809.

6 A. M. Bünzli, E. C. Constable, C. E. Housecroft, A. Prescimone, J. A. Zampese, G.

Longo, L. Gil-Escrig, A. Pertegás, E. Ortí and H. J. Bolink, *Chem. Sci.*, 2015, **6**, 2843–2852.

7 S. Sprouse, K. A. King, P. J. Spellane and R. J. Watts, *J. Am. Chem. Soc.*, 1984, **106**, 6647–6653.

8 *Iridium(III) in Optoelectronic and Photonics Applications*, Wiley, 2017.

9 N. Zhao, Y. H. Wu, H. M. Wen, X. Zhang and Z. N. Chen, *Organometallics*, 2009, **28**, 5603–5611.

10 S. Ladouceur, D. Fortin and E. Zysman-Colman, *Inorg. Chem.*, 2010, **49**, 5625–5641.

11 F. Lafolet, S. Welter, Z. Popović and L. De Cola, *J. Mater. Chem.*, 2005, 15, 2820–2828.

12 D. Brynn Hibbert and P. Thordarson, *Chem. Commun.*, 2016, **52**, 12792–12805.

13 Supramolecular.org - Binding Constant Calculators | Supramolecular, http://supramolecular.org/, (accessed 19 December 2022).

14 P. Thordarson, *Chem. Soc. Rev.*, 2011, **40**, 1305–1323.

15 I. Rivilla, B. Aparicio, J. M. Bueno, D. Casanova, C. Tonnelé, Z. Freixa, P. Herrero, C. Rogero, J. I. Miranda, R. M. Martínez-Ojeda, F. Monrabal, B. Olave, T. Schäfer, P. Artal, D. Nygren, F. P. Cossío and J. J. Gómez-Cadenas, *Nature*, 2020, **583**, 48–54.

16 D. A. Dougherty, *Acc. Chem. Res.*, 2013, **46**, 885–893.

17 S. K. Behera, S. Y. Park and J. Gierschner, *Angew. Chemie - Int. Ed.*, 2021, 60, 22624–22638.

18 K. A. King and R. J. Watts, *J. Am. Chem. Soc.*, 1987, **109**, 1589–1590.

19 A. P. Wilde, K. A. King and R. J. Watts, *J. Phys. Chem.*, 1991, **95**, 629–634.

20 Y. Ohsawa, S. Sprouse, K. A. King, M. K. DeArmond, K. W. Hanck and R. J. Watts, *J. Phys. Chem.*, 1987, **91**, 1047–1054.

21 P. A. Scattergood, A. M. Ranieri, L. Charalambou, A. Comia, D. A. W. Ross, C. R. Rice, S. J. O. Hardman, J. L. Heully, I. M. Dixon, M. Massi, F. Alary and P. I. P. Elliott, *Inorg. Chem.*, 2020, **59**, 1785–1803.

22 Y. You, Y. Han, Y. M. Lee, S. Y. Park, W. Nam and S. J. Lippard, *J. Am. Chem. Soc.*, 2011, **133**, 11488–11491.

23 S. H. Wu, J. W. Ling, S. H. Lai, M. J. Huang, C. H. Cheng and I. C. Chen, *J. Phys. Chem. A*, 2010, **114**, 10339–10344.

24 T. Yoshihara, Y. Yamaguchi, M. Hosaka, T. Takeuchi, S. Tobita, T. Yoshihara, Y. Yamaguchi, S. Tobita, M. Hosaka and T. Takeuchi, *Angew. Chemie Int. Ed.*, 2012, **51**, 4148–4151.

25 T. Yoshihara, S. Murayama and S. Tobita, *Sensors (Switzerland)*, 2015, **15**, 13503–

13521.

26 H. Shi, H. Sun, H. Yang, S. Liu, G. Jenkins, W. Feng, F. Li, Q. Zhao, B. Liu and W. Huang, *Adv. Funct. Mater.*, 2013, **23**, 3268–3276.

27 H. Shi, X. Ma, Q. Zhao, B. Liu, Q. Qu, Z. An, Y. Zhao and W. Huang, *Adv. Funct. Mater.*, 2014, **24**, 4823–4830.

28 H. F. Shi, S. J. Liu, H. Bin Sun, W. J. Xu, Z. F. An, J. Chen, S. Sun, X. M. Lu, Q. Zhao and W. Huang, *Chem. - A Eur. J.*, 2010, **16**, 12158–12167.

29 Y. Wu, G. D. Sutton, M. D. S. Halamicek, X. Xing, J. Bao and T. S. Teets, *Chem. Sci.*, 2022, **13**, 8804–8812.

30 K. S. Choung, K. Marroquin and T. S. Teets, *Chem. Sci.*, 2019, **10**, 5124–5132.

31 A. Y. Gitlina, M. V. Ivonina, V. V. Sizov, G. L. Starova, A. P. Pushkarev, D. Volyniuk, S. P. Tunik, I. O. Koshevoy and E. V. Grachova, *Dalt. Trans.*, 2018, **47**, 7578–7586.

32 S. K. Gupta, A. Haridas and J. Choudhury, *Chem. - A Eur. J.*, 2017, **23**, 4770–4773.

33 R. Gui, H. Jin, X. Bu, Y. Fu, Z. Wang and Q. Liu, *Coord. Chem. Rev.*, 2019, 383, 82–103.

34 Z. Freixa, I. Rivilla, F. Monrabal, J. J. Gómez-Cadenas and F. P. Cossío, *Phys. Chem. Chem. Phys.*, 2021, 23, 15440–15457.

35 H. Luo, S. Dai and P. V. Bonnesen, *Anal. Chem.*, 2004, **76**, 2773–2779.

36 W. Hughes, A. Rananaware, D. D. La, L. A. Jones, S. Bhargava and S. V. Bhosale, *Sensors Actuators, B Chem.*, 2017, **244**, 854–860.

37 J. Ru, X. Chen, L. Guan, X. Tang, C. Wang, Y. Meng, G. Zhang and W. Liu, *Anal. Chem.*, 2015, **87**, 3255–3262.

38 Y. You, S. Lee, T. Kim, K. Ohkubo, W. S. Chae, S. Fukuzumi, G. J. Jhon, W. Nam and S. J. Lippard, *J. Am. Chem. Soc.*, 2011, **133**, 18328–18342.

39 W. Wang, Z. Mao, M. Wang, L. J. Liu, D. W. J. Kwong, C. H. Leung and D. L. Ma, *Chem. Commun.*, 2016, **52**, 3611–3614.

Chapter 4

Functionalization and immobilization on surfaces

In the last chapter, initially the functionalization and immobilization on surface of two model complexes used as luminescent dyes will be discussed. In a last section, the functionalization and immobilization on surface of the selected C6 complex will be presented.

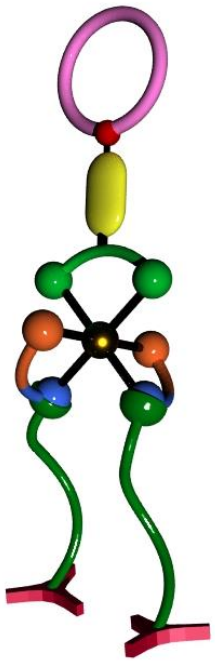

4.1 INTRODUCTION

In the context of barium tagging within the NEXT experiment, the system requires a homogeneously distributed monolayer of emissive efficient and selective sensors covering the entire cathode surface in an HPXe-TPC.

As described in Chapter 1, the addition of a linker to the chemosensor is required to anchor it onto a suitable surface or substrate (**Figure 4.1**). The use of linkers to immobilize defined systems to a substrate has been widely applied to support other structures such as nanoparticles, catalysts, choromophores, proteins or other biomolecules, etc.[1–6]

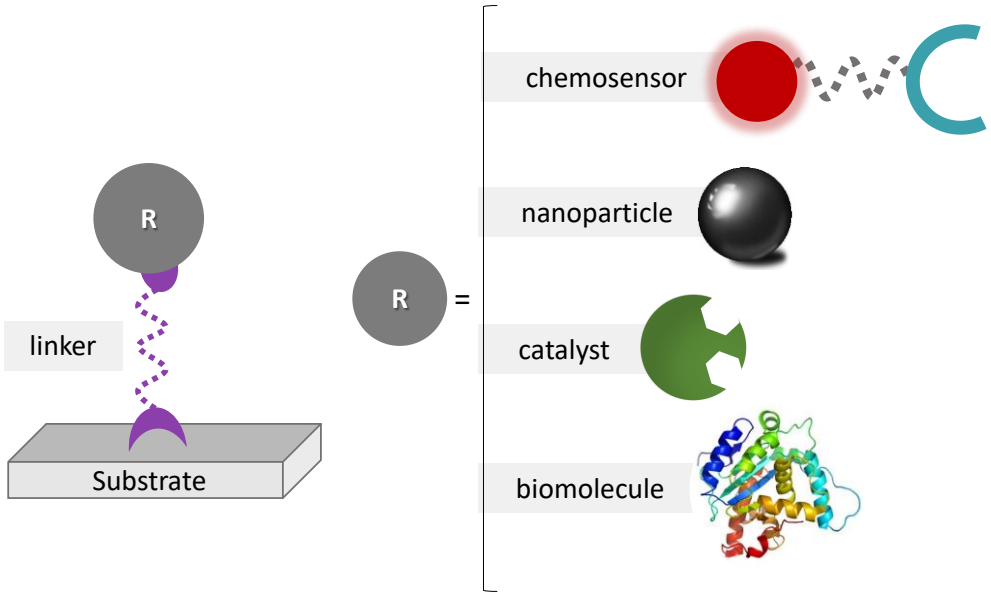

Figure 4.1. *Schematic representation of an immobilized system. Systems, such as chemosensors, nanoparticles, catalysts, biomolecules, etc.*

The linker provides a tool to construct self-assembled monolayers, or SAMs. SAMs are assemblies formed by the adsorption of molecular constituents from solution or the gas phase onto the surface of solids: the adsorbates organize spontaneously and sometimes epitaxially into crystalline or semicrystalline structures, such as metallic or metal oxide surfaces. As illustrated in **Figure 4.2**, the linker, in purple, is constructed with a head group that has a strong affinity to the substrate and anchors the molecule to it. It is attached to a tail group, which possesses a terminal or end group that can be further chemically functionalized with a wide range of chemical modifications, either pre- or post-assembly on the surface, to provide surfaces with defined chemistries.

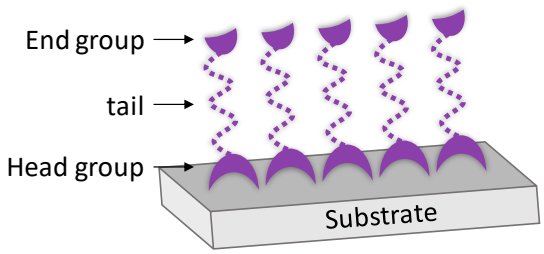

Figure 4.2. *Representation of a Self-Assembled Monolayer, SAM, structure.*

The most well-known and extensively studied SAMs are based on alkanethiols anchored on gold surfaces.[7–10] The high affinity of the thiol head group to gold leads to a spontaneous formation of an Au–S bond. Therefore, it is often presented as a model system of SAMs. On the other hand, trialkoxysilane linkers are commonly used for modifying metal oxide substrates. They have been widely studied for the modification of silica-based materials and have since been extended to other metal oxides, including ZnO, TiO_2, Al_2O_3, and Fe_3O_4.[11–13]

As a transparent surface was required for the NEXT experiment (as the excitation and read-out processes must be outside the Xenon chamber), quartz was proposed as model substrate (**Figure 4.3**). Quartz is a hard, crystalline mineral composed of silica. Accordingly, silane-based functionalization was studied for immobilization of the sensor. This methodology is usually referred as surface silanization.

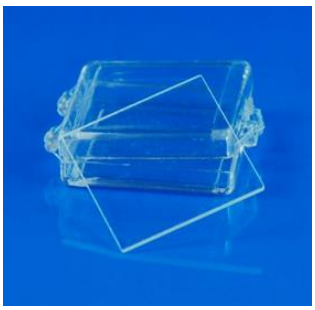

Figure 4.3. *Quartz slide of 1 cm^2*

The silanization process is based on the adsorption, self-assembly and covalent binding of silane-based organic molecules onto surfaces resulting in a densely packed SAM. Silane-anchored layers, in particular, are mechanically robust, thermally stable up to at least 250 °C and are not subject to swelling in the presence of solvents.[14,15] The main advantage of using organosilanes for monolayer formation on SiO_2 surfaces is the rapid

formation of a covalent linkage between the substrate and the anchoring group. This covalent bond stabilizes the monolayer, and also allows for easy further chemical modification without compromising the integrity of the monolayer.

Metal oxide surfaces (like quartz or ITO, indium tin oxide) can all be silanized, because they contain exposed hydroxy groups after activation, which form a covalent -M-O-Si_{silane}- bond.. Generally, the surface is activated by strong acids or oxygen plasma to clean the surface and generate (M-OH) at the surface, silanol in the case of quartz. Then, the formation of the monolayer occurs in a three-step mechanism **Scheme 4.1**.[16] The organosilane molecules are hydrolysed in solution at the anchoring moment to create hydroxysilanes or silanols, which then self-assemble by hydrogen bonding interactions with the substrate and attractive forces between the chains. Attachment to the surface occurs via a condensation reaction with surface hydroxyl groups. Sometimes, the silanol condensation between organosilane chains is described in a previous step to the hydrogen binding to the surface.[17,18]

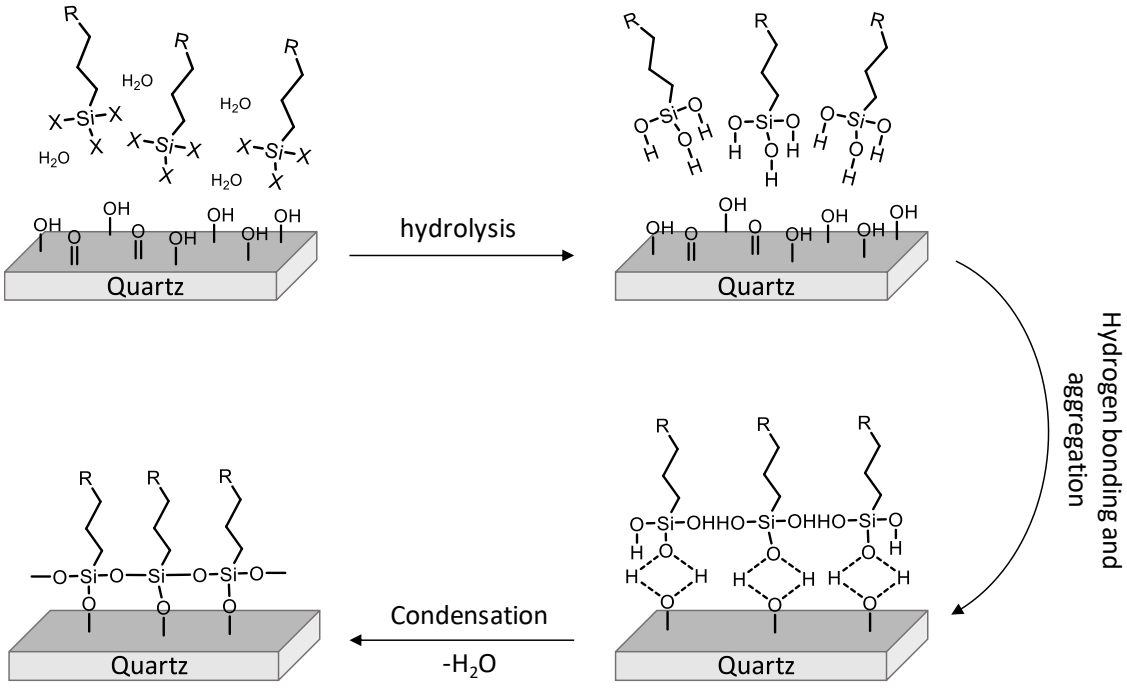

Scheme 4.1. *The three main steps involved in the silanization process.*

The conditions employed for the silanization are critical to the SAMs properties (thickness, homogeneity, etc) as well as the desired follow-up reactivity or functionality. Several studies indicate that the deposition process strongly depends on the solvent,[19]

deposition time,[20,21] temperature,[22] water content, and age of the solution.[23] In addition, the storage of organosilanes is typically subjected to the formation of polysiloxane aggregates in solution, which is fast at high water contents and lower temperatures.[24] The aggregates lose their reactivity to covalently conjugate on surfaces but are physically deposited on surfaces, giving rise to an unstable and inhomogeneous film containing aggregates (**Figure 4.4**).

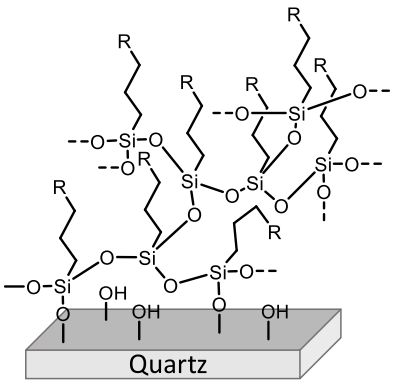

Figure 4.4. *Inhomogeneous polysiloxane aggregate deposited in a quartz surface.*

Among organosilanes (**Figure 4.5**), the most often employed head groups (SiX_3) are the trialkoxysilanes, such as methoxy and ethoxy terminated groups. At the same time, this organosilanes can be classified according to their end or terminal functional group of the alkylic chain (R): aminosilanes –with a primary or secondary amine–, mercaptosilanes –bearing a thiol as end group– or glycidosilanes –with an epoxide group–.

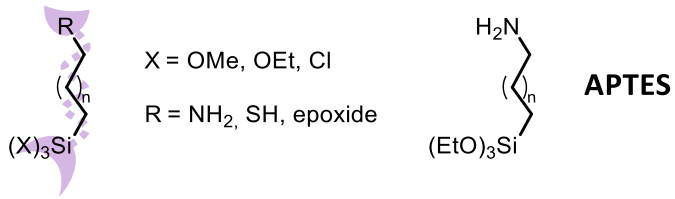

Figure 4.5. *Linker structure of an organosilane, based on their head (R) and end (SiX_3) groups.*

In this context, one of the most widely used linkers to incorporate a molecular entity to a surface is the aminopropyltriethoxysilane, APTES (**Figure 4.5**). APTES possesses three hydrolysable ethoxy groups, which serve to anchor compunds onto the surface through silanization of the surface. It is especially well-suited for activated quartz or ITO substrates as the end group is terminated with a primary amine capable of reacting with

other functional groups. Thus, this amine provides a reacting group to covalently or ionically bond a desired compound to the APTES and, eventually, to the surface. When silanization is performed directly using APTES, it rendersamine-terminated surfaces that have been applied for promoting protein adhesion[25–27] and cell growth on biological implants[28] and in lab-on-a-chip applications,[29–31] making it probably the best-known reagent used for surface functionalization.[32] APTES has also been used to attach metal nanoparticles to silica substrates because of the strong interaction between the amine group and the metal particles.[33,34]

One of the most widely employed functionalization reactions when using APTES as linker is based on the amide formation, by reacting the amine-terminated APTES, with an organic carboxylic acid , as shown in **Scheme 4.2**. The usual pathway involves the acid halide formation, from the carboxylic acid, to subsequently perform the coupling. The typical reagent employed for this synthesis is thionyl chloride ($SOCl_2$). Another route would rely on the utilization of coupling agents such as DCC and EDC, carbamides, which make the carboxylic acid more reactive towards a nucleophilic attack. For instance, this last methodology is often used for the immobilization of antibodies on surfaces.[35–37]

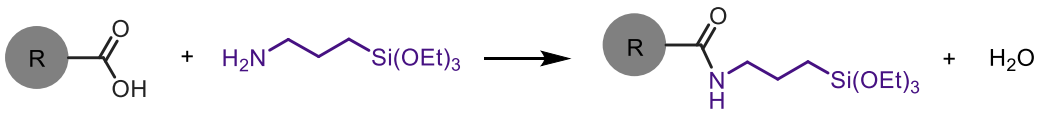

Scheme 4.2. *Condensation reaction between a system bearing a carboxylic acid and the primary amine of the APTES.*

Due to the feasibility of achieving a sensor with an appended carboxylic acid functionality and to the thoroughly studied coupling reaction on the surface chemistry context, this coupling was chosen to immobilize the sensors onto the surface.

In this direction, two strategies have been applied in the literature for the immobilization, as resumed in **Figure 4.6**. The first strategy, which is the conventional method, is based on the anchoring of the APTES spacer to the substrate, and react the amino-terminated substrate with the desired compound post-assembly. Most of the references found in the literature follow this methodology.[38–44] The second approach relies on the synthesis pre-assembly of the APTES appended compound, followed by the immobilization of the whole system to the surface.[45–48]

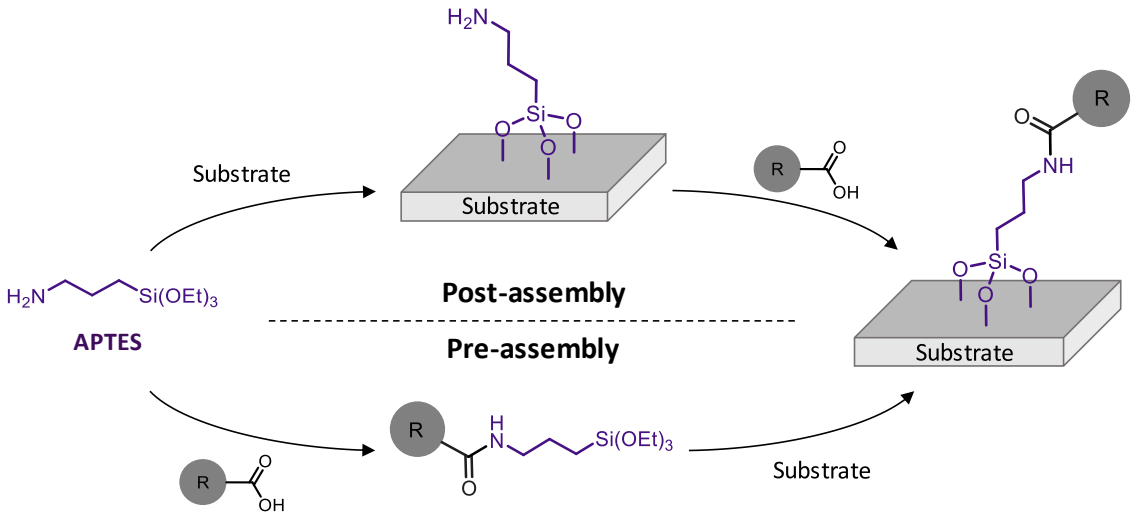

Figure 4.6. *Schematic representation of the two approaches used to anchor a compound to a surface using APTES as spacer and linker.*

The pre-assemblyprocedure was considered more appropriate in our case as it circumvents some drawbacks associated with the post-assembly procedure. Namely, in the post-assembly approach: a) unreacted amines would be left on the surface, that could compete with the sensor for Ba^{2+} binding, and could hinder the sensing performance; b) higher loadings of carboxylic acid derivatives are needed for the coupling reaction between an acid in solution and an amine on the surface. Additionally, the isolation of the APTES bearing sensor, allows a direct comparison of the photophysical behavior of the same compound in solution and upono immobilization on the surface.

Thus, first the functionalization of the desired compounds with the linker was addressed, to later proceed with the immobilization step onto a quartz surface.

4.2 MODEL COMPOUNDS

Before beginning with the immobilization of a sensor of interest, the anchoring process was studied with two simpler iridium and ruthenium complexes, **Ir_APTES** and **Ru_APTES** (**Figure 4.7**). These two model complexes were used to optimize the conditions needed for the immobilization of the desired sensors, (reaction time, temperature, solvents, etc) on quartz substrates. As exposed previously, good control over the structure and formation of functional organosilane coatings appears to be fundamentally critical and challenging.

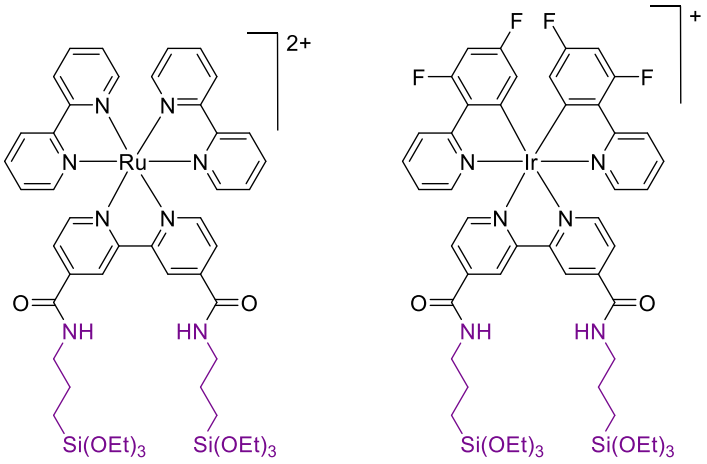

Ru_APTES **Ir_APTES**

Figure 4.7. *Structure of the two model organometallic compounds functionalized with the APTES linker,* ***Ir_APTES*** *and* ***Ru_APTES****.*

Additionally, these organometallic compounds were selected due to their intense emission at two different colors (**Ru_APTES** in red and **Ir_APTES** in yellow/green), which makes them perfectly suited to simulate the situation of free and bound bicolor sensors –the latest generations of organic **FBI** sensors under development at Prof. Cossío's group shine in these two colors–. The surfaces functionalized with these compounds, independently (a and b in **Figure 4.8**) and in hybrid mixtures of controlled composition (c in **Figure 4.8**), were intended to be used as testers to optimize the optics setup that needs to be developed for the NEXT experiment.

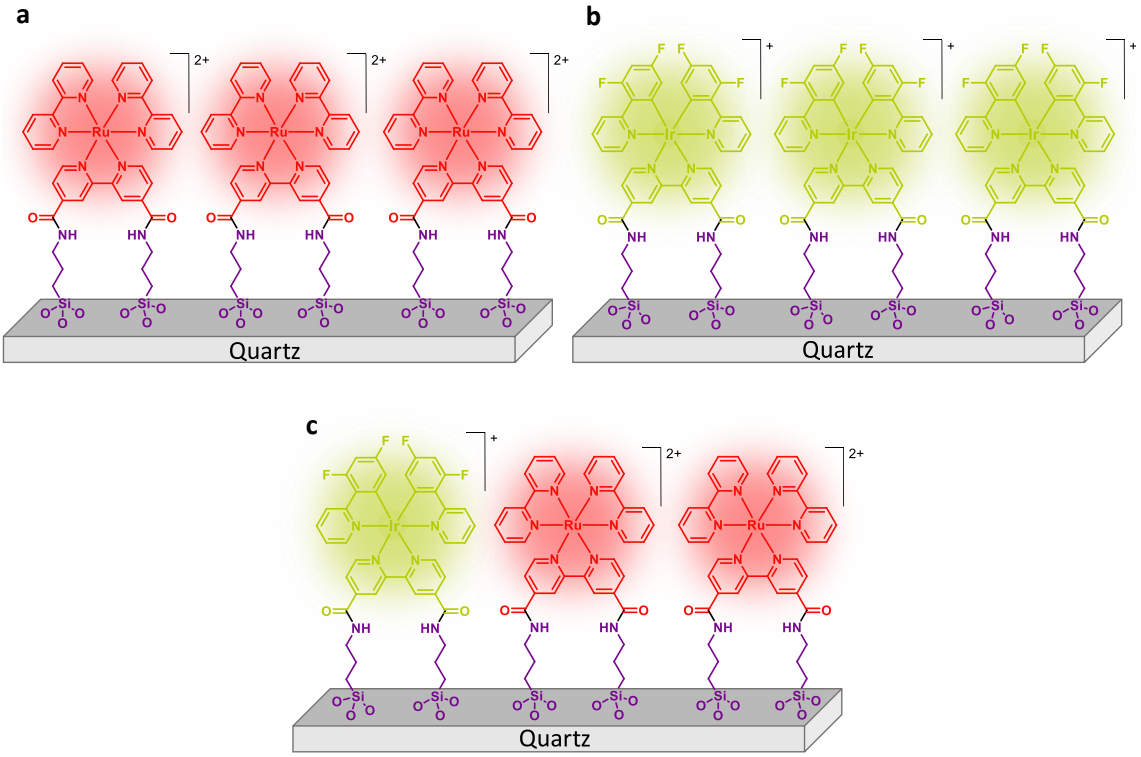

Figure 4.8. *Representation of* ***Ir_APTES*** *and* ***Ru-APTES*** *immobilized onto quartz surfaces, as pure surfaces (a and b) or hybrid surface (c).*

Thus, in this section, the synthesis and photophysical characterization of these model compounds will be described. Additionally, immobilization process of these sensors on quartz substrates will be detailed, together with the photophysical properties of the functionalized surfaces.

4.2.1 Functionalization

For the addition of the spacer APTES to the ancillary 2,2'-bipyridyl ligand in the complexes, two different approaches can be considered, as depicted in **Scheme 4.3**: the APTES functionalization to a 4,4'-dicarboxylic acid-2,2'-bipyridine and its subsequent coordination to the metal center (Approach A),[49] or the direct functionalization of the corresponding organometallic compound containing a coordinated 4,4'-dicarboxylic acid-2,2'-bipyridine (Approach B).[50]

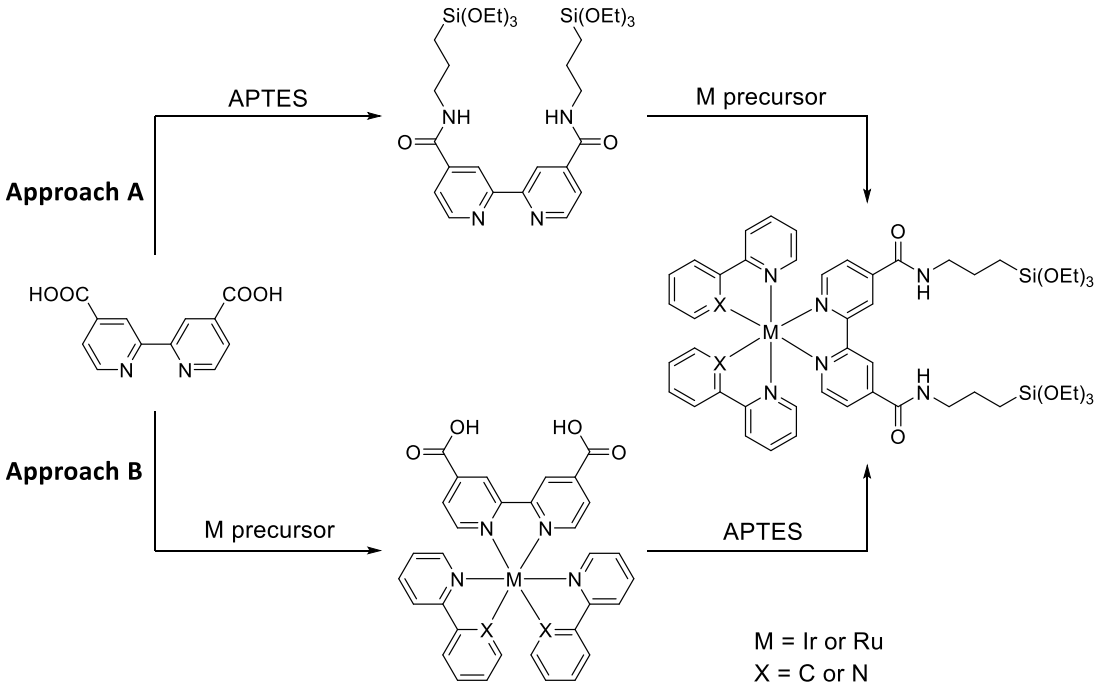

Scheme 4.3. *Two possible approaches for the addition of APTES to the metal complexes.*

Approach A, the functionalization of the free bipyridine seemed more appropriate, compared to the modification of a whole complex, and additionally, the APTES functionalized bipyridine moiety would be a suitable synthon to obtain both model compounds **Ir_APTES** and **Ru_APTES**. Therefore, approach A in **Scheme 4.3** was chosen, and the synthetic details will be described in the next paragraphs.

The route involved the synthesis of the APTES bearing bipyridine ligand **21** in two steps, to later coordinate this triethoxysilane-appended ligand to the metal center, iridium or ruthenium (**Scheme 4.4**).

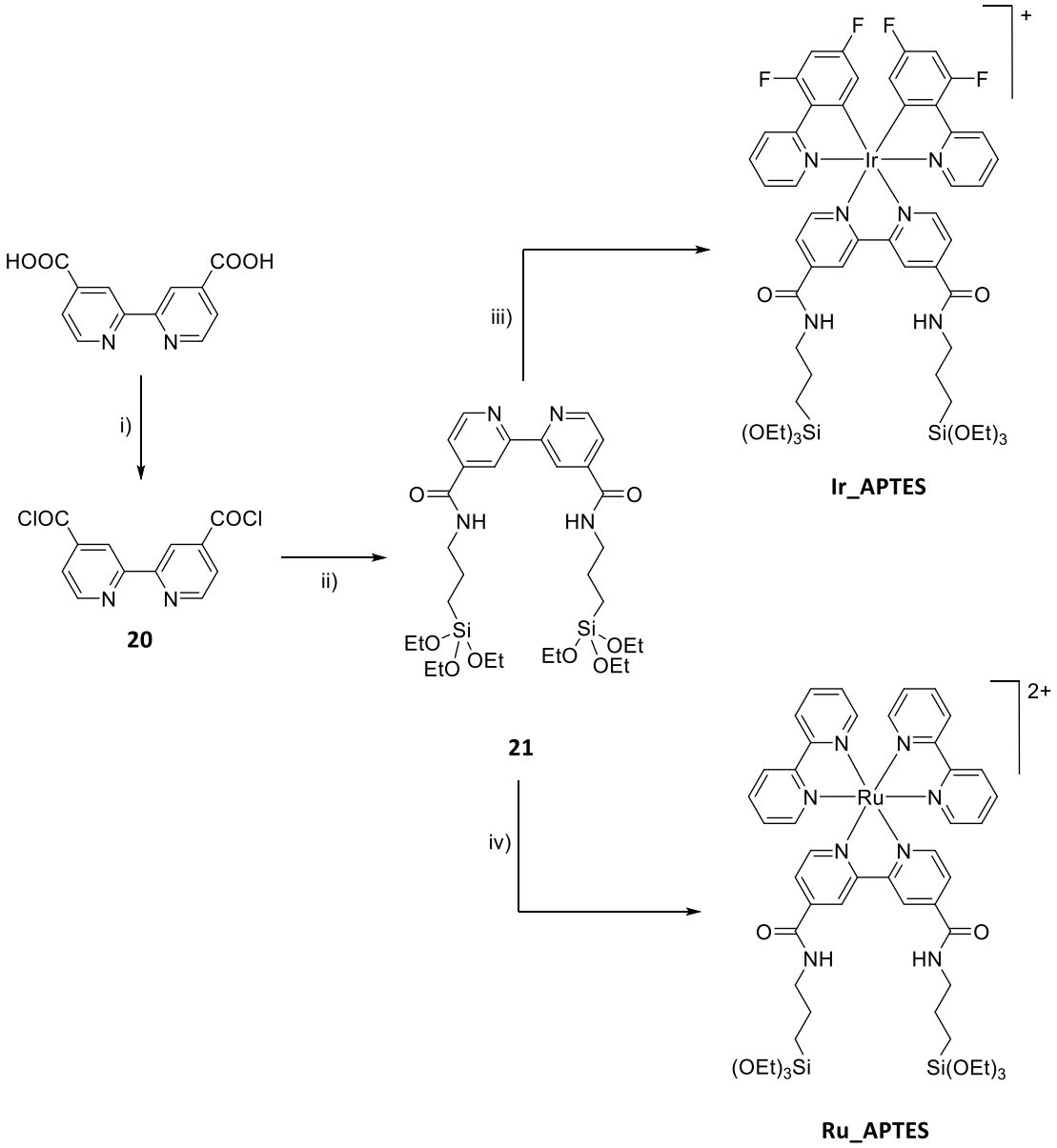

Scheme 4.4. *Synthetic route toward* ***Ir_APTES*** *and* ***Ru_APTES****. i) $SOCl_2$, 76 °C. ii) Et_3N, APTES, CH_2Cl_2/toluene, 60 °C. iii) $[Ru(bipy)_2Cl_2]$, EtOH, 82 °C. iv) $[Ir(F\text{-}ppy)_2Cl]_2$, AgOTf, acetone, 56 °C.*

A procedure published by Wu et al. was followed for the synthesis of **21**.[49,51] Bipyridine-4,4'-dicarboxylic acid was dissolved in excess $SOCl_2$ and refluxed for 16 h. The excess of $SOCl_2$ was eliminated by evaporation to give **20**. Due to the moisture sensitivity of **20**, it was directly used without further purification in the next step. A solution containing Et_3N and CH_2Cl_2 was added to the residue, and the resulting solution was added under nitrogen over a solution of toluene containing APTES. The reaction mixture was heated at 60 °C for 1 h, followed by a 12 h stirring at ambient temperature. The solvent was removed under vacuum and the product was purified by Soxhlet with CH_2Cl_2. Ligand **21** was obtained in 56% yield.

The product formation of **21** was confirmed by ^{1}H NMR spectroscopy in **Figure 4.9**. The signal corresponding to the amine proton of the APTES, shifted from around 2.5 ppm to 9 ppm after amide formation. All the signals of the spectrum were in agreement with the reported data in the literature.[49]

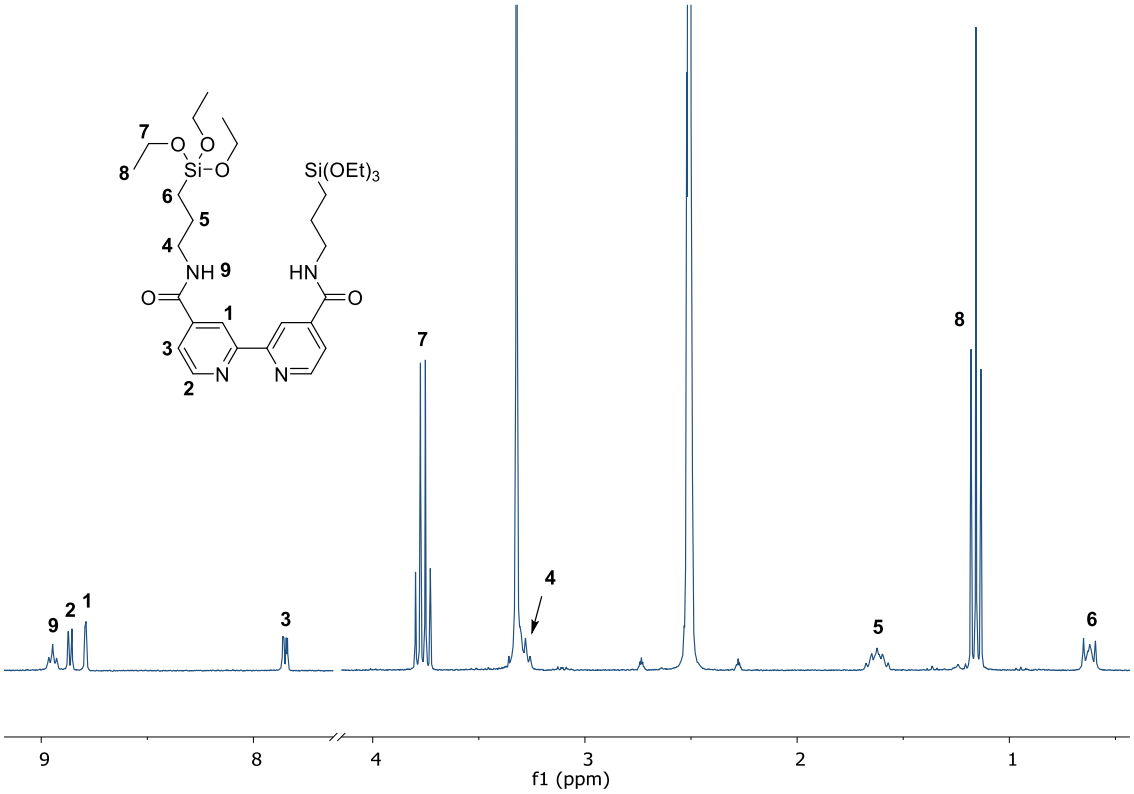

Figure 4.9. *^{1}H NMR of purified **21** and the assigned structure (DMSO-d_6, 300 MHz).*

Initially, the synthesis of the complex **Ru_APTES** was addressed. To do so, the commercially available ruthenium precursor [Ru(bpy)$_2$Cl$_2$] was reacted with the bipyridine derivative **21** in refluxing EtOH for 16 h. After this time, the solvent was removed under vacuum, and the residue was analyzed by ^{1}H NMR spectroscopy. The spectrum showed the signals assigned to the product **Ru_APTES**, although signals attributed to the hydrolysed **Ru_APTES** species were also detected. Some pure compound was obtained by recrystallization in acetone and precipitation at 0 °C. The precipitate formed was confirmed to be the desired **Ru_APTES** species by ^{1}H NMR (**Figure 4.10**), bearing two triethoxy protected APTES spacers. The peaks corresponding to the ancillary ligand could be partially assigned.

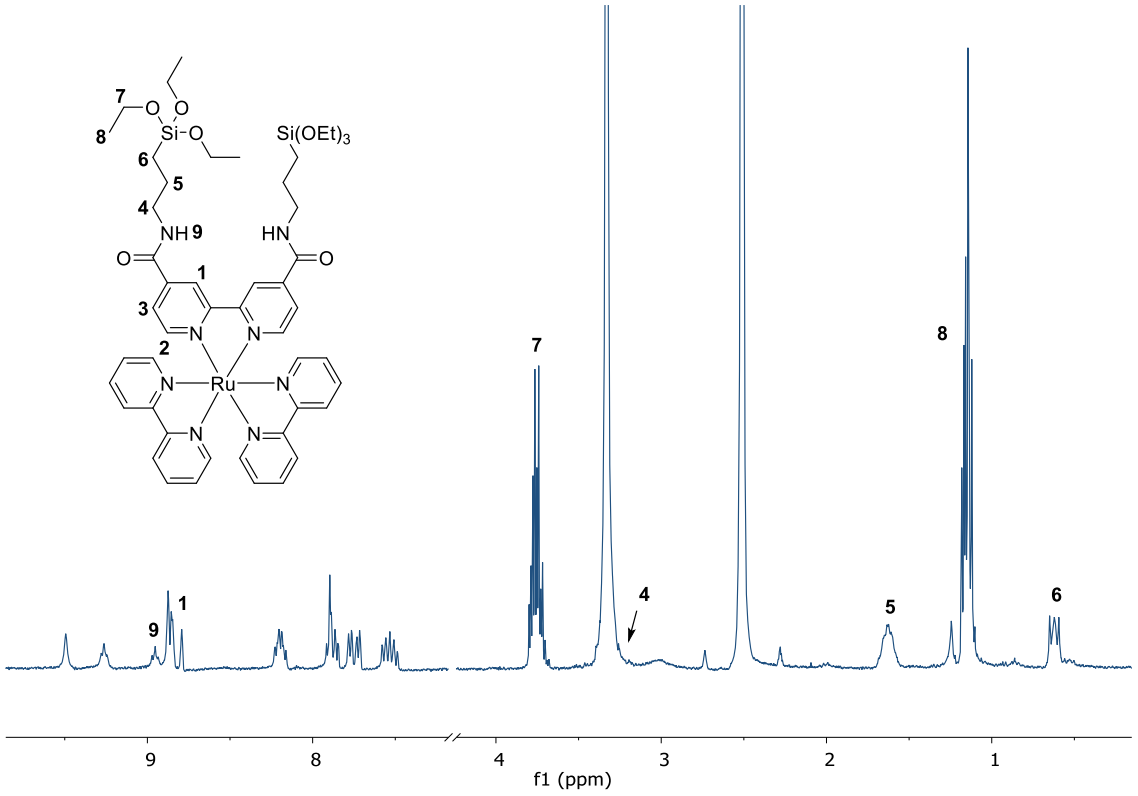

Figure 4.10. *^{1}H NMR spectrum of compound **Ru_APTES** and its partially assigned structure (DMSO-d_6, 300 MHz).*

Nevertheless, as described in the literature, the ethoxy-protected silane is unstable in aqueous media and tends to hydrolyse with the minimum moisture present during the reaction or the workup process.[52] Hence, the formation of the pure triethoxy-protected product, either **Ir_APTES** or **Ru_APTES**, required to proceed with caution, which hinders their application for surface functionalization, as it will be difficult to store and dose with precision.

To bypass the problem of the hydrolysis of the triethoxysilane organometallic derivatives, an alternative design of a triethanolamine-protected silane (silatrane) was proposed, as described in the literature.[53] Silatranes are chemically more stable to hydrolysis than trialkoxysilanes, primarily due to a strong intramolecular donor–acceptor interaction between the nitrogen and silicon atoms, whilst preserving a high reactivity towards activated quartz and ITO surfaces.[54] The low rate of hydrolysis of the silatrane molecule could also be beneficial to prevent the formation of large polymer clusters on the surface, which is very important for desired clean and ordered surface modification. As explained in the introduction, silanization reactions have the possibility

of forming disordered multilayers at the surface due to condensation reactions occurring between adjacent molecules rather than the substrate.[16]

Therefore, as depicted in **Scheme 4.5**, the new modified pathway would involve the synthesis of the aminopropylsilatrane (APSIL) **22**, followed by the amidation reaction with the dicaborxylic acid bipyridine and the subsequent coordination of the silatrane-bipyridine (**23**) to the metal center. Hence, the synthesis of **Ir_APTES** was omitted.

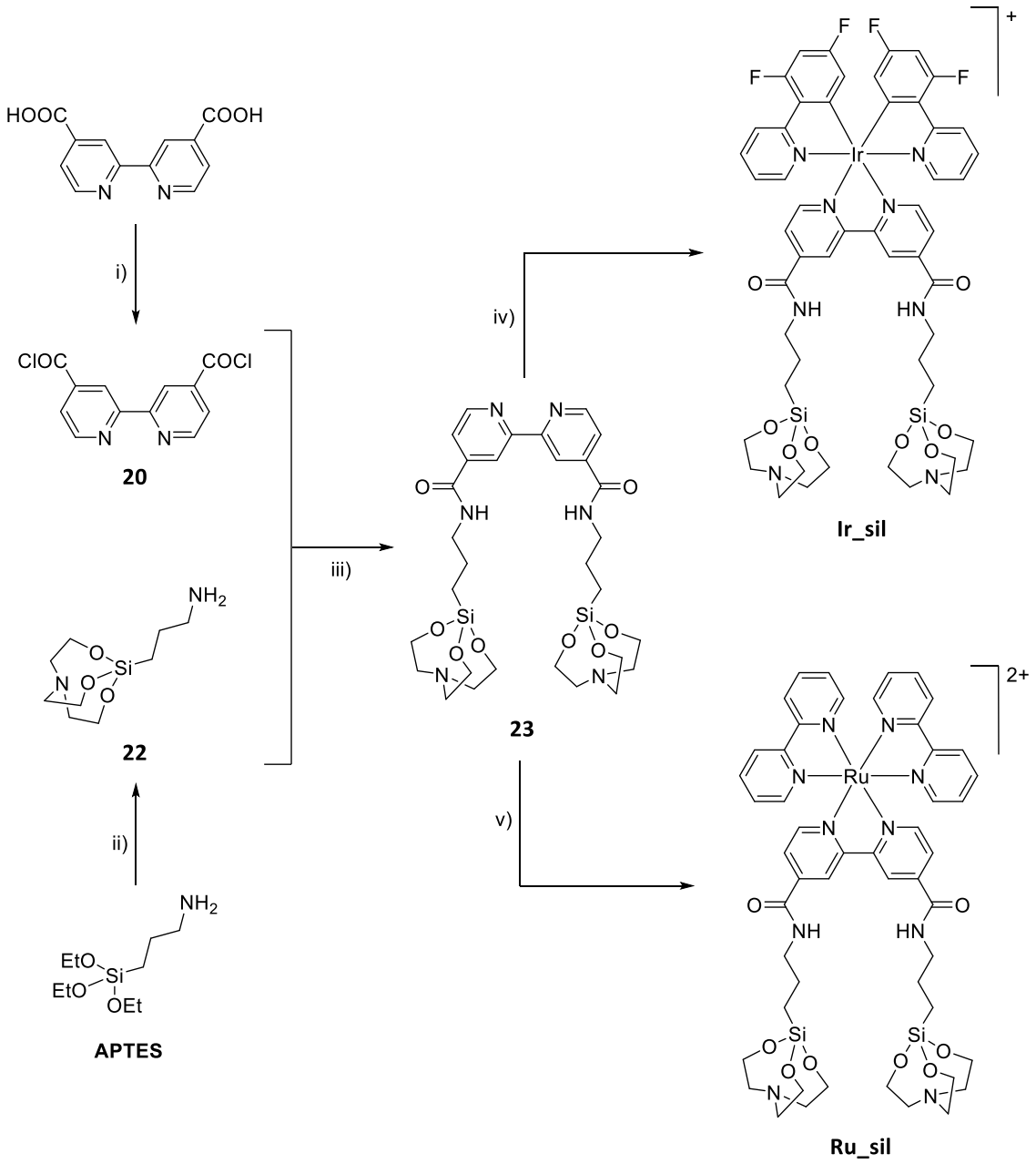

Scheme 4.5. *Synthetic route toward* ***Ir_sil*** *and* ***Ru_sil****. i) $SOCl_2$, 76 °C. ii) $(EtOH)_3N$, NaOH, MeOH, 65 °C. iii) Et_3N, CH_2Cl_2, RT. iv) $[Ru(bipy)_2Cl_2]$, EtOH, 82 °C. v) $[Ir(F\text{-}ppy)_2Cl]_2$, AgOTf, acetone, 56 °C.*

To synthesize APSIL **22**, APTES was refluxed with triethanolamine, in a basic environment in MeOH. The solvent was removed to obtain the product as a white solid. The ^{1}H NMR of the product showed two triplets assigned to the CH_2 of the triethanolamine-protected silane (4 and 5 in **Figure 4.11**), which agreed with the expected pattern. The condensation was further confirmed by ^{13}C, COSY and HSQC-NMR experiments, as well as by ^{1}H-^{29}Si HMBC, where the coupling of the two triplets with the silicon atom is observed.

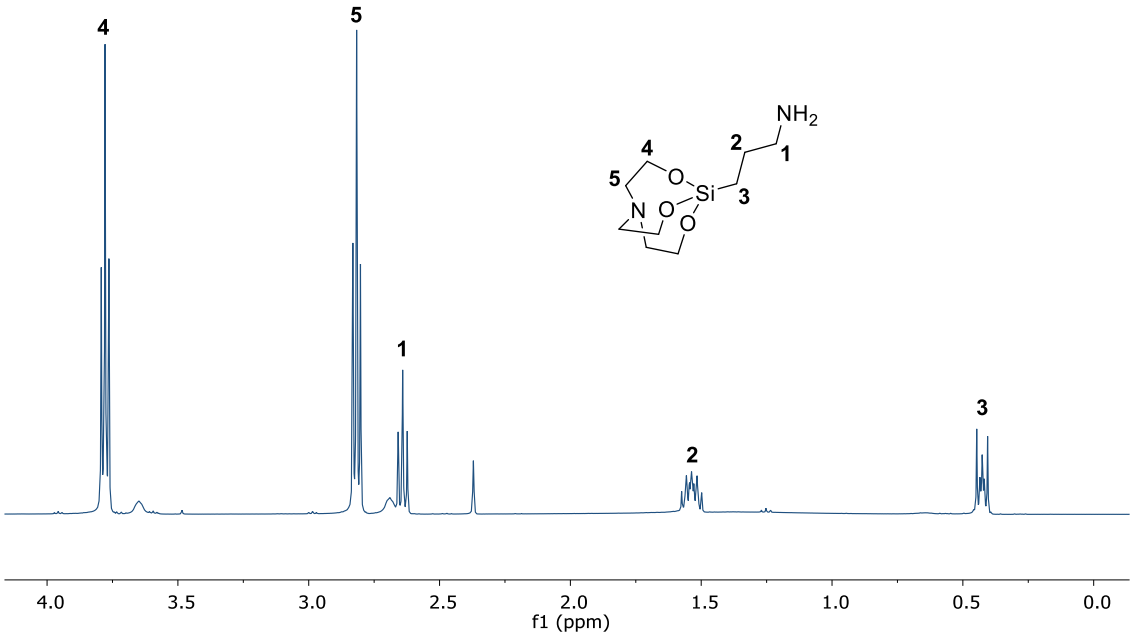

Figure 4.11. *^{1}H NMR spectrum of compound **22** and its assigned structure ($CDCl_3$, 300 MHz).*

To synthesize silatrane-protected bipyridine **23**, the procedure described by Brudvig et al. was followed, similar to the previous analogous condensation of APTES.[55] The thoroughly dried bipyridine-4,4'-dicarboxylic acid was dissolved in excess of $SOCl_2$ and refluxed for 16 h. After this time, the excess of $SOCl_2$ was eliminated by evaporation and to the residue CH_2Cl_2, APSIL (**22**) and Et_3N were added. The solution was stirred at room temperature for 3h and the precipitate formed was left overnight in the freezer. The precipitate was filtered to obtain the ligand **23** 85% yield. The purity of the product was confirmed by ^{1}H NMR (**Figure 4.12**).

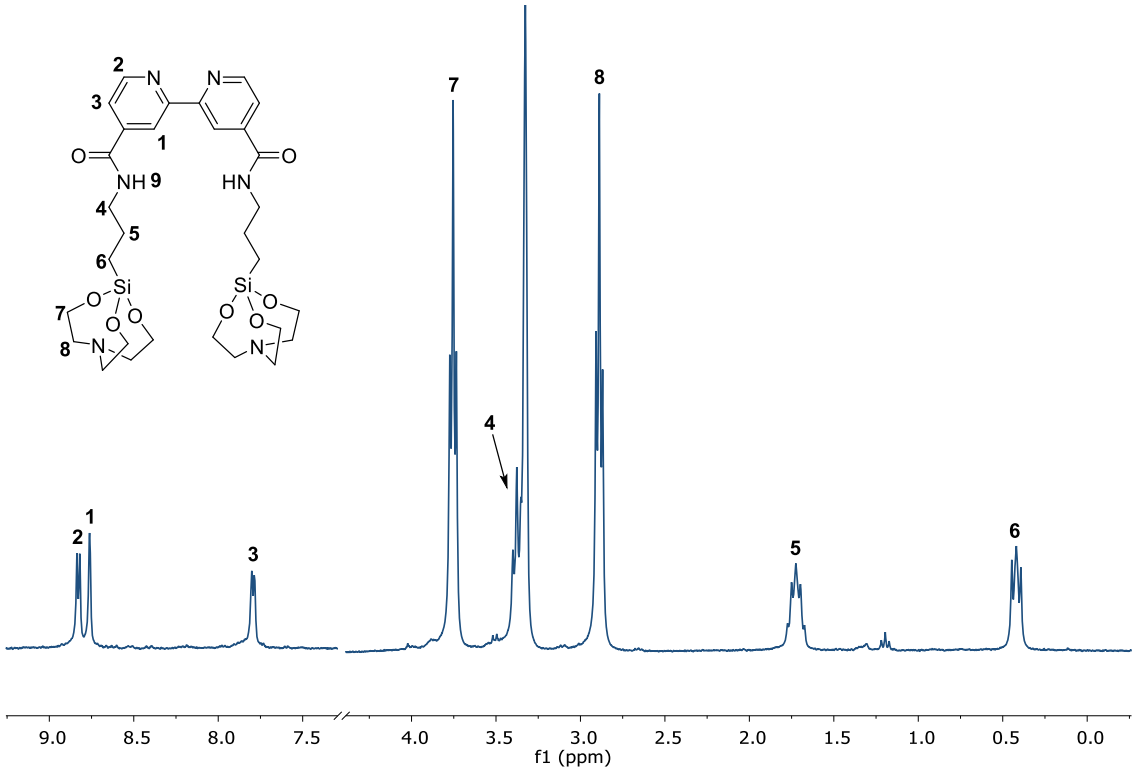

Figure 4.12. *^{1}H NMR spectrum of compound **23** and its assigned structure (MeOD-d_4, 300 MHz).*

The coordination of the **23** to ruthenium was obtained by refluxing the intermediate $[Ru(bipy)_2Cl_2]$ with the silatrane-functionalized ligand **23** in EtOH for 16 h. After this time, the solvent was removed under vacuum, and the counterion was exchanged by salt metathesis with KPF_6 in a concentrated dissolution of MeOH. The desired product **Ru-sil** precipitated from the reaction mixture and was isolated by filtration to obtain a red solid in 54% yield. The ^{1}H NMR of the precipitate is shown in **Figure 4.13**. The very symmetric spectroscopic pattern was assigned to compound **Ru_sil**, which was further characterized by multinuclear NMR spectroscopy and DOSY experiments.

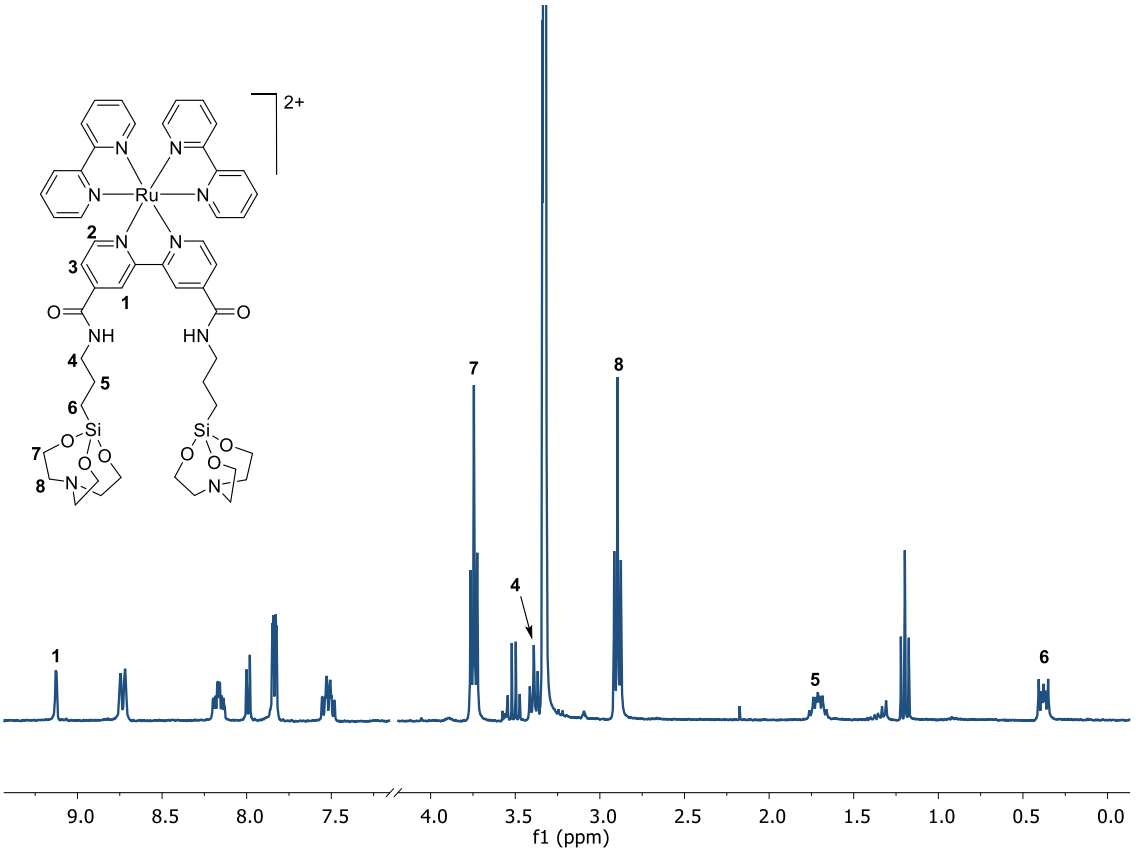

Figure 4.13. *^{1}H NMR spectrum of compound **Ru_sil** and its partially assigned structure (CD_3OD, 300 MHz).*

For the synthesis of **Ir_sil**, the dimeric iridium precursor $[Ir(F\text{-}ppy)_2Cl]_2$, synthesized according to literature procedures, REF was stirred with AgOTf in an acetone reflux for 16 h, to form the corresponding bis-solvato cationic compound $[Ir(F\text{-}ppy)_2(acetone)_2]OTf$.[56] The reaction crude was filtered through a celite pad, and the filtrate was added over a solution of **23** in acetone, and refluxed for additional 48 h. After this time, the mixture was filtered through a celite pad for the second time. The filtrate was evaporated, and the residue was washed with H_2O and diethyl ether, to obtain pure **Ir_sil** in 37% yield. The ^{1}H NMR of the isolated compound is shown **Figure 4.14**.

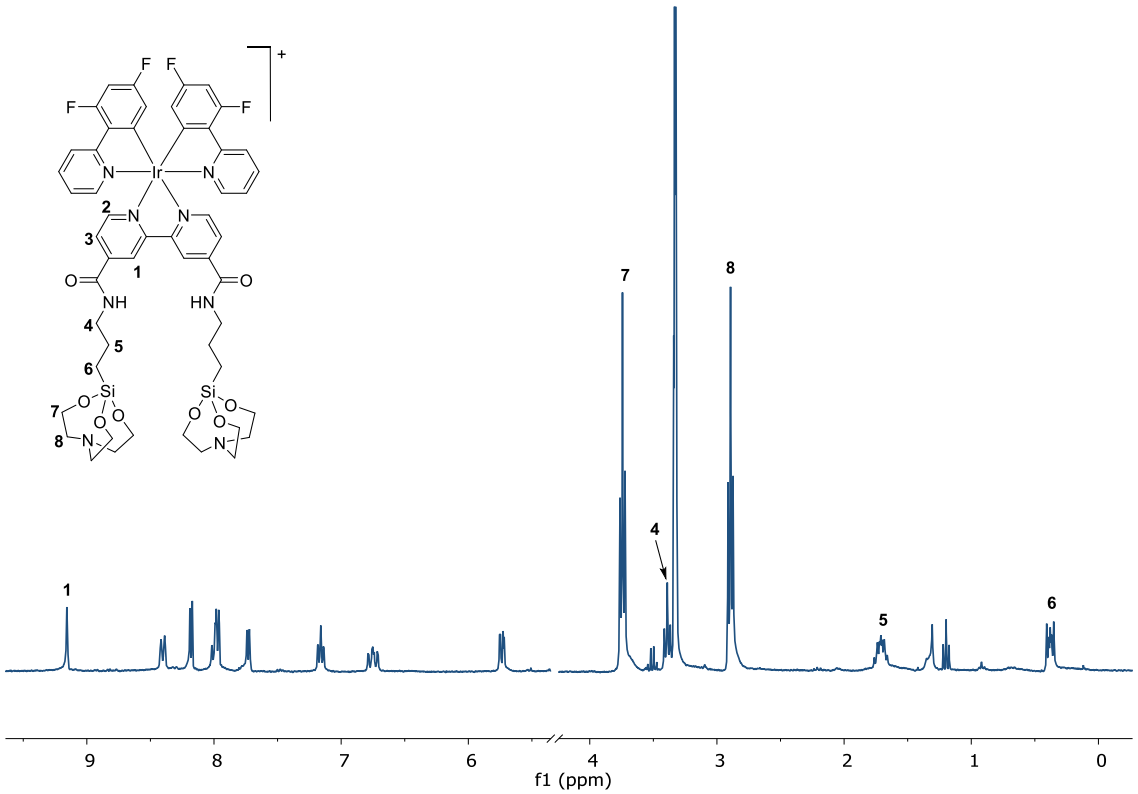

Figure 4.14. *^{1}H NMR spectrum of compound **Ir_sil** and its partially assigned structure (CD_3OD, 300 MHz).*

The photophysical characterization of the model compounds **Ir_sil** and **Ru_sil** was performed in methanol solutions. The absorption and emission spectra are shown in **Figure 4.15**. In the absorption spectra, as described in Chapter 1, the more intense band of higher energy is generally associated with $\pi \longrightarrow \pi^*$ transitions of the ligands, while the less intense bands at lower energies are associated with metal-ligand charge transfer (MLCT) between metal HOMO orbitals and LUMO orbitals of bipyridine ligands. The wavelength of excitation did not affect the emission spectra, assigned to the ^{3}MLCT in both cases, showing the emission maximum at 665 nm and 585 nm for **Ru_sil** for **Ir_sil**, respectively.

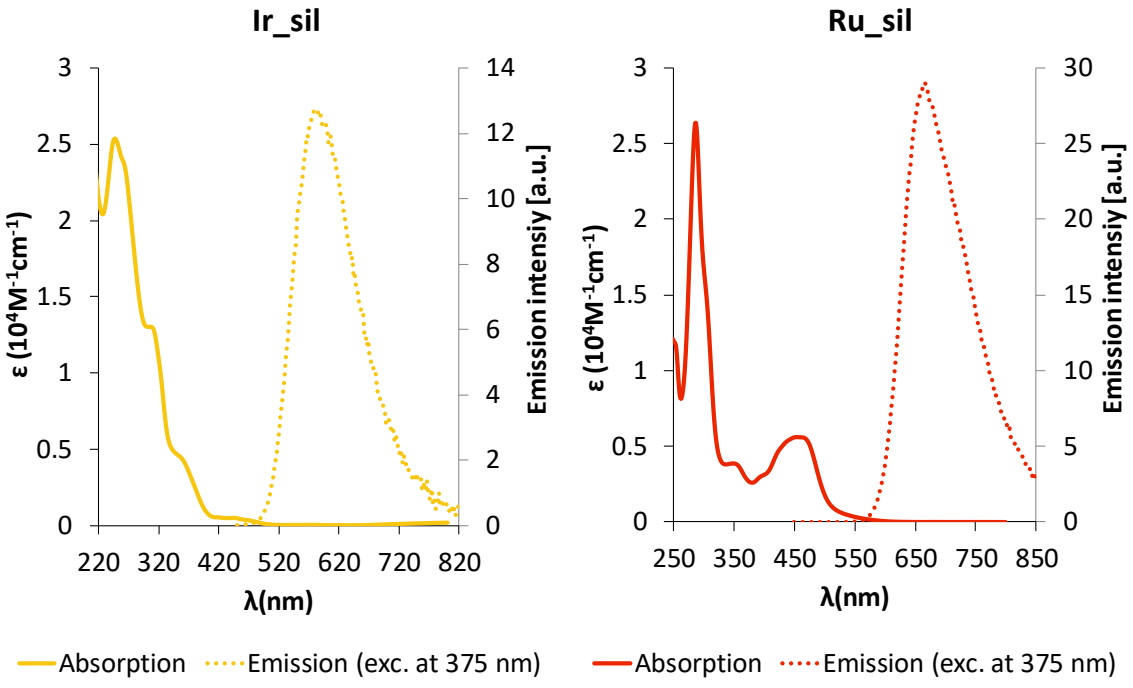

Figure 4.15. *Absorption and emission spectra of* ***Ir_sil*** *and* ***Ru_sil*** *in MeOH.*

Additionally, lifetime and quantum yield experiments were performed for the model complexes. The observed lifetimes are consistent with an emission from a triplet excited state and the quantum yields are similar to those described for related compounds. [57,58] The most relevant data is compiled in **Table 4.1**.

Table 4.1. *Absorption and emission data of* ***Ru_sil*** *and* ***Ir_sil*** *in MeOH.*

	absorption	emission		
	λ_{max} [nm] (ε [$10^4 M^{-1}cm^{-1}$])[a]	λ_{max} [nm][b]	Φ [%][b]	τ [µs]
Ru_sil	250 (2.62), 290 (5.61), 375 (0.60), 460 (1.24)	665	10	735
Ir_sil	254 (4.74), 313 (2.36), 365 (0.79), 450 (0.12)	585	23	586

Argon-equilibrated MeOH solutions. a) Based on linear regression of the measured absorption of 6 concentrations in the range 10^{-4} M–10^{-6}M. b) Excitation at 375 nm. c) excitation EPLED 385 nm, TCSPC, 1 MHz, 5000 counts.

4.2.2 Immobilization on quartz substrates.

Once **Ir_sil** and **Ru_sil** were successfully synthesized and characterized, these compounds were immobilized over quartz substrates. Quartz slides of 1 cm^2 were employed (**Figure 4.3**). The immobilization of a monolayer of the model complexes onto the slides was proceeded in a self-assembly approach by dip coating using methanol

solutions of the model compounds **Ir_sil** and **Ru_sil**. The slides were plasma activated for 1h before immersing the quartz slides for a fixed period of time in **Ir_sil** and **Ru_sil** methanol mother solutions of controlled concentration, as represented in **Figure 4.16**. After a fixed immersion time, the surfaces were extracted from the solutions and washed in a three-step procedure: rinsed with 10 mL of MeOH, ultrasonicated in 10 mL of clean MeOH for 10 minutes and, again rinsed with another 10 mL of MeOH. After the washing phase, the surfaces were argon dried. During the whole procedure, the main face of the surface, the one looking up in the immobilization step, was monitored for the washings and characterization routine and considered "the functionalized surface", being aware that, in principle, both sides of the support will be functionalized by this procedure.

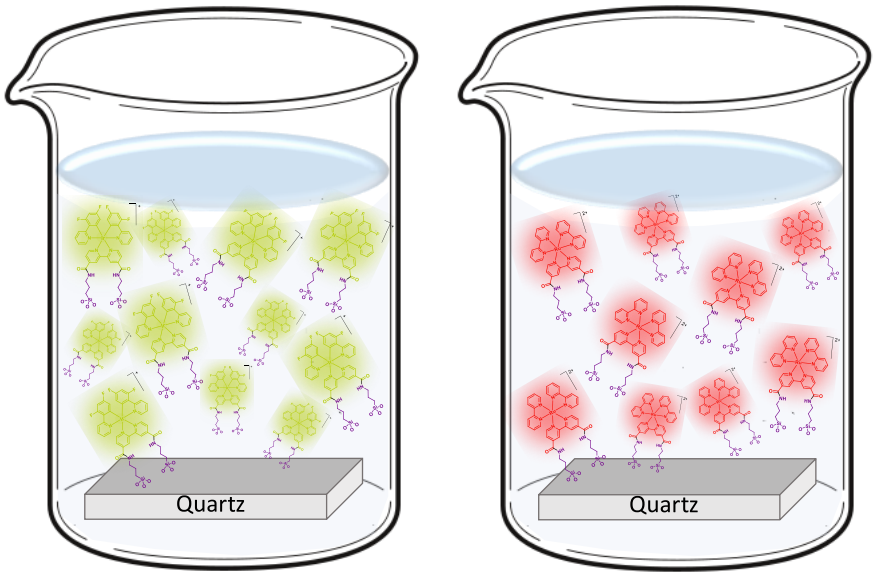

Figure 4.16. *Representation of the dip-coating process. Quartz slides immersed in* ***Ir_sil*** *and* ***Ru_sil*** *MeOH solutions.*

This way **Ir_Q** and **Ru_Q** samples were obtained. As shown in **Figure 4.17**, the effective immobilization of the organometallic compounds to the quartz slides could be observed by "naked eye" under UV light when using concentrated mother solutions.

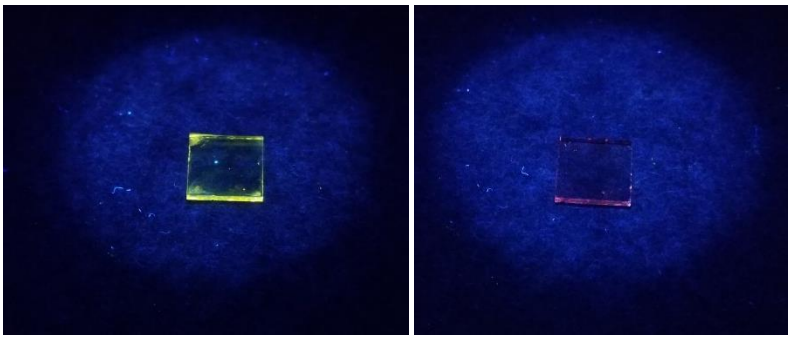

Figure 4.17. *Emission of two* ***Ir_Q*** *and* ***Ru_Q*** *quartz samples, excited under 365 nm.*

After some optimization process, the immersion time was fixed to 30 min, and the coverage was controlled by using different concentrations of the mother solutions of the complexes in methanol. They ranged from very diluted solutions of $1 \cdot 10^{-8}$ M to more concentrated ones, $5 \cdot 10^{-5}$ M. Mixed surfaces were also obtained by dip-coating using mother solutions containing a mixture of both compounds **IrRu_Q**.

The absorption and emission of quartz samples **Ir_Q** and **Ru_Q** was measured to determine the coverage and their photoluminescent properties. **Figure 4.18** shows an example of the normalized absorption and emission spectra of two different quartz slides functionalized with **Ir_sil** and **Ru_sil**, and compared to their respective spectra in solution. As it can be noticed, the absorption spectra preserve the same shape in solution and anchored to the surface. On the contrary, both complexes suffer a slight hypsochormic shift in their emission maxima upon deposition, which is especially evident for the **Ir_sil** compound.

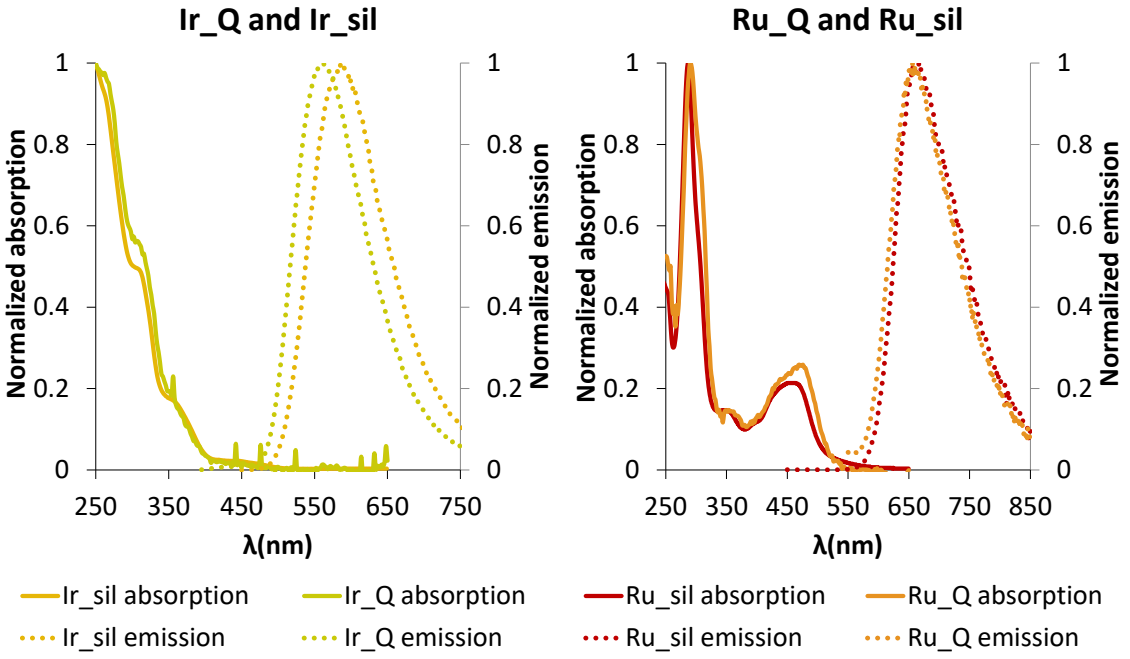

Figure 4.18. *Normalized absorption and emission spectra of a representative* ***Ir_Q*** *and* ***Ir_sil*** *and a representative* ***Ru_Q*** *and* ***Ru_sil****.*

As reported in literature, the absorption spectra of the functionalized surface can be used to estimate the fluorophores surface coverage.[59]

The surface coverage equation is defined as follows (equation 1):

$$\Gamma\left(\frac{molecules}{cm^2}\right) = N_A(molecule \cdot mol^{-1}) \cdot c_{surf}(mol \cdot cm^{-2}) \qquad (1)$$

By substituting the resolved Beer-Lambert law surface equation 2, in the surface coverage equation 1, yields the general equation employed in literature, equation 3.

$$c_{surf}\ (mol \cdot cm^{-2}) = \frac{\mathrm{A}_{surf}}{\varepsilon_\lambda(M^{-1})} = \frac{\mathrm{A}_{surf}}{1000 \cdot \varepsilon_\lambda(cm^2 \cdot mol^{-1})} \qquad (2)$$

$$\Gamma\left(\frac{molecules}{cm^2}\right) = \frac{A_\lambda \cdot N_A}{\varepsilon_\lambda \cdot 1000} \qquad (3)$$

where, A_λ is the measured absorbance of the modified surface at a given wavelength, ε_λ is the extinction coefficient of the compound in solution at the same wavelength and N_A is the Avogadro´s number. Using this equation, the coverage (Γ) is obtained in molecules/cm^2.

For these calculations, the molar extinction coefficient is presumed to be the same for the compounds in solution and anchored on the surface.[55,60] This approximation seem reasonable considering the resemblance of the shape of both spectra, as mentioned before. Often, for the estimation, the extinction coefficient of the Soret band is used.[61] In our case, in order to obtain a more accurate estimation, instead of using a single wavelength extinction coefficient, the whole spectra of **Ir_sil** and **Ru_sil** in MeOH solutions and their corresponding surfaces were used in the range of 250–650 nm (**Figure 4.18**). In other words, equation 3 was transformed into equation 4, and the coverage (Γ) was calculated by least squares fit of this expression in the selected range (250-650 nm).

$$A_\lambda = \frac{1000 \cdot \Gamma}{N_A} \varepsilon_\lambda \qquad (4)$$

As mentioned before, this method allows the use of the whole spectrum to estimate the degree of the surface coverage, which could lead to a more precise estimation compared with the use of a single point measurements. This methodology is especially relevant when small deviations in the "shape" of the UV-vis spectra are observed upon immobilization. For samples **Ir_Q** and **Ru_Q** it renders the same result as when the coverage is calculated using only the molar extinction coeficient at the Soret band.

Since the absorption measurements render the coverage in molecules per surface area, in order to estimate the coverage in terms of "number of dense monolayers", it is necessary to know the volume of the sensor to calculate the maximum number of molecules that could be present per surface unit in a SAM. For this purpose, the average volume of **Ir_sil** on a SiO_2 oxide was calculated by the group of Prof. Cossío, by means of DFT (**Figure 4.19**). The calculations show that **Ir_sil** has a volume of 1.4 x 0.76 x 1.12 nm^3. Thus, one could estimate that a SAM of sensors represents a coverage of $1 \cdot 10^{14}$ molecules/cm^2.

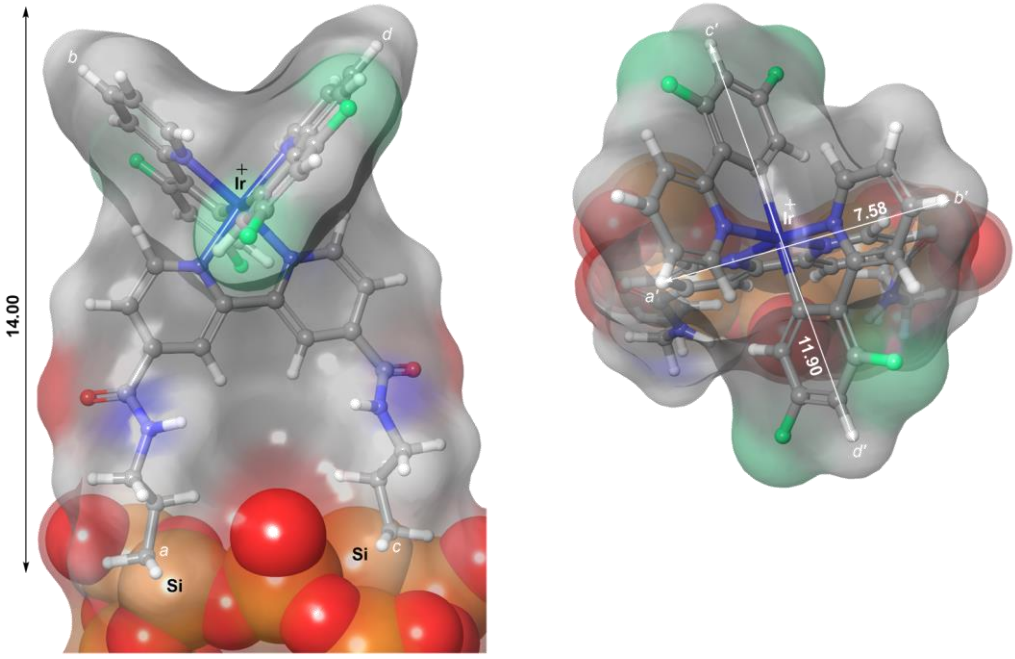

Figure 4.19. *Calculated area of* ***Ir_sil*** *compound over a silicon oxide surface*

Hence, the surface coverage value obtained from the iteration approach can be easily transformed in number of monolayers (ML) using the simple conversion 1ML = $1 \cdot 10^{14}$ molecules per cm^2.

Figure 4.20 shows the absorption and emission spectra of **Ir_Q** samples prepared by dip-coating on mother solutions of **Ir_sil** of different concentrations. Additionally, the calculated coverage of **Ir_Q** samples, in terms of molecules/cm^2 and number of monolayers, and the mother solution concentrations of some of the samples prepared are summarized in **Table 4.2**. All the modified surfaces were produced in duplicate, to confirm the reproducibility of the methodology.

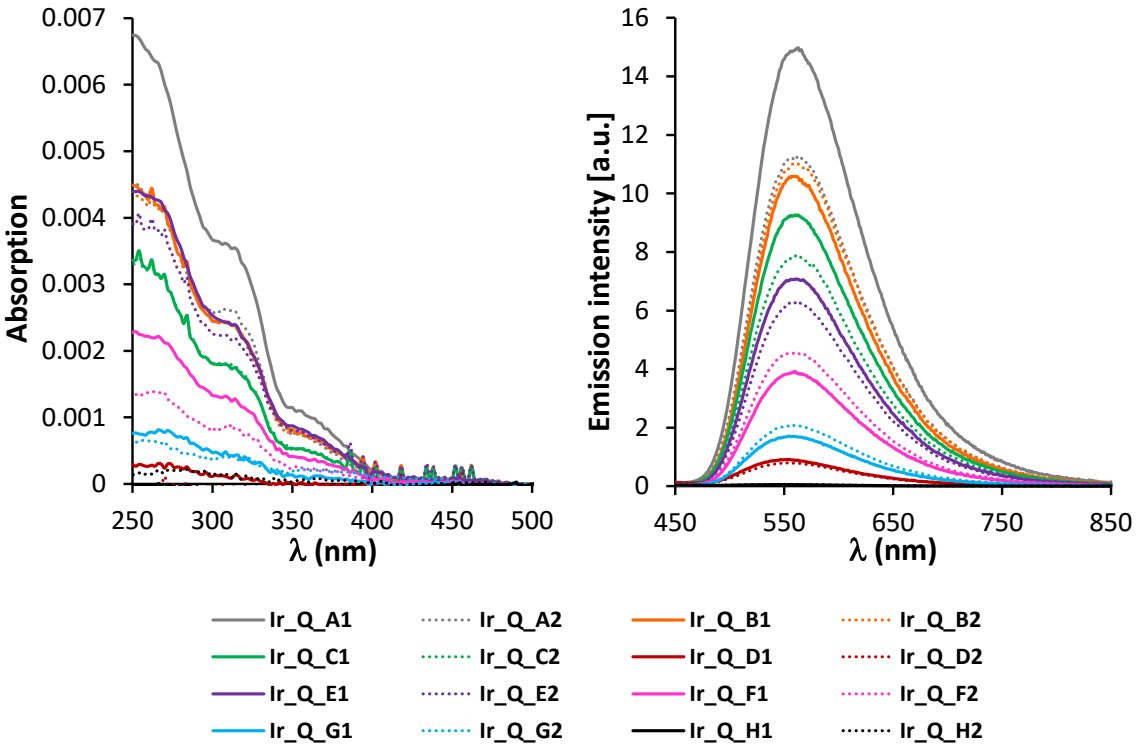

Figure 4.20. *Absorption and emission spectra of several* ***Ir_Q*** *samples.*

Table 4.2*. Calculated coverage of* ***Ir_Q*** *surfaces.*

Code	[Ir_sil] M	ML	molec/cm^2
Ir_Q_A1	5.00E-05	0.845	8.45E+13
Ir_Q_A2	5.00E-05	0.637	6.37E+13
Ir_Q_B1	1.00E-05	0.600	6.00E+13
Ir_Q_B2	1.00E-05	0.625	6.25E+13
Ir_Q_C1	5.00E-06	0.525	5.25E+13
Ir_Q_C2	5.00E-06	0.445	4.45E+13
Ir_Q_D1	5.00E-06	0.401	4.01E+13
Ir_Q_D2	5.00E-06	0.355	3.55E+13
Ir_Q_E1	2.50E-06	0.222	2.22E+13
Ir_Q_E2	2.50E-06	0.259	2.59E+13
Ir_Q_F1	1.25E-06	0.097	9.66E+12
Ir_Q_F2	1.25E-06	0.118	1.18E+13
Ir_Q_G1	1.00E-06	0.051	5.07E+12
Ir_Q_G2	1.00E-06	0.044	4.45E+12
Ir_Q_H1	6.13E-07	0.003	3.19E+11
Ir_Q_H2	6.13E-07	0.003	3.09E+11

When the quartz supports were functionalized with mother solution of concentrations of $1 \cdot 10^{-6}$ M or lower, the degree of coverage was too low to obtain a reliable absorption spectrum and estimate the monolayer coverage. Thus, for these samples, the number of monolayers was estimated based on the emission intensity (a more sensitive

technique) by comparing the emission with a previously measured sample, set as a reference, whose degree of coverage was measured based on the absorption spectrum and considered reliable. **Figure 4.21** shows the emission spectra of the diluted surfaces and **Table 4.3** summarizes the degree of coverage of the samples.

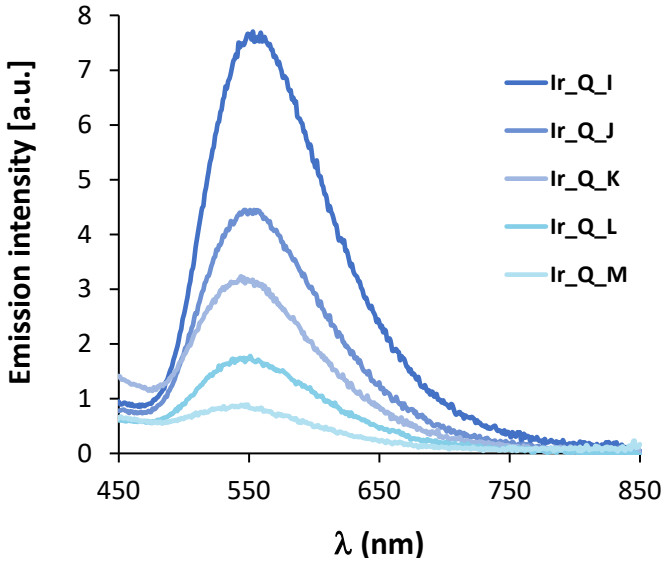

Figure 4.21. *Absorption and emission spectra of diluted* ***Ir_Q*** *samples.*

Table 4.3. *Calculated coverage of* ***Ir_Q*** *diluted surfaces and* ***Ir_Q_B1*** *used as reference.*

Code	[Ir_sil] M	Intensity[a]	ML	molec/cm^2
Ir_Q_B1	1.00E-05	105830	0.600	6.00E+13
Ir_Q_I	1.00E-06	7528	0.043	4.27E+12
Ir_Q_J	8.00E-07	4369	0.025	2.48E+12
Ir_Q_K	6.00E-07	3090	0.018	1.75E+12
Ir_Q_L	4.00E-07	1646	0.009	9.33E+11
Ir_Q_M	2.00E-07	822	0.005	4.66E+11

MeOH mother solutions. a. Emission intensity measured at 560 nm, exited at 375 nm. ***Ir_Q_B1*** *used as reference sample.*

The same approach was followed for **Ru_sil** functionalized surfaces. **Figure 4.22** shows the absorption and emission spectra of several **Ru_Q** samples. The degree of coverage of these samples, in terms of number of monolayers, and the concentration of the mother solutions employed are summarized in **Table 4.4**.

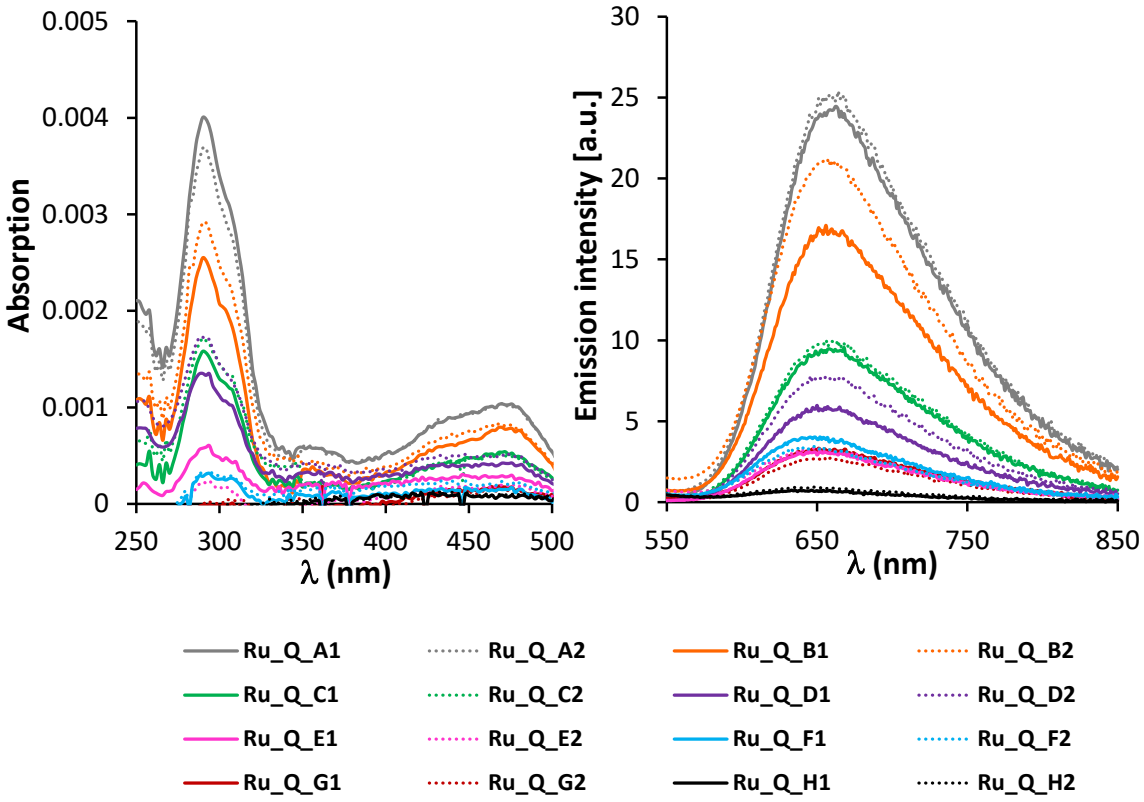

Figure 4.22. *Absorption and emission spectra of several* ***Ru_Q*** *samples.*

Table 4.4. *Calculated coverage of* ***Ru_Q*** *surfaces.*

Code	[Ru_sil] M	ML	molec/cm^2
Ru_Q_A1	5.00E-05	0.55	4.8E+13
Ru_Q_A2	5.00E-05	0.52	5.0E+13
Ru_Q_B1	1.00E-05	0.34	3.4E+13
Ru_Q_B2	1.00E-05	0.41	4.3E+13
Ru_Q_C1	5.00E-06	0.21	1.9E+13
Ru_Q_C2	5.00E-06	0.23	2.0E+13
Ru_Q_D1	5.00E-06	0.21	1.2E+13
Ru_Q_D2	5.00E-06	0.23	1.6E+13
Ru_Q_E1	2.50E-06	0.18	6.0E+12
Ru_Q_E2	2.50E-06	0.11	6.7E+12
Ru_Q_F1	1.25E-06	0.13	8.0E+12
Ru_Q_F2	1.25E-06	0.13	6.8E+12
Ru_Q_G1	1.00E-06	-	-
Ru_Q_G2	1.00E-06	-	-
Ru_Q_H1	6.13E-07	-	-
Ru_Q_H2	6.13E-07	-	-

Also in this case, for substrates modified with diluted mother solutions (of $1 \cdot 10^{-6}$ M or lower), the **Ru_Q_B1** surface was employed as reference. **Figure 4.23** shows the emission spectra of the diluted surfaces and **Table 4.5** summarizes the degree of coverage of the samples.

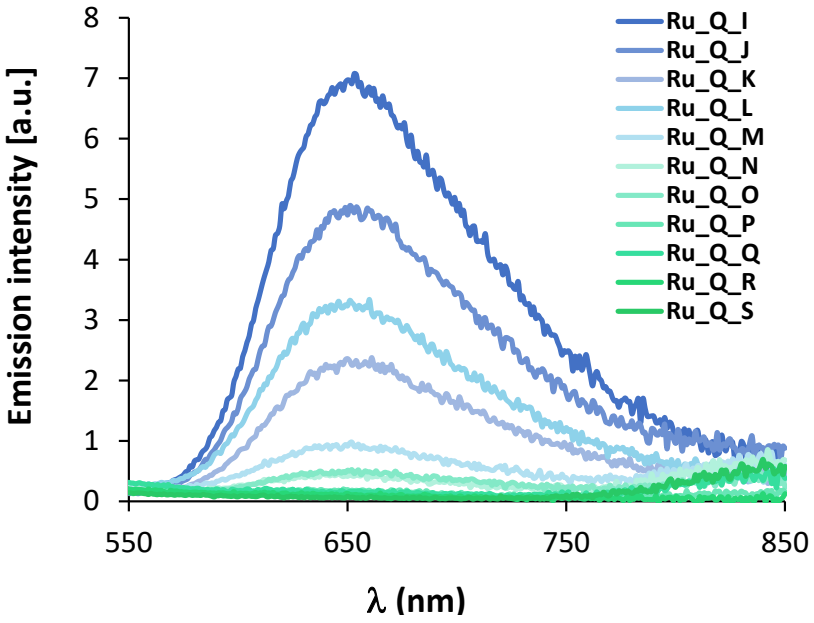

Figure 4.23. *Emission spectra of diluted **Ru_Q** samples.*

Table 4.5.*Calculated coverage of **Ru_Q** diluted surfaces and **Ru_Q_B1** used as reference.*

Code	[Ir_sil] M	Intensity[a]	ML	molec/cm^2
Ru_Q_B1	1.00E-05	1.69E+04	0.340	3.4E+13
Ru_Q_I	1.00E-06	6.85E+03	0.140	1.4E+13
Ru_Q_J	8.00E-07	4.80E+03	0.097	9.7E+12
Ru_Q_K	6.00E-07	2.24E+03	0.048	4.8E+12
Ru_Q_L	4.00E-07	3.34E+03	0.066	6.6E+12
Ru_Q_M	2.00E-07	8.57E+02	0.019	1.9E+12
Ru_Q_N	1.00E-07	4.39E+02	0.008	8.4E+11
Ru_Q_O	8.00E-08	4.91E+02	0.011	1.1E+12
Ru_Q_P	6.00E-08	1.84E+02	0.004	4.0E+11
Ru_Q_Q	4.00E-08	1.38E+02	0.003	3.1E+11
Ru_Q_R	2.00E-08	1.00E+02	0.003	2.6E+11
Ru_Q_S	1.00E-08	7.32E+01	0.002	1.7E+11

Figure 4.24 shows the degree of coverage obtained in terms of number of monolayers against the concentration of the starting mother solution, for both **Ir_Q** and **Ru_Q** samples. The results obtained showed that there is a direct correlation between the starting concentration and the amount of deposited compound, which permits having a

reliable methodology to deposit dense and sparse layers of organometallic compound on a quartz surface. Duplicates confirm the reproducibility of the method.

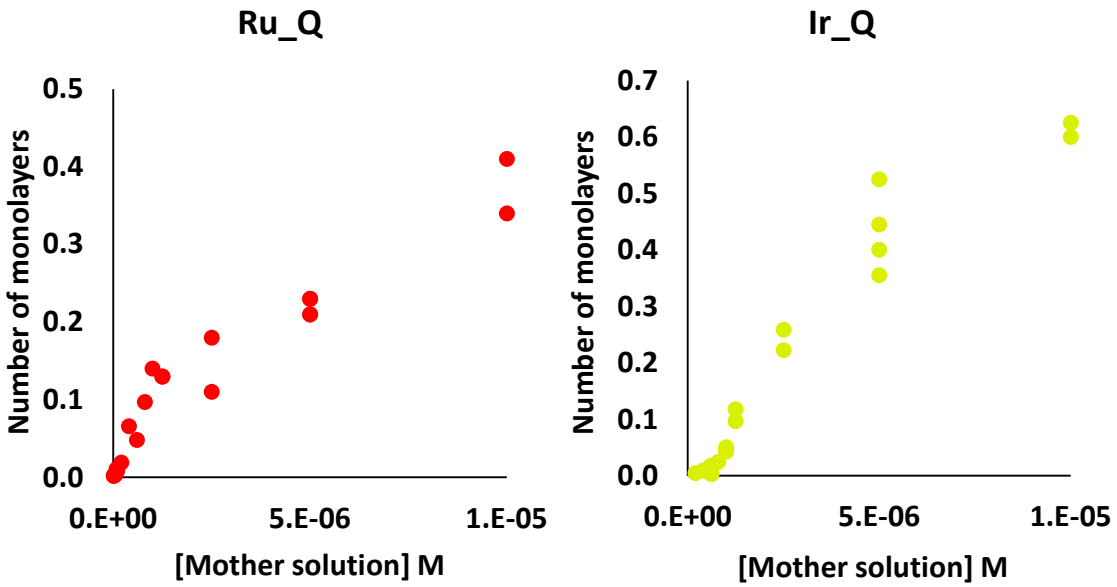

Figure 4.24. *Degree of coverage of **Ru_Q** and **Ir_Q** samples, in monolayer, against the concentration of the mother solution employed in the synthesis.*

Furthermore, the emission of these iridium surfaces was tested in the set up built by the responsibles of the optical part of the NEXT project, with an EPL picosecond pulsed diode laser. As it can be observed in **Figure 4.25**, the emission of very diluted **Ir_Q** samples could be measured.

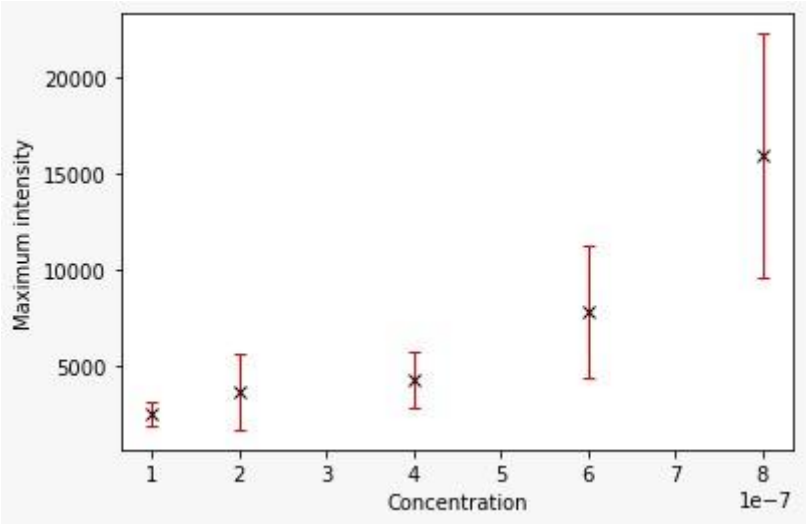

Figure 4.25. *Maximum intensity of emission of **Ir_Q** samples against the concentration of the starting mother solutions.*

In consonant with the our previously described emission measurements, the linear trend can be observed from $7 \cdot 10^{-7}$ to $4 \cdot 10^{-7}$ M. The last two points do not follow the linearity, due to the low concentration of the samples, where the quartz reflection starts to hinder the sensitivity. For this reason, the same test is aimed to carry out with **Ru_Q** samples, as the emission of **Ru_Q** and the reflection of quartz do not coincide in the same region.

In addition to the surfaces containing only one type of phosphorescent organometallic model complex, mixed surfaces were likewise prepared. In that respect, the assembling of hybrid surfaces in a controlled and systematic manner, required the quantification of the deposited amount of each model compound.

The coverage of one and other compound in hybrid surfaces is based on the assumption that the total emission is a convolution of the emission of both compounds. Therefore, equation (5) can be applied. Again, knowing the absorption spectra of both compounds in solution and assuming that the molar absorptivities are identical in solution and on the surface, the coverage was calculated by least-squares regression applying equation 5 in the range of 250–650 nm.

$$A_{\lambda_{tot}} = A_{\lambda_{Ir}} + A_{\lambda_{Ru}} = \frac{1000}{N_A}(\Gamma_{Ir} \cdot \varepsilon_{\lambda_{Ir}} + \Gamma_{Ru} \cdot \varepsilon_{\lambda_{Ru}}) \quad (5)$$

where, $A_{\lambda_{Ir}}$ and $A_{\lambda_{Ru}}$ are the contribution of one and other component to the total absorption of the functionalized surface at a given wavelength, ε_{λ} is the extinction coefficient of the compound in solution at the same wavelength and N_A is the Avogadro´s number. Using this equation, the coverage (Γ) is obtained in molecules/cm^2.

The same deconvolution methodology was initially tested to confirm the composition of a mixed mother solution of known concentrations, based on the analogous equation 6, for solutions.

$$A_{\lambda_{tot}} = c_{Ir} \cdot \varepsilon_{\lambda_{Ir}} + c_{Ru} \cdot \varepsilon_{\lambda_{Ru}} \quad (6)$$

Figure 4.26 shows the absorption of the MeOH solutions of the pure compounds (**Ir_sil** (in yellow) and **Ru_sil** (in red), at $1 \cdot 10^{-5}$ M concentration. The blue absorption is the experimental absorption of a mixed solution containing $2.3 \cdot 10^{-5}$ M concentration of each

model compound. The dashed blue line is the calculated absorption, which comes from a convolution of both spectra, according to equation 6. The least fit adjustment confirms that it is formed by $2.2 \cdot 10^{-5}$ and $2.4 \cdot 10^{-5}$ M concentration for **Ru_sil** and **Ir_sil**, respectively.

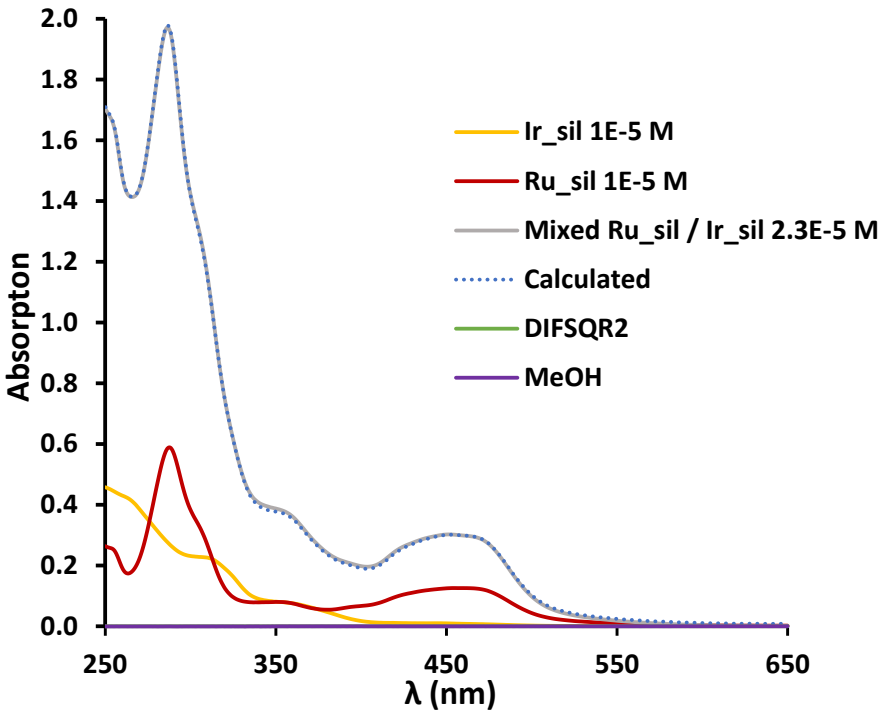

Figure 4.26. *Absorption spectra of* ***Ir_sil*** *1E-5 M (in yellow),* ***Ru_sil*** *1E-5 M (in red), a mixture solution of* ***Ir_sil*** *and* ***Ru_sil*** *of 2.3E M for each compound (in grey) and the calculated with the least squares fit of equation 6 (dotted line in blue).*

As mentioned before, these functionalized surfaces were aimed to be used as model substrates for the optimization of the optical setup. In this venue, mixed surfaces were also aimed to determine the limit of detection of the optical instrumentation (i.e. the minimum number of molecules of one color that can be detected on a surface covered by molecules emitting in a different color).

Therefore, some preliminary experiments were carried out. Several surfaces were prepared with different proportions of **Ir_sil** and **Ru_sil**. Again, based on the spectra of these surfaces, the estimation of the deposited quantity of **Ir_sil** and **Ru_sil** was calculated, by combining the calculus previously described for mixed solutions and pure compound functionalized surfaces.

With the obtained coefficients, the amount of deposited model compound was estimated for each slide with the equation of the surface coverage introduced earlier. **Table 4.6** summarizes 5 substrates with different proportions of immobilized **Ir_sil** and **Ru_sil**. As an example, the absorption spectrum of the substrate C in **Table 4.6** is shown in **Figure 4.27**, together with the calculated absorption of the corresponding **Ir_sil** and **Ru_sil** and their summed absorption spectra.

Table 4.6. *Concentration of the mother solutions and quantification of some* ***Ir_Ru_Q*** *surfaces.*

	solutions				surfaces	
	[Ir_sil] · $1E^5$ M	[Ru_sil] · $1E^5$ M	%Ir exp.	%Ru exp.	%Ir exp.	%Ru exp.
Ru_sil		4.73	0	100		
A	0.34	4.00	8	92	1	99
B	0.70	3.48	17	83	2	98
C	1.69	2.19	44	56	8	91
D	2.64	0.88	75	25	46	54
E	2.96	0.41	88	12	67	36
Ir_sil	3.50		100	0		

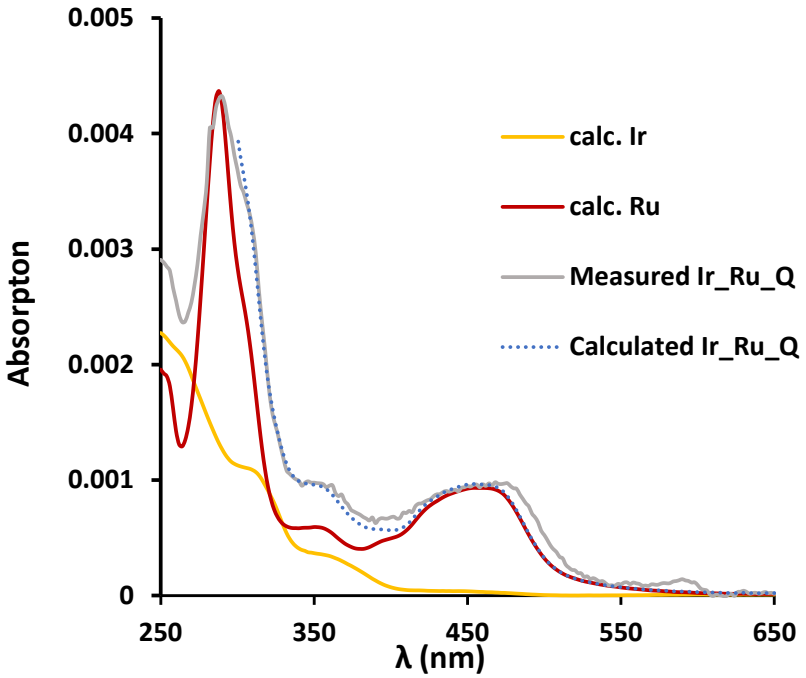

Figure 4.27. *Absorption spectra of calculated* ***Ir_sil*** *and* ***Ru_sil*** *and the sum of them, and the experimental spectrum of the* ***Ir_Ru_Q*** *sample.*

Based on these results (**Table 4.6**), the immobilization of **Ru_sil** appeared to be faster compared to **Ir_sil**. This was contradictory, if these results were compared to the pure surface deposition, where by using the same concentration of mother solution of $1 \cdot 10^{-5}$

M, the amount of deposited **Ru_sil** and **Ir_sil** was around 0.4 ML and 0.6 ML, respectively. Based on the similar structure of **Ru_sil** and **Ir_sil**, one could imagine a comparable deposition effectivity. Several reasons could explain the unpaired coverage obtained: some kind of hindrance or competition between the two compounds, or an erroneous mother solution concentration as a result of salt impurities in their batches, since Thus, further experiments are currently under development to clarify this result.

4.3 COMPOUND C6

As described in Chapter 3, **C6** complex showed the best results for Ba^{2+} sensing. Thus, **C6** was chosen to be immobilized over a quartz surface and study its behaviour. **Figure 4.28** shows the linker-fluorophore-receptor design, **C6_sil**, envisaged for the deposition of **C6**.

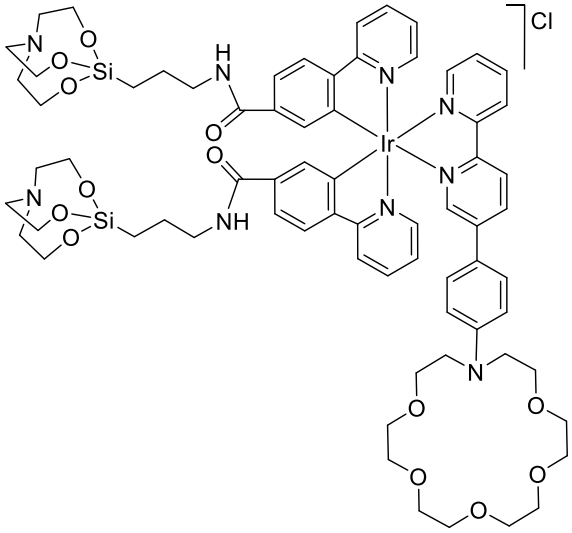

C6_sil

Figure 4.28. *Structure design for compound* ***C6_sil****.*

To introduce the appended silatrane groups, the same approach described before for **Ru_sil** and **Ir_sil** was attempted (amide formation). However, in this case, unlike in the compounds described before (**Ru_sil** and **Ir_sil**) the ancillary bipyridyl ligand could not bear the spacers, as they allocate the receptor unit for Ba^{2+}. Thus, the **C6_sil** has been designed to incorporate two APSIL spacers appended to the two cyclometalating phenylpyridines.

In the following section, the synthesis of **C6_sil** and its immobilization on a quartz surface will be described, together with the photophysical characterization of the samples.

4.3.1 Synthesis

The synthetic route of **C6_sil** involved the synthesis of complex **C6_COOH**, starting from the commercially available 4-(2-pyridinyl)benzoic acid and iridium precursor, to form the dimer and the iridium complex, and lastly, append the APSIL. Since the design of **C6_sil** incorporated the two appended anchoring groups in the ppy ligands –not in the bipyridyl ligand– the addition of the APSIL was performed in the last step. This reactions sequence was designed to avoid the degradation of the silatrane during the harsh conditions employed for the synthesis of the iridium-dimer, if it was introduced directly on the 4-(pyridin-2-yl)benzoic acid . Thus, the designed pathway to obtain the **C6_sil** is shown in **Scheme 4.6**.

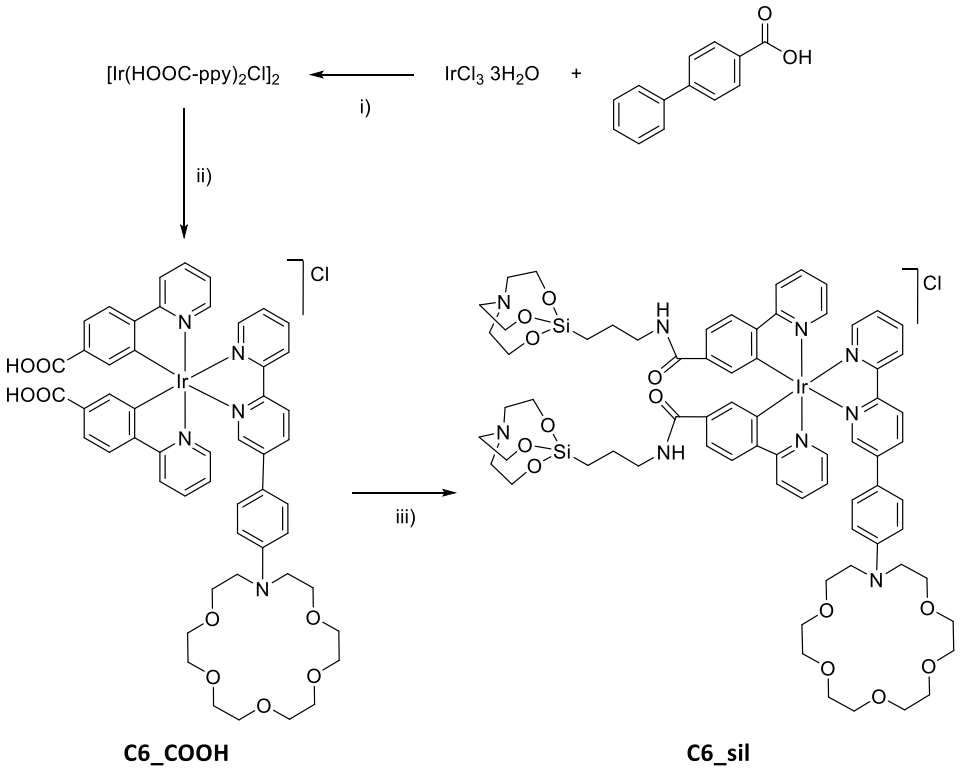

Scheme 4.6. *Synthetic route toward **C6_sil**. i) H_2O/2-ethoxyethanol (1:4, v/v), 110 °C. ii) **L2**, CH_2Cl_2/MeOH (2:1, v/v), 35 °C. iii) EDC·HCl, NHS, **22**, DMF, RT.*

The carboxylic acid-containing dimer was obtained by refluxing iridium precursor $IrCl_3 \cdot 3H_2O$ and 4-(pyridin-2-yl)benzoic acid in a mixture of H_2O and 2-ethoxyethanol (1:4, v/v).

The precipitate formed during the reaction was filtered and dried, giving an orange solid in 60% yield.

The coordination of **L2** ligand with iridium to yield **C6_COOH** was performed by following the same conditions described previously for the parent cationic complex **C6** in Chapter 3. The dimer and **L2** were refluxed for 16 h in a CH_2Cl_2 and MeOH mixture. After that time, the solvents were evaporated and the residue was washed with small amounts of CH_2Cl_2, to yield a red solid with a 70% yield. The ^{1}H NMR of the isolated **C6_COOH** confirmed the purity of the product (**Figure 4.29**), although the signals could not be assigned due to the complexity of the spectrum. Despite the complexity, the two doublets corresponding to the rotating phenyl unit in the ligand could be clearly distinghished at 6.73 and 7.17 ppm.

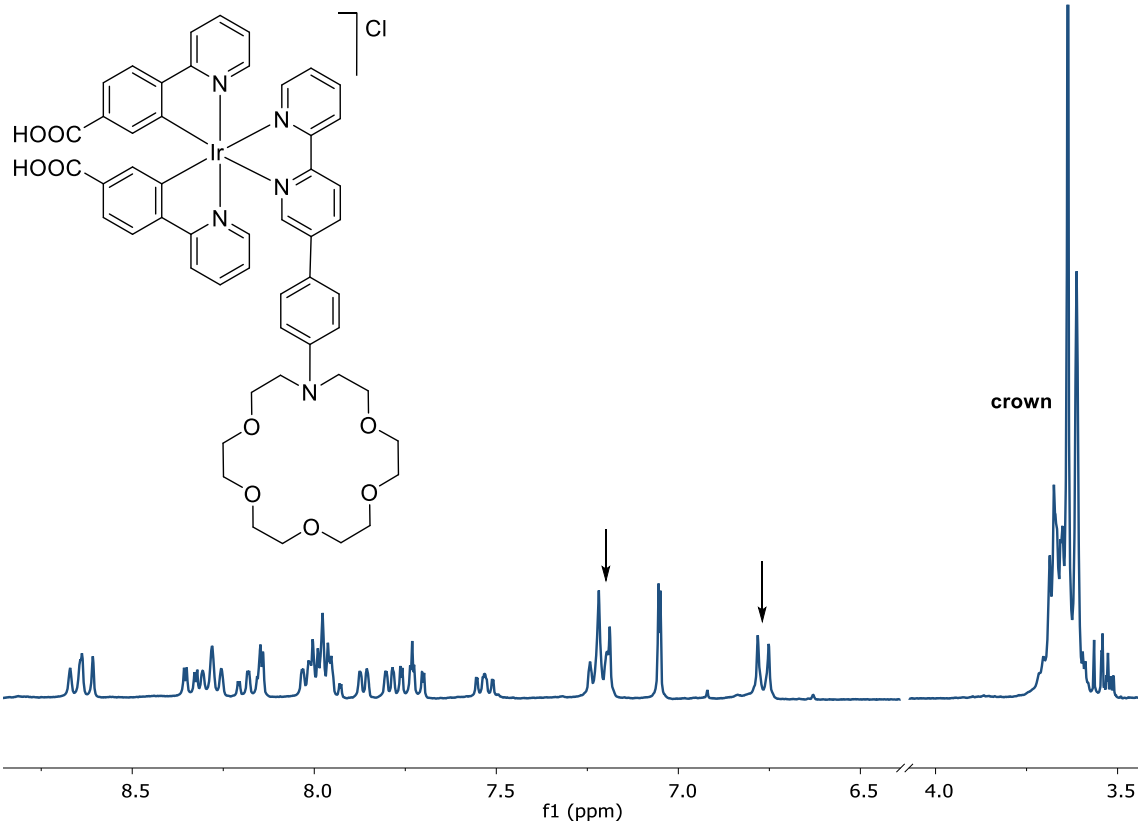

Figure 4.29. *^{1}H NMR of purified **C6_COOH** and its structure (CD_3OD, 300 MHz). The doublets corresponding to the rotating pehyl unit in **C6_COOH** are marked with an arrow.*

The procedure followed for the synthesis of **19** was reproduced for the last step to synthesize **C6_sil**. The complex **C6_COOH** was refluxed in $SOCl_2$ for 16 h. After this time, the excess of $SOCl_2$ was evaporated under reduced pressure, and the residue was

dissolved in CH_2Cl_2. This solution was added over a previously prepared solution of **20** and Et_3N in CH_2Cl_2. The reaction was stirred for 16 h, after checking the basicity of the mixture (and correcting if necessary by addition of NEt_3), the solvent of the reaction was evaporated, and the residue was analyzed by H^1 NMR. The spectrum did not show any signals that could correspond to the formation of the product. In addition, signals assigned to the decomposition of the starting complex **C6_COOH** were observed. It was concluded that the azacrownether present in the ancillary the ligand decomposed under the reaction conditions ($SOCl_2$), which was necessary to form the acyl chloride intermediate formation.

Therefore, an alternative methodology to form the corresponding amide was attempted, based on a procedure described by Eswaramoorthy et al. for the modification of APTES-covered surfaces by amidation. This methodology is also widely used to form amide functionalizations in proteins.[62–64] EDC·HCl, 1-ethyl-3-(3-dimethylaminopropyl)carbodiimide hydrochloride, is a cross-linking agent generally used to facilitate the formation of amide bonds between a carboxylic group and a primary amine. As depicted in **Scheme 4.7**, first, it reacts with the carboxylic acid forming the intermediate (O-acyl isourea), which reacts with an amino group generating the respective amide bond and forming the isourea as a by-product. The intermediate formed is not very stable, and it is easily hydrolysed, so to increase the effectiveness of the reaction NHS, N-hydroxysuccinimide, is used, which stabilizes the intermediate product for the subsequent attack of the amino group.

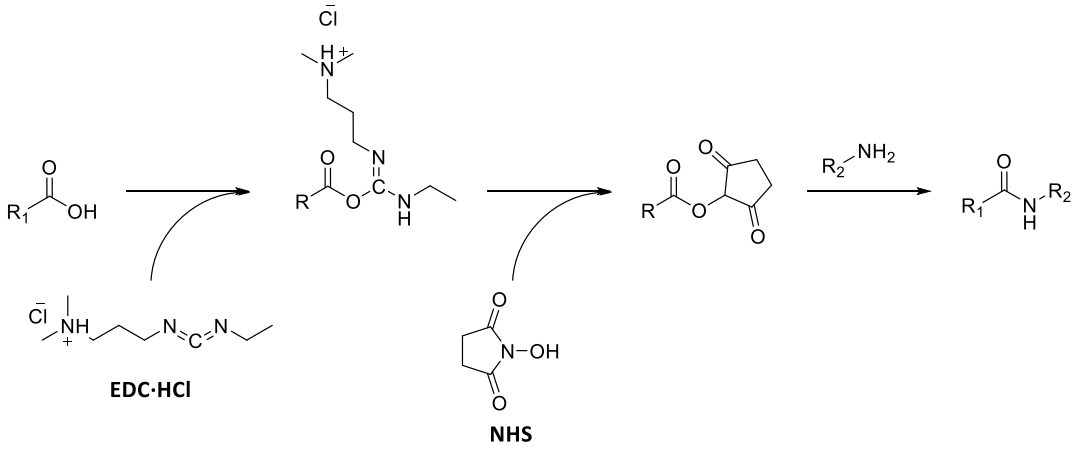

Scheme 4.7. *EDC·HCl/NHS chemistry.*

Thus, the EDC·HCl/NHS chemistry was attemted for the amide formation. This way, a solution of NHS (5 equiv.) and EDC (5 equiv.) in anhydrous DMF was stirred for 10 minutes. After this time, this solution was added over a solution of **C6_COOH** in DMF and, ultimately, **22** (10 equiv.) was added. The mixture was stirred for 16 h at room temperature. The desired product **C6_COOH** was extracted with CH_2Cl_2 and washed with brine several times. The red residue was analyzed by H^1 NMR (**Figure 4.30**).

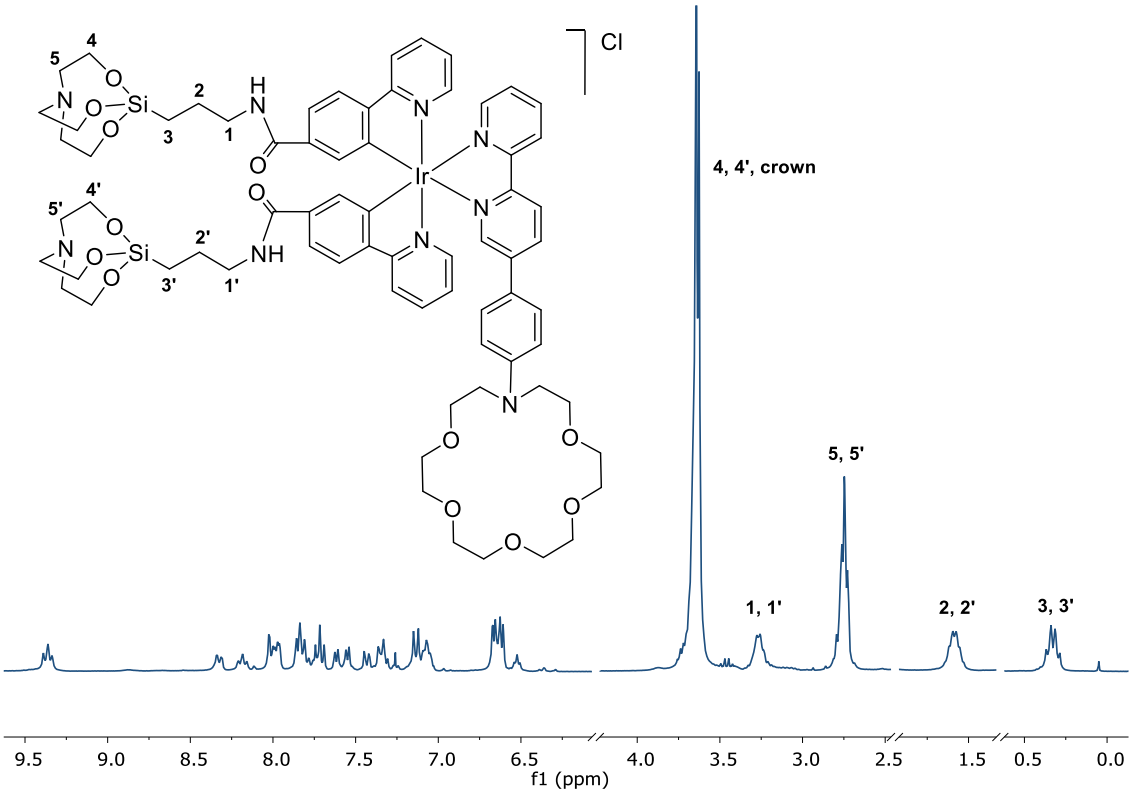

Figure 4.30. *^{1}H NMR of purified **C6_sil** and its partially assigned structure (CD_3OD, 300 MHz).*

The aromatic region of the spectrum, although not assigned due to its complexity, showed a spectroscopic pattern compatible with the expected compound. The aliphatic region showed the shift anticipated for the CH_2 next to the nitrogen, 1 and 1' in the structure, from 2.64 ppm to 3.27 ppm. The spectrum showed another four aliphatic signals assigned to position 3 and 3', 2 and 2', 5 and 5'and the characteristic signals of the azacrownether.

The peak corresponding to 4 and 4', masked by the intense signal of the azacrownether, was identified by COSY experiments (**Figure 4.31**).

To further ensure the identity of the compound, a DOSY NMR experiment was performed (**Figure 4.32**). The spectrum confirmed that the protected APTES reacted with the iridium complex. The purity and identity of the compound **C6_sil** was completed by ^{13}C NMR, HSQC and mass spectrometry.

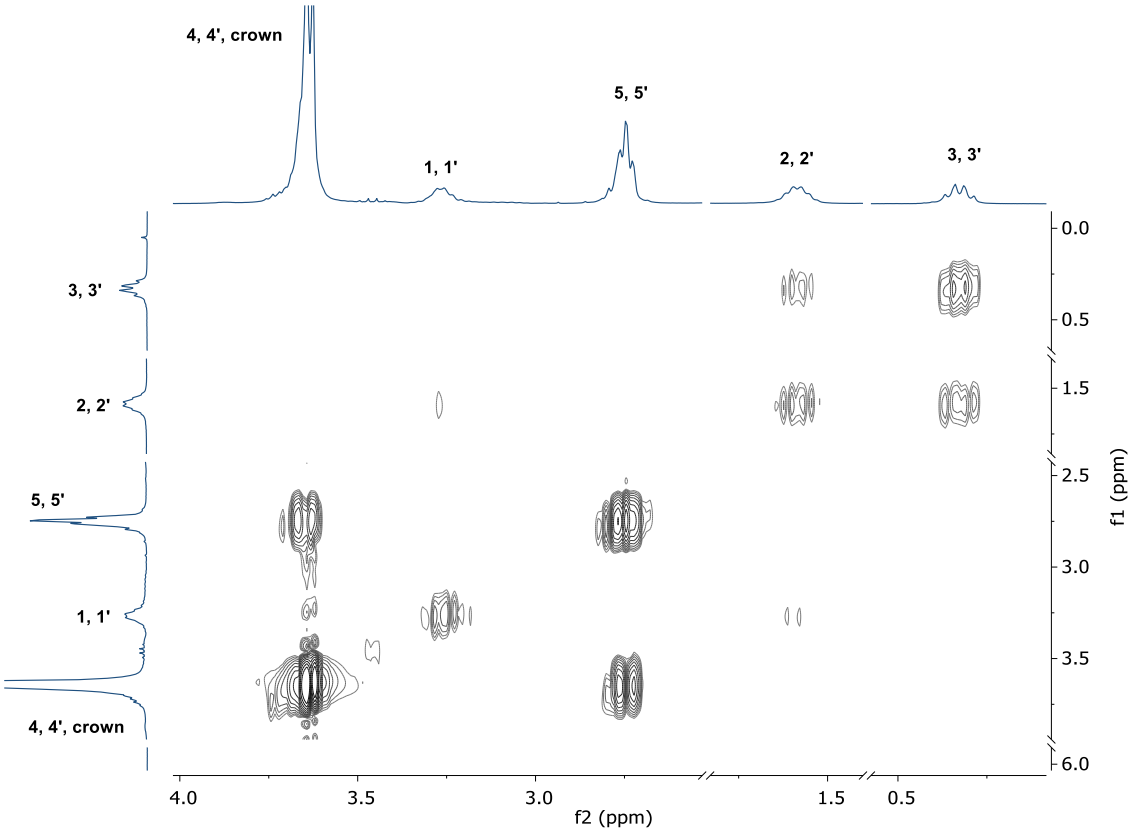

Figure 4.31. *Aliphatic region of COSY NMR of isolated* ***C6_sil*** *(CD_3OD, 300 MHz).*

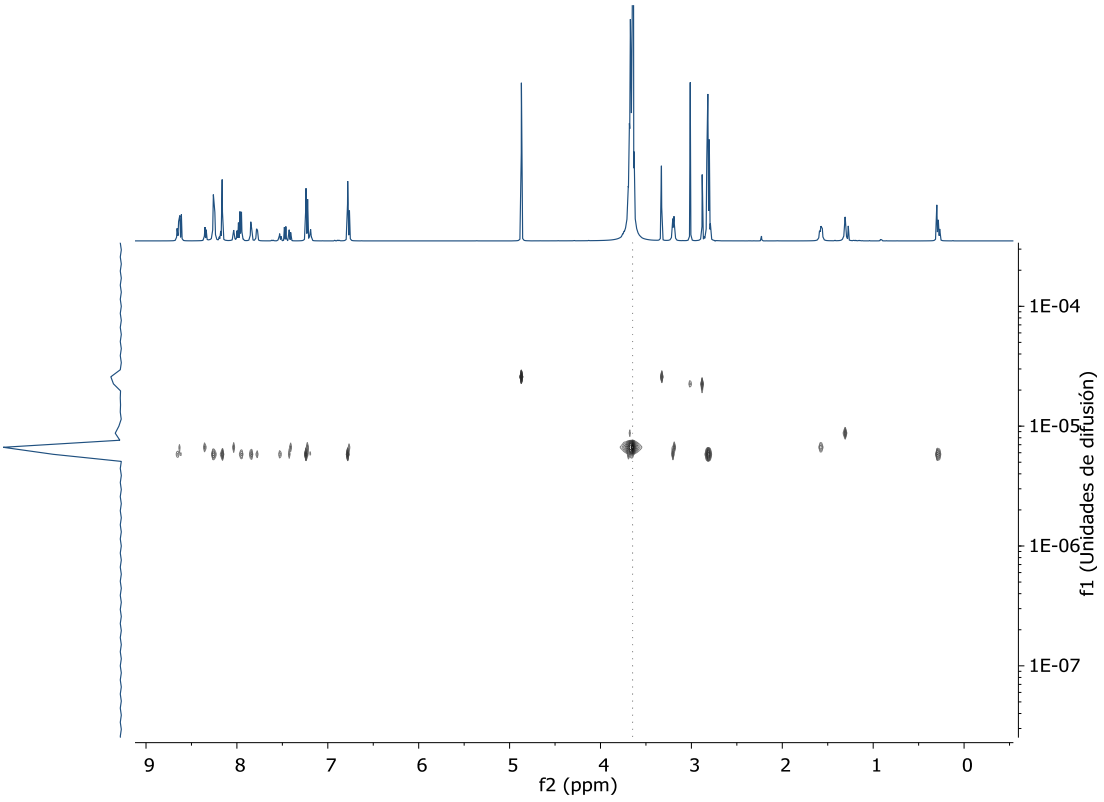

Figure 4.32. *DOSY NMR of isolated* ***C6_sil*** *(CD_3OD, 500 MHz).*

4.3.2 Photophysical characterization

The absorption and emission spectra of **C6_COOH** and **C6_sil** were measured in MeCN solution, and compared to the spectra of the parent **C6**. The data is summarized in **Table 4.7**. **Figure 4.33** shows the absorption spectra of **C6**, **C6_COOH** and **C6_sil**, in their free and Ba^{2+}-bound form. The spectra of the three **C6**-derivatives present very similar features.

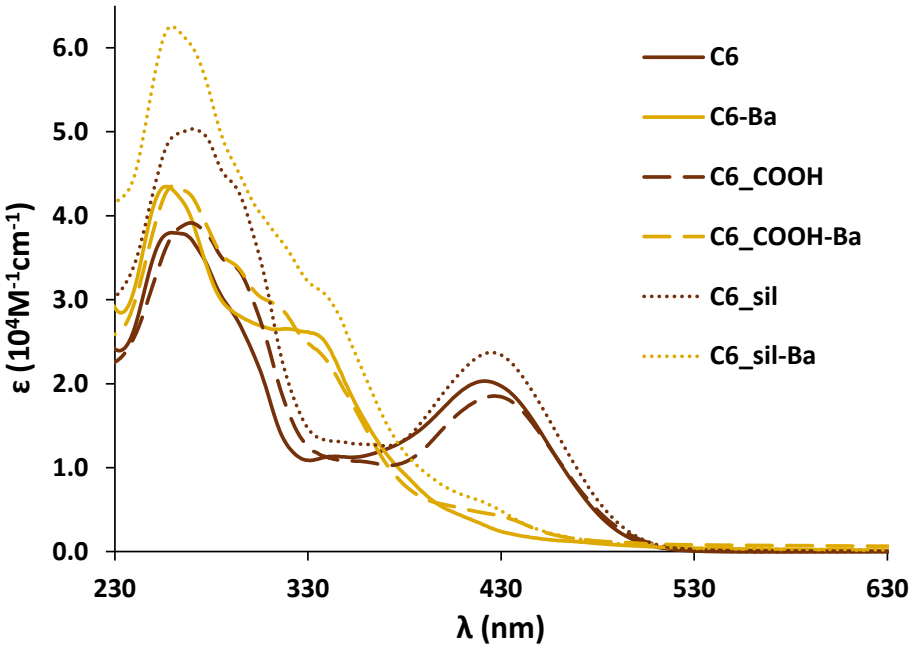

Figure 4.33. *Absorption spectra of* ***C6****,* ***C6_COOH*** *and* ***C6_sil*** *without and with* Ba^{2+}.

Figure 4.34 shows the normalized emission spectra of the three adducts, in their free and bound form, excited at their corresponding isosbestic point. Clearly, the emission maxima of the free compounds concur in the same exact wavelength, unaffected by the addition of functional groups in the phenylpyridines. This is consistent with the hypothesis that the green emission of **C6** is centered in the bipyridine ligand.[65] Unfortunately, the band attributed to a ^{3}MLCT transition (the main band for the chelated compounds), is marginally present in the free form of **C6_COOH** and **C6_sil** compounds.

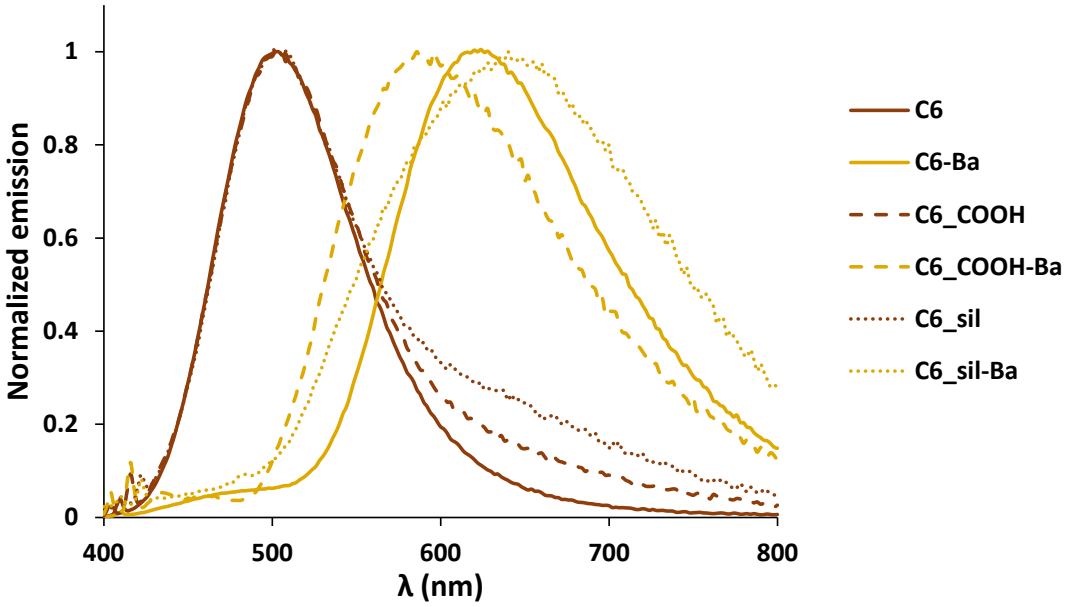

Figure 4.34. *Emission spectra of **C6**, **C6_COOH** and **C6_sil** without and with Ba^{2+}.*

Table 4.7. *Absorption and emission properties of **C6**, **C6_COOH** and **C6_sil** without and with Ba^{2+}.*

	K_a (M^{-1})	Absorption		Emission		
		Isosb. point	λ_{max} [nm] (ε [$10^4 M^{-1}cm^{-1}$])[a]	λ_{max} [nm][b]	τ [ns] (contribution)[d]	Φ [%][c]
C6	$4.3 \cdot 10^5$	370	263, (4.00), 293 (3.02), 349 (1.24), 424 (2.14)	502	2.8	0.04
C6-Ba			259 (4.13), 323 (2.67), 337 (2.59), 413 (0.34)	478 618	2.5 11 (12%), 121 (64%), 371 (24 %)	0.1
C6_COOH	$4.8 \cdot 10^6$	373	265 (5.61), 293 (4.70), 363 (1.51), 429 (2.44)	500	2.8	0.022
C6_COOH-Ba			250 (5.58), 277 (4.41), 394 (3.73), 428 (2.85), 451 (0.68)	590	8.4 (32%), 83.8 (14%), 458.4 (53%)	0.062
C6_sil	$1.5 \cdot 10^5$	378	276 (5.31), 297 (4.39), 347 (1.39), 366 (1.35), 429 (2.50)	500	2.8	0.013
C6_sil-Ba			260 (5.58), 297 (3.95), 317 (3.31), 342 (2.65), 420 (0.46)	470 600	3.5 7.2 (23%), 499 (77%)	0.046

MeCN solutions. a) Based on linear regression of the measured absorption of 6 concentrations in the range 10^{-4} M–10^{-6}M. b) Excitation at their corresponding isosbesting points. c) Φ Measured at the corresponding isosbestic point at 0.1 optical density in argon-equilibrated MeCN. d) Acquired on argon-equilibrated solutions using EPLED 340 nm, TCSPC mode at 10MHz or 20MHz for the HB and MCS mode at 10KHz or 20 KHz for the LB. e) All χ^2 values were between 1.0-1.2.

As described in the last section of the introduction, there are counted examples in the literature of sensors anchored onto a surface with ratiometric response. Additionally, for all of them, their emission change is based on the analyte-induced structural change

on the sensor (i.e. chemodosimeters).[66–68] Thus, as far as we know, no ratiometric chemical sensor for cations on surfaces have been reported to date.

Preliminary experiments to deposit the **C6_sil** over quartz surfaces were carried out, to test the response of **C6**-based sensors on solid supports. The same procedure used for the model immobilization was followed. In this case, the mother solution concentration was varied from $4.6 \cdot 10^{-4}$ to $4.6 \cdot 10^{-6}$ M. The normalized absorption spectrum of **C6_Q** is compared to **C6_sil** dissolution in **Figure 4.35**. It is worth mentioning that the relative intensity of the different absorption bands is slightly different when the compound is anchored onto a surface compared with the spectrum in solution. At this moment, we do not have a clear explanation for this observation.

Another unexpected difference could be observed in the emission spectrum of **C6** anchored on the surface: the emission maxima appears at 585 nm, with 80 nm redshift compared to **C6_sil**. This is a rather remarkable unfortunate shift, as the emission of Ba^{2+} chelated **C6** also falls in this region.

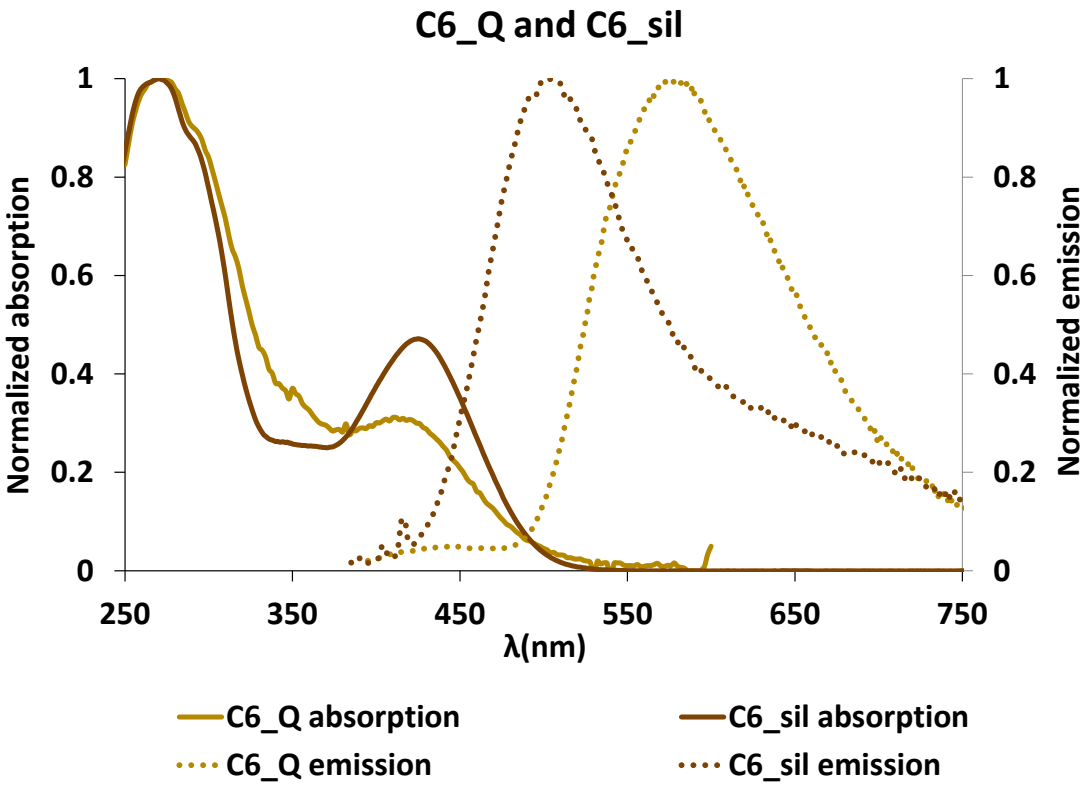

Figure 4.35. *Absorption (solid line) and emission (dotted line) spectra of **C6_Q** and **C6_sil**.*

The degree of coverage of the substrates was calculated based on the UV-vis absorption of **C6_Q** samples (**Figure 4.36**), using the same method described before for **Ir_Q** and **Ru_Q** samples. The data is summarized in **Table 4.8**. In the case of the surfaces prepared using the mother solution of $4.6 \cdot 10^{-6}$ M concentration, the degree of coverage could not be quantified, due to the low signal. However, the emission could be measured, as shown in **Figure 4.36**. it is worth noticing that the emissions observed in the region 400–500 nm are due to quartz fluorescence, which is noticeable at this sub-monolayer degree of coverage.

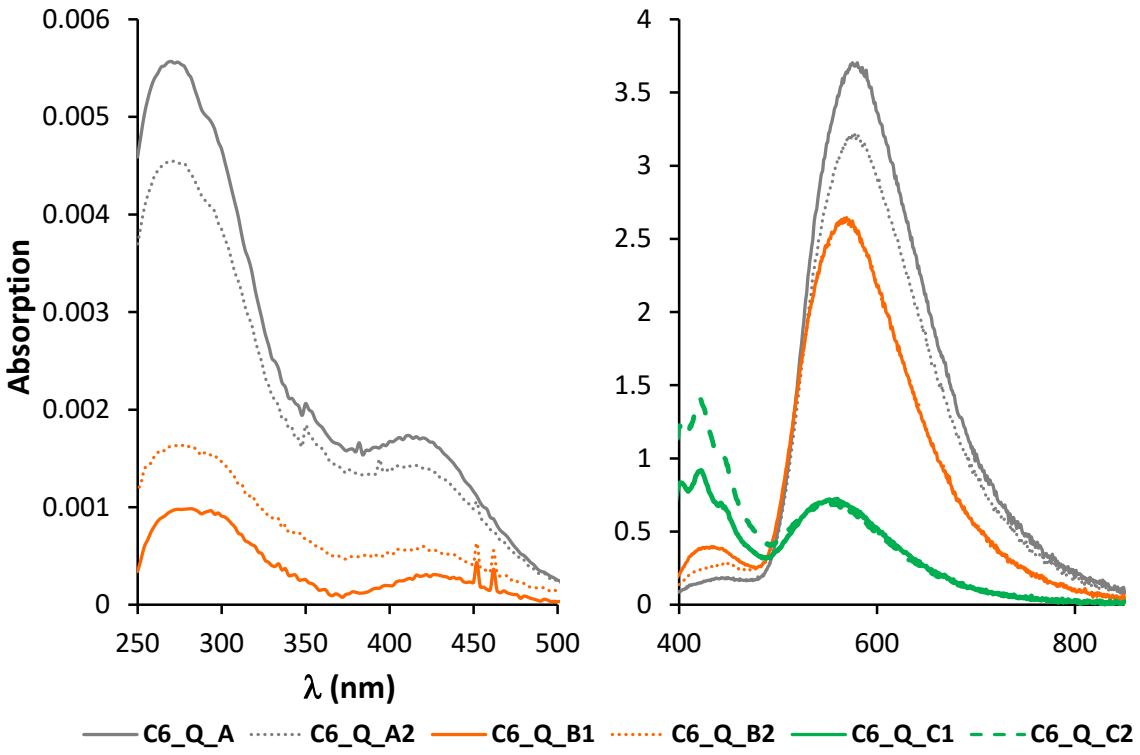

Figure 4.36. *Absorption and emission spectra of* ***C6_Q*** *samples.*

Table 4.8. *Measured* ***C6_Q*** *surfaces.*

code	[C6_sil] M	ML	molec/cm^2
C6_Q_A1	0,46 mM	0.660	6.60E+13
C6_Q_A2	0,46 mM	0.540	5.40E+13
C6_Q_B1	0,046 mM	0.110	1.10E+13
C6_Q_B2	0,046 mM	0.190	1.90E+13
C6_Q_C1	0,0046 mM	-	-
C6_Q_C2	0,0046 mM	-	-

After the surfaces were characterized, in a preliminary test, the addition of Ba^{2+} to the surfaces was studied. This was performed by dipping the functionalized quartz surface on a $Ba(ClO_4)_2$ containing MeCN solution. The surfaces were washed afterwards with MeCN. The absorption and emission spectra of the Ba^{2+} containing **C6_Q** is compared to **C6_Q** in **Figure 4.37**.

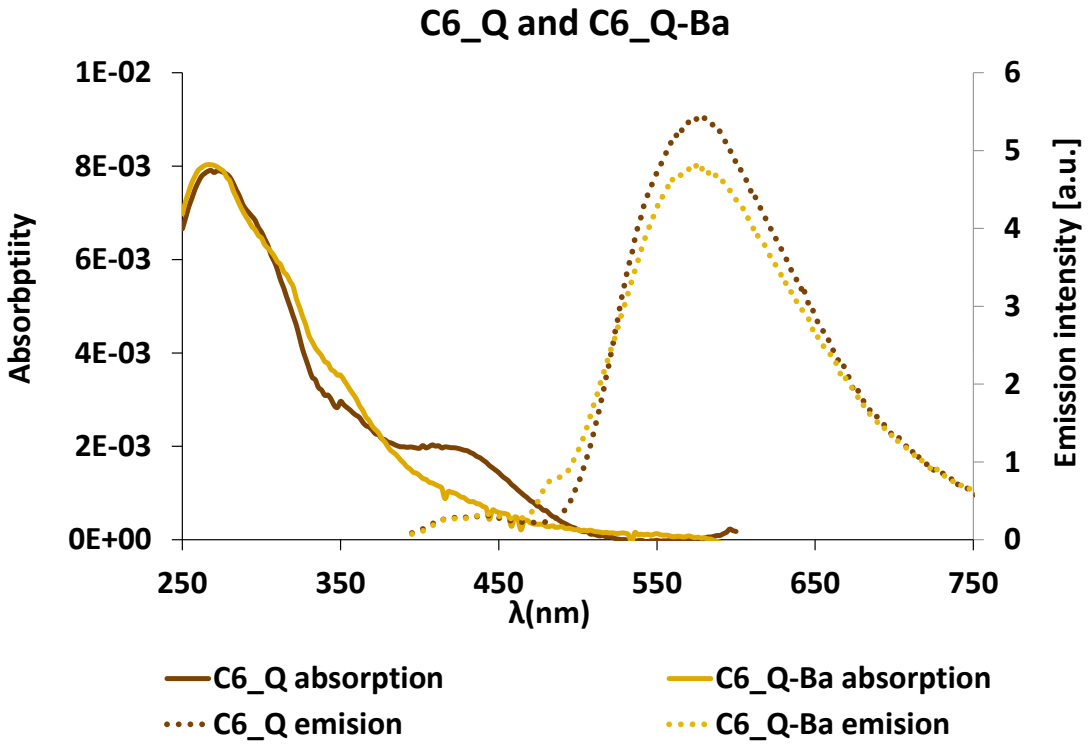

Figure 4.37. *Absorption and emission spectra of Ba^{2+} containing **C6_Q** and **C6_Q** samples.*

The absorption band at 430 nm, present in **C6_Q**, diminishes upon Ba^{2+} addition, which could be a good signal. However the emission did not change if **C6_Q** and Ba^{2+} containing **C6_Q** are compared. The emission of the free **C6_Q** at 600 nm, could be the residual emission present for **C6** and derivates in solution. And the fluorescence emission could be dead.

Despite this discouraging preliminary result, further studies will be carried out in the following experiments, to understand this behavior and achieve the desired color change upon Ba^{2+}.

4.4 References

1 J. B. Shein, L. M. H. Lai, P. K. Eggers, M. N. Paddon-Row and J. J. Gooding,

Langmuir, 2009, **25**, 11121–11128.

2 L. Rösler, M. V. Höfler, H. Breitzke, T. Wissel, K. Herr, H. Heise, T. Gutmann and G. Buntkowsky, *Cellulose*, 2022, **29**, 6283–6299.

3 G. Pieters and L. J. Prins, *New Journal of Chemistry*, 2012, 36, 1931–1939.

4 A. F. Raigoza, W. Fies, A. Lim, K. Onyirioha and L. J. Webb, *Applied Surface Science*, 2017, **394**, 288–296.

5 T. Narayan, S. Kumar, S. Kumar, S. Augustine, B. K. Yadav and B. D. Malhotra, *Talanta*, 2019, **201**, 465–473.

6 S. H. Lee, W. Y. Rho, S. J. Park, J. Kim, O. S. Kwon and B. H. Jun, *Scientific Reports*, 2018, **8**, 1–8.

7 E. Pensa, E. Cortés, G. Corthey, P. Carro, C. Vericat, M. H. Fonticelli, G. Benítez, A. A. Rubert and R. C. Salvarezza, *Accounts of Chemical Research*, 2012, **45**, 1183–1192.

8 C. Vericat, M. E. Vela, G. Benitez, P. Carro and R. C. Salvarezza, *Chemical Society Reviews*, 2010, **39**, 1805–1834.

9 H. Häkkinen, *Nature Chemistry*, 2012, 4, 443–455.

10 D. P. Woodruff, *Physical Chemistry Chemical Physics*, 2008, **10**, 7211–7221.

11 J. Zhao, M. Milanova, M. M. C. G. Warmoeskerken and V. Dutschk, *Colloids and Surfaces A: Physicochemical and Engineering Aspects*, 2012, **413**, 273–279.

12 S. Mallakpour and M. Dinari, *Materials Research Bulletin*, 2013, **48**, 3865–3872.

13 A. R. Mahdavian and M. A. S. Mirrahimi, *Chemical Engineering Journal*, 2010, **159**, 264–271.

14 R. Helmy and A. Y. Fadeev, *Langmuir*, 2002, **18**, 8924–8928.

15 J. N. Ding, P. L. Wong and J. C. Yang, *Wear*, 2006, **260**, 209–214.

16 S. P. Pujari, L. Scheres, A. T. M. Marcelis and H. Zuilhof, *Angewandte Chemie - International Edition*, 2014, 53, 6322–6356.

17 T. Dey and D. Naughton, *Journal of Sol-Gel Science and Technology*, 2016, 77, 1–27.

18 J. Sabek, L. Torrijos-Morán, A. Griol, Z. D. Betancor, M. J. Bañuls Polo, Á. Maquieira and J. García-Rupérez, *Biosensors*, 2019, **9**, 6.

19 N. Rozlosnik, M. C. Gerstenberg and N. B. Larsen, *Langmuir*, 2003, **19**, 1182–1188.

20 Y. Liu, L. K. Wolf and M. C. Messmer, *Langmuir*, 2001, **17**, 4329–4335.

21 A. M. Salvi, R. Pucciariello, M. R. Guascito, V. Villani and L. Intermite, *Surface and Interface Analysis*, 2002, **33**, 850–861.

22 C. Carraro, O. W. Yauw, M. M. Sung and R. Maboudian, *Journal of Physical Chemistry B*, 1998, **102**, 4441–4445.

23 T. Vallant, H. Brunner, U. Mayer, H. Hoffmann, T. Leitner, R. Resch and G. Friedbacher, *Journal of Physical Chemistry B*, 1998, **102**, 7190–7197.

24 A. Glaser, J. Foisner, H. Hoffmann and G. Friedbacher, *Langmuir*, 2004, **20**, 5599–5604.

25 A. R. El-Ghannam, P. Ducheyne, M. Risbud, C. S. Adams, I. M. Shapiro, D. Castner, S. Golledge and R. J. Composto, *Journal of Biomedical Materials Research - Part A*, 2004, **68**, 615–627.

26 K. E. Sapsford and F. S. Ligler, *Biosensors and Bioelectronics*, 2004, **19**, 1045–1055.

27 G. Balasundaram, M. Sato and T. J. Webster, *Biomaterials*, 2006, **27**, 2798–2805.

28 P. Filippini, G. Rainaldi, A. Ferrante, B. Mecheri, G. Gabrielli, M. Bombace, P. L. Indovina and M. T. Santini, *Journal of Biomedical Materials Research*, 2001, **55**, 338–349.

29 T. Nakagawa, T. Tanaka, D. Niwa, T. Osaka, H. Takeyama and T. Matsunaga, *Journal of Biotechnology*, 2005, **116**, 105–111.

30 S. N. Kim, J. M. Slocik and R. R. Naik, *Small*, 2010, **6**, 1992–1995.

31 H. Tang, W. Zhang, P. Geng, Q. Wang, L. Jin, Z. Wu and M. Lou, *Analytica Chimica Acta*, 2006, **562**, 190–196.

32 H. H. Kyaw, S. H. Al-Harthi, A. Sellai and J. Dutta, *Beilstein Journal of Nanotechnology*, 2015, **6**, 2345–2353.

33 D. Enders, T. Nagao, A. Pucci and T. Nakayama, *Surface Science*, 2006, **600**, L71–L75.

34 E. S. Kooij, E. A. Martijn Brouwer, H. Wormeester and B. Poelsema, *Langmuir*, 2002, **18**, 7677–7682.

35 S. Gao, J. M. Guisán and J. Rocha-Martin, *Analytica Chimica Acta*, 2022, 1189, 338907.

36 D. Maraldo and R. Mutharasan, *Sensors and Actuators, B: Chemical*, 2007, **123**, 474–479.

37 J. Huang, Z. Xie, L. Xie, S. Luo, T. Zeng, Y. Zhang, M. Zhang, S. Wang, M. Li, Y. Wei, Q. Fan, Z. Xie, X. Deng and D. Li, *Scientific reports*, 2022, **12**, 22444.

38 M. J. Saif, H. M. Asif and M. Naveed, *Journal of the Chilean Chemical Society*, 2018, 63, 4109–4125.

39 E. Honarvarfard, M. Gamella, N. Guz and E. Katz, *Electroanalysis*, 2017, **29**, 324–329.

40 B. V. V. S. P. Kumar, K. Salikolimi and M. Eswaramoorthy, *Langmuir*, 2014, **30**, 4540–4544.

41 M. Matsunaga, T. Ueno, T. Nakanishi and T. Osaka, *Electrochemistry Communications*, 2008, **10**, 1844–1846.

42 Y. Fang, H. M. Wang, Y. X. Gu, L. Yu, A. J. Wang, P. X. Yuan and J. J. Feng, *Analytical Chemistry*, 2020, **92**, 3206–3212.

43 B. Azadbakht, H. Afarideh, M. Ghannadi-Maragheh, A. Bahrami-Samani and M. Asgari, *Nuclear Medicine and Biology*, 2017, **48**, 26–30.

44 P. Mandal, R. A. Molla, A. P. Chattopadhyay, S. Poddar and H. S. Biswas, *Inorganic Chemistry Communications*, 2022, **144**, 109825.

45 Q. M. Wang, *Solid State Sciences*, 2009, **11**, 1617–1620.

46 K. R. Kim, Y. D. Han, H. J. Chun, K. W. Lee, D. K. Hong, K. N. Lee and H. C. Yoon, *Biosensors*, 2017, **7**, 48.

47 T. Kao, F. Kohle, K. Ma, T. Aubert, A. Andrievsky and U. Wiesner, *Nano Letters*, 2018, **18**, 1305–1310.

48 K. Fidecka, J. Giacoboni, P. Picconi, R. Vago and E. Licandro, *RSC Advances*, 2020, **10**, 13944–13948.

49 G. M. Greenway, A. Greenwood, P. Watts and C. Wiles, *Chemical Communications*, 2006, **85**, 85–87.

50 H. Wei, Y. Du, J. Z. Kang, G. B. Xu and E. K. Wang, *Chinese Journal of Chemistry*, 2007, **25**, 159–163.

51 X. Wu, L. Song, B. Li and Y. Liu, *Journal of Luminescence*, 2010, **130**, 374–379.

52 A. Glaser, J. Foisner, H. Hoffmann and G. Friedbacher, *Langmuir*, 2004, **20**, 5599–5604.

53 K. W. Huang, C. W. Hsieh, H. C. Kan, M. L. Hsieh, S. Hsieh, L. K. Chau, T. E. Cheng and W. T. Lin, *Sensors and Actuators, B: Chemical*, 2012, **163**, 207–215.

54 K. L. Materna, B. J. Brennan and G. W. Brudvig, *Dalton Transactions*, 2015, **44**, 20312–20315.

55 K. L. Materna, J. Jiang, R. H. Crabtree and G. W. Brudvig, *ACS Applied Materials*

and Interfaces, 2019, **11**, 5602–5609.

56 Y. You and S. Y. Park, *Journal of the American Chemical Society*, 2005, **127**, 12438–12439.

57 D. L. Ma, H. Z. He, H. J. Zhong, S. Lin, D. S. H. Chan, L. Wang, S. M. Y. Lee, C. H. Leung and C. Y. Wong, *ACS Applied Materials and Interfaces*, 2014, **6**, 14008–14015.

58 S. Ji, W. Wu, W. Wu, P. Song, K. Han, Z. Wang, S. Liu, H. Guo and J. Zhao, *Journal of Materials Chemistry*, 2010, **20**, 1953–1963.

59 T. Tang, J. Qu, K. Müllen and S. E. Webber, *Langmuir*, 2006, **22**, 26–28.

60 A. L. Bramblett, M. S. Boeckl, K. D. Hauch, B. D. Ratner and T. Sasaki, *Surface and Interface Analysis*, 2002, **33**, 506–515.

61 A. L. Bramblett, M. S. Boeckl, K. D. Hauch, B. D. Ratner and T. Sasaki, *Surface and Interface Analysis*, 2002, **33**, 506–515.

62 R. Pugliese and F. Gelain, *International Journal of Molecular Sciences*, 2020, **21**, 1–14.

63 C. Wang, Q. Yan, H. B. Liu, X. H. Zhou and S. J. Xiao, *Langmuir*, 2011, **27**, 12058–12068.

64 D. Bartczak and A. G. Kanaras, *Langmuir*, 2011, **27**, 10119–10123.

65 A. Y. Gitlina, M. V. Ivonina, V. V. Sizov, G. L. Starova, A. P. Pushkarev, D. Volyniuk, S. P. Tunik, I. O. Koshevoy and E. V. Grachova, *Dalton Transactions*, 2018, **47**, 7578–7586.

66 J. R. Acharya, H. Zhang, X. Li and E. E. Nesterov, *Journal of the American Chemical Society*, 2009, **131**, 880–881.

67 B. G. Imsick, J. R. Acharya and E. E. Nesterov, *Advanced Materials*, 2013, **25**, 120–124.

68 B. G. Imsick, J. Raj Acharya and E. E. Nesterov, *Chemical Communications*, 2013, **49**, 7043–7045.